UNIVERSITÀ DEGLI STUDI DI CATANIA

DOTTORATO DI RICERCA IN FISICA

Diana Carbone

First experimental evidence of the Giant Pairing Vibration in atomic nuclei

Ph.D. Thesis

Ph.D. Coordinator: Prof. F. Riggi

Tutor: Prof. F. Cappuzzello

Co-Tutor: Dr. M. Cavallaro

XXV CICLO 2009 – 2012

"… Datemi una curva e partirò per la tangente…"

Lorenzo Cherubini – Megamix (2011)

Contents

Introduction

The main purpose of the present work is the understanding of the effects of the pairing force between nucleons in the structure of the atomic nuclei and in the nuclear reactions. This research is focused on the study of two-neutron transfer reactions, which are among the most effective probes to excite the nuclear pairing field. In particular, the (^{18}O,^{16}O) reactions at 84 MeV incident energy on ^{12}C and ^{13}C thin targets are investigated. Such study is inserted into the research line conducted at INFN Laboratori Nazionali del Sud by the DREAMS experiment.

A large body of articles, reports, essays is available nowadays on the subject of the pairing correlations and two-neutron transfer reactions. Particularly interesting for the deepening and the completeness of the description and the bibliography are the volumes of A. N. Bohr and B. R. Mottelson [1], P. Ring and P. Schuck [2] and G.R. Satchler [3], the report of R.A. Broglia, O. Hansen and C. Riedel [4] and the recent work of W. A. von Oertzen and A. Vitturi [5]. Despite the intensive research activity in this field and the significant progresses achieved, some key questions need still to be answered and the interest that these issues raise in the community of nuclear physicists is intact.

In the first Chapter, the main features of the pairing force are described. The existence of the pairing force was established since the early stages of nuclear physics, in order to explain the experimental evidence of the greater stability of even-even nuclei with respect to odd-even and odd-odd nuclei. A deeper understanding of pairing phenomena was obtained when the theory of Bardeen, Cooper and Schrieffer [6], developed to describe the behavior of electrons in superconductors, was extended to nuclear physics. Afterwards a strong emphasis was given to the discovery of excitation modes with harmonic behavior in (p,t) and (t,p) transfer reactions on even Pb isotopes [1]. This proved the existence of vibrations where the system oscillates between states (ground states of the different isotopes) characterized by angular momentum and parity 0^+ but differing by two neutrons.

The collective character due to the pairing interaction is not limited to transitions to ground states, but in principle it can extend to specific excitations at higher energies. The

elementary excitation mode known as Giant Pairing Vibration (GPV) was predicted by the theory in the 70's [7] and should lie at energies about two times the single particle harmonic oscillator quantum. The excitation of the GPV should be induced by two-nucleon transfer reactions where the angular momentum transfer is $L = 0$ and a correlated pair of nucleons in a relative *S*-wave is transferred. The prediction of the GPV was established in analogy with the Giant Resonances (GR) [8] observed in almost all nuclei from ^{3}He to the heaviest stable isotopes. The link between GPV and GR is the symmetry between particles and holes single particle states, assumed for quantum-mechanical systems of fermions, as the nuclei. In both cases a system whose structure, at zero temperature, is governed by mean field is the only required condition. GR are collective states, manifestation of a coherence mechanism in the particle-hole (*p-h*) excitations connecting major shells of the harmonic oscillator like mean field. In a symmetric manner the GPV represents the particle-particle (*p-p*) or the hole-hole (*h-h*) counterpart of the GR.

Traditionally, the theoretical predictions about the GPV are limited to the Sn and Pb even-even isotopes [9] [10], since the effects coming from the pairing condensate (Sn) or shell clousure (Pb) can be better disentangled. Nevertheless, recent *p-p* Continuum Quasi-Particle Random Phase Approximation (cQRPA) calculations in oxygen isotopes [11][12] show that the GPV is expected also in light nuclei. Despite the strong theoretical indications in favor of the existence of the GPV mode and the large amount of proves of giant modes in the p-h side, the GPV has never been clearly identified in any nucleus. Experimental attempts driven by (p,t) reaction on Pb and Sn isotopes have been performed for many years searching for GPV with scarce success [13][14][15][16].

The puzzling question about the existence of the GPV has important consequences on the quantum mechanics particle-hole symmetry, which would be broken if the non-existence of the GPV was proven. The discovery of the GPV and the study of its properties has also other important implications, which deals with a more general matter: the understanding of the structure of atomic nuclei, which is one of the most challenging problems in physics since decades. The pairing force between nucleons is in fact a key ingredient for the development of microscopic nuclear models beyond the simple hypothesis of mean field, which has governed the physics of nuclear structure in the last 60 years [3].

There are few observable directly related to the pairing force and complex analyses are needed to isolate their features. One of the most common is the measure of the energy gap of nuclei, which can be also easily extracted from many theories. However, these measures do not give enough constraints to the theoretical models, usually characterized by several free parameters. The excitation and subsequent characterization of collective motions as the GPV would greatly increase the availability of reliable observables, such as the centroid, the width and strength of that mode. Therefore, two-nucleon transfer reactions acquire a great importance in the understanding of the pairing force, since they are the specific tools to investigate nucleon-nucleon correlations inside the nuclei. Typically two-neutron transfer reactions are performed in order to avoid the complication due to the Coulomb field.

The status of the art theory regarding transfer reactions induced by heavy ions is summarized in Chapter 2, focusing on two-neutron transfer reactions. A massive literature has been constructed during the last decades on spectroscopic studies driven mainly by (p,t) or (t,p) reactions, accompanied by complementary studies on heavier projectiles [4]. Excellent reports about the latter topic are available, where the most advanced analyses are presented [5][17][18]. An important issue when dealing with two-neutron transfer reactions is that the direct one-step transfer of a correlated pair and the transfer of uncorrelated neutrons by two-step mechanisms contribute coherently to the observed cross section [5]. The former only allows the excitation of pair modes in the residual nucleus, where the two neutrons cluster together with an intrinsic angular momentum S orbiting around the core with an angular momentum L (L-S coupling). Sequential routes are, however, more effective in exciting configurations where each neutron independently couples with the core with an angular momentum j (j-j coupling). As a consequence, if a dominance of the direct one-step transfer is observed, features of the pairing correlations in nuclei are likely to be disentangled.

From the considerations above, it emerges the crucial role of the reaction mechanism in order to populate the GPV resonance, which requires a transfer of two correlated neutrons coupled to angular momentum $L = 0$. A suitable two-neutron transfer reaction with the lowest possible angular momentum transfer must be chosen in order to observe the GPV. Typically, the transfer of two nucleons is characterized by a sizeable exchange of linear momentum at the surface of the colliding systems. Transfer at small impact parameters is

hindered by strong absorption, while for peripheral collisions the Coulomb repulsion pushes away the colliding systems thus preventing the pair transfer. The reaction tends to be spatially localized at the surface and the cross section for the $L = 0$ modes is expected low. This feature tends to be more evident when heavy-ion beams are used for the transfer and large negative Q-values are involved [18]. All of these aspects are discussed in Chapter 3, where the best conditions to populate the GPV are examined. In this context, the (^{18}O,^{16}O) reactions on light targets seems to be more appropriate for populating the GPV than the (p,t) reaction on heavy nuclei (as Pb and Sn) because of the better kinematical matching between the colliding systems which favors the $L = 0$ transfer [19]. Furthermore, in the ^{18}O projectile there is a preformed neutron-pair in the $2s_{1/2}$ or $1d_{5/2}$ orbitals out of a magic core of ^{16}O. The survival of this pair in the target nucleus is more likely favored if the same orbitals are available in it, as in the case of carbon targets. The ^{14}C and ^{15}C nuclei are good benchmarks for such studies, since their spectroscopic structure is very well known, as demonstrated by the wide literature on this subject [20][21][22], reported in Chapter 4.

Chapters 5 and 6 are focused on the description of the experimental set-up and data reduction of the ^{12}C(^{18}O,^{16}O)^{14}C and ^{13}C(^{18}O,^{16}O)^{15}C two-neutron transfer reactions. The investigation of such reactions belongs to a research line that aims to a systematic exploration of the reaction mechanism and the possible population of the GPV resonance via the (^{18}O,^{16}O) reaction on medium-light nuclei (in the mass region $10 \leq A \leq 20$). The ^{18}O beam at 84 MeV incident energy was delivered by the Tandem van der Graaf installed at the Laboratori Nazionali del Sud (LNS-INFN) in Catania and the MAGNEX magnetic spectrometer was used to detect the ejectiles. MAGNEX is an ideal instrument in order to study such kinds of reactions, since it conjugates good energy and angular resolutions with a large acceptance both in solid angle and momentum. Spectra up to 22 MeV residual nucleus excitation energy were extracted, allowing for the discovery of new broad structures in an unexplored energy region. The cross section angular distributions were also built, from which many aspects of the reaction mechanism and spectroscopic features are understood.

The last two Chapters are devoted to the data analysis of the experimental results, from both the reaction mechanism and the nuclear structure points of view. As regards the reaction mechanism the relative importance of the one-step correlated transfer and the

sequential transfer of uncorrelated neutrons in the (^{18}O,^{16}O) reaction is discussed. From the nuclear structure point of view, the origin of observed broad structures is investigated performing QRPA microscopic calculations about the 0^+ excitations on ^{14}C nucleus and looking at the angular distributions. The obtained results demonstrate that such bumps correspond to the excitation of the long searched GPV, since they are found at the right predicted excitation energy and width, they are populated with an $L = 0$ transfer and a large strength.

Chapter 1
Pairing correlations of nucleons

The importance of nucleon pairing in nuclear structure has been established in the early stages of nuclear physics by the determination of the binding energies of nuclei. In fact, the occurrence of a systematic difference between even and odd nuclei was associated with a pairing effect and provided the basis for understanding the striking difference in the fission of the odd and even isotopes of U [23]. A more detailed understanding of the pairing phenomena has been initiated in the 1960s, after the discovery of the appropriate concepts for treating the electronic correlations in superconductors by Bardeen, Cooper and Schrieffer [6] (awarded with the Nobel prize in 1972). In fact, it was recognized that these concepts could provide a basis for analyzing the pair correlations in nuclei [24]. Indeed, the pairing force creates specific excitations in closed and near-closed shell nuclei, which are referred to as *pairing vibrations* [1], as described in Section 1.2. These excitations with spin/parity 0^+ have collective features and have been extensively studied with two-nucleon transfer reactions around the magic ^{208}Pb nucleus [4] (see Section 1.2.1). In case of excitations of a pair across major shells, high-lying pairing vibrational states were also predicted (*giant pairing vibrations*) at energies of the order of $2\hbar\omega$, as discussed in Section 1.3.

A vast literature is available nowadays on the subject of the pairing correlations and two-nucleon transfer reactions. In particular, the present Chapter is referred to the interesting volumes of A. N. Bohr and B. R. Mottelson [1], P. Ring and P. Schuck [2] and G.R. Satchler [3], the report of R.A. Broglia, O. Hansen and C. Riedel [4] and the recent work of W. A. von Oertzen and A. Vitturi [5].

Despite many efforts have been devoted in the last years to investigate and better clarify the deep nature of the pairing interaction in several nuclear systems, some key questions need still to be answered and the interest that these issues raise in the community of

nuclear physicists is intact. The pairing force between nucleons is in fact a key ingredient for the development of microscopic nuclear models beyond the simple hypothesis of mean field, which has governed the physics of nuclear structure in the last 60 years.

It is known from the Hartree-Fock theory that the nucleon-nucleon interactions give rise to a self-consistent mean field inside the nuclear matter [2][3] (and therefore inside the nuclei). Each nucleon in a nucleus feels the action of a single field, generated by all the nucleons, with the consequent reduction of the degrees of freedom necessary to describe the nuclear structure. The mean-field, however, generates higher order effects associated with its possible excitations or polarizations, represented as the residual interactions. In stable nuclei, the energy related to these interactions is usually small compared to the mean field term, which guarantees the validity of the perturbation approach. However, the weakly bound systems far from stability are strongly influenced by the details of these residual interactions and the effects tend to be much more evident. The pairing force between two nucleons is one of the main residual interactions, although it is still unclear the microscopic mechanism which determines it.

Recent studies show that a part of the pairing force derives from the correlation of the single particle states of the two paired nucleons with vibrational excitations of the mean-field [25]. The mean-field can couple independently to the two single particle states, determining a correlation which favors two-particle states with zero angular momentum and positive parity. This only partially explains one of the most obscure features of this force, i.e. the fact that it requires short-range forces (1-2 fm), as those between nucleons or between the nucleons and the mean field, but determines correlation lengths (15-20 fm) much larger than the size of the nucleus. Indeed, in Fermi systems, the coherence length ξ is of the order of the spatial extent of the correlated pairs, and is thus determined by the momentum interval δp of the single-particle states that contribute to the correlation

$$\xi \sim \frac{\hbar}{\delta p} \sim \frac{\hbar v_F}{\Delta} \tag{1.1}$$

where v_F is the Fermi velocity and 2Δ the energy gap resulting from the binding of the pairs, which is about 2 MeV. Assuming a standard value for v_f of ~ 0.2 c, it is obtained for ξ ~ 15 – 20 fm [1].

From a theoretical point of view, there are several approaches to the pairing force. The most ambitious, but less intuitive, corresponds to microscopic methods based on modifications of the Random Phase Approximation theory including *p-p* and *h-h* excitations, beside the *p-h*, or Hartree-Fock-Bogoliubov schemes (see [12][26]). Certainly the most intuitive and easy to use are the macroscopic models, such as the Bès model [27], based on a description of collective oscillations and deformations of the pairing field. In addition, there are intermediate models, such as the cluster model, which approximates the many-body wave function of the nuclei in a core plus a cluster identified as a di-neutron. The open questions are many, such as the issue of the prior and post formalism for the calculation of the transfer form factors or to the development of an approach that can be easily extended to the drip-lines or the assessment of the effect of the continuous states (both the final and the intermediate states) in the process of transfer of a pair.

In this context, the study of observables related to pairing vibrations could be considered as useful additional constraints for the pairing force, in particular for the fitting procedures of phenomenological interactions [28]. For example, in a recent paper by Pllumbi et al. [29], the cross section calculations about ^{136}Sn(p,t)^{134}Sn for proton energies $E_p < 50$ MeV are found to be sensitive to the surface/volume mixing of the adopted zero-range density dependent pairing interaction. Therefore, two-nucleon transfer reactions acquire a great importance in the understanding of the pairing force, since they are the specific tools to investigate nucleon-nucleon correlations inside the nuclei.

1.1 Pairing energy

It was experimentally observed that the nuclear binding energies (B) exhibit a systematic variation (δB) depending on the evenness or oddness of the proton (Z) and neutron (N) number

$$\delta B = \begin{cases} \Delta & Z \text{ even } N \text{ even} \\ 0 & A \text{ odd} \\ -\Delta & Z \text{ odd } N \text{ odd} \end{cases} \tag{1.2}$$

From the Fermi gas model, which is an oversimplified but still reliable tool to describe the nucleon kinetic energies inside the nucleus, it is expected an odd-even difference (called *pairing energy*). This results from the fact that each orbit, $\boldsymbol{k}$, can be occupied by

two protons and by two neutrons. Thus, the even-odd parameter Δ should be of the order of the spacing between the one-particle energies in the neighborhood of the Fermi energy ε_F

$$(\Delta)_{kin} \approx \frac{2}{3}\frac{\varepsilon_F}{A} \approx \frac{25}{A} MeV \tag{1.3}$$

where A is the mass number of the nucleus. The observed pairing energies are shown in Fig. 1.1. Considering the region of heavy ions, where the Fermi model is more appropriate, the reported values are almost an order of magnitude larger than the estimate (1.3) [1]. The large observed odd-even effect may be described in terms of a pair correlation of identical particles, which contributes with an additional binding energy of 2Δ per pair (for nucleons near the top of the Fermi distribution). The correlation of the nucleons in the pair is associated with a superposition of single-particle states within an energy interval of about Δ. Thus, the transition from occupied to unoccupied states, which in a non-interacting Fermi gas takes place sharply at the energy ε_F (left panel of Fig. 1.2), is smeared out over an interval of about Δ (right panel of Fig. 1.2).

The odd-even mass parameter Δ can be determined from the empirical masses of a sequence of isotopes or isotones. Assuming that the masses are a smooth function of Z and N except for the pairing effect, it is possible to define a local average of the masses of odd-A nuclei, and obtain Δ from a comparison of this value with the observed masses of the even-even nuclei.

For even-N, Δ can be written as [1]

$$\begin{aligned} \Delta_n &= \frac{1}{4}\Big\{B(N-2,Z) - 3B(N-1,Z) + 3B(N,Z) - B(N+1,Z)\} \\ &= -\frac{1}{4}\{S_n(N-1,Z) - 2S_n(N,Z) + S_n(N+1,Z)\} \end{aligned} \tag{1.4}$$

while for odd-N the opposite of expression (1.4) is taken as the neutron pairing energy. Similarly, for even-Z

$$\begin{aligned} \Delta_p &= \frac{1}{4}\Big\{B(N,Z-2) - 3B(N,Z-1) + 3B(N,Z) - B(N,Z+1)\} \\ &= -\frac{1}{4}\big\{S_p(N,Z-1) - 2S_p(N,Z) + S_p(N,Z+1)\big\} \end{aligned} \tag{1.5}$$

while for odd-Z the opposite of eq. (1.5) is used.

In the definition of the pairing energies (eqs. (1.4) and (1.5)) the neutron separation energy (S_n) and the proton separation energy (S_p) are used. They are defined as

$$\begin{aligned} S_n(N,Z) &\equiv B(N,Z) - B(N-1,Z) \\ S_p(N,Z) &\equiv B(N,Z) - B(N,Z-1) \end{aligned} \tag{1.6}$$

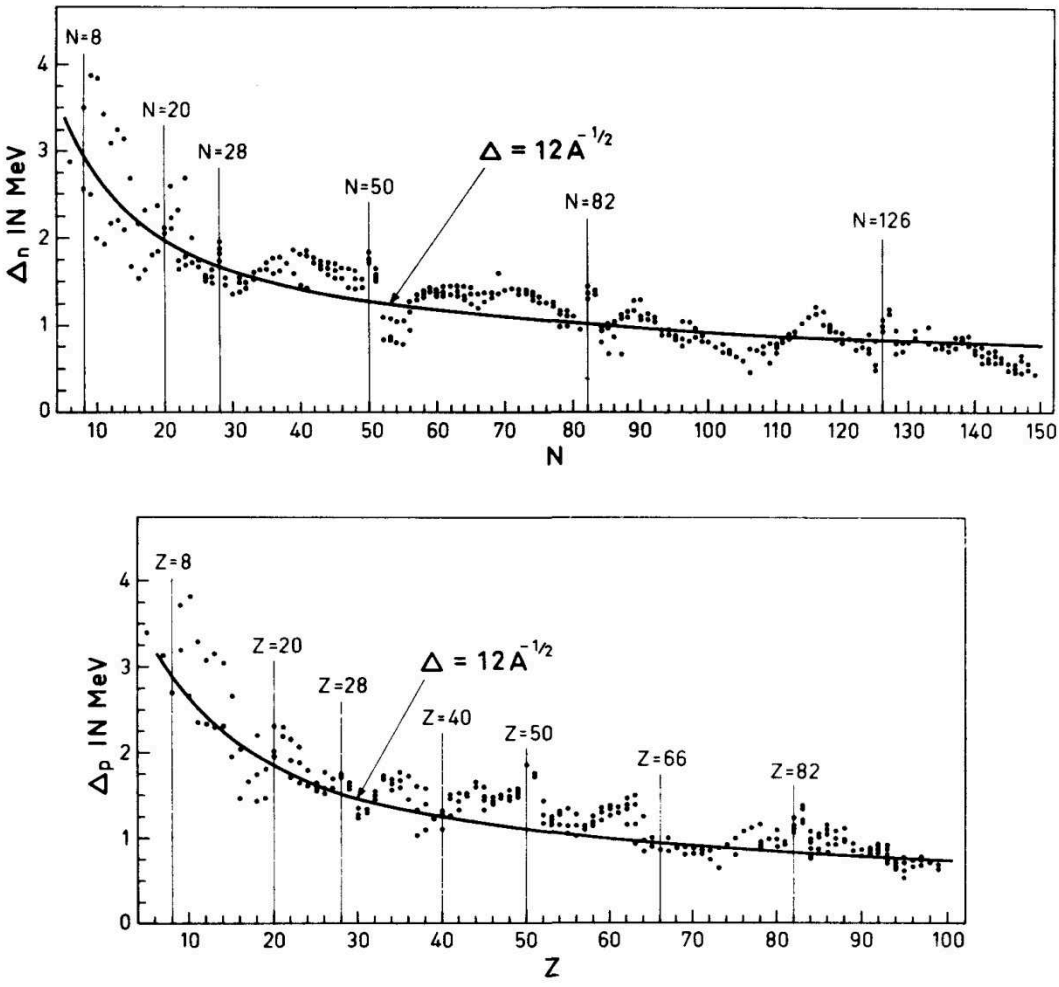

Fig. 1.1. The odd-even mass differences for neutron and protons [1].

The general trend in the observed pairing energies can be fitted by the simple expression

$$\Delta \approx \frac{12}{A^{1/2}} MeV \tag{1.7}$$

although significant local variations occur which are correlated with the shell structure (as it is shown in Fig. 1.1). There is a slight tendency for Δ_p to exceed Δ_n. This fact leads to a predominance of odd-N nuclei among the β-stable species as compared with the odd-Z (in particular, there are 53 odd-Z compared to 68 odd-N β-stable nuclei with $A < 238$).

The simple description of the pairing energy used in eq. (1.2) implies that the extra energy for an odd-odd nucleus, as compared with an even-even configuration, is

$$\varepsilon_{odd-odd} - \varepsilon_{even-even} \approx \Delta_n + \Delta_p \approx 2\Delta \tag{1.8}$$

Comparison with the observed masses of odd-odd nuclei are consistent with this relation, but there is a systematic tendency for the odd-odd masses to be slightly lower than this estimate. This extra binding energy of the odd-odd nuclei amounts on the average to about $20A^{-1}$ MeV [30] and may be related to the attractive residual interaction between the unpaired neutron and the unpaired proton, also considered as a neutron-proton pairing correlation. Recently, the isoscalar neutron-proton pairing was experimental observed considering the level structure of ^{92}Pd [31].

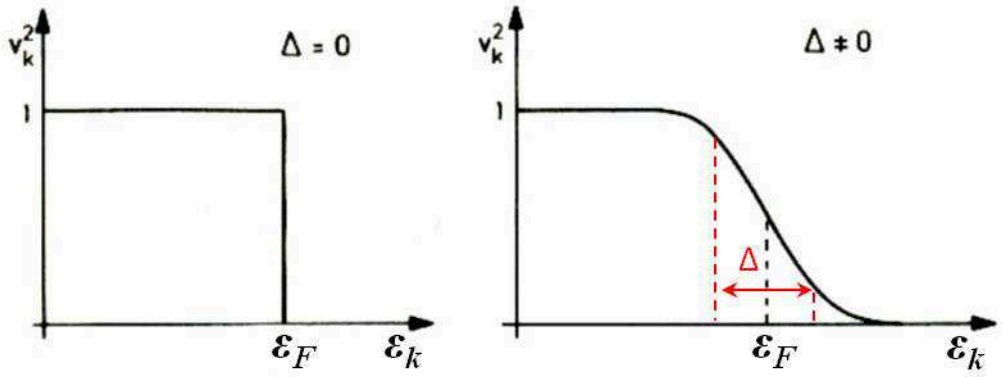

Fig. 1.2. Occupation probabilities $|v_k|^2$ in a non-interacting Fermi gas ($\Delta = 0$) and in the interacting one ($\Delta \neq 0$).

1.2 Pair vibrations

The nuclear modes of excitation can be characterized by appropriate quantum numbers, as for example the nucleon spin σ, isospin τ and transfer number α. The latter represents the change in nucleon number associated with the excitation of a quantum. Collective vibrations such as the giant isovector dipole resonance or the giant isoscalar quadrupole resonance [32] preserve the number of nucleons and thus have $\alpha = 0$. When viewed in terms of the nucleonic degree of freedom these collective modes are built out of particle-hole excitations [1]. Similarly, Fermi or Gamow-Teller resonances are characterized by $\alpha = 0$ although they transform neutrons into protons and vice versa [33].

Differently, collective modes with $\alpha = \pm 2$ are associated with correlations of pairs of particles or holes. The tendency of nucleons to form correlated pairs with angular momentum and parity 0^+ was observed in nuclei out of a closed shell, as for example in ^{6}He and ^{18}O.

The spectra of nuclei with two particles added or removed from a closed-shell configuration exhibit low-lying states with correlations in the motion of the two particles [1]. In particular, this is the case for the $I^{\pi} = 0^+$ ground states involving configurations with pairs of identical particles or holes. The correlation can be understood as a consequence of a short-range attractive force acting between the nucleons, which produces a superposition of single-particle configurations resulting in a pronounced spatial overlap of the two particle or holes (see Section 1.2.1). When the correlation involves the superposition of a large number of different configurations of the two particles, the addition or removal of the correlated pair may be treated as an elementary mode of excitation (*pair vibration*), which can be repeated and combined with other modes in the description of the total excitation spectrum.

The pattern of $\lambda^{\pi} = 0^+$ neutron pair vibration is schematically illustrated in Fig. 1.3. The spectrum involves two elementary modes with neutron transfer numbers $\alpha = +2$ and $\alpha = -2$, corresponding to the formation of the ground states of the nuclei with neutron numbers $N_0 + 2$ and $N_0 - 2$, respectively, where N_0 is the neutron number of the closed-shell configuration. These states are labeled by $(n_{\alpha=-2}, n_{\alpha=+2})$, which give the number of quanta of the two modes. If the interaction between the quanta can be neglected (*harmonic approximation*) the energies of the vibrational states can be written

$$E = \hbar\omega_{-2} n_{-2} + \hbar\omega_{+2} n_{+2} \tag{1.9}$$

in the energy scale employed in Fig. 1.3.

Since the pair addition quanta result from the spatial correlation of the particles, this mode is strongly excited by the two-particle transfer reactions, such as the (t,p) process, that involve the transfer of two nucleons closely related in space. Therefore, these processes play a role in the study of pairing vibrations similar to that of the inelastic scattering reactions in the study of the shape vibrations with $\alpha = 0$. The transition operator for a two-nucleon addition process is linear in the operators $c^{+}_{\alpha=2}$ and $c_{\alpha=-2}$ that create a quantum with $\alpha = 2$ and annihilate a quantum with $\alpha = -2$, respectively. Since the operator creates two identical particles at the same position, the pair is in a spin-singlet state ($\sigma = 0$), the associated quanta have total angular momentum k equal to the orbital momentum λ and the parity is $\pi = (-1)^{\lambda}$.

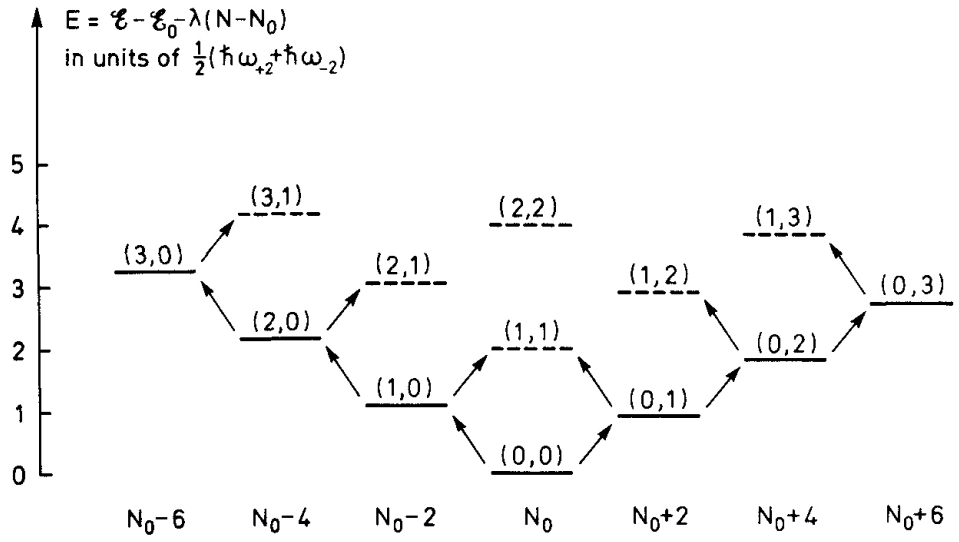

Fig. 1.3. Neutron pair vibrations with $\lambda^{\pi} = 0^{+}$. The states are labeled by the quantum numbers ($n_{\alpha=-2}$, $n_{\alpha=+2}$). Solid lines represents ground states and the arrows indicate strong two-particle transfer transitions from these states. The spectrum illustrated corresponds to the harmonic approximation, in which the excitation quanta are regarded as non-interacting entities. The energy scale E is the total energy relative to the value ε_0 for the closed-shell configuration (ground state for $N = N_0$), from which is subtracted a linear function of the neutron number [1].

A specific way to reveal the collectivity of the pairing modes is to study the spatial correlation of nucleons moving in time-reversal state, a property which is specifically probed in the transfer of two nucleons. In the case of an uncorrelated pair of nucleons and fixing the position of one of them, the probabilities to find the second close to the first or on the opposite side of the nucleus are equal. Pairing correlations lead to a marked increase of the probability for the two particles to move close to one another [34] [35].

To evidence the effect of the pairing interaction, in the work of Lotti et al. [36], the probability distribution associated with the correlated particle-particle Random Phase Approximation (*pp*-RPA) solution were compared with the corresponding quantity associated with the two neutrons independently moving in the pure $1g_{9/2}$ orbit. They did such investigation in both closed-shell and superfluid systems, choosing ^{208}Pb and ^{118}Sn as paradigmatic examples of the two phases. Considering the pure configuration (Fig. 1.4-a), the probability distribution for the second particle resembles the associated single-particle density, which is independent of the position of the first particle. In the correlated case (Fig. 1.4-b) the probability distribution of the second particle is concentrated around the first one.

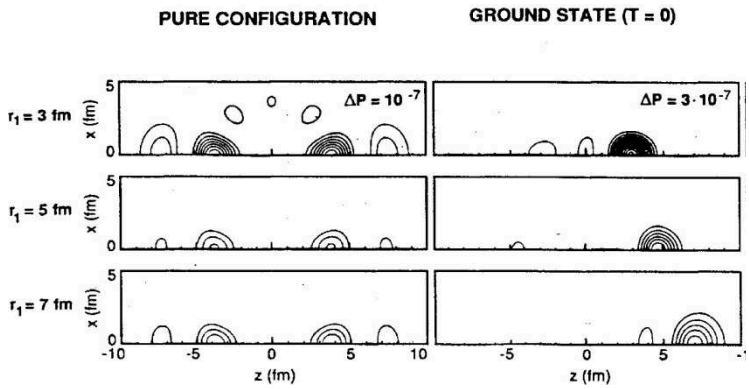

Fig. 1.4. Contour plot of the two particle probability distribution for the ground state of ^{210}Pb. The function $P(\boldsymbol{r}_1,\boldsymbol{r}_2)$ is displayed in the *x*-*z* plane for different fixed values of $\boldsymbol{r}_1$ as a function of the position $\boldsymbol{r}_2$ of the other particle. The position of the first particle is indicated on the left. The pure configuration refers to the uncorrelated case, corresponding to two particles moving in the $1g_{9/2}$ orbital [36].

1.2.1 Pair vibrations in Pb isotopes

The properties of the ground state of ^{206}Pb provided the opportunities for a rather detailed analysis of the pair correlations between the two neutron holes in the closed-shell configuration of ^{208}Pb. The separation energies of ^{208}Pb for one and two neutrons are S_n = 7.375 MeV and S_{2n} = 14.110 MeV, respectively [37]; the ground state of ^{206}Pb, with I^π = 0^+, is therefore bound by 640 keV with respect to the lowest unperturbed two-hole configuration $(p_{1/2})^{-2}$. It was experimentally observed that the two-particle transfer reaction ^{208}Pb(p,t)^{206}Pb populates the ground state with an intensity an order of magnitude larger than the excited 0^+ states [38]. The ^{206}Pb ground state can be described in terms of a collective phonon with quantum numbers α = -2 and $\lambda^\pi = 0^+$.

The observed states in the Pb isotopes that arise from superposition of quanta of the neutron pair addition and removal modes based on ^{208}Pb are shown in Fig. 1.5. In the harmonic approximation, the energy is linear in the number of quanta and the corresponding values are indicated in Fig. 1.5 as dashed lines. The leading-order anharmonicity can be described in terms of the interactions between pairs of quanta and give rise to small energy shifts.

The states in Fig. 1.5 are linked by enhanced two-particle transfer reactions. The two-nucleon quanta are found to behave as elementary modes also in the presence of single-particle or single-hole excitations in odd nuclei. Examples are provided by the $I^\pi = 9/2^+$ state at E_x = 2.71 MeV in ^{207}Pb ($(n_- = 1, g_{9/2})9/2^+$) and the $I^\pi = 1/2^-$ state at E_x = 2.15 MeV in ^{209}Pb ($(n_+ = 1, p_{1/2}^{-1})1/2^-$). These states are populated in the one-particle transfer reactions ^{206}Pb(d,p) [39] and ^{210}Pb(d,t) [40] with approximately the full single-particle strength. The $(n_+ = 1, p_{1/2}^{-1})$ state has also been observed in the reaction ^{207}Pb(t,p) with a strength similar to that between the ground states of ^{208}Pb and ^{210}Pb [41]. This demonstrates that the excitations modes due to the pair quanta are almost independent on the single-particle or single-hole excitations.

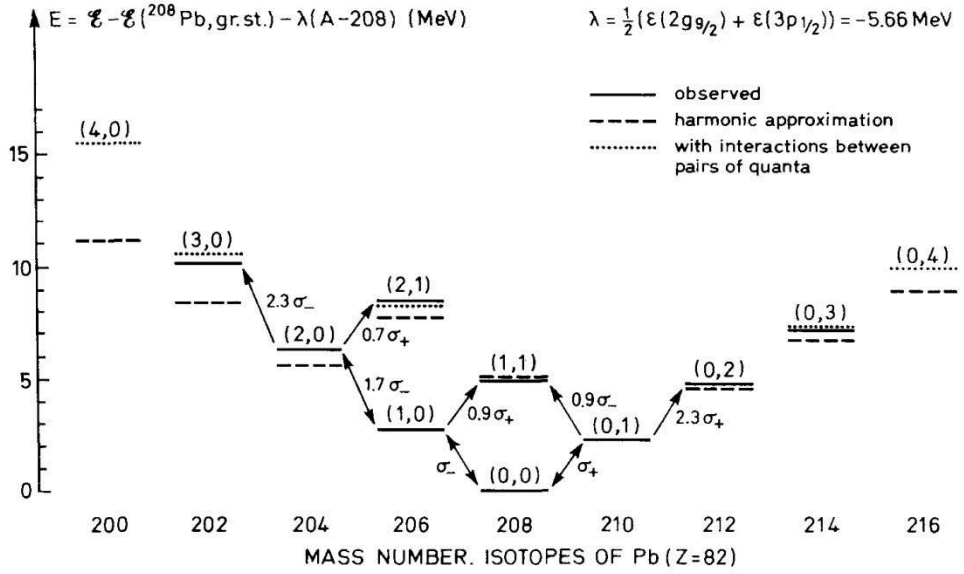

Fig. 1.5. Neutron pair vibrational spectrum based on ^{208}Pb. The levels are labeled by the number of quanta (n_-, n_+) of the pair removal and pair addition modes. The energy scale is similar to that of Fig. 1.3. The arrows indicate the transitions that have been observed as collective two-particle transfer processes ((t,p) or (p,t)) and the number on the arrows gives the cross sections, in units of σ_- and σ_+ for the processes (0,0)↔(1,0) and (0,0)↔(0,1) respectively, for the same projectile energy [1].

1.3 Giant Pairing Vibrations

It is known since many years that a formal equivalence between particle-hole and pairing vibrations exists [4]. As a consequence, some of the standard approaches used to describe particle-hole vibrations have been extended to the pairing case. For example, the use of a macroscopic description for nucleon pair transfer in heavy-ion reactions [42].

The study of giant resonances in inelastic scattering within the framework of particle-hole excitations is an old subject [43]; the corresponding study for two-particle transfer reactions was done in the seventies by Broglia and Bes [7]. The predicted collective state was called "*giant pairing resonance*" to maintain the analogy with the particle-hole case. It corresponds to a concentration of strength of an $L = 0$ character in the high excitation energy region and it is microscopically explained as the coherent superposition of $2p$ (or $2h$) states in the next major shell above the Fermi level, with a total energy $2\hbar\omega$. The situation is depicted in Fig. 1.6.

The collectivity of the giant pairing resonance would be manifested in two-particle transfer reactions, where this state would be the most strongly excited state if the energy of the projectile is big enough.

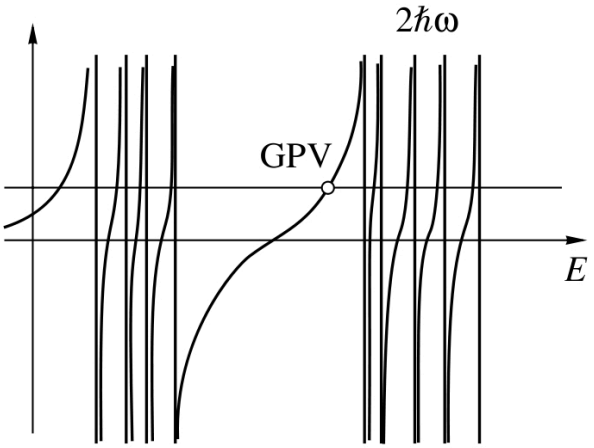

Fig. 1.6. Raw picture of the dispersion relation. The two bunches of vertical lines represent the unperturbed energy of a pair of particles placed in a given single-particle energy level. The graphical solution of the secular (RPA [2]) equation is the intersection of the horizontal line with the curves. The GPV is the collective state relative to the second major shell [44].

The distribution of the pair transfer strength should be strongly affected by the existence of major nuclear shells such that the inter-shell distance is appreciably larger than the distance between the levels within a shell. In such cases a concentration of pairing strength in a single state is expected for each major shell. In the present discussion only the lowest of the high-lying pairing resonances is considered. In particular, the discussion id focused on the monopole pairing modes which refers only to the 0^+ states.

1.3.1 GPV in heavy nuclei

The low-lying pair addition and pair subtraction modes in heavy nuclei have been theoretically studied in many papers [7] [9] [10][44]. Although these calculations are quite complex, it was obtained a simple estimate of the GPV excitation energy for the closed-shell nuclei, using the RPA approach [7]. The energy of the lowest giant pairing mode is given by the dispersion relation

$$\frac{1}{G} = F(W) = \frac{4\hbar\omega\Omega}{(2\hbar\omega)^2 - W^2} \tag{1.10}$$

where $\hbar\omega$ is the harmonic oscillator photon energy, Ω ($\approx \frac{2}{3}A^{2/3}$) is the degeneration of the harmonic oscillator valence band, W is the GPV energy and G is the constant matrix element for the pairing force. The value of the G constant depends on the number of levels in which the interacting particles can move. It was empirically determined that, for the case of three harmonic oscillator shells, $G \approx (17/A)$ MeV [7]. Also, it is possible to demonstrate that for large A [16]

$$\hbar\omega = \frac{5}{4}\frac{\hbar^2}{Mr_0^2}\left(\frac{3}{2A}\right)^{1/3} \approx \frac{41}{A^{1/3}}\,\text{MeV} \tag{1.11}$$

thus, the GPV should be found at energy

$$E_{giant} = W = \sqrt{(2\hbar\omega)^2 - 4\hbar\omega\Omega G} \approx \frac{69.7}{A^{1/3}}\ \text{MeV} \tag{1.12}$$

The cross section associated with this mode was found to be

$$\sigma_{giant} \propto \langle giant|T|0\rangle^2 \approx 1.2\ \Omega \tag{1.13}$$

The pair transfer operator T was defined as

$$T = \sum\nolimits_j \left(\Omega_j/2\right)^{1/2}\left[a_j^+ a_j^+\right]_{J=0} \tag{1.14}$$

where $\left[a_j^+ a_j^+\right]_{J=0}$ is the singlet component of the monopole ($J = 0$) Cooper pair creation operator and the index j labels the single-particle levels.

In ref. [7] the properties of the giant pairing modes were predicted also for nuclei far away from closed shell. The excitation energy obtained in such cases was found to be

$$E_{giant} \approx \frac{72}{A^{1/3}} \tag{1.15}$$

and the cross section

$$\sigma_{giant} \propto \langle giant|T|0\rangle^2 \approx 0.6\ \Omega \tag{1.16}$$

It is interesting to note that the estimates (1.15) and (1.16) coincide within 20% with the corresponding values obtained for nuclei around closed shells (eqs. (1.12) and (1.13)). Thus, the properties of the giant pairing mode are expected to be rather independent of the particular valence shell of the considered nucleus. The estimate of the excitation energy of the GPV obtained in ref. [7] corresponds to a rather extreme situation in which all levels belonging to a major shell are degenerate. If this is not the case, the energy of the pairing resonance should decrease as the lowest shell is being fulfilled. The behavior of the giant pairing modes is quite different from that of the ground state, i.e. the lowest pair addition or pair removal modes. In particular, the ground state cross section was found to be $\sigma_{g.s.} \propto 2.2\ \Omega$ for normal systems and $\sigma_{g.s.} \propto 0.5\ \Omega^2$ for superfluid systems [7]. Therefore, the pairing modes carry a cross section which is equal to ~ 0.2 – 1.0 times the cross section of the lowest pair addition or pair removal mode ($\sigma_{giant}/\sigma_{g.s.} \sim 0.5$ for normal systems and $\sigma_{giant}/\sigma_{g.s.} \sim 1.2/\Omega$ for superfluid ones).

The spatial correlation effects of the pairing interactions described in Section 1.2 (Fig. 1.4) were also found in the calculations for the giant pairing vibrations [36]. Other theoretical predictions about the GPV in heavy ions were developed in ref. [10] where the authors performed *pp*-RPA calculations on Pb isotopes and BCS + RPA on Sn ones, as paradigmatic example of closed-shell and superfluid systems, evaluating the response to the pairing operator. The results are reported in Fig. 1.7, where in addition to the strong collectivity associated with the ground state transition, a strong collective state with about half of the g.s. strength at high excitation energy is evident. This can be interpreted as the giant pairing vibration and is present in both addition and removal modes and in both nuclei. The energy of the pairing resonance obtained from these calculations were in agreement with the Broglia and Bes estimates [7].

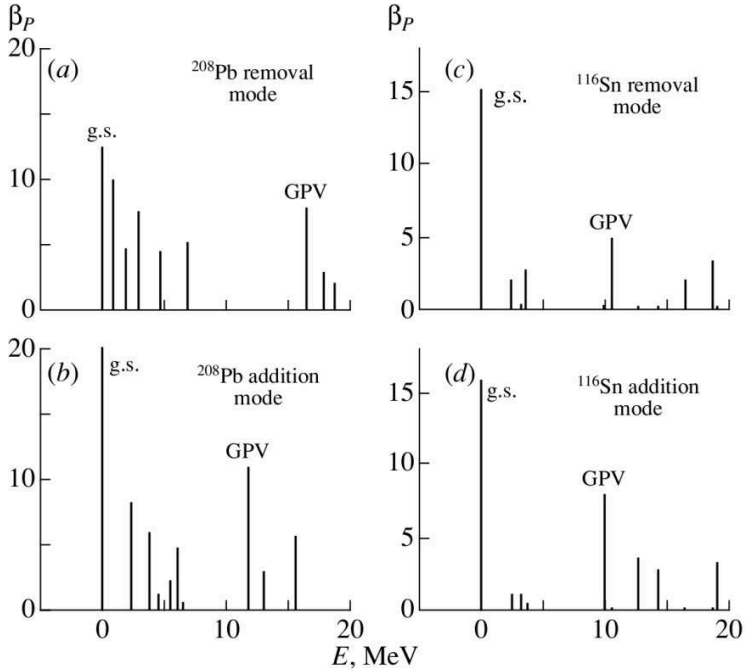

Fig. 1.7. Pairing response for removal and addition modes in ^{208}Pb and ^{116}Sn [10].

1.3.2 Search for the GPV with neutron-rich nuclei

Recently, it was considered the possibility to populate the GPV in two-neutron transfer reactions induced by unstable beams as a new tool to enhance the excitation of such modes [10]. The main point is that, with standard available beams, there is a large energy mismatch that strongly hinders the excitation of high-lying 0^+ resonances and favors the transition to the ground state of the final system. Instead, the optimum Q-value condition [19] in transfer reactions induced by weakly bound projectiles (as the (^{6}He,^{4}He) stripping reaction) suppresses the ground state and should allow the transition to the energy region of 10-15 MeV, where the GPV is predicted to be.

The authors of ref. [10] performed DWBA calculations for two neutron transfer reactions on ^{208}Pb and ^{116}Sn considering the reactions (^{14}C,^{12}C) and (^{6}He,^{4}He) in order to make a comparison between the use of stable and unstable beams. In the case of the stripping reaction induced by ^{6}He, the population of the GPV is found to display cross sections of the order of a millibarn, dominating over the mismatched transition to the ground state. The results are shown in Fig. 1.8, where a considerable gain in using unstable beams is evident, especially in the case of ^{208}Pb.

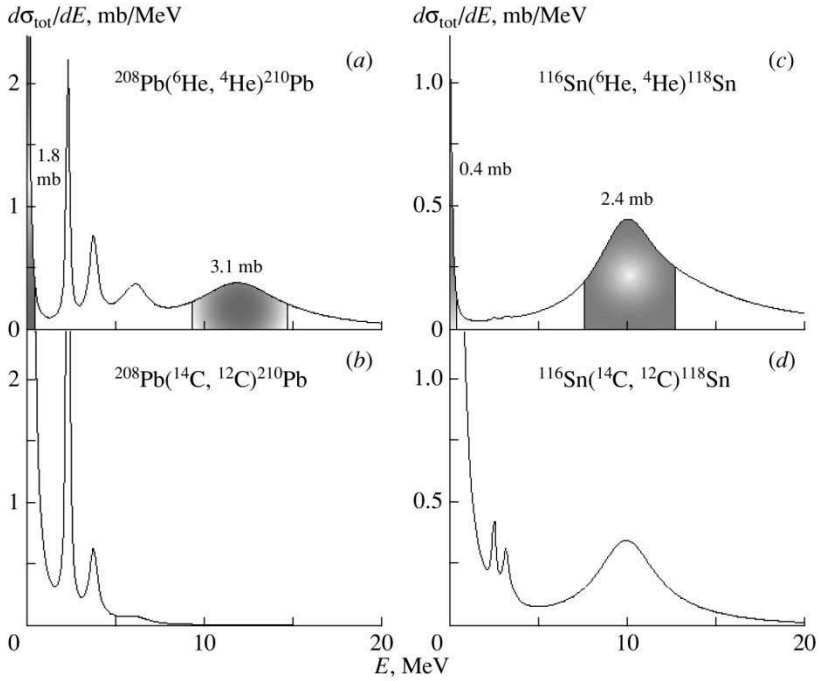

Fig. 1.8. Differential cross sections as a function of the excitation energy. The shaded areas for the (^{6}He,^{4}He) reactions allows a comparison between integral cross sections for the transitions to the ground state and to the GPV[44].

1.3.3 GPV in light nuclei

Recently the continuum-quasiparticle-RPA (cQRPA) approach was developed in order to calculate the pairing response function of neutron rich oxygen isotopes [11].

The two-particle transfer modes are commonly described by the pp-RPA [45] [46] in the case of closed shell nuclei and by the quasiparticle-RPA (QRPA) [4] [10] in open shell nuclei. The calculation of the two-particle transfer modes in nuclei far from stability presents additional difficulties compared to the case of stable nuclei. One is related to the coupling of such modes to the broadly distributed continuum states, which become important in nuclei close to the drip lines. Therefore a consistent description must be employed such as the cQRPA approach recently developed in ref. [12]. In the cQRPA the continuum is treated exactly and the residual interaction is derived from the same effective force used in the Hartree-Fock-Bogoliubov (HFB) calculation of the ground state vacuum. In ref. [11] the response function for the two-particle transfer to the neutron rich oxygen isotopes calculated within the cQRPA model is discussed. The results for ^{18,20,22}O oxygen

isotopes are shown in Fig. 1.9. For all the studied cases, narrow resonances appear corresponding to a pair transfer in the *sd* single-particle shell and a broad peak at around 20 MeV. The latter is mainly built upon the $1f_{7/2}$ single-particle orbital and its cross section is much larger than the one associated with the lower energy transfer modes. Since this high energy transfer mode is formed by single-particle states above the valence shell, this two quasi-particle broad resonance has the characteristics of a giant pairing vibration. The influence of the residual interaction on the pair transfer modes is illustrated in Fig. 1.10 for the case of $^{22}O + 2n$, emphasizing the collective nature of the pairing vibrations.

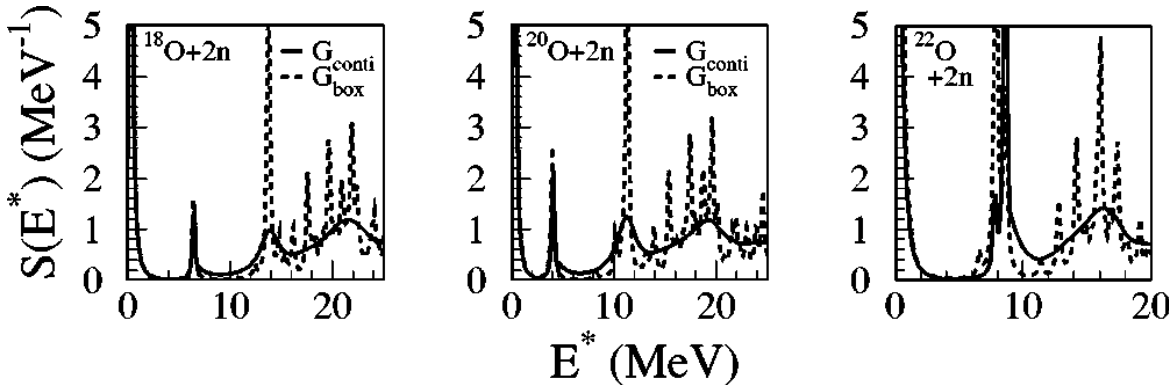

Fig. 1.9. The QRPA response for the two-neutron transfer on $^{18,20,22}O$. The exact continuum calculations are in solid lines whereas the calculations with box boundary conditions are in dashed lines. The results are displayed as function of E*, the excitation energy with respect to the parent nucleus ground state [11].

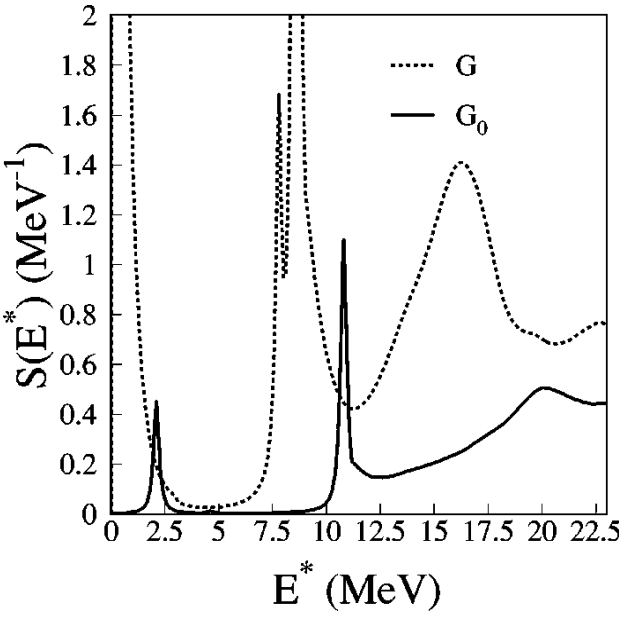

Fig. 1.10. The response function for the two-neutron transfer on ^{22}O. The unperturbed response is in solid line and the QRPA response in dashed line [11].

1.4 Search for the GPV with (p,t) experiments

During the 1970s and 1980s several studies of (p,t) reactions were undertaken on Sn and Pb nuclei in order to discover the GPV. However, all these attempts did not succeed. Probably the reasons for these failures have to be detected in the crucial role of the reaction mechanism. First of all, the proton incident energy should be high enough to populate the GPV mode, which is predicted to be located at high excitation energy (~ 15-20 MeV) [7] [36], and at the same time small enough to favor the $L = 0$ transfer. Indeed, at bombarding energies above ~ 80 MeV the L matching conditions hinders the $L = 0$ transfer, and the GPV is thus suppressed [13]. An appropriate energy range for the incident proton could be located around 50 MeV. It is important also the use of a spectrometer in order to precisely measure the triton in the exit channel. As an example, an attempt to search for the GPV with E_{beam} ~ 50 MeV was done using Si detectors, yielding a strong background [14].

A systematic study of (p,t) reaction on the even-even tin isotopes (around ^{120}Sn) was done by Crawley et al. [14][47] using a 42 MeV proton beam. For any tin isotope a broad structure around 8.5 MeV excitation energy was observed. The angular distribution of these bumps were also measured showing no structures and a slowly decreasing trend with increasing angle. This behavior was clearly in contrast with that of the low-lying states, for which the angular distributions showed a shape characteristic of the L transferred. It was concluded that the observed structure was composed by states with different J and so different angular momentum transfers. The experimental efforts during the 80s were exclusively devoted to understand the origin of this mode. Finally this bump turned out not to be the GPV, but the *deep hole state*, where the two neutrons are picked up from a deep orbit of the same harmonic oscillator shell. These states were present in both one- and two-neutron removal reactions (see Fig. 1.11), thus they cannot correspond to a pairing collective mode.

It was recently proposed to use exotic nuclei to detect the GPV [10] (as described in Section 1.3.2) because of their high positive Q-value in a stripping reaction, as in the (^{6}He,^{4}He) one. However, the background is expected to be large, due to the strong channel of two-neutron emission from ^{6}He (elastic break-up [48]). Moreover, the beam intensity is several order of magnitude lower than for stable beams and this makes the investigation of the GPV difficult with such reactions, as demonstrated recently in ^{208}Pb(^{6}He,^{4}He) experiment performed at GANIL [49].

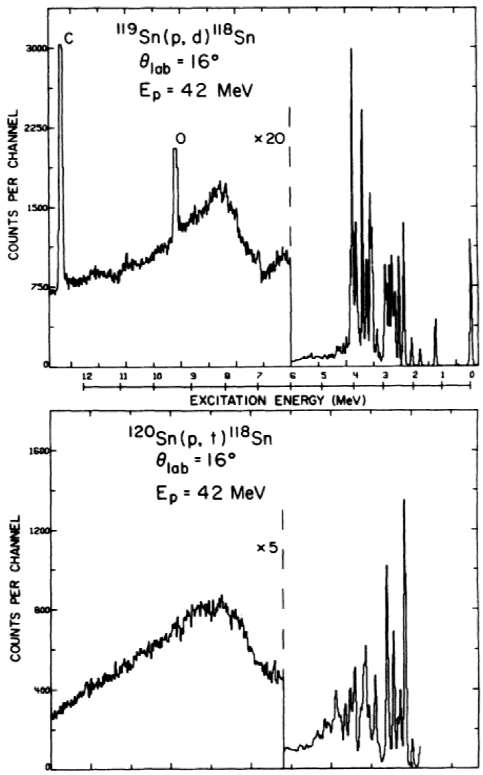

Fig. 1.11. Energy spectra from the ^{119}Sn(p,d)^{118}Sn and ^{120}Sn(p,t)^{118}Sn reactions at 42 MeV incident energy [47].

Recently, the possible existence of the GPV was investigated again by (p,t) reactions around 50 MeV on ^{120}Sn and ^{208}Pb targets using a magnetic spectrometer to measure the outgoing tritons [15]. As the L = 0 cross sections are known to increase much when approaching 0°, the measurements were done at small angles including zero degree. The experiment was performed at the iThemba LABS, South Africa, using the K = 600 QDD magnetic spectrometer [50]. The excitation energy spectra for the ^{118}Sn residual nucleus are shown in Fig. 1.12. Similar results were obtained when the ^{208}Pb target was used. No clear evidence of the GPV was found at 7° for a proton beam of 60 MeV (blue curve in Fig. 1.12). The spectrum shows the deep hole state between 8 and 10 MeV as well as low-lying states, in agreement with previous measurements [13][14]. The sharp peak above 13 MeV was originated by an oxygen contamination in the target. A small bump may be present in the expected GPV area around 12 MeV. However, the statistics was not large enough to give a clear answer to the existence of the GPV. This was mainly due to the unfavored L = 0 transfer at 7°.

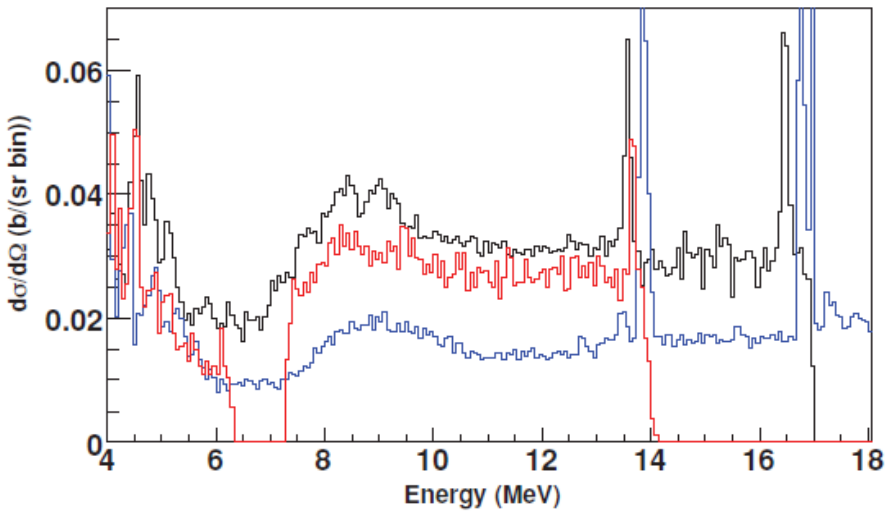

Fig. 1.12. Excitation energy spectra of ^{118}Sn from the ^{120}Sn(p,t) reaction for 0° measurement at 50 MeV (black curve) and 60 MeV incident energy (red curve) and 7° measurement at 60 MeV incident energy (blue curve) [15].

When considering the 0° measurements (black and red curves in Fig. 1.12), a larger background than for 7° was observed, perhaps indicating the possible low L composition of it. Again, a bump was observed between 8 and 10 MeV excitation energy, which corresponds to the deep hole state. After the subtraction of a linear background, the fit of the spectrum at 0° and 50 MeV incident energy allowed for the study of possible structures. A large bump was observed in the deep-hole area whereas a much smaller bump was extracted in the GPV area. The corresponding analysis is displayed in Fig. 1.13. From the integral of the possible GPV, the authors indicated an upper limit for the GPV cross section. It was estimated at σ_{max} = 0.2 mb with a GPV width of about 0.8 MeV. This value is one order of magnitude lower than the one usually predicted for the GPV [10] and the authors concluded that this could explain the historical difficulty to detect it.

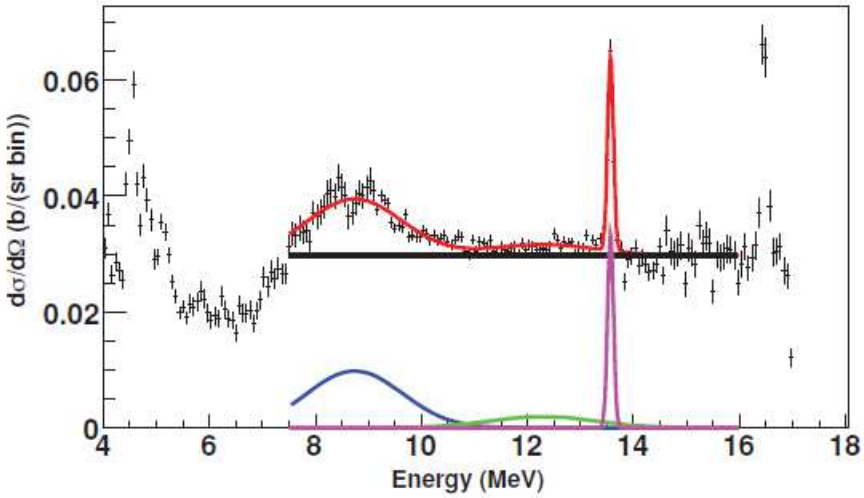

Fig. 1.13. Excitation energy spectrum of ^{118}Sn from the ^{120}Sn(p,t) reaction at 0° and 50 MeV incident energy. The linear background (black line), deep-hole states (blue curve), fit for a possible GPV (green curve), oxygen contaminant (pink curve) and total fitting function (red curve) are shown [15].

Chapter 2
Transfer reactions with heavy ions

Two-nucleon transfer reactions are of great importance in the understanding of the pairing force, since they are the specific tools to investigate nucleon-nucleon correlations inside the nuclei [5]. In fact, the influence of the pairing force manifest itself in transitions induced by the operator associated with the creation (or annihilation) of a pair of nucleons coupled to angular momentum zero. A massive literature has been constructed during the last decades on spectroscopic studies driven mainly by (p,t) or (t,p) reactions, accompanied by complementary studies on heavier projectiles [4]. Excellent reports about the latter topic are available, where the most advanced analyses are presented [5] [17][18].

From an experimental point of view, the availability of heavy-ion beams has strongly increased the number of reactions that can be used to reach the same residual nucleus. Thus, an enormous amount of experimental and theoretical work has been devoted to the study of heavy-ion transfer reactions [3] [17][18][51]. In order to understand the involved reaction mechanism, many one-nucleon transfer data have been measured and analyzed, establishing the basic features of heavy-ion induced reactions dynamics: a strong dependence of the cross section on Q-value and angular momentum matching conditions, and the evolution of the angular distributions from bell shapes to forward peaked cross sections with increasing incident energies.

In the present Chapter some of the main features of transfer reactions between heavy nuclei are summarized, following the formalism used in ref. [3][5].

2.1 Direct reactions

The first description of nuclear reactions was done in terms of the formation of a compound nucleus in which the input energy is distributed in an essentially random manner over all the constituent nucleons [52]. This picture accounts for a major part of the reaction cross section in many cases, but there is an important element missing from this description. Although nuclei have relatively sharp surfaces due to the short range nature of nuclear force; there is a region of transition between a condition of no interaction and one in which a strong interaction occurs. In this surface region a projectile can interact inelastically with just one target nucleon or just one simple mode of nuclear motion (such as a shape oscillation) and then the residual particle escapes. These processes are called *direct reactions* because the involved nuclei go directly from initial to final states without the formation of an intermediate compound system. When the projectile penetrates deeply and suffers subsequent collisions the compound nucleus is more likely to be formed. Direct reactions occur quickly, the time in which the reaction is completed is of the order of the transit time of the projectile across the target. A consequence of this is that the observed cross section in a direct reaction vary slowly with the incident energy [3].

Whenever there is a good overlap between the wavefunctions in the incident and exit channels, the collision may occur with a minimum of rearrangements of the constituents nucleons and it can be considered a direct reaction. This condition corresponds to the involvement of very few degrees of freedom, better highlighted when the appropriate representation is used. For instance, a collective vibration is simple and may involve only one coordinate if a collective model description is used. On the other hand, if the collective vibration is observed from a shell-model point of view, it involves a correlated superposition of many independent-particle excitations.

Since decades, the direct reactions attracts a major interest in the nuclear physics community, as they are the most effective source of information on nuclear structure. In fact, since they proceed through a single step, the reaction amplitudes depend on the overlap of the initial and final states. For instance, in a (d,p) stripping reaction where a neutron is transferred to the target, it is possible to learn how much the residual nucleus can be described as the target in its ground state plus a neutron moving in a single-particle orbit. This represents the so-called *spectroscopic factor* which is a measure of this probability. Such information has proven to be essential in order to test the predictions of

the nuclear shell-model. Similar remarks hold for other reactions, if two nuclear states differ only in the excitation of a single fundamental mode, whether it be of single particle of collective type, they will be connected strongly by the appropriate direct reaction.

Direct reactions are much selective in the final states that they populate. They feed particular channels in a way that depends sensitively on their character. For instance: inelastic scattering excites collective states strongly; one-nucleon transfer effectively populates *single-particle* states; two-nucleon transfer goes preferentially to states that exhibit strong pairing correlations, and so on. This is of particular value in probing different aspects of nuclear structure.

A particular class of direct reactions are the rearrangement collisions $A(a,b)B$. They consist in a process in which one or more nucleons are transferred from the projectile a to the target A, or vice versa, leaving the final nuclei b and B in bound states. There are irrefutable indications for the existence of direct reactions involving the transfer of one to four nucleons and claims have been made for the transfer of even large numbers [53]. These transfers may occur under a wide variety of conditions, ranging from sub-Coulomb (bombarding energy below the Coulomb barrier) to very high energies, from the use of light beams or targets to ever heavier ones. In some cases, when more than one nucleon is transferred, there is evidence of the dominance of the sequential (two-step) transfer.

2.2 Selection rules for one-step transfer

Considering a transfer reaction like

$$a(= b + x) + A \rightarrow b + B(= A + x) \tag{2.1}$$

occurring in one step where a nucleon, or cluster of nucleons, x is transferred from a projectile a to a target A forming the residual nuclei b and B.

If x is a well-defined entity, even if it does consist of more than one nucleon, and it has a definite spin s, it is possible to suppose that, within a, x has orbital angular momentum l_1 relative to b and a total angular momentum j_1

$$\boldsymbol{j}_1 = \boldsymbol{l}_1 + \boldsymbol{s}, \qquad \boldsymbol{I}_a = \boldsymbol{I}_b + \boldsymbol{j}_1. \tag{2.2}$$

defining with $\boldsymbol{I}_a$ and $\boldsymbol{I}_b$ the total angular momenta of a and b, respectively. Similarly, let x within the final nucleus B have orbital angular momentum l_2 relative to A and a total of j_2

$$\boldsymbol{j}_2 = \boldsymbol{l}_2 + \boldsymbol{s}, \qquad \boldsymbol{I}_B = \boldsymbol{I}_A + \boldsymbol{j}_2. \tag{2.3}$$

where $\boldsymbol{I}_B$ and $\boldsymbol{I}_A$ are the total angular momenta of B and A, respectively. Then, it is possible to identify the transfer angular momenta

$$\boldsymbol{J}_{BA} = \boldsymbol{I}_B - \boldsymbol{I}_A = \boldsymbol{j}_2, \qquad \boldsymbol{J}_{ba} = \boldsymbol{I}_b - \boldsymbol{I}_a = -\boldsymbol{j}_1 \tag{2.4}$$

so that

$$\boldsymbol{L} = \boldsymbol{J}_{BA} - \boldsymbol{J}_{ba} = \boldsymbol{j}_2 - \boldsymbol{j}_1 \qquad \text{or} \qquad |j_2 - j_1| \leq L \leq (j_2 + j_1) \tag{2.5}$$

Provided the particle x itself has even intrinsic parity, the change in internal parity is governed by

$$\pi_a \pi_b = (-1)^{l_1} \qquad \pi_A \pi_B = (-1)^{l_2} \tag{2.6}$$

So the overall change in internal parity is given by

$$\Delta\boldsymbol{\pi} = \boldsymbol{\pi_A \pi_a \pi_B \pi_b} = (-\mathbf{1})^{\boldsymbol{l_1 + l_2}} \tag{2.7}$$

Equations (2.5) to (2.7) represent the selection rules imposed by this simple three body model of a transfer reaction. It is important noticing that the quantum numbers l_1 and j_1 are not unique when the ejectile b is a composite nucleus with stable excited states. Even the spin s of the cluster can be not unique when more than one nucleon is transferred. For example in (t,p) reactions the principal component is the transfer of two neutrons in a singlet state, with $s = 0$, $l_1 = j_1 = 0$. However, because of the small mixed s and d components in the triton wavefunction, $l_1 = 1$ is also allowed with the two-neutron cluster in a ^3P_s configuration and $s = 0$, 1 or 2.

2.3 Qualitative features of angular distributions

2.3.1 Light ions

When dealing with light ions induced transfer reactions, the position of the first and main peak or at least the shape of the forward part of the cross section angular distribution usually provides a clear signature of the *L* transfer (see for example Fig. 2.1) [54]. This signature can be recognized either by comparison with theoretical predictions (e.g. the Distorted Wave (DW) method [3]) or by comparison with the transitions of known *L* value. The position and shape of the angular distributions around the most forward peak is usually predicted unambiguously by the DW method, but the distribution in other regions is often sensitive to details of the calculations such as the optical-potential parameters, finite-range and non-locality effects, and so forth.

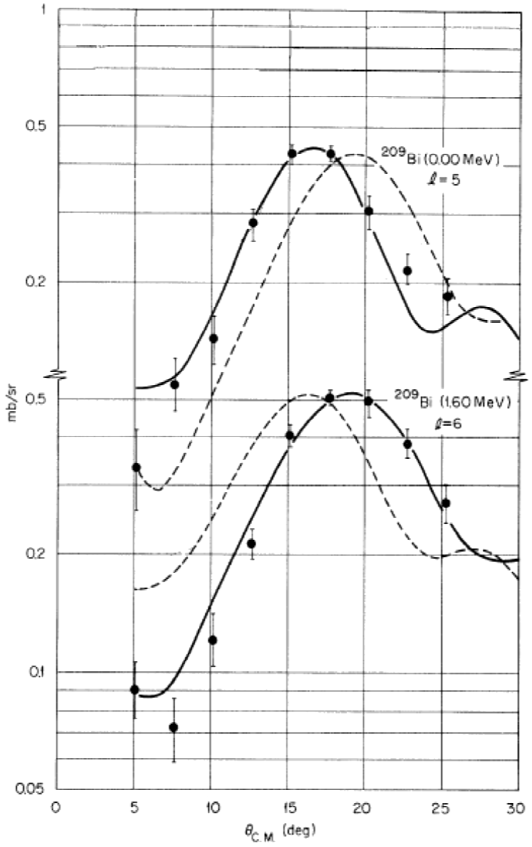

Fig. 2.1. Experimental angular distributions of the ground state and 1.6 MeV level of ^{209}Bi excited in the reaction ^{208}Pb(^{3}He,d)^{209}Bi at 51.26 MeV incident energy. The curves are from DW calculations. The solid ones fit the data and correspond to the *l*-values shown. The dashed curves correspond to the other *l* value in each case [54].

The angular distributions are influenced by the matching of the momenta and angular momenta of the entrance and exit channel waves. When the two waves are poorly matched, as for example the (^{3}He,α) reactions or their inverse, this leads to a preference for large *L* transfers. The corresponding angular distributions are often structureless or, where there is structure, the theoretical interpretation may be uncertain so that is frequently difficult to identify the *L* transfer unambiguously (see Fig. 2.2) [55].

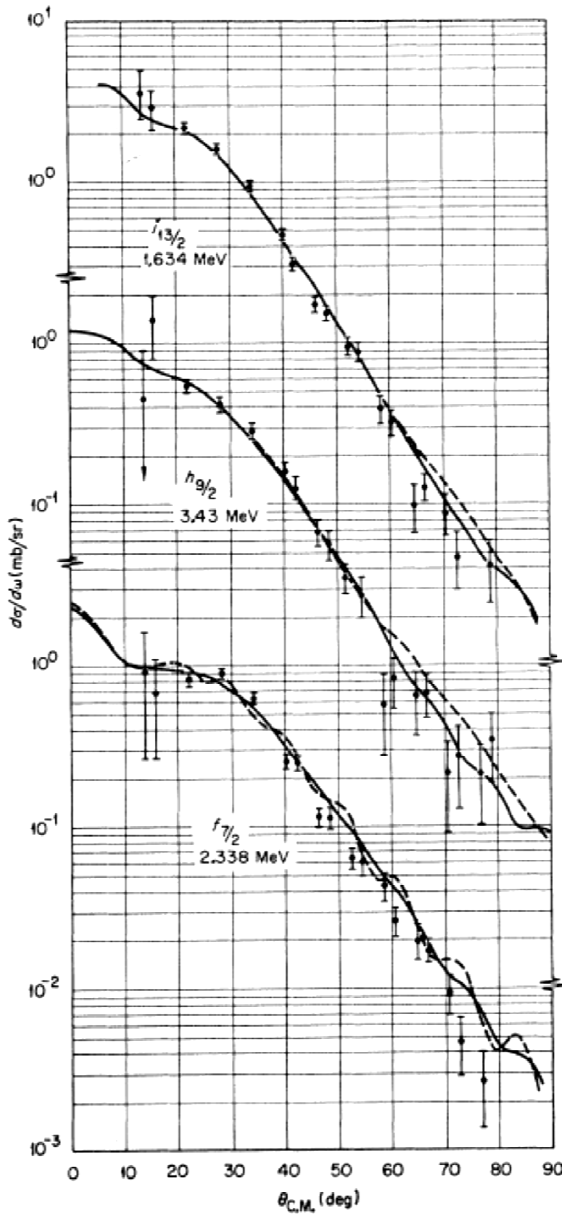

Fig. 2.2. Rather featureless angular distributions for ^{208}Pb(^{3}He,α) at 47.5 MeV for the transitions indicated [55].

2.3.2 Heavy ions: semi-classical features

When comparing transfer reactions induced by heavy ions with those ones by light ions, some peculiar features appear for the former: (i) stronger absorption of the incident flux; (ii) shorter wavelength and (iii) larger angular momentum transfers. These characteristics result in a sharper localization of the reaction and make semi-classical conceptualization more plausible [51]. Many authors have treated in detail the almost classical aspects of heavy-ion induced reactions [56][57][58]. This approach can be used when the reactions are at sufficient low energies (close to the Coulomb barrier), such that the nuclear potential plays a small role in determining orbits and classical trajectories determined by the Coulomb forces can be considered.

In all heavy-ion transfer reactions the important interactions seem to take place when the centers of the interacting nuclei are separated by a distance R_0 which is a little bigger than the sum $R_1 + R_2$ of their radii. For larger separations the probability for transfer becomes small, while for smaller separations the incident flux is absorbed to form a compound nucleus. Semi-classical methods can only be used if R_0 is much larger than the wave-length λ of relative motion, i.e. $kR_0 \gg 1$, where $k = 1/\lambda$ is the wave-number of relative motion.

The large masses imply large charge products Z_1Z_2 (Z_1, Z_2 being the charges of the nuclei) and a small value of the de Broglie wavelength λ. Thus, the Sommerfeld parameter

$$\eta = \frac{Z_1 Z_2 e^2}{\hbar v} = \frac{Z_1 Z_2 e^2 p}{2E\hbar} = \frac{R^0_{min}}{2\lambda} \tag{2.8}$$

gets a rather large value. In eq. (2.8) v is the relative velocity of colliding nuclei in the center of mass (CM) system, E is the energy in the CM system, p is the momentum and R^0_{min} is the distance of closest approach in a head-on collision neglecting nuclear forces:

$$R_{min}(\theta, k, \eta) = \frac{\eta}{k}\left(1 + \frac{1}{\sin\theta/2}\right) = \frac{R^0_{min}(k,\eta)}{2}\left(1 + \frac{1}{\sin\theta/2}\right) \tag{2.9}$$

Eq. (2.9) show that, when the condition $\eta \gg 1$ is fulfilled, the minimum distance becomes large relative to the de Broglie wavelength, and $kR_0 \gg 1$ is verified. In such

cases, the classical orbits for the relative motion of the two nuclei are well defined [59], and the connection between scattering angle and projectile-target separation is established through

$$R_0 = \left(\frac{\eta}{k}\right)\left(1 + \csc\frac{\theta_g}{2}\right) \tag{2.10}$$

which is the purely Coulomb formula for distance of closest approach [60], where θ_g is the *grazing angle*. From eq. (2.10) it appears that the differential cross-section show a peak near θ_g, because it is suppressed at backward angles by strong absorption and at forward angles by bound-state or form factor dependences [3]. Therefore, the angular distributions are essentially independent of the L transfer. Examples of bell-shaped angular distributions are shown in Fig. 2.3 for some one-proton transfer (^{16}O,^{15}N) reactions [61].

The situation should be different when the projectile energy is increased. In fact, at low energies, the transfer occurs only from waves scattering from the near-side of the target because of the Coulomb *diverging-lens* effect, whereas with increasing energy the Coulomb deflection is reduced, and contributions from the far-side become non-negligible [3]. The interference between the near- and far-side amplitudes show up in the angular distributions oscillations, characterized by an angular period $\Delta\theta \sim \pi/kR$.

In some cases the appearance of the oscillating pattern was observed at surprising low energies, in the presence of a strong Coulomb field ($\eta \sim 20$), thus implying that the far-side amplitude is greater than would be expected simply from diffraction and that additional refraction by the attractive nuclear potential is required. An example is the single-proton transfer reaction ^{48}Ca(^{14}N,^{13}C) displayed in Fig. 2.4 [62][63]. The angular distributions to the ground ($f_{7/2}$) and excited ($p_{3/2}$) states show a classical grazing shape modulated by the interference maxima and minima, which increases in amplitude towards smaller angles. The most forward peak in the angular distribution shows a distinct L-dependence similar to that of light-ion induced reactions. The peak corresponding to the excited state transition (predominantly $L = 2$) is shifted considerably forward with respect to that relative to the $L = 4$ ground state transition.

Distorted Wave Born Approximation (DWBA) calculations were performed reducing the imaginary depth of the optical potential and reproduce well the experimental cross section (solid line in Fig. 2.4). Indeed, a way of explaining the forward raising of the cross section is to reduce the absorption in the surface region of projectile-target interaction,

allowing the projectile to reach the region where attractive nuclear forces dominate. In such conditions the semi-classical approach becomes less reliable, unless more than one orbit is allowed to contribute. This results in interference between widely spaced orbits on opposite side of the target (near-side and far-side) and explain the narrow oscillations observed in the DWBA calculations and experimental data.

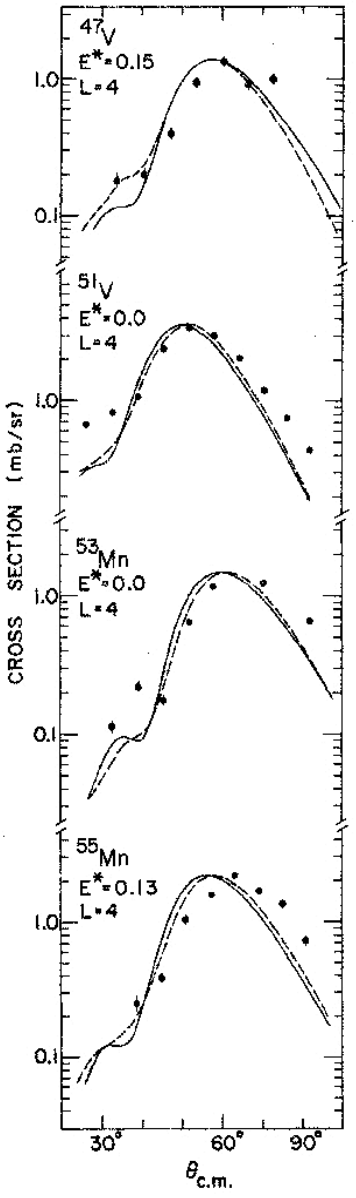

Fig. 2.3. Angular distributions for (^{16}O,^{15}N) reactions at 48 MeV to prominent states in ^{47,51}V and ^{53,55}Mn. Distorted Wave Born Approximation (DWBA) calculations are shown with solid and dashed lines [61].

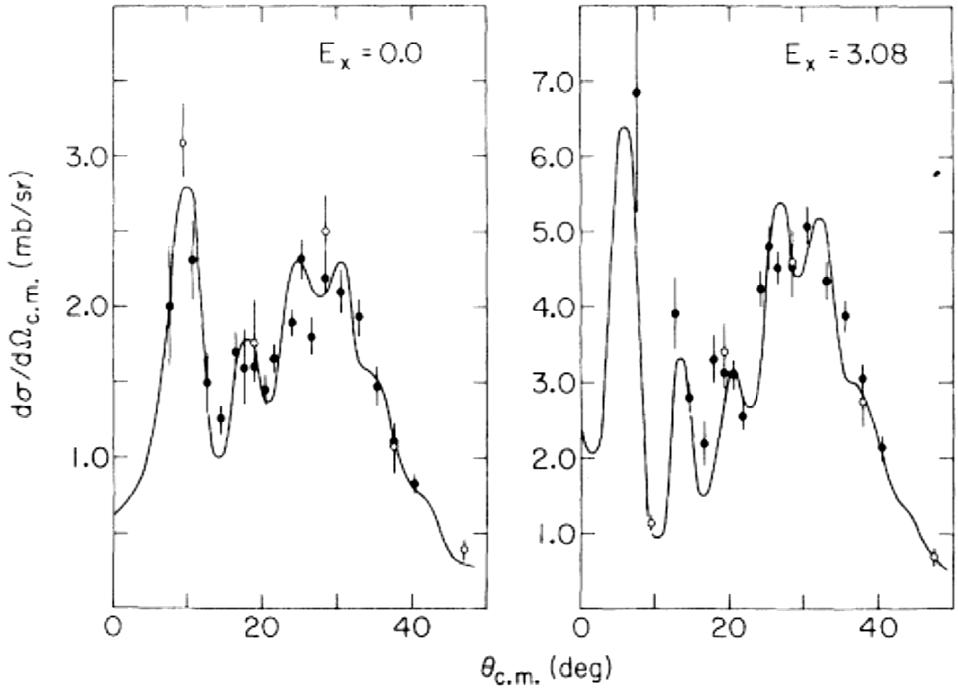

Fig. 2.4. Angular distributions for ^{48}Ca(^{14}N,^{13}C) to the ground state ($1f_{7/2}$) and 3.08 MeV ($2p_{3/2}$) states in ^{49}Sc. DWBA calculations made with a weakly absorbing potential are shown with the solid line [63].

The few examples reported above (mainly taken from ref. [18]) are confined to energies about 1-2.5 times the Coulomb barrier. For higher energies, five to eight times the barrier on light targets, many important results are summarized in the review of Anyass-Weiss et al. [17]. In all the reported reactions at these energies, smooth, exponentially falling differential cross sections were observed.

2.4 Kinematical matching conditions

One of the peculiar features of transfer reactions induced by heavy ions is the observed strong absorption of the incident flux. In such conditions, the partial waves from each channel that can contribute to a reaction are confined to a band or *window* of L values centered near the grazing L_g for that channel. Waves with L appreciably less than L_g are absorbed, while those with L larger than L_g, corresponding to larger separations of the two ions, contribute less because the interaction and the bound-state wavefunctions fall exponentially as separation increases. The selectivity of the reaction in the L transferred is

influenced by this behavior in the following way. The *L* transfer is defined by conservation of angular momentum as

$$\boldsymbol{L} = \boldsymbol{L_\alpha} - \boldsymbol{L_\beta} \tag{2.11}$$

Thus, the small *L* transfers become inhibited when there is a large difference between $L_{g\beta}$ and $L_{g\alpha}$ and conversely the large *L* transfers become more important. This occurs when there is not a good matching between the two channels. The (^{3}He,α) and (p,α) reactions are examples in which this often happens.

The values of $L_{g\beta}$ and $L_{g\alpha}$ are determined by the energy, the *Q* value and the mass transfer. It is possible to identify a range of *Q*-values that are optimum for a particular *L* transfer in a given reaction at a given energy, known as the *Q-window*. Considering heavy ions, the short wavelengths involved suggest using classical or semi-classical estimate of these effects. An example is the model used by Brink for one-nucleon transfer reactions [19], in which it is assumed that there is a grazing collision and the nucleon is transferred at the touching point (i.e. on the line of centers when they are separated by the distance $R = R_1 + R_2$) (Fig. 2.5). Typically, *R* would be taken as the strong absorption radius for the system. Three kinematical conditions should be satisfied in the Brink's model if the transfer probability has to be large.

Taking in mind a transfer reaction like (2.1), the first condition express the conservation of the linear momentum of the transferred nucleon *x* in the scattering plane and perpendicular to the line of centers:

$$\Delta k = k_0 - (\lambda_1/R_1) - (\lambda_2/R_2) \approx 0 \tag{2.12}$$

where $k_0 = mv/\hbar$ is the momentum of *x* due to the motion of *a*, and *v* is the initial relative velocity of the two ions (*a* and *A*) at the point where the transfer is taking place. The restriction $\Delta k \approx 0$ is equivalent to the requirement that the *y*-component of the momentum of *x* should be almost conserved. $\lambda_1\hbar$ is the component of angular momentum of *x*, perpendicular to the scattering plane, about the center of the nucleus *a* (to which it is bound before the transfer), while $\lambda_2\hbar$ is the component about the center of the other nucleus *B* where *x* is found after the transfer. $R_1 = r_0 A_1^{1/3}$ and $R_2 = r_0 A_2^{1/3}$ are the radii of the two nuclei, with $r_0 \sim 1.25$ fm.

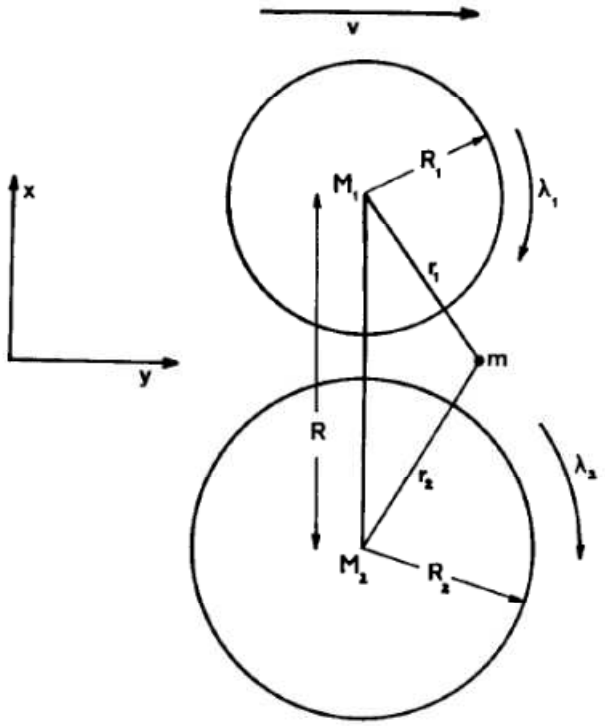

Fig. 2.5. Diagram of the transfer process.

The second condition corresponds to the conservation of the total angular momentum perpendicular to the scattering plane, expressed as

$$\Delta L = (\lambda_2 - \lambda_1) + \tfrac{1}{2}k_0(R_1 - R_2) + Q_{eff}\, R/\hbar v \approx 0 \qquad (2.13)$$

where Q_{eff} is the actual change in kinetic energy of relative motion of the two ions at the point of transfer, defined as

$$Q_{eff} = Q - (Z_b Z_B - Z_a Z_A)\, e^2/R \qquad (2.14)$$

which is the Q-value corrected for the change in the Coulomb potential that occurs if the transferred x is charged.

It is worth noticing that the total angular momentum should be exactly conserved in any process so that ΔL should be zero in (2.13). However, the discussion of ref. [19] is not fully consistent because the internal angular momentum is quantized while the angular momentum of relative motion is treated classically. This inconsistency generates small deviations of ΔL from zero.

The third condition

$$l_1 + \lambda_1 = even, \qquad l_2 + \lambda_2 = even \tag{2.15}$$

arises because the transfer probability is larger when the nucleon *x* is near the reaction plane.

The physical arguments leading to conditions (2.12) and (2.13) are rather general and seem to hold also for transfer of several nucleons, but probably they will be relaxed to some degree because some assumptions in ref. [19] depend on the single-nucleon model.

The Brink's matching conditions may have other consequences. For instance, if λ_1 is small, because of transfer out of an orbital with small angular momentum (as it happens if the donor is an heavy ion), (2.12) and (2.13) result in large values for λ_2 when:

(i) the incident energy is high so that the relative velocity *v* is large. Thus, the momentum transfer $k_0 = m_k v/\hbar$ is large favoring a large positive value for $(\lambda_1 + \lambda_2)$ from condition (2.12) (especially when the reactions studied are such that $R_1 \approx R_2$).

(ii) the reaction has a large negative *Q*-value. This gives a large positive value of $|\lambda_1 - \lambda_2|$, from the condition (2.13).

Therefore, if λ_1 is small both (i) and (ii) determine a large value of λ_2 giving preferential excitation of high spin states [17].

2.5 M-states

The cross section angular distributions are influenced also by the orientation of the angular momentum transfer (*M*). In fact, for a given *L*, the amplitudes for odd-*M* and even-*M* show oscillations with θ that are out of phase (where *M* is defined as the component of *L* with respect to a *z*-axis along the incident beam direction). Under favorable conditions (good matching and energy sufficiently above the Coulomb barrier), the amplitude with *M* = *L* dominates the cross section and the resulting angular distributions are sensitive to the *L* transfer [18]. On the contrary, poor matching results in a more even distribution of the *M* population, and the incoherent superposition of oscillatory cross sections for different *M* states results in a strong damping of the oscillations and lack of *L* dependence.

The dominance of a single *M*-state ($|M| = L$) is called *good L-matching* and corresponds to

$$|\Delta^0| = |l_f^0 - l_i^0| < L/2 \tag{2.16}$$

where l_f^0 and l_i^0 are the peak values of l_f and l_i in the allowed *l*-window. The *M*-population is more evenly distributed in case of *bad L-matching* ($|\Delta^0| > L/2$).

The energy dependence of this condition has been experimentally confirmed in one-neutron transfer reactions, studying the ^{40}Ca(^{13}C,^{12}C)^{41}Ca from 40 to 68 MeV beam energy, as shown in Fig. 2.6.

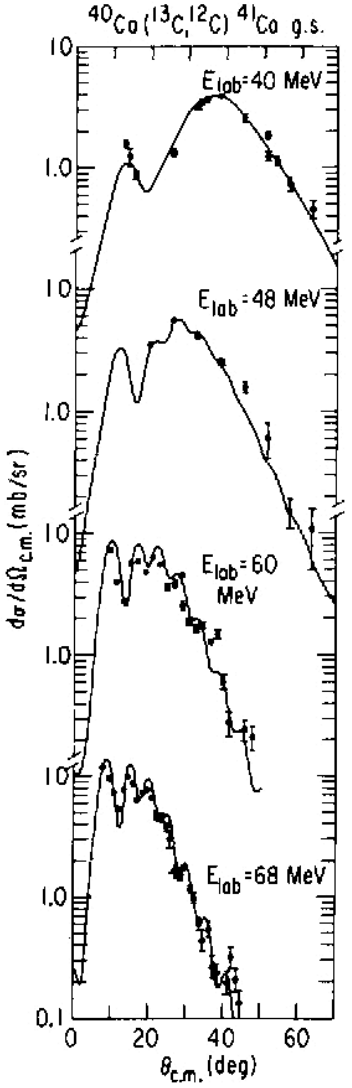

Fig. 2.6. Example of the evolution from a bell-shaped distribution to the appearance of diffraction structure as the beam energy is increasing [20].

2.6 Optical model

The description of heavy-ion induced transfer reactions using the semi-classical approximation permits to understand the qualitative features of the cross sections angular distributions. However, a quantum mechanical approach is necessary in order to obtain quantitative information [3].

One of the main ingredients of the quantum mechanical approach is the optical model, which represents the average nucleus-nucleus interaction as a simple, weakly absorbing, potential well. The model start with the idea that elastic scattering is the most important single event which occurs when two nuclei collide. The description of the elastic scattering channel includes the absorption of the incident flux into many other reaction channels, no one of which is of major importance, although their sum can result in a complete absorption of the flux in the nuclear interior (strong absorption). These many couplings can be represented in an average way by using a complex optical potential.

The relative motion between projectile and target, in terms of a separation $\boldsymbol{r}$, is assumed to be describable by a one-body Schrödinger equation with a potential energy

$$U(\boldsymbol{r}) = V(\boldsymbol{r}) + iW(\boldsymbol{r}) \tag{2.17}$$

where the imaginary part is responsible for the incident flux absorption.

The real part is further divided into nuclear and Coulomb pieces. A Woods-Saxon shape is often used for the nuclear potential

$$\begin{aligned} V_N(\boldsymbol{r}) &= -V_0 f(r) \\ f(r) &= \left[1 + exp\left(\frac{r-R}{a}\right)\right]^{-1} \end{aligned} \tag{2.18}$$

and the potential derived from a uniform charge distribution for the Coulomb part,

$$\begin{cases} \frac{Z_1 Z_2 e^2}{R}\left(\frac{3}{2} - \frac{1}{2}\frac{r^2}{R^2}\right) & r < R \\ \frac{Z_1 Z_2 e^2}{r} & r > R \end{cases} \tag{2.19}$$

The radii entering in eq.s (2.18) and (2.19) are parametrized by

$$R = r_0\left(A_1^{1/3} + A_2^{1/3}\right) = R_1 + R_2 \tag{2.20}$$

with $A_{1,2}$ and $Z_{1,2}$ the projectile, target masses and charges and $r_0 \approx 1.25 \times 10^{-13}$ cm.
The imaginary potential may have a volume piece plus a surface contribution

$$W(\boldsymbol{r}) = -W_0 f(r) + 4aW_s \frac{df(r)}{dr} \tag{2.21}$$

2.7 Models for transfer reactions

The total wavefunction of a colliding system may be expanded in a complete and infinite set of internal states ψ_α for one particular partition α

$$\Psi = \sum_\alpha \xi_\alpha(\boldsymbol{r}_\alpha)\psi_\alpha(x_\alpha) \tag{2.22}$$

where $\boldsymbol{r}_\alpha$ is the channel coordinate for the α partition (see ref. [3] for definition) and x_α represents the corresponding internal coordinates. The usual boundary conditions for (2.22) are that only the term representing the entrance channel has both incoming and outgoing waves asymptotically, while all other terms have only outgoing waves. The Hamiltonian of the α partition can be written as $H = H_\alpha + K_\alpha + V_\alpha$, where H_α is the sum of the internal Hamiltonians for the two nuclei, K_α is the kinetic energy of their relative motion and V_α is their mutual interaction. Considering the Schrödinger equation $(E - H)\,\Psi = 0$, multiplying the left by one of the ψ_α^* and integrating over the internal coordinates x_α, the infinite set of coupled equations for the channel functions $\xi_\alpha(\boldsymbol{r}_\alpha)$ is obtained, which have the form

$$[E - \varepsilon_\alpha - K_\alpha - (\alpha|V_\alpha|\alpha)]\xi_\alpha(\boldsymbol{r}_\alpha) = \sum_{\alpha' \neq \alpha} (\alpha|V_\alpha|\alpha')\,\xi_{\alpha'}(\boldsymbol{r}_\alpha) \tag{2.23}$$

The interaction matrix elements are integrals over the internal coordinates x_α, so they remain function of only $\boldsymbol{r}_\alpha$

$$(\alpha|V_\alpha|\alpha') \equiv \int \psi_\alpha^*(x_\alpha) V_\alpha(\boldsymbol{r}_\alpha, x_\alpha) \psi_{\alpha'}(x_\alpha) dx_\alpha = V_{\alpha\alpha'}(\boldsymbol{r}_\alpha) \tag{2.24}$$

In the practical case, the exact wavefunction Ψ is replaced by a model one Ψ_{model}, where the sum over α in (2.22) is truncated to a limited number N of terms

$$\Psi_{model} = \sum_{\alpha=1}^{N} u_\alpha(\boldsymbol{r}_\alpha)\psi_\alpha(x_\alpha) \tag{2.25}$$

The symbol u_α instead of ξ_α is used, since the model and exact channel functions differ. The correspondent effective Hamiltonian H is such that $(E - H)\,\Psi_{model} = 0$. Applying the same manipulations that led to (2.23), a finite set of coupled equations for the channel functions $u_\alpha(\boldsymbol{r}_\alpha)$ is obtained, in the same form of (2.23) but where V_α is the model effective interaction in the α channel. It is possible to introduce an arbitrary auxiliary potential $U_\alpha(\boldsymbol{r}_\alpha)$ which cannot change the internal states of the α partition, since it depends only on the channel radius $\boldsymbol{r}_\alpha$. Then, eq. (2.23) for the model space become [3]

$$[E - \varepsilon_\alpha - K_\alpha - U_\alpha(\boldsymbol{r}_\alpha)]u_\alpha(\boldsymbol{r}_\alpha) = \sum_{\alpha' \neq \alpha} (\alpha|W_\alpha|\alpha')\,\xi_{\alpha'}(\boldsymbol{r}_\alpha) \tag{2.26}$$

where $W_\alpha = V_\alpha(x_\alpha, \boldsymbol{r}_\alpha) - U_\alpha(\boldsymbol{r}_\alpha)$ is called *residual interaction*. The motivation for introducing the auxiliary potential is to include in it a large part of the average effects of the interaction V_α, so that the residual interaction W_α can be treated as a perturbation.

2.7.1 Spectroscopic factor

The nuclear structure information relevant to the transition (2.1) is contained in the matrix element of the residual interaction

$$(\psi_B\psi_b|W|\psi_A\psi_a) \tag{2.27}$$

This factor has a shape and a strength; both are important for the interpretation of the reaction. One important aspect of this matrix element is represented by the overlaps (ψ_B, ψ_A) and (ψ_b, ψ_a). A measure of overlaps of this kind gives the spectroscopic factor $S_{l_1 j_1}(b, x|a)$ for the system *a* that gives the probability that when it is in the state ψ_a it will be found to be composed of the entity *x* with orbital angular momentum l_1 and total j_1 relative to the nucleus *b* in the state ψ_b. Similarly, the spectroscopic factor $S_{l_2 j_2}(A, x|B)$ for the system *B* represent the probability that when *B* is in the state ψ_B it is composed of *x* with angular momenta l_2, j_2 relative to the nucleus *A* in state ψ_A. Any transfer reaction involves two spectroscopic factors, one for the donor and one for the acceptor. The measurements of such quantities are of considerable interest for probing the nuclear structure.

The spectroscopic factor is the structural link between the actual wave functions of the initial and final products of a given reaction and the bound-state structure probed. In heavy-ion induced transfer reactions the product of two spectroscopic factors, for target and projectile, enters in the calculation of the cross sections.

2.7.2 Post and prior representation of the residual interaction

The transition amplitude in the Distorted Wave (DW) approximation has the form[3]:

$$T_{\beta\alpha}^{DW}(\boldsymbol{k}_\beta, \boldsymbol{k}_\alpha) = \iint d\boldsymbol{r}_\beta \, d\boldsymbol{r}_\alpha \chi_\beta^{(-)}(\boldsymbol{k}_\beta, \boldsymbol{r}_\beta)^* (\psi_B\psi_b|W|\psi_A\psi_a)\chi_\alpha^{(+)}(\boldsymbol{k}_\alpha, \boldsymbol{r}_\alpha) \tag{2.28}$$

There are three main ingredients in eq. (2.28): (1) the distorted waves χ; (2) the residual interaction *W*; and (3) the nuclear wavefunction overlaps (ψ_B, ψ_A) and (ψ_a, ψ_b).

The standard prescription is to generate the distorted waves from an optical potential obtained by fitting elastic scattering data for the entrance channel and, where possible, the exit channel at the same energies involved in the transfer reaction. If such data are not available, potentials obtained from data at similar energies on targets with nearby mass and atomic number may be used; this is frequently necessary for the exit channel. In particular, *global* potentials obtained from simultaneous analysis of a number of data sets for targets in the appropriate mass region may be used [3].

The residual interaction W in (2.28) may be taken in either post or prior form that give identical answers provided the interaction and the wavefunctions are chosen consistently[3]. The post interaction for the rearrangement reaction (2.1) is

$$W_\beta \equiv V_{bB} - U_\beta = V_{bx} + (V_{bA} - U_\beta) \tag{2.29}$$

where U_β is the distorting potential used to generate the χ_β in the exit channel, V_{bB} is the interaction potential between b and B, V_{bx} is the interaction that binds x to form the nucleus a and V_{bA} is the interaction between the two cores A and b. In an extreme binary-cluster model for $a = b + x$, V_{bx} is simply the interaction binding the two clusters. For example this is the appropriate approach for deuteron stripping $d = p + n$. In other cases it is more realistic to take V_{bx} as a sum of nucleon-nucleon interactions. The interaction is usually simplified for heavy-ion reactions by using the shell-model potential experienced by the one nucleon of x moving in the core b.

The prior interaction for the process (2.1) is

$$W_\alpha \equiv V_{aA} - U_\alpha = V_{xA} + (V_{bA} - U_\alpha) \tag{2.30}$$

where U_α is the distorting potential used for the entrance channel wave χ_α, V_{aA} is the interacting potential between a and A and V_{xA} is the interaction that binds x to A to form B.

When a is a light ion and A is appreciably heavier, the product $V_{bx}\psi_A$ (in the post form) will have a shorter range than the product $V_{xA}\psi_B$ (in the prior form) and thus it is more appropriate when the zero-range approximation is used. This has led the post interaction (2.29) being often used for light-ion stripping reactions. This distinction does not hold for heavy-ion reactions, where the target and projectile may be of comparable size.

2.7.3 One-nucleon transfer

Consider the rearrangement process (2.1) where x is a single nucleon. The corresponding interaction matrix element is

$$I_{\beta\alpha}(\boldsymbol{r}_\beta, \boldsymbol{r}_\alpha) = J_{\beta\alpha} \int d\zeta_\beta \, \psi_B^*(\boldsymbol{r}_{xA}, \zeta_x, \zeta_A)\psi_b^*(\zeta_b) W \psi_A(\zeta_A)\psi_a(\boldsymbol{r}_{xb}, \zeta_x, \zeta_b) \tag{2.31}$$

where ζ_β stands for the set of internal coordinates $\{\zeta_x, \zeta_b, \zeta_A\}$ and $J_{\beta\alpha}$ is the Jacobian of the transformation from the coordinates $x_\beta = (r_{xA}, \zeta_\beta)$ to (r_α, ζ_β). The residual interaction W can be represented in the post form (2.29) or in the prior form (2.30). If excitation of the nuclei by W is neglected and if it is assumed to contain no spin-dependence, W commutes with ψ_A and ψ_a. The integrand in (2.31) then reduces to a product of W with two overlap functions (ψ_B, ψ_A) and (ψ_b, ψ_a) related to the spectroscopic factors. Each term of the residual interaction is composed by a nuclear part and a Coulomb part. It is usual to assume that the nuclear parts depend only on r and a Woods-Saxon shape is used, although occasionally folded potentials have been used [3][5].

In a multinucleon transfer, if the transferred nucleons could be regarded as a cluster x in a well-defined internal state, the single-nucleon transfer theory can be directly applied [3]. A typical case is represented by the α transfer reactions as for example (^{7}Li,d) or (^{7}Li,t).

2.7.4 Two-nucleon transfer

The theoretical description of two-nucleon transfer reactions has been developed much further than for other multinucleon transfers. This is mainly because of its usefulness in probing pairing correlations in nuclei [4].

The appropriate coordinates for treating two-nucleon transfer reactions are shown in Fig. 2.7. The (ψ_B, ψ_A) overlap can always be expressed as a superposition of products of single-nucleon wavefunctions [64]:

$$\left[\psi_{l_v j_v}(\boldsymbol{r}_{1A}, \sigma_1) \times \psi_{l'_v j'_v}(\boldsymbol{r}_{2A}, \sigma_2)\right]_{j_2}^{m_2} \tag{2.32}$$

which corresponds to the tensor product of spherical harmonics coupled to a resultant j_2,m_2. The total angular momentum is $\boldsymbol{j}_2 = \boldsymbol{j}_v + \boldsymbol{j}'_v$ where $\boldsymbol{j}_2 = \boldsymbol{I}_B - \boldsymbol{I}_A$. In order to obtain the same representation used for single-nucleon transfer, usually the interaction matrix element $\langle B, b|V|A, a\rangle$ is transformed so that it can be expressed as a function of the variables $\boldsymbol{r}_{xA}$ and $\boldsymbol{r}_{xb}$. The first step of this procedure is to transform the overlap (2.32) from *j-j* coupling to *L-S* coupling, thereby separating the spatial and spin parts [65]. The angular momentum coupling becomes

$$\boldsymbol{l}_v + \boldsymbol{l}'_v = \boldsymbol{L}_2, \qquad \tfrac{1}{2} + \tfrac{1}{2} = \boldsymbol{S}, \qquad \boldsymbol{L}_2 + \boldsymbol{S} = \boldsymbol{j}_2. \tag{2.33}$$

Here L_2 is the total orbital angular momentum of the pair, made up partly of the centre of mass motion of the pair relative to the core nucleus A and partly of motion relative to each other. The next step is to transform the spatial part of Eq. (2.32), that is now a function of $\boldsymbol{r}_{1A}$ and $\boldsymbol{r}_{2A}$, into a function of the *center-of-mass* and *internal* variables for the cluster x:

$$\boldsymbol{r}_{xA} = \tfrac{1}{2}(\boldsymbol{r}_{1A} + \boldsymbol{r}_{2A}), \qquad \boldsymbol{r}_{12} = \boldsymbol{r}_{1A} - \boldsymbol{r}_{2A}. \tag{2.34}$$

The radial part of each single-particle function may be expanded in an harmonic oscillator basis, then each product of oscillator functions will be subjected to the standard Talmi transformation [66][67]. After this transformation, the angular momentum coupling becomes

$$\boldsymbol{j}_2 = \boldsymbol{l}_2 + \boldsymbol{s}, \qquad \boldsymbol{l}_2 = \boldsymbol{L}_2 - \boldsymbol{l}_{12}, \qquad \boldsymbol{s} = \boldsymbol{l}_{12} + \boldsymbol{S} \tag{2.35}$$

where l_2 is the angular momentum of the center of mass of the two-nucleon *cluster* relative to A (the same as (2.3)), l_{12} is the 'internal' angular momentum of the pair relative to one another and s is the total internal angular momentum (or spin) of the cluster. If the two nucleons are identical, $l_{12} + S$ must be even.

When considering two-nucleon transfer reactions between heavy ions, the same transformations are applied to the overlap $(\psi_b, V\psi_a)$, in order to transform the dependence on $\boldsymbol{r}_{1b}$ and $\boldsymbol{r}_{2b}$ in a dependence on $\boldsymbol{r}_{xb}$ and $\boldsymbol{r}_{12}$, with a transformation analogue to (2.34). The final result is the matrix element $\langle B, b|V|A, a\rangle$ in the desired form as a function of $\boldsymbol{r}_{xA}$ and

$\boldsymbol{r}_{xb}$, that can be handled in the same way as for single-nucleon transfer, whether in DW approximation or in CRC equations. Further details can be found in ref. [68].

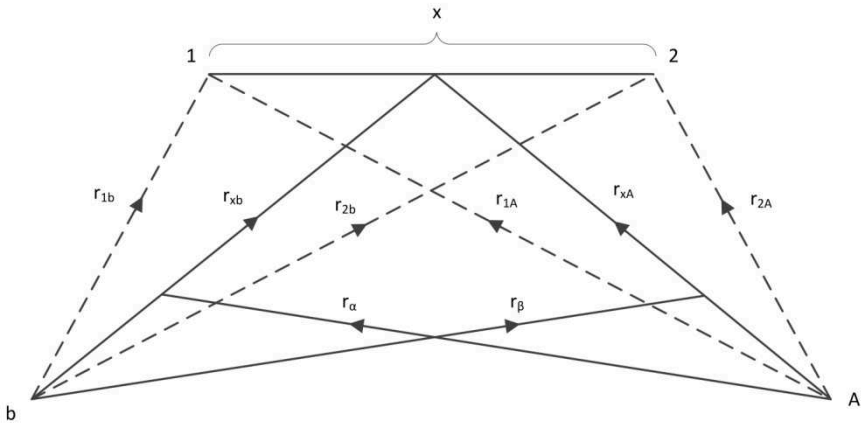

Fig. 2.7. Coordinates for the description of the two-nucleon transfer reaction $a\ (= b + x) + A \rightarrow b + B\ (= A + x)$, where x = nucleon 1 + nucleon 2.

2.8 Second order DWBA for two-nucleon transfer reactions

Early analyses [69][70][71] of two-nucleon transfer data with light ions involved simple generalizations of the one-particle transfer first-order DWBA available codes. Because these generalizations did not use a normalizable interaction, it was impossible to use them to calculate absolute cross sections. They were limited to the calculation of the shapes of angular distributions, or the calculation of the relative cross section for the population of different final states in the residual nucleus.

The first attempts [72][73] to calculate two-nucleon transfer cross sections using a realistic, normalized interaction in a DWBA calculation underestimated the observed cross section by factors of 3 to 10. Similarly, first-order DWBA calculations of two-nucleon transfer between heavy ions [74] [75][76], performed with careful treatment of recoil effects, underestimated the cross section.

This was due mainly to the fact that the physical transfer process involves multi-step routes that were not included in the one-step calculation. One type of multi-step route involves inelastic excitation of the target, projectile, ejectile, or residual nucleus. If such inelastic excitations are strong, it is important to include them, and this can readily be done by replacing the optical model calculations of DWBA by coupled-channels calculations

(CRC). For two-nucleon transfer a multi-step route involving two successive single-nucleon transfers is also possible.

However, some main features of the process can be understood in terms of a semi-classical description of the relative motion of the colliding nuclei (an approximation normally valid for of heavy-ion reactions above the Coulomb barrier), and in perturbation theory for the form factor calculation. Namely, first order DWBA is adopted for one-particle and second order DWBA for two-particle transfer channels. Excellent and complete reviews of the proper reaction formalism can be found, for example, in [3][51][77][78].

In this Section a brief summary of the basic ingredients of the perturbative semi-classical formalism for one- and two-particle transfer is presented, based on the review done in ref. [5]. The basic idea of a semi-classical formalism is the possibility of describing the relative motion of the centers of mass of the two ions in terms of classical dynamics. At the same time the time dependent quantal coupled equations corresponding to the internal excitations (or rearrangements) of the two ions are solved.

The basic role in the description of the transfer process is played by the one-particle transfer form factors, which are the building blocks of the formalism for both single- and multi-nucleon transfer. The situation can be treated in analogy with the inelastic processes due to single-particle excitation, but with the complication that, due the particle transfer from one core to the other, the center of mass of the two colliding nuclei changes from the initial to the final channel. As a result, the corresponding single-particle form factor has a non-local nature, depending on the coordinates of the relative motion in both entrance and exit channels. As extensively discussed in ref.[51], this non-locality can be transformed into a momentum dependence, and it is found to give the smaller effects the lower is the bombarding energy and the heavier are the systems.

2.8.1 Formalism

Considering the no-recoil approximation, the radial transfer matrix element for the one-nucleon transfer ($a + A \rightarrow b\ (= a - 1) + B(= A + 1)$) has the form

$$F_{L,M}(\vec{r}) = F_L^{i,f}(r)Y_{L,M}(\hat{r}) = \int d\vec{r}_a \psi_B^{i*}(\vec{r}_B)\left(V_a(r_a) - \langle V_a\rangle(r_a)\right)\psi_a^f(\vec{r}_a) \qquad (2.36)$$

where the unique core-core relative coordinate $\vec{r} = \vec{r}_{aA} = \vec{r}_{bB}$ and the post representation for the interaction $V_a(r_a)$ were used [5]. This form factor is given in terms of the initial and final single-particle states *i* and *f* in nuclei *a* and *B*, respectively. The angular momentum *L* is the total angular momentum transferred between the two nuclei from the relative motion, while *M* is its third component. In the region normally explored in the reaction, i.e. outside the Coulomb barrier, the form factors behave approximately as exponentials, and simple and useful parametrizations can be found, for example in ref. [51][79]. Within this scheme the first-order perturbation amplitude for the transition corresponding to the transfer of a particle from the single-particle orbital *i* in nucleus *a* to the single-particle orbital *f* in nucleus *B* is given by

$$a_{i,f}^{(1)} = -\frac{i}{\hbar}\int_{-\infty}^{\infty} dt\, F_L^{i,f}\big(r(t)\big) exp[\left(\frac{i}{\hbar}\right)\big(E_\beta - E_\alpha\big)t + \gamma_{\beta\alpha}(r(t)) + i\mu\phi(t)] \qquad (2.37)$$

where the radial function $\gamma_{\beta\alpha}$ accounts for the different phases of distorted waves in initial and final channels, and the time dependence of the coordinates *r* and ϕ for the relative motion is obtained by solving the classical equations of motion for the *average trajectory* of the colliding ions for a definite value of the impact parameter (and reaction angle).

When moving to the case of two-nucleon transfer, as for example a stripping reaction $a + A \rightarrow b\ (= a - 2) + B(= A + 2)$, the situation is complicated by the presence of all intermediate channels corresponding to the sequential one-particle transfer contributions. In fact, as the external field is of one-body character, in addition to the initial (α) and the final (β) channels, also the intermediate channels γ corresponding to $c(= a - 1) + C(= A + 1)$ have to be included. This corresponds to an additional term in the perturbation expansion of the total amplitude, i.e. the second-order sequential transfer contributions $a_{\beta\alpha}^{(seq)}$, even if the non-orthogonality of the model channel wavefunctions in the different partitions still gives rise to a first-order contribution. Thus,the total amplitude up to second order assumes the form

$$a_{\beta\alpha}^{(2)} = a_{\beta\alpha}^{(1)} + a_{\beta\alpha}^{(seq)} + a_{\beta\alpha}^{(orth)} \qquad (2.38)$$

where $a_{\beta\alpha}^{(1)}$, $a_{\beta\alpha}^{(seq)}$ and $a_{\beta\alpha}^{(orth)}$ are the simultaneous transfer, sequential transfer and non-orthogonality term, respectively (the complete expression for them can be found in ref.

[5]). To calculate the total pair transfer amplitude, a sum of the contributions associated with each mean field contribution, labeled by the quantum numbers (j_i, j_f), is to be carried out leading to

$$T_{2NT} = \sum_{j_f j_i} B_{j_f} B_{j_i} \left(a_{\beta\alpha}^{(1)}(j_f, j_i) + a_{\beta\alpha}^{(seq)}(j_f, j_i) + a_{\beta\alpha}^{(orth)}(j_f, j_i) \right) \tag{2.39}$$

the quantity B_j represents the two-nucleon spectroscopic amplitude[80]. It is important noticing that in eq. (2.39) the nuclear structure information, which is essentially all contained in the amplitudes B_j, is closely interweaved with the reaction amplitudes. Therefore, quantitatively accurate description of pair transfer requires to treat on a par both structure and reaction aspects of the process.

The differential cross section associated with the two-particle transfer amplitudes discussed above can be written as

$$\frac{d\sigma}{d\Omega} = \frac{\mu_i \mu_f}{(4\pi\hbar^2)^2} \frac{k_f}{k_i} |T_{2NT}|^2 \tag{2.40}$$

where μ_i, μ_f are the reduced masses in entrance and exit channels, respectively, while k_f, k_i are the corresponding relative momenta [80].

2.8.2 Examples of applications

In some cases the sum of the three contributions to the two-nucleon transfer amplitude of eq. (2.38) becomes particularly simple. The first is the case of a purely independent two-particle transfer process, which implies equal form factors and Q-values for the different roots (only two intermediate channels are clearly active in this case, or just one if the two particles are transferred in the same single-particle orbital, as in the case of a $L = 0$ transfer). In this condition the one-step contribution precisely cancels the non-orthogonality term and the second-order amplitude becomes simply proportional to the product of the one-step amplitudes for each individual step. In the particular case of the transfer of a pair with angular momentum $L = 0$ therefore, the uncorrelated sequential transfer gives an amplitude, and consequently a probability, which are the square of the

corresponding quantities for the single-particle transfer. An example of this cancellation is provided by the results of the analysis of the ^{132}Sn(t,p)^{130}Sn reaction at a laboratory energy of 20 MeV, carried out by Potel et al. [80]. The resulting calculations are shown in Fig. 2.8, where the simultaneous (red dashed line) and non-orthogonal (red line) contributions are in anti-phase, so that the contribution corresponding to the coherent superposition of these two amplitudes (blue line) tend to cancel out. The calculated cross section thus essentially coincides with the successive (black dashed line) process.

The sequential process was found to be predominant also in the ^{208}Pb(^{16}O,^{18}O)^{206}Pb reaction at an energy slightly above the Coulomb barrier [81]. The experimental angular distribution for the transition to the ^{206}Pb$_{g.s.}$ is shown in Fig. 2.9 together with the one-step and two-step calculations. The complete calculation is able to reproduce the absolute value with sufficient success and the multi-step route involving two successive single-nucleon transfers gives the larger contribution. It is worth noticing also that the two contributions give rather similar angular distributions, and therefore this issue cannot be used as a way of discriminating their relative importance.

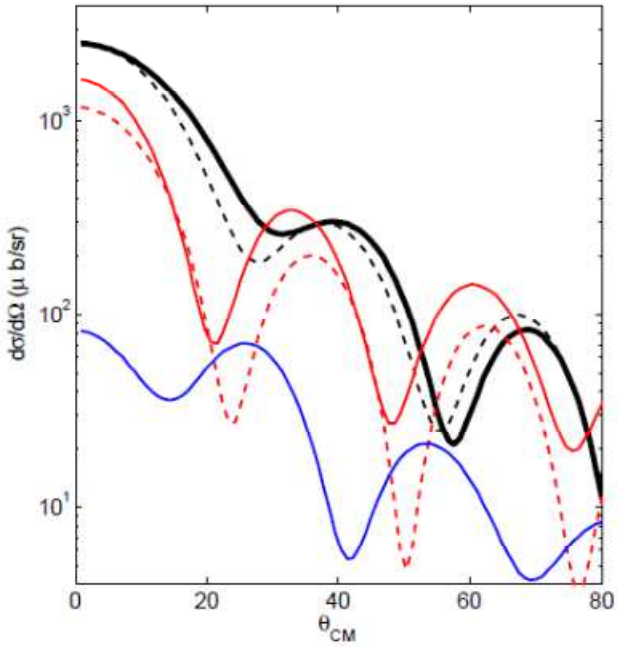

Fig. 2.8. Total two-neutron transfer cross section (thick black line) for the ^{132}Sn(p,t)^{130}Sn reaction at 20 MeV incident energy. The simultaneous (red dashed line), non-orthogonal (red line) and successive (black dashed line) amplitudes contributions are also shown. The coherent superposition of the simultaneous and non-orthogonal processes is indicated with the blue line[80].

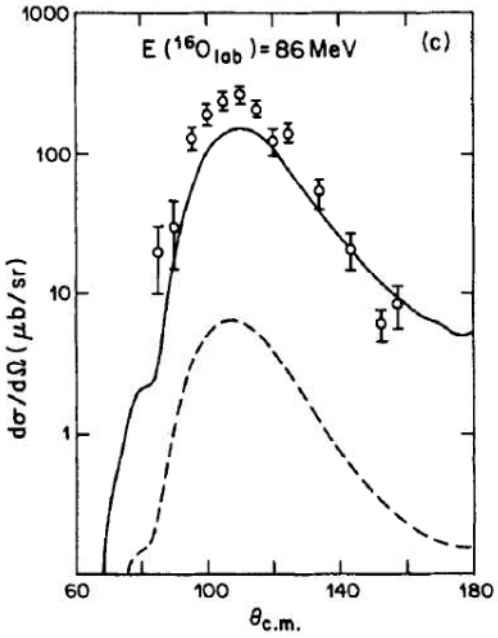

Fig. 2.9. Angular distribution for the two-neutron transfer reaction ^{208}Pb(^{16}O,^{18}O)^{206}Pb at 86 MeV incident energy, populating the ground state of ^{206}Pb. The result of the one-step calculation and the result of the one-step plus two-step calculations are shown with the dashed and the full curves, respectively [81].

The opposite behavior is obtained in the limit of very strong two-particle correlation. In the 'hypothetical' case of extremely strong correlation, the intermediate state cannot be populated since the extremely correlated pair should be broken in this case. From an analytic point of view, the strong pair correlation implies intermediate states with high excitation energies. This implies the dominance of the principal part contribution with respect to the real sequential amplitude, and in the limit of infinitely strong correlation this contribution exactly cancels the non-orthogonality term and the process can be entirely ascribed to the one-step mechanism.

Real cases will not correspond to either extreme situations: pairing correlations are present but not extremely strong, so it can be envisaged from one side an enhancement of the sequential transfer probability and at the same time a non-negligible contribution from the one-step process. The precise interplay of the two contributions will depend on the specific case.

Recently, the second order DWBA approach has been applied [80][82] to calculate the absolute differential cross sections for the reactions ^{A}Sn(p,t)$^{A-2}$Sn$_{g.s.}$ ($102 \leq A \leq 130$). In all cases, the successive, simultaneous and nonothogonality contributions were considered.

The results of the theoretical predictions are shown in Fig. 2.10, in comparison with the experimental data for all the six mass numbers (A = 124, 122, 120, 118, 116 and 112) which were studied in ref. [83][84][85][86]. Such theory provided, without any free parameters, an explanation of the absolute value of all the measured differential cross sections within the experimental errors.

What is missing in such kind of calculations are the routes involving inelastic excitations of the target, projectile, ejectile, or residual nucleus, which are found to be not relevant for (p,t) reactions but can correspond to a major part of the cross section when considering heavy-ion induced reactions [87].

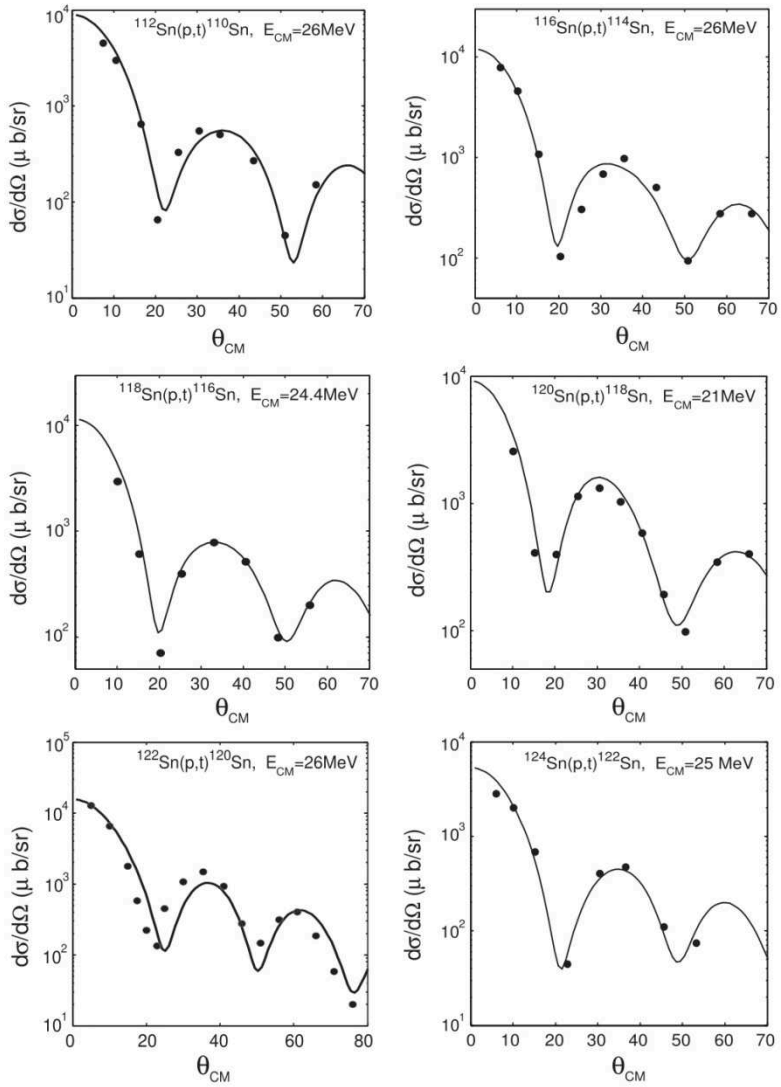

Fig. 2.10. Absolute cross section predictions calculated with a second order DWBA approach [82] in comparison with the experimental results [83][84][85][86].

Chapter 3
Search for the GPV with (^{18}O,^{16}O) reactions

The collectivity induced by the pairing correlations manifests itself in the transitions induced by the operator associated with the creation (or annihilation) of a pair of nucleons coupled to angular momentum zero. Thus, the relevant matrix elements are those connecting a system with the neighboring nuclei differing by two units of atomic mass. The appropriate reactions to test these collective matrix elements are therefore the two-nucleon transfer reactions. Because of the pairing interaction the two-neutron transfer reactions can proceed with a direct transfer of one correlated pair. If the correlation is strong the one-step mechanism is expected to prevail, the two-step sequential process being instead dominant in the case of pure uncorrelated nucleons. The quantitative characterization of these two processes is a key point in the understanding of pairing correlations in nuclei.

Despite an intensive research activity in this field, some key questions need still to be answered and the interest of the scientific community is unchanged. One of the issues still unresolved concerns the existence of the GPV. In the past several theoretical studies were developed investigating the properties of the GPV and the best experimental conditions by which observe it [7] [10][11]. The main results have been reported in Chapter 1. On the other hand, many experimental attempts were performed using (t,p) or (p,t) transfer reactions on tin and lead isotopes [14][15][47] (see Section 1.4). However these attempts remained unsuccessful.

Probably the reason for these failures lies in the tricky reaction mechanism required for the population of the GPV. Indeed, the GPV requires an $L = 0$ one-step transfer of a correlated pair, but typically in transfer reactions, which tends to be peripheral processes, a

large amount of angular momentum is transferred. In this context, it is important to choose the best kinematical conditions in order to favor the $L = 0$ transfer and the appropriate beam energy. From a detailed analysis of these aspects, transfer reactions induced by heavy ions seems to be more appropriate in order to populate the GPV than those one by light ions (as the (t,p) or (p,t) reactions). In particular, the (^{18}O,^{16}O) reaction on target in the mass region $10 \leq A \leq 20$ and at ~ 4 times the Coulomb barrier seems to be an interesting probe for the observation of the GPV, as will be described in the following Sections.

3.1 Best experimental conditions for populating the GPV

The main features of the transfer reactions between heavy ions have been described in Chapter 2. These reactions serve as a unique tool for the study of the dynamical aspects of pairing correlations in nuclei. A survey of some results concerning heavy-ion transfer reactions can be found in ref. [5]. Two-neutron transfer reactions induced by heavy ions offer a number of possibilities and specific features, which have allowed significant progress in the study of dynamical pairing correlations with respect to the more traditional transfer reactions induced by light projectiles.

3.1.1 The role of the beam energy

The choice of the proper beam energy is crucial in order to favor the experimental conditions suitable for observing the GPV. It is possible to distinguish three relevant energy regions. Reactions between heavy ions at energies near the Coulomb barrier minimize the angular momentum transfer. On the other hand, as it was shown in Section 2.3.2, the angular distributions are characterized by a bell-shape, peaked at the grazing angle. There is no sensitivity to the L transferred and it is therefore difficult to identify the $L = 0$ channel. Moreover, the Q-value matching rules typically suppress the cross section for high excitation energy states.

Moving towards high incident energies the favored angular momentum transferred become sensibly larger than $L = 0$. In ref. [17] the authors presented data on a large number of multi-nucleon transfer reactions induced by heavy ions with energies of approximately

10 MeV/A. These high energy transfers were found to be highly selective since only a few states of the residual nuclei were strongly populated. Furthermore, a marked preference for populating high spin states emerged, a characteristic which is generally lost at lower bombarding energies. This property was interpreted using a semi-classical model of the reaction in which it was assumed that the transfers take place near the nuclear surface when the projectile and target undergo a grazing collision. The adopted model implied a rather simple dependence of the cross section on the bombarding energy and Q-value of the reaction and on the angular momentum of the transferred nucleons relative to the cores of the incident ion and the final nucleus [19]. They obtained results in reasonable agreement with observations which indicated selection of high spin states in reactions at higher incident energy. Another feature of this energy region is the opening of more dissipative reaction channels, e.g. deep inelastic collisions.

There is an intermediate energy region, between about three and ten times the Coulomb barrier, in which the angular distributions are sensitive to the structure of the final populated states, because they start to depend on the L transferred [17][18]. This region seems to be the most appropriate for populating and recognizing the GPV.

3.1.2 The role of the involved nuclei

In the past, the search for the GPV was performed using only (p,t) reactions on tin and lead isotopes, as reported in Section 1.4. However, when looking carefully at the kinematical matching conditions for transfer reactions deduced by Brink [19] (see Section 2.4), it appears that the (p,t) reactions on heavy targets are not favored for populating the L = 0 channel. Indeed, in order to have a large probability for a certain L, eq. (2.13) should be satisfied. The final orbital angular momentum λ_2 could be close to the initial one λ_1 (and so the L = 0 transfer could be favored) if the other two terms of eq. (2.13) are small. In particular, the second term depends on the difference between the two radii of projectile and target nuclei. In a (p,t) reaction on tin or lead this term is very large and this hinders the L = 0 transfer. It seems to be more appropriate to choose an initial channel in which the projectile and the target have similar masses and radii. For example, a good candidate is the (^{18}O,^{16}O) reaction on light ions as beryllium, boron, carbon or oxygen isotopes. Furthermore, in the ^{18}O projectile there is a preformed neutron-pair in the $2s_{1/2}$ or $1d_{5/2}$

orbitals out of a magic core of ^{16}O. The survival of this pair in the target nucleus is more likely favored if the same orbitals are available in it, as in the case of the above mentioned target nuclei.

3.2 Searching for the GPV with (^{18}O,^{16}O) reactions at 84 MeV

Considering all the crucial aspects of the reaction mechanism described in the previous Sections, an experimental campaign was started using an ^{18}O Tandem beam at 84 MeV incident energy impinging on medium-light targets, searching for the GPV and aiming to understand better the transfer reaction mechanism. These experiments were performed in March 2010 at the Laboratori Nazionali del Sud (LNS-INFN) in Catania. The ejectiles were momentum analyzed using the MAGNEX large acceptance magnetic spectrometer in order to select the two neutron transfer channel. Several targets were used: ^{9}Be, ^{11}B, ^{12}C, ^{13}C and ^{16}O. The beam energy chosen corresponds to about 3.5 times the Coulomb barrier for all targets. In this energy range the angular distributions should be sensitive to the angular momentum transferred, as indicated in Section 3.1.1.

These experimental conditions should be the adequate in order to populate the GPV and to better understand the two-neutron transfer reaction mechanism.

In this thesis work, the results obtained from the reactions ^{12}C(^{18}O,^{16}O)^{14}C and ^{13}C(^{18}O,^{16}O)^{15}C will be described in details. The data analysis for the other targets is still in progress. The spectroscopic information regarding ^{14}C and ^{15}C nuclei is quite vast and is summarized in Chapter 4.

Chapter 4
Spectroscopy of the ^{14}C and ^{15}C nuclei

The present work is focused on the study of the (^{18}O,^{16}O) reaction at 84 MeV incident energy on ^{12}C and ^{13}C targets, populating the ^{14}C and ^{15}C residual nuclei. In the past, such nuclei have been investigated deeply and the relating literature is quite vast. Many different reaction channels were used, e.g. one-, two- and three-neutron transfer, fusion-evaporation reactions, charge exchange reactions. The present Chapter is devoted to the description of some known spectroscopic features of the ^{14}C and ^{15}C nuclei, focusing on two-neutron transfer channel.

4.1 The ^{14}C nucleus

The ^{14}C nucleus was studied using several channel reactions and the consequent spectroscopic information is massive. An almost complete spectroscopy for ^{14}C up to 18 MeV excitation energy can be found in ref. [88].

The ^{14}C nucleus can be viewed as a ^{12}C core plus two neutrons. From shell-model calculations, the ^{12}C nucleus has an almost closed ($1p_{3/2}$)-shell in its ground state, with a 71% ($p_{3/2}$) and 27% ($p_{1/2}$) configuration occupation [89]. The lower-lying states of ^{14}C would then result from adding two particles in the partially open $p_{3/2}$ (due to the ground-state correlations), and the higher almost empty $1p_{1/2}$, $2s_{1/2}$, $1d_{5/2}$ or $1d_{3/2}$ orbitals. However, since ^{12}C does not have a completely closed $1p_{3/2}$ subshell, some of the lower levels in ^{14}C also have admixtures of $1p_{3/2}$ neutron excitation. For example, the lowest 2^+ state at 7.012 MeV has as the main configuration π-$(p_{3/2})^{-1}(p_{1/2})^{1}$, and higher-lying states have neutron configurations with excitations from the $1p_{3/2}$ to higher orbitals. Another possible view of

the structure of states in ^{14}C is provided by coupling a single neutron to the ground and excited states of ^{13}C, through core excitations of ^{12}C [90].

The ^{14}C one-neutron emission threshold is at S_n = 8.176 MeV. Below this value there are seven bound states, the 0^+ ground state, and states at 6.09 (1^-), 6.59 (0^+), 6.73 (3^-), 6.90 (0^-), 7.01 (2^+) and 7.34 (2^-) MeV [91]. For the $^{14}C_{g.s.}$, which is considered to be a closed-shell nucleus, a mixing with the *sd*-shell configurations of about 5% of the total strength was found in the analysis of neutron stripping reactions [92]. The second 0^+ state at 6.59 MeV and the ground state are often discussed as states with mixed configurations, due to the mixing introduced by the pairing interaction [93].

4.2 The ^{15}C nucleus

The one neutron energy threshold for ^{15}C is quite low (S_n = 1.218 MeV) and below it there are only two weakly-bound states, the $1/2^+$ ground and the $5/2^+$ first excited one at E_x = 0.74 MeV. The spin and parity of the ^{15}C ground state have been firmly assigned to be $J^{\pi}_{g.s.} = 1/2^+$ by neutron stripping reactions, which were the first experiments devoted to the spectroscopic study of ^{15}C (see Section 4.3). All these experiments agree on the J^{π} values of the ^{15}C ground and first excited state. The ground state wave function is given mainly by the $^{14}C_{g.s.}(0^+) \otimes (2s_{1/2})$ configuration with a spectroscopic factor S = 0.88, while the wave function of the 0.74 MeV excited state is given by $^{14}C_{g.s.}(0^+) \otimes (1d_{5/2})$ with S = 0.69 [94]. However, non negligible contributions from configurations with excited states of the ^{14}C core were found by nuclear break-up of ^{15}C [95]. In ^{15}C the $1d_{5/2}$ and $2s_{1/2}$ neutron orbitals are inverted with respect to the independent-particle model levels.

The simplest structure possible for the ^{15}C states is the one particle-two hole[1] ($1p$-$2h$), obtained by coupling a *sd*-shell neutron to the 0^+ ground state of the ^{14}C core. These states are predicted with angular momentum and parity J^{π} of $1/2^+$, $3/2^+$ and $5/2^+$, determined by the valence neutron. The ^{15}C ground and first excited state are almost entirely $1p$-$2h$ states, while the $1p$-$2h$ $3/2^+$ state has been found at an energy of 4.78 MeV [96]. Next in complexity are the negative-parity $2p$-$3h$ states, with J^{π} from $1/2^-$ to $9/2^-$, which consist of

[1] In the present work, the particle (p) and hole (h) operators act on a ^{16}O ground state vacuum. As a consequence ^{14}C and ^{15}C states are characterized by $2h$ in the proton side and possible p-h excitations in the neutron side.

two *sd*-shell neutrons coupled to three *p*-shell holes. Single-neutron transfer reactions can populate the 1*p*-2*h* ^{15}C states, but not the 2*p*-3*h* ones, except via the weak core-excited components of the $^{14}C_{g.s.}$. On the contrary, two-neutron transfers can populate 2*p*-3*h* and 1*p*-2*h* states, the latter only by the sequential transfer of two independent neutrons.

4.3 The (d,p) stripping reactions

A ^{13}C(d,p)^{14}C reaction was studied in 1984 by Peterson et al. [97] using a deuteron beam at 17.7 MeV. The spectrum measured at a laboratory angle of $\theta_{lab} = 55°$ is shown in Fig. 4.1. Experimental angular distributions of the absolute cross section for some positive- and negative-parity states of ^{14}C were compared to DWBA calculations. The positive-parity states of ^{14}C may be formed by arrangements within the 1*p* proton shell or, more likely, by 2*p*-2*h* excitations involving promotions of two neutrons from the *p* to the *sd* shell as well. The (d,p) data to some positive-parity states of ^{14}C are shown in Fig. 4.2. The first positive-parity state is the 0^+ 6.59 MeV, then there are the first two 2^+ states at 7.01 and 8.32 MeV and the 4^+ state at 10.74 MeV. The DWBA predictions for all these states differ greatly from the experimental angular distributions. In the 2^+ angular distributions near 20° some mechanism seems to interfere with both transitions, with opposite sign.

The shell-model structures of the negative-parity states of ^{14}C are sensitively probed by (d,p) reactions, requiring $L = 0$ or $L = 2$ transfers. The experimental angular distributions for the 6.09 (1^-), 6.90 (0^-), 6.73 (3^-), 7.34 (2^-), 9.80 (3^-) MeV states are shown in Fig. 4.3 together with the DWBA calculations. These calculations are consistent with the data and allow to determine the spectroscopic factors.

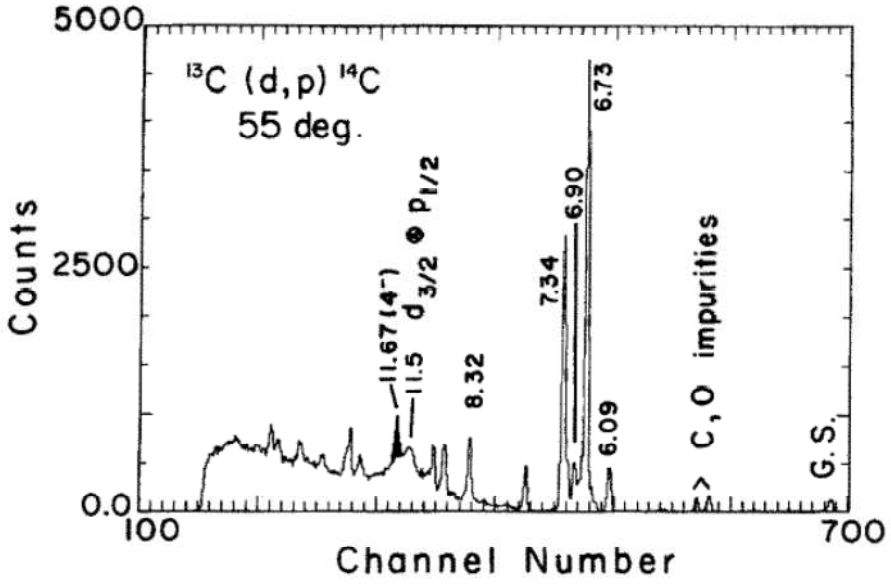

Fig. 4.1. Proton spectrum from the ^{13}C(d,p)^{14}C reaction at 17.7 MeV. The ground state peak is weak due to inefficient particle identification [97].

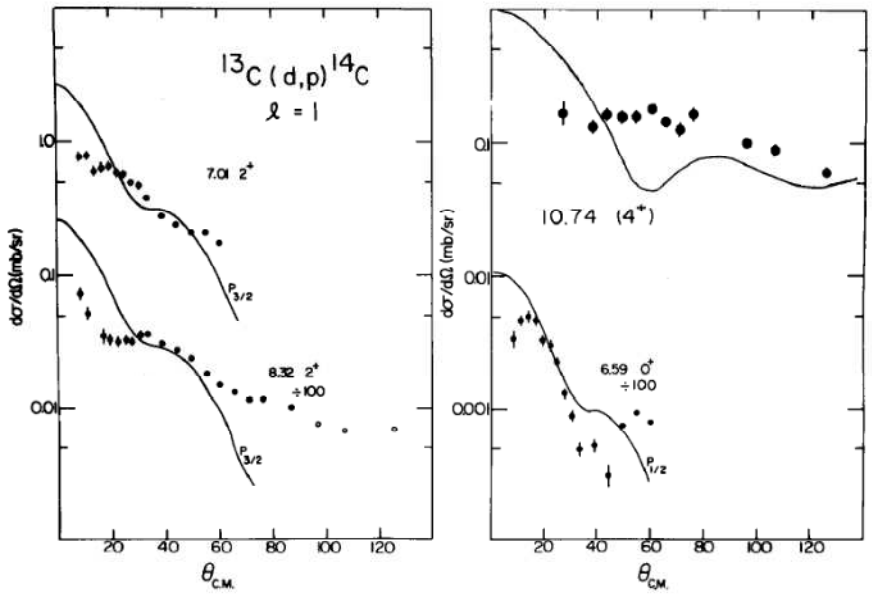

Fig. 4.2. Angular distributions from the ^{13}C(d,p) reaction to the positive-parity states of ^{14}C compared to DWBA calculations (solid lines) [97].

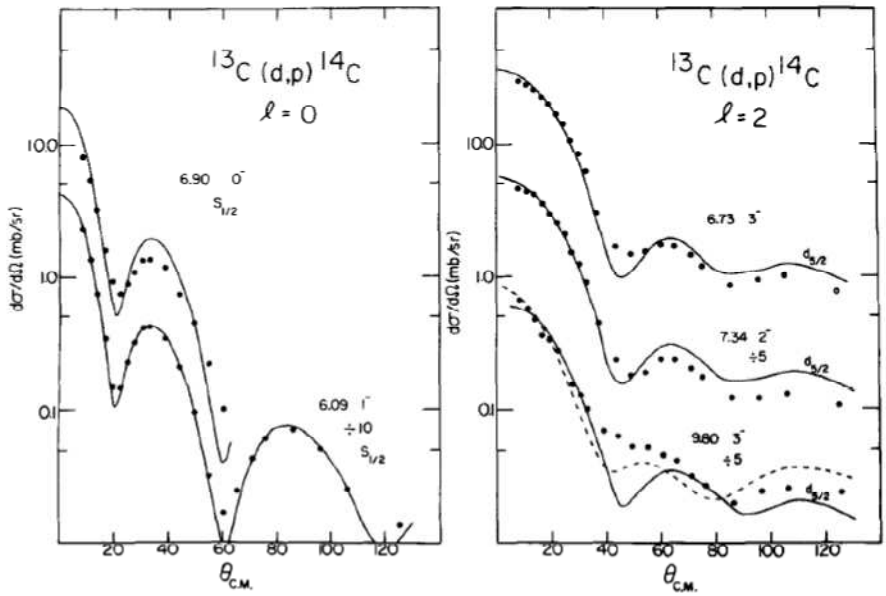

Fig. 4.3. Angular distributions from the ^{13}C(d,p) reaction to the negative-parity states of ^{14}C compared to DWBA calculations (solid lines). Sequential calculation is shown for the 9.80 MeV state (dashed line) [97].

The ^{14}C(d,p)^{15}C stripping reaction was first studied in 1959 by Moore and Mc Gruer [98] in the angular range between 2° and 90°, populating the ^{15}C ground and excited states at E_x = 0.75, 3.09, 4.21, 5.94, 6.38 and 7.32 MeV. The same reaction was studied in 1973 by Goss et al. [99] at 12, 13 and 14 MeV incident energies and θ_{lab} = 60°, 90° and 120°. A magnetic spectrograph was used, allowing for a high experimental energy resolution (~ 14 keV). The resulting proton spectrum, measured at the bombarding energy of 14 MeV and 60°, is shown in Fig. 4.4, where the excitation energy of the populated ^{15}C states are indicated in MeV. Nine excited states were observed, starting from the ground to the 7.35 MeV one, with a better determination of the excitation energies. Two wider levels were found at 3.1053 MeV (Γ ~ 42 keV) and 6.4281 MeV (Γ ~ 61 keV). The presence of a large continuum background in the spectrum made it impossible to observe weakly populated states with Γ > 100 keV.

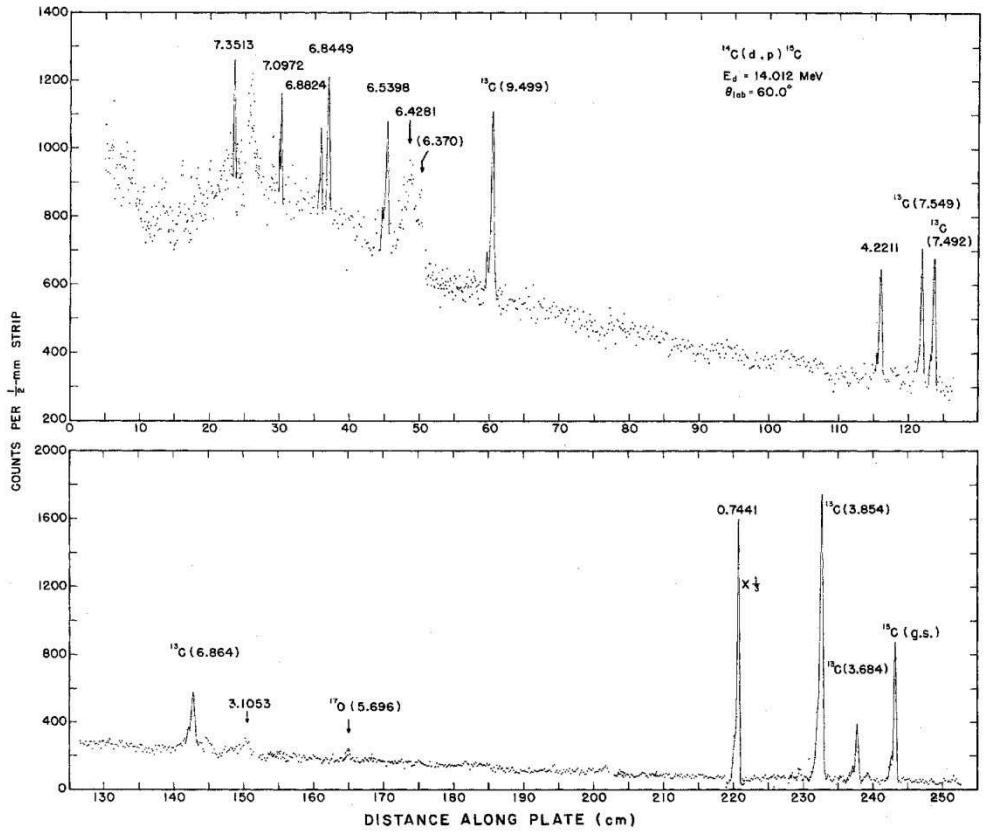

Fig. 4.4. Proton spectrum from the ^{14}C(d,p)^{15}C reaction measured at 14 MeV bombarding energy and θ_{lab} = 60° [99]. Proton groups leading to the ^{15}C states are labeled with the excitation energy in MeV. The contaminants groups are also labeled with the symbol for the residual nucleus and related excitation energy.

The same authors performed a second experiment using a polarized deuteron beam at 14 MeV [94]. The angular distributions were obtained for ten final states up to E_x ~ 7 MeV. DWBA calculations were performed with two different set of optical-model parameters and allowed to assign spin and parity to the ^{15}C ground and first excited states together with the related spectroscopic factors S = 0.88 and 0.69, respectively. These were obtained from the set of optical parameters giving the best fit to the respective angular distributions, as shown in Fig. 4.5. While the second $5/2^+$ state was located at E_x = 6.428 MeV, no evidence for second $3/2^+$ state was found. Besides, many states with high spin (from $7/2^+$ to $13/2^+$) were found in the region between 6 and 7 MeV excitation energy. However, the authors underlined that such assignments may be erroneous if the states are populated predominantly by two-step processes.

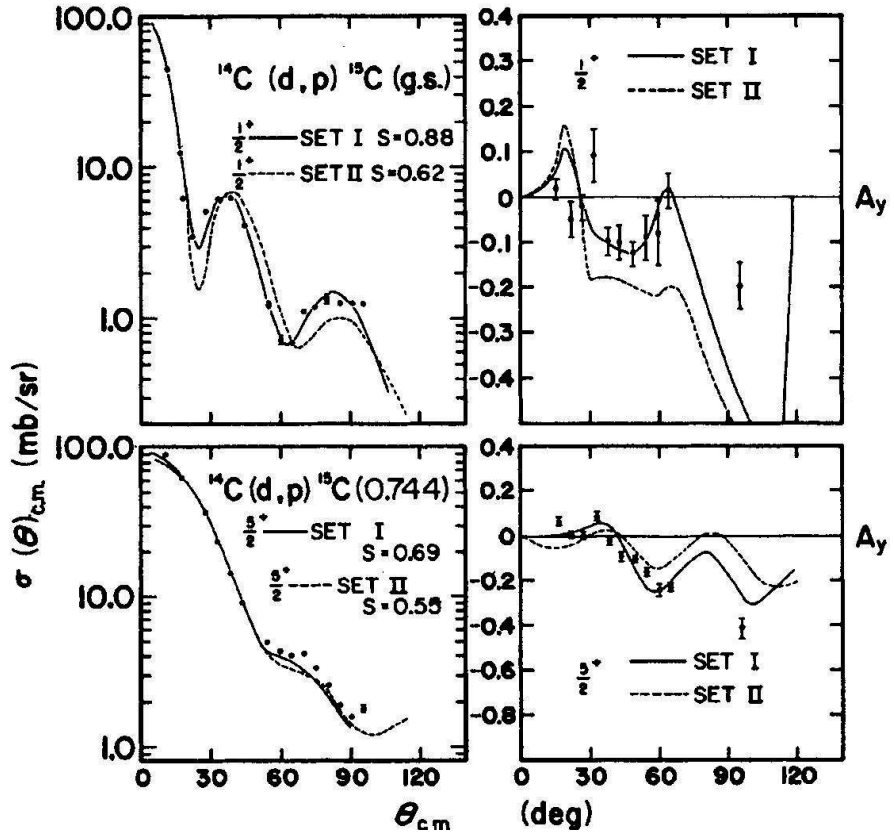

Fig. 4.5. Cross sections and analyzing powers for the two bound states of ^{15}C. DWBA calculations obtained using two different sets of optical-model parameters are shown with the solid line ^{15}C [94].

Another (d,p) experiment was performed with a 16 MeV polarized deuteron beam [100] in order to search for the $d_{3/2}$ strength in the particle-unbound region of ^{15}C, where the $1p$-$2h$ $J^{\pi} = 3/2^{+}$ state is expected to lie. Proton spectra were obtained over the angular range θ_{lab} = 15° to 110° in 5° steps. The experimental results are shown in Fig. 4.6. Two $3/2^{+}$ levels (indicated by the arrows in Fig. 4.6), one broad (Γ = 1.74 ± 0.40 MeV) and one relatively narrow (Γ ~ 64 keV), were observed at E_x = 4.78 and 5.81 MeV, respectively. The authors identified these states with the $1p$-$2h$ and $3p$-$4h$ $3/2^{+}$ levels predicted by shell model calculations.

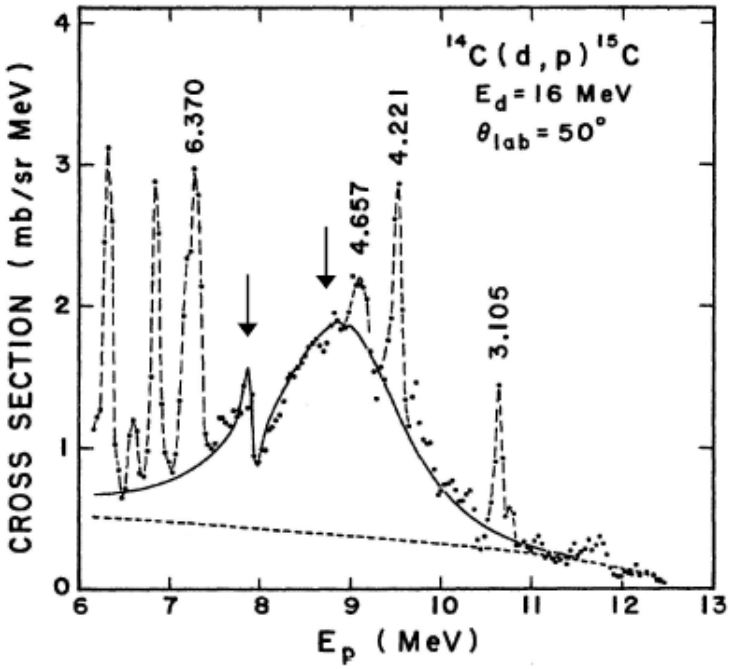

Fig. 4.6. Proton spectrum measured at θ_{lab} = 50° in the ^{14}C(d,p)^{15}C reaction at 16 MeV [100]. Levels candidates to have $J^{\pi} = 3/2^{+}$ are indicated with the arrows. The phase-space contribution due to the deuteron break-up and a fit of the spectrum are indicated with the dashed and solid line, respectively.

4.4 Two-neutron transfer reactions

While one-neutron transfer reactions, such as the ^{14}C(d,p), described in Section 4.3, excite mainly the 1p-2h strength, two-neutron transfers may excite both the 1p-2h and 2p-3h ones. In the past, the most used two-neutron transfer reactions were the (α,^{2}He) and the (t,p) ones.

4.4.1 The (α,^{2}He) reactions

The (α,^{2}He) reactions are found to be very selective, only few states of the residual nucleus are populated and these are usually characterized by high spin. The selectivity of these reactions is due to their large negative *Q*-values which kinematically favour transitions to high-spin states characterized by the configurations with *nn* pair in a relative singlet moving on an undisturbed core.

In 1978 Jahn et al. studied the (α,^{2}He) reaction at 55 and 65 MeV bombarding energies on several targets, among which ^{12}C and ^{13}C, in the angular range θ_{lab} from 12° to 35° [101]. The unbound reaction product ^{2}He was identified by measuring its two break-up protons in coincidence. At 65 MeV bombarding energy on a $^{12\text{-}13}$C target, the transferred angular momentum is about (4-5)$\hbar$ and thus transitions to levels formed by capturing the two stripped neutrons into d orbitals with configurations of $(d_{5/2}{}^2)^{4+}$ is enhanced. Representative ^{2}He energy spectra from the (α,^{2}He) reaction on ^{12}C and ^{13}C are shown in Fig. 4.7. In ^{14}C strong transitions are observed to a 3^- level at 6.73 MeV and to a 4^+ level at 10.72 MeV. Much weaker transitions populate to the ground and an excited states at 14.67 MeV (Fig. 4.7-a). The 3^- state has a dominant $(p_{1/2}d_{5/3})_3$ character whereas the 10.72 has a $(d_{5/2})^2{}_4$ character. The ^{15}C spectrum shows only strong transitions to the 0.74 MeV state ($J^\pi = 5/2^+$) and to two states at E_x = 6.74 and 7.35 MeV (Fig. 4.7-b). Since the ^{12}C and ^{13}C only differ by a $p_{1/2}$ neutron, it is expected that the (α,^{2}He) on ^{13}C populates preferentially the same two-neutron configurations observed in reactions on ^{12}C, but now coupled to the $1/2^-$ target core. In the weak coupling limit the states observed in the ^{14}C spectrum should be split into two components in the ^{15}C one. As an example, the states populated at 6.74-7.34 MeV in ^{15}C (Fig. 4.7-b) are interpreted as a doublet with a configuration $\left\{\left[^{12}C(0^+)p_{1/2}\right]_{1/2^-}\otimes\left(d_{5/2}\right)^2_{4^+}\right\}_{7/2^-,9/2^-}$. The assignment of the spin to the two components of the split state was done considering the $(2J + 1)$ statistical factor which enhances the cross section for the higher spin state. Thus, the 7.35 MeV state should have the higher spin ($9/2^-$) because of its larger cross section.

The above-mentioned split is not present in the $5/2^+$ state at 0.74 MeV because this has a configuration $\left\{\left[^{12}C(0^+)p_{1/2}\right]_{1/2^-}\otimes p_{1/2}d_{5/2}\right\}_{5/2^+}$, in which the $p_{1/2}$ neutron of ^{13}C and the transferred $p_{1/2}$ neutron couple to spin 0.

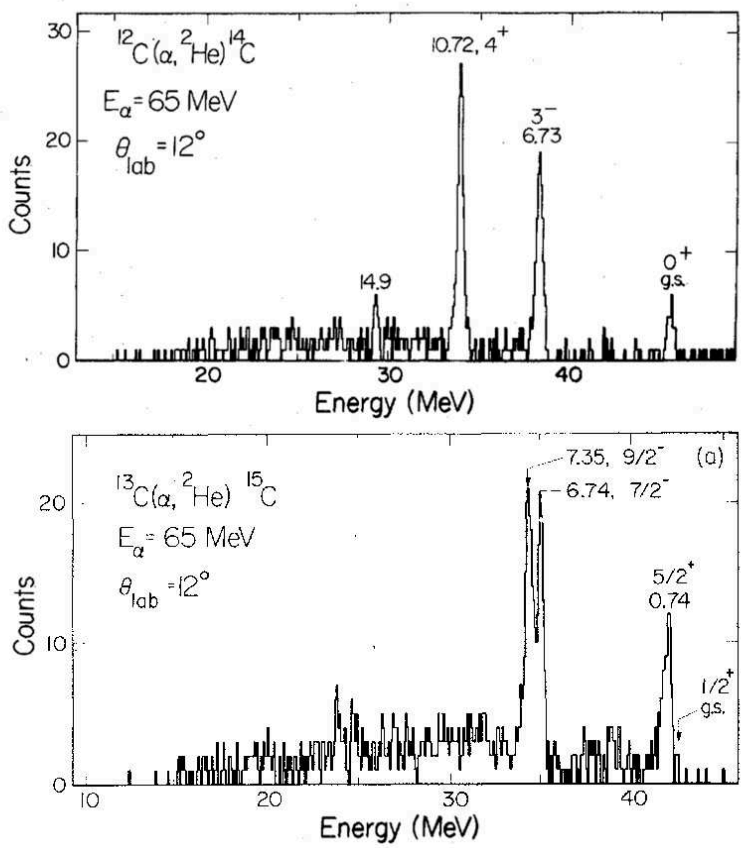

Fig. 4.7. ^{2}He energy spectra obtained from the ^{12}C(α,^{2}He)^{14}C (upper panel) and ^{13}C(α,^{2}He)^{15}C (lower panel) reactions at 65 MeV bombarding energy [101].

4.4.2 The (t,p) reactions

The ^{12}C(t,p)^{14}C reaction was studied in 1978 by Mordechai et al. [89] using a 18 MeV triton beam. Twenty levels of ^{14}C were identified up to 13 MeV excitation energy. The spectrum from the ^{12}C(t,p)^{14}C reaction at θ_{lab} = 3.75° is shown in Fig. 4.8. The level parameters of the bound states of ^{14}C were well known from previous works [102]. These are the g.s. (0^+) and states at 6.09 (1^-), 6.58 (0^+), 6.73 (3^-), 6.90 (0^-), 7.01(2^+) and 7.34 (2^-) MeV. Except for the unnatural parity states at 6.90 and 7.34 MeV, all the other states are strongly populated in the ^{12}C(t,p) reaction. The authors performed DWBA calculations for these strong transitions and the comparison with the experimental cross section angular distributions confirmed the previous assignments. As regards the unnatural parity states, their population is forbidden in a one-step transfer. In fact, in order to explain their small yield it was assumed a two-step reaction mechanism for the (t,p) reaction. Sequential

transfer calculations were carried out, obtaining a satisfactory description of the angular distribution of the 7.34 MeV state assuming a contribution from sequential transfer and another from inelastic excitation of the target before the transfer [89].

Considering the region above the one-neutron emission threshold, several states were populated at 8.31 (2^+), 9.75 (0^+), 9.81 (1^-), 10.43 (2^+), 10.50 (3^+), 10.74 (4^+), 11.4 (1^-), 11.67 (1^-), 11.73 (5^-), 12.58 (2^+,3^-), 12.87 (2^+,3^-), 12.96 (1^-) MeV. These spin and parity assignments were deduced by DWBA calculations, none of them was known prior to ref. [89]. The most striking feature was the discovery of a new state in ^{14}C at 9.75 MeV, which shows a clear L = 0 shape in the angular distribution. It was concluded that, this is the second 0^+ 2p-4h state of ^{14}C (being the state at 6.58 MeV the first).

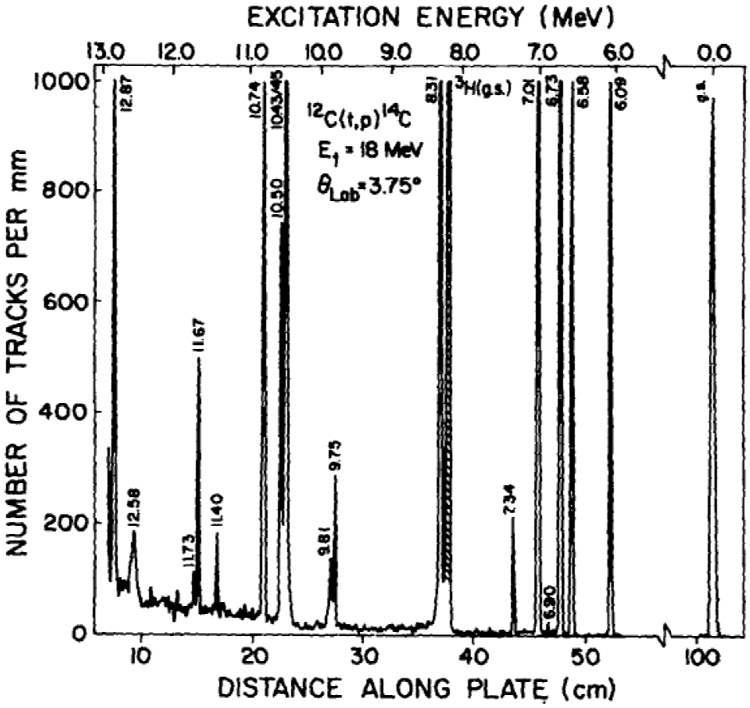

Fig. 4.8. Proton spectrum from the ^{12}C(t,p)^{14}C reaction measured at 18 MeV incident energy and at θ_{lab} = 3.75°. The levels in ^{14}C are given with their excitation energies in MeV [89].

The ^{13}C(t,p)^{15}C reaction at 18 MeV incident energy was studied by Truong and Fortune [22]. The resulting proton spectrum at θ_{lab} = 11.25° is shown in Fig. 4.9. All the groups in the spectrum were identified as states of ^{15}C, except for peaks arising from impurities of ^{12}C and hydrogen in the target. The spectrum is dominated by six excited states at E_x = 0.74, 3.10, 4.22, 4.66, 6.84, 7.39 MeV. All other excited states are quite weakly populated.

Because the g.s. of ^{13}C has $J^{\pi} = 1/2^-$, a given state of ^{15}C will be populated with a unique L value in (t,p) reaction provided the transferred two neutrons are coupled to zero intrinsic angular momentum. The measured angular distributions for the strongest transitions plus the transition to the g.s. were consistent with DWBA calculations [22]. The transitions to the $1/2^+$ g.s. and the $5/2^+$ 0.74 MeV bound state were well fitted with L = 1 and 3, respectively. No other strong excitation was observed with either L = 1 or 3 characteristic angular distributions. In particular, two L = 0, two L = 2 and two L = 4 transitions were found. The first L = 0 transition is that populating the 3.10 MeV state, which was known to have $J^{\pi} = 1/2^-$. The authors assigned the same spin and parity to the 5.87 MeV state. The L = 2 transitions correspond to the states at 4.22 and 4.66 MeV, to which a $J^{\pi} = 5/2^-$ and $3/2^-$ were assigned, respectively. Finally, the two L = 4 transitions are to 6.84 and 7.35 MeV states, both of them with $J^{\pi} = 9/2^-$ or $7/2^-$.

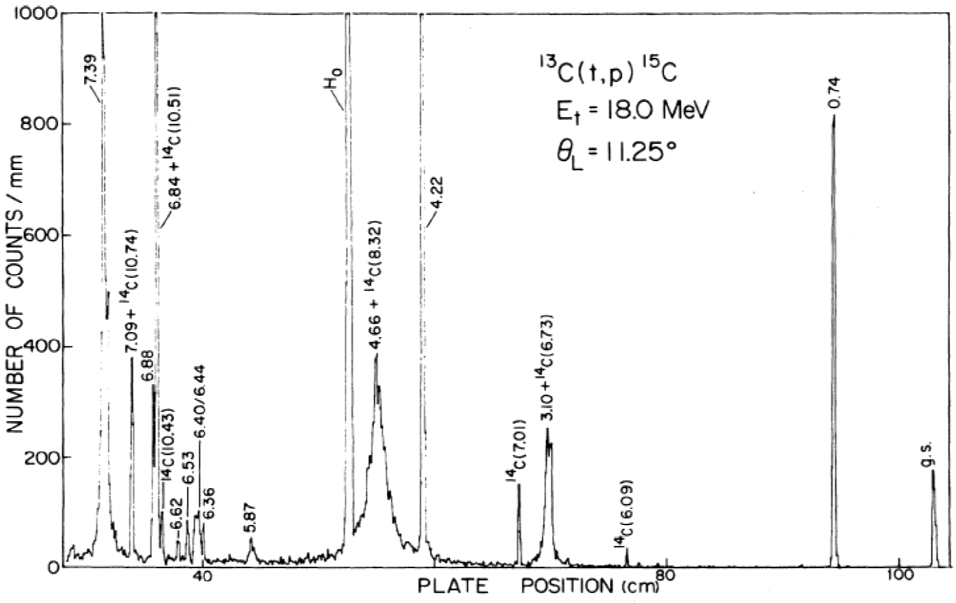

Fig. 4.9. Proton spectrum from the ^{13}C(t,p)^{15}C reaction measured at 18 MeV incident energy and at θ_{lab} = 11.25°. The levels in ^{15}C are given with their excitation energies in MeV [22].

4.5 Three-neutron transfer reactions

Recently the (^{12}C,^{9}C) three neutron transfer reactions were measured on ^{12}C and ^{13}C targets at 230.7 MeV incident energy [21] in order to study the particle-hole states of ^{16}C. The detected ejectile ^{9}C is particle stable only in its ground state, all the excited states are unstable against proton emission (S_p = 1.296 MeV). Therefore, the measured spectra show

only transitions to the states of the recoil nuclei (^{16}C and ^{15}C) in combination with the ground state of ^{9}C. The measured spectrum from the reaction ^{12}C (^{12}C,^{9}C) ^{15}C is shown in Fig. 4.10, where a broad three-body contribution from the ^{9}C + n + ^{14}C reaction channel is observed in the high excitation energy region. This three-body contribution arises from two sources: (i) sequential decay of highly excited ^{10}C* into $^{9}C_{g.s.}$+n and (ii) one-neutron knock-out in the projectile in combination with a two-neutron transfer to the target.

The doublet at 6.84 and 7.39 MeV is well populated in this reaction. A unique spin assignment for this two states was not possible with the ^{13}C(t,p) reaction [22] reported in Section 4.4.2. This doublet has a dominant 2*p*-1*h* structure with a $\nu 1p_{1/2}$ hole, which couples to a $^{14}C_{4^+}$ core. In the spectrum shown in Fig. 4.10 the 6.84 MeV state is populated much stronger than the 7.39 MeV one. It is even the strongest state in ^{15}C spectrum, which suggests stretched spin configuration. Therefore, it was possible to assign uniquely $9/2^-$ as the correct spin-parity for the 6.84 MeV state. The 7.39 MeV was then assigned as $7/2^-$. It was further discussed that this doublet can be populated in two ways, either to add a $1d_{5/2}$ neutron to the particle component of the 1*p*-1*h* doublet of ^{14}C, or to fill a hole in the $1p_{1/2}$ shell of the 2*p*-2*h* positive-parity multiplet, i.e. the 4^+ state at 10.74 MeV of ^{14}C. In both ways the $4^+ \otimes 1/2^-$ coupling is obtained. Applying the same procedure to the 2^+ member at 8.32 MeV of the 2*p*-2*h* multiplet of ^{14}C results in a doublet for ^{15}C at 4.22 and 4.66 MeV. These doublets show a very regular behavior in two respects: (i) the anti-parallel ($\uparrow\downarrow$) coupling partner is always located above the partner with parallel ($\uparrow\uparrow$) coupling, and (ii) the energy splitting between the doublet partners is always in the range of 0.4-0.6 MeV.

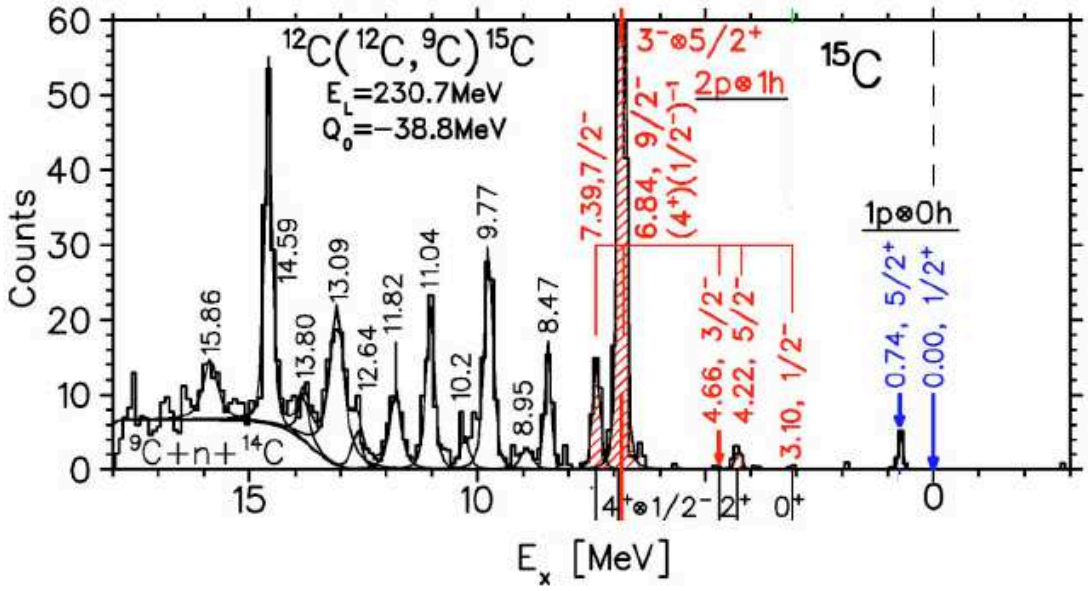

Fig. 4.10. ^{15}C spectrum obtained from the ^{12}C(^{12}C,^{9}C) ^{15}C three neutron transfer reaction at 230.7 MeV. A broad distribution from the indicated three-body reaction channel (^{9}C + n + ^{14}C) is assumed at high excitation energy, as ^{9}C only was detected [21].

4.6 Fusion-evaporation reactions

The (^{6}Li,p) or (^{7}Li,p) reactions at low energy proceed through the formation of an intermediate compound system and therefore are less selective than the (d,p) stripping reactions. For a compound system populated at sufficient excitation energy and with a distribution of large angular momenta, the total cross section is proportional to $(2J_f + 1)$, where J_f is the angular momentum of the final state.

The ^{9}Be(^{6}Li,p)^{14}C at 20 MeV incident energy was studied in 1973 by Ajzenberg-Selove et al. [103]. A typical proton spectrum is shown in Fig. 4.11. Thirty excited states of ^{14}C with E_x < 18.2 MeV were identified and the absolute cross sections for the first eighteen states were measurable. The latter were found to be proportional to $2J_f + 1$ as predicted by the statistical model and thus demonstrating that the reaction proceeds through the formation of an intermediate compound system.

The ^{9}Be(^{7}Li,p)^{15}C reaction was studied at 20 MeV bombarding energy in ref. [104]. The authors identified 27 states in ^{15}C, all the levels reported from the ^{14}C(d,p) reaction plus five additional states at E_x = 4.55, 5.84, 5.86 and 6.64 MeV. A proton spectrum measured at θ_{lab} = 11.25° is shown in Fig. 4.12-a. Several narrow resonances in the continuum were

observed. Angular distributions of the absolute cross section were extracted for many of the ^{15}C levels. Consistent with the compound reaction mechanism, they are almost shapeless and approximately symmetric at 90°, except for the two narrow levels (Γ ~ 40 keV) at E_x = 8.50 and 8.56 MeV (see Fig. 4.12-b).

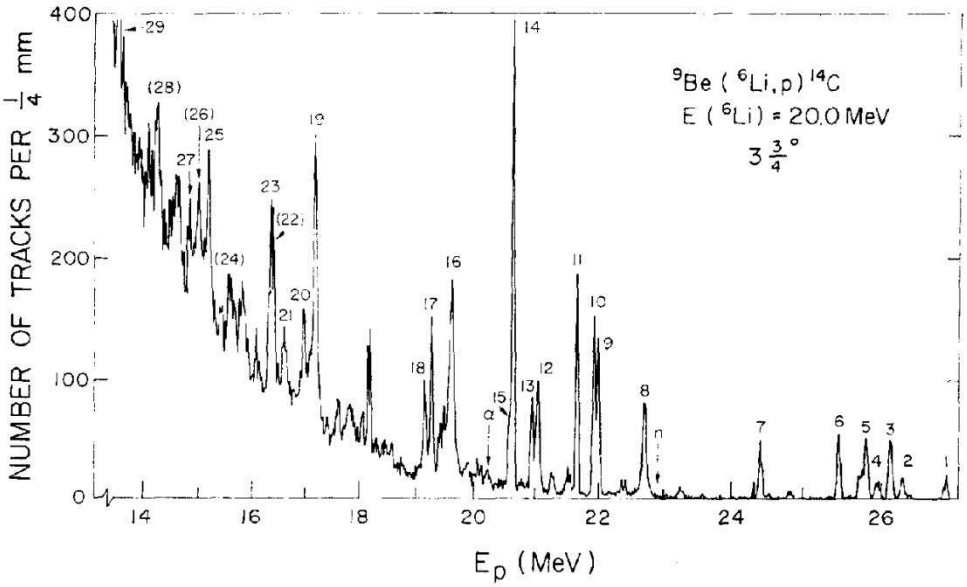

Fig. 4.11. Proton spectrum from the ^{9}Be(^{6}Li,p)^{14}C reaction at 20 MeV incident energy and θ_{lab} = 3.75°. The numbers identifying the peaks correspond to the states listed in Table 1 of ref. [103].

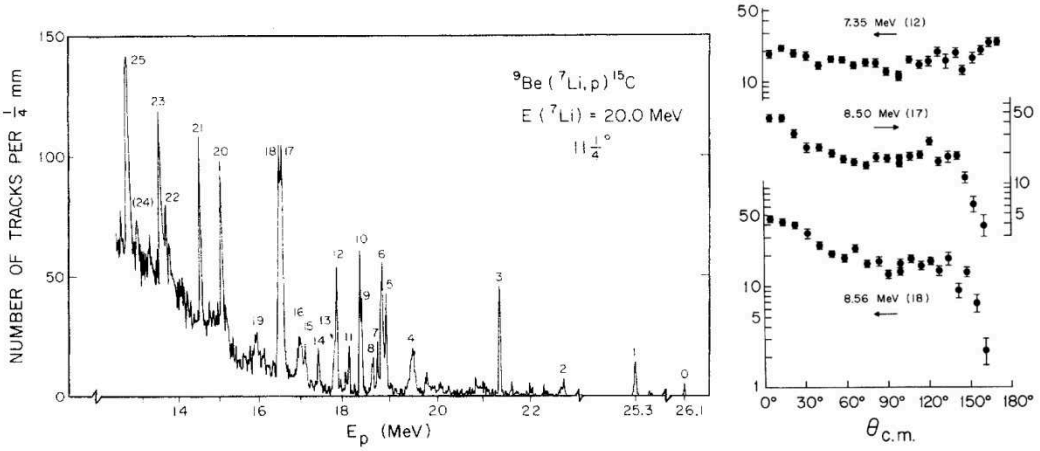

Fig. 4.12. Proton spectrum from the ^{9}Be(^{7}Li,p)^{15}C reaction at 20 MeV incident energy and θ_{lab} = 11.25° (left panel). The populated states indicated with the numbers are listed in Table 1 of ref. [104]. Angular distributions for the ^{15}C unbound states at E_x = 7.35, 8.50 e 8.56 MeV [104] (right panel).

4.7 Charge exchange reactions

The (n,p)-like Charge Exchange Reactions (CEX) excite the one-neutron-particle–one-proton-hole strength of the considered nucleus. The (n,p)-like CEX reactions proceed with isospin component transfer $\Delta T_z = +1$. The response of the ^{15}C nucleus to such an isovector probe was limited in the past because of the difficulties in realizing a high-purity ^{15}N target.

The ^{15}N(n,p)^{15}C reaction was studied using a 288 MeV neutron beam and a high-pressure ^{15}N gas target at the TRIUMF facility [105]. Proton spectra were measured at different angles in the range θ_{lab} from 0° to 20°. The experimental spectra compared to the calculated ones are shown in Fig. 4.13. The authors were interested in the study of the strength distribution of the Spin Dipole (SD) transitions ($\Delta L = 1$, $\Delta S = 1$), in connection with the problem of the missing Gamow-Teller (GT) strength ($\Delta L = 0$, $\Delta S = 1$).

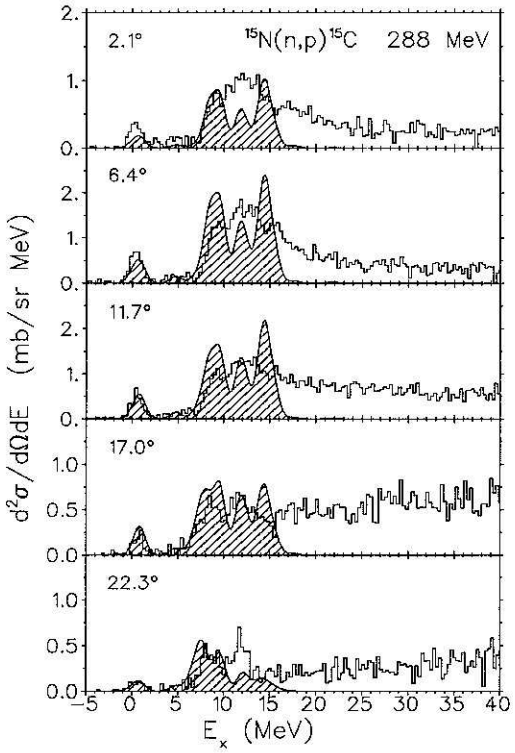

Fig. 4.13. Comparison between the experimental spectra at different angles from the reaction ^{15}N(n,p)^{15}C at 288 MeV and the corresponding theoretical strength distribution (shaded areas) for excitation of positive parity states [105].

The CEX reaction ^{15}N(^{7}Li,^{7}Be)^{15}C was studied at 55 MeV incident energy [106], in order to extract information about both the nuclear structure and the reaction mechanism. The measured energy spectra shown the population of the ground state and states at E_x = 0.77, 6.77, 7.30, 8.50 MeV (see Fig. 4.14). Among these, three narrow resonances at E_x = 6.77, 7.30, 8.50 MeV are found above the one neutron emission threshold. From the comparison of the experimental data with some CEX-QRPA calculations, the authors concluded that such narrow resonances are connected with a core polarization.

The narrow resonaces at E_x = 6.64 e 7.35 MeV were populated also in the ^{9}Be(^{7}Li,p)^{15}C reaction [104](see Section 4.6) and there were suggested high spin values for these states. From the analysis of the ^{15}N(^{7}Li,^{7}Be)^{15}C reaction it appears that these resonances are the result of an interference between the *Bound States Embedded in the Continuum* (BSEC) and the l = 2 single-particle continuum, where the neutrons move in a *d*-wave with respect to the core [106].

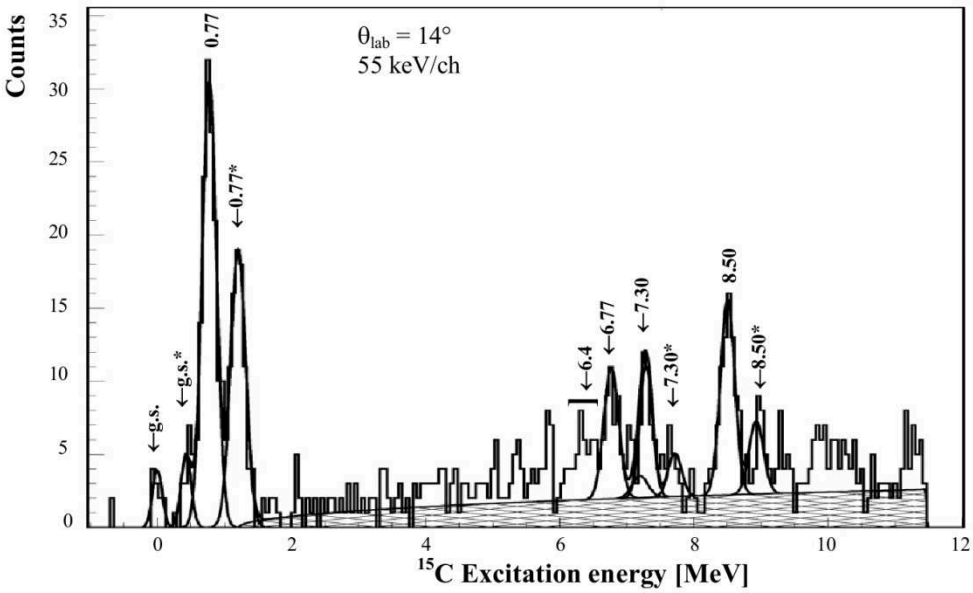

Fig. 4.14. ^{15}C excitation energy spectra from the ^{15}N(^{7}Li,^{7}Be)^{15}C reaction at θ_{lab} =14°. Peaks related to the excited state of ^{7}Be at 0.429 MeV are indicated with the asterisk. The three-body phase space ^{15}N(^{7}Li,n^{7}Be)^{14}C is indicated with the shaded area [106].

Chapter 5
The $^{12}C(^{18}O,^{16}O)^{14}C$ and $^{13}C(^{18}O,^{16}O)^{15}C$ reactions: experimental set-up

From the detailed analysis of the reaction mechanism required for the population of the GPV, discussed in Chapter 3, two-neutron transfer reactions between heavy nuclei turn up to be more appropriate for searching the GPV than (p,t) or (t,p) reactions on heavy nuclei. In particular, interesting candidates are the ($^{18}O,^{16}O$) reactions at 84 MeV incident energy on carbon isotopes targets.

The use of heavy-ion beams was very limited in the past due to both experimental and theoretical limitations. From an experimental point of view, there were difficulties in identifying the ejectiles and also in producing high resolution spectra at forward angles covering a large range of excitation energy. These requirements are particularly important when looking for a giant resonance as the GPV. In particular the peculiar conditions which are needed to be satisfied can be listed as:

- spectra up to high excitation energy, since the GPV is expected to be at E_x ~10-20 MeV;
- high energy resolution, in order to disentangle a wide resonance like the GPV (predicted Full Width at Half Maximum (FWHM) ~ 2 MeV) among narrow peaks;
- high angular resolution, in order to extract cross section angular distributions in which the oscillations are clearly visible, allowing to identify the $L = 0$ channel, which populate the GPV.

An ideal instrument to perform such kind of studies is the MAGNEX large acceptance magnetic spectrometer, since it conjugates good energy and angular resolutions with a

large acceptance both in solid angle and momentum. In the present Chapter, the main features of the instruments are reported together with the description of the experimental set-up used to measure the $^{12}C(^{18}O,^{16}O)^{14}C$ and $^{13}C(^{18}O,^{16}O)^{15}C$ reactions.

5.1 Experimental set-up

The $^{18}O^{6+}$ beam at 84 MeV incident energy was produced and accelerated by the Tandem Van de Graaff facility of INFN-LNS with a current ranging from 10 to 50 enA. It was not possible to use the $^{18}O^{6+}$ beam for all the measurements due to the Tandem instability at the used high voltage of 12 MV. Parts of the measurements were performed using an $^{18}O^{7+}$ beam at the same incident energy. Such choice requires a lower voltage at the accelerator terminals (10.5 MV) but correspond also to a reduction of the current due to the less effective production of the $^{18}O^{7+}$ ions in the accelerator stripper.

The beam spot size at the target, defined by a collimation system, was about 1.2 mm horizontal and 2.3 mm vertical, warranting a good match with the optical properties of the spectrometer. The collimation system was mounted inside the scattering chamber upstream the target ladder and was composed by:

- a rectangular diaphragm (1 x 2 mm^2), mounted at 15 cm from the target ladder;
- a 5 cm hole diaphragm at 5 cm from the target ladder, used as anti-scattering screen;
- four slits (two for the horizontal and two for the vertical) located in the beam line at 2 m from the target ladder.

Thanks to the use of such collimating system, the horizontal angular divergence was ~ 0.8 mrad whereas the vertical one was ~ 3 mrad. An accurate optical alignment (within 0.1 mm) of the target ladder with the collimation system and the beam line was done by bubble-level, in order to make the beam hitting the target at the object point of the spectrometer.

A 8 mm diameter Faraday cup was located in the scattering chamber 15 cm downstream the target ladder along the incident beam direction. The electrons suppressor at the entrance of the Faraday cup was polarized at -200 V in order to improve the efficiency of the charge collection. The beam current measured by the cup, integrated by a Digital Integrator [107] was stored in the memory of a Latching Scaler [108] and gave a

measurement of the overall charge at each acquisition run. Laboratory tests have shown that in this configuration an accuracy better that 1% is obtained in the integrated current. A picture of the scattering chamber containing the Faraday cup, the target ladder and the collimating system is shown in Fig. 5.1.

A 49 ± 3 μg/cm^2 self-supporting ^{12}C and a 50 ± 3 μg/cm^2 self-supporting 99% enriched ^{13}C targets were used. They were produced at the LNS chemical laboratory. The runs with ^{12}C were used also for estimating the background coming from ^{12}C impurities in the ^{13}C target. A picture of the used ^{12}C mounted in the target ladder is shown in Fig. 5.2, where it is visible the mask leaved by the beam onto the target.

The ^{16}O ejectiles were momentum analyzed by the MAGNEX spectrometer working in the full acceptance mode (solid angle Ω ~ 50 msr and momentum range $\Delta p/p$ ~ 24%). The spectrometer main features will be described in Section 5.2. The data analyzed in the present work correspond to three different runs for each target, in which the spectrometer optical axis was located at θ_{lab}^{opt} = 6°, 12° and 18° in the laboratory reference frame. The accuracy in the angle determination is better than 0.01°. Due to the large angular acceptance of MAGNEX (-5.16°, +6.3° horizontal and ± 7.16° vertical), these angular settings correspond to a total covered angular range $3° < \theta_{lab} < 24.3°$ in the laboratory reference frame, with an overlap of ~ 6° between two consecutive runs.

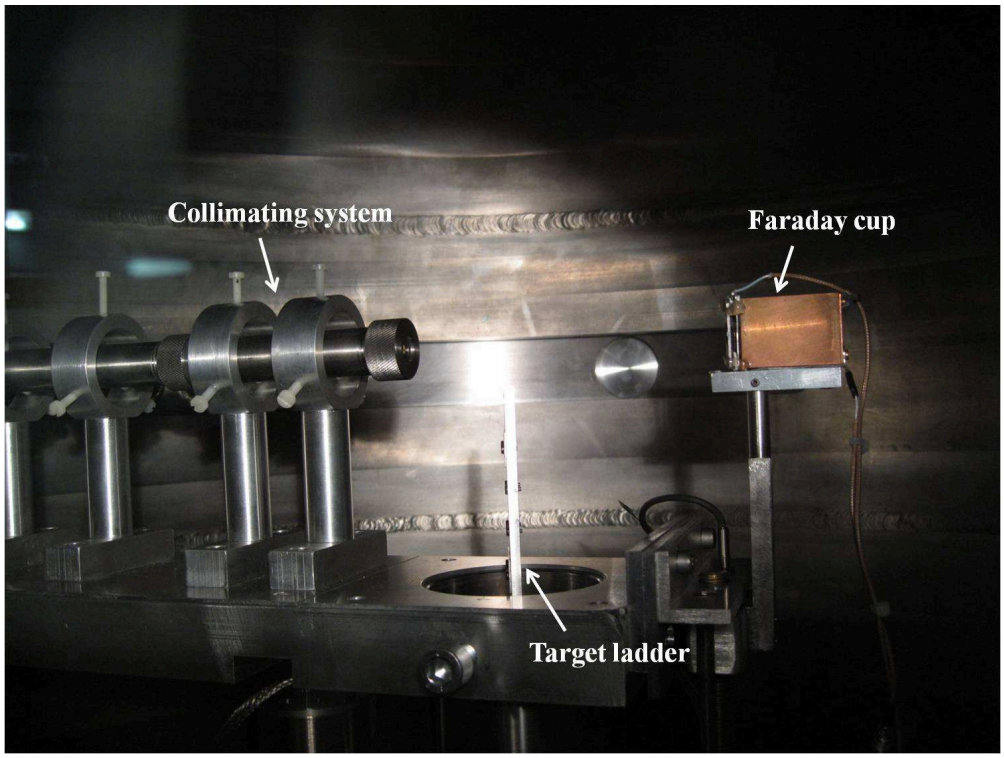

Fig. 5.1. Scattering chamber. The collimating system, the target ladder and the Faraday cup are visible.

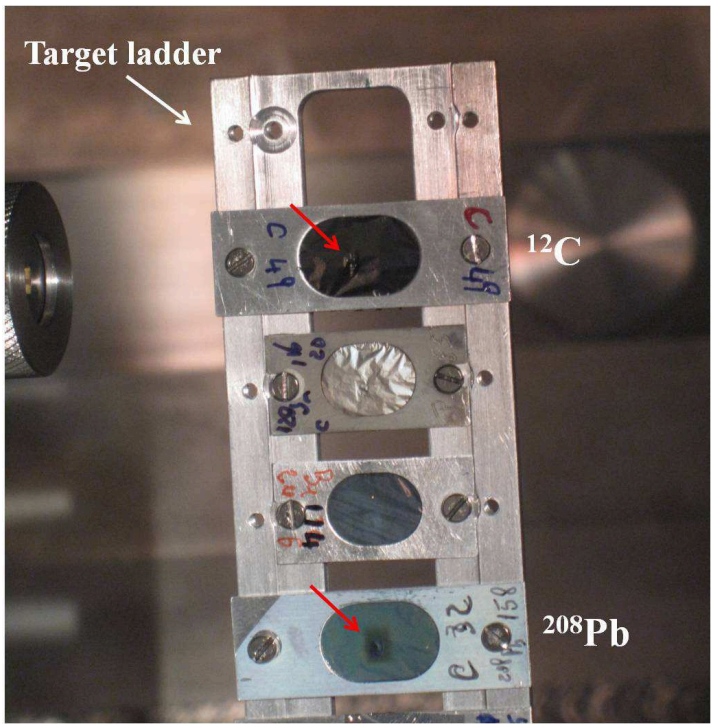

Fig. 5.2. Target ladder. The 49 $\mu g/cm^2$ ^{12}C target is mounted in the top of the ladder. The mark leaved by the beam is visible in the ^{12}C target and in the ^{208}Pb target, as indicated by the red arrows.

5.2 The MAGNEX spectrometer

The MAGNEX large acceptance magnetic spectrometer [109][110] is an high-performance device, installed at the LNS-INFN, offering a high energy, angular and mass resolution in a large-accepted phase space. It is a multipurpose spectrometer, intended for the investigation of a broad series of nuclear reactions induced by beams from the 15 MV Tandem Van de Graaff accelerator, from the K800 superconducting cyclotron and also with radioactive ion beams delivered at the LNS [111]. The MAGNEX spectrometer joins the attributes demonstrated by the traditional magnetic spectrometry [112] with a large angular (50 msr) and momentum (-14.3%, +10.3%) acceptance. This is possible thanks to a good compensation of the enhanced aberrations effects produced by the large acceptance elements, which is the result of the interplay between the innovative designs of magnetic elements and new techniques for the reconstruction of the ions motion through the spectrometer.

MAGNEX is a QD spectrometer consisting of a vertically focusing quadrupole magnet (Q) and a 55° dipole magnet (D) providing the dispersion and the horizontal focusing strength. The latter is achieved by a rotation of both the entrance and exit dipole boundaries by an angle of -18°. The accepted magnetic rigidities range from 0.2 to 1.8 Tm, which correspond to a covered energy range approximately from 0.2 MeV/*u* to 40 MeV/*u* depending on mass and charge of the ions. In particular, the possibility to use the spectrometer even with low-rigidity particles requires a detection system at the focal plane with a low-energy threshold and designed to minimize straggling effects. A picture of the MAGNEX spectrometer is shown in Fig. 5.3.

The large acceptance requirement strongly influenced the design of MAGNEX. A self-consistent method, suitable for the layout design of a large acceptance spectrometer, was used successfully to define the optical configuration of MAGNEX, as described in details in ref. [109]. The main actual parameters of MAGNEX are listed in Table 5.1. They are the result of a compromise between the optimized calculated configuration of ref. [109] and the effective construction requirements.

Fig. 5.3. General view of the MAGNEX spectrometer. From the left to the right, the scattering chamber, the quadrupole (red) and the dipole (blue) magnets and the Focal Plane Detector are visible.

Table 5.1. Main optical characteristics of the MAGNEX spectrometer.

Optical characteristics	**Actual values**
Maximum magnetic rigidity (Tm)	1.8
Solid angle (msr)	50
Horizontal angular acceptance (mr)	-90, +110
Vertical angular acceptance (mr)	± 125
Momentum acceptance	-14%, +10%
Central path length (cm)	596
Momentum dispersion	3.68
First order momentum resolution	5400
Focal plane rotation angle	59.2°
Focal plane length (cm)	92
Focal plane height (cm)	20

5.2.1 Matrix formalism and aberrations

The standard way to describe the motion of charged particles in a beam is based on the choice of the motion of one of them as a reference (see, e.g., Ref. [113]). Its momentum and path through the magnetic elements are the reference momentum p_0 (used to set the magnetic strength of the bending magnets) and trajectory, respectively. The positions and momenta of the other particles are defined relative to the reference ones. At any point along the reference trajectory, a longitudinal or ***t*** axis lying in the direction of the reference momentum is defined, while the two transverse axes ***x*** and ***y*** are usually chosen perpendicular to it. To specify the momentum of a particle three quantities are used: p_x, p_y, the momentum components along the x and y directions, and the fractional deviation from the reference momentum modulus $\delta = (p - p_0)/p_0$. It is more convenient to consider the quantities $x' = p_x/p_t$ and $y' = p_y/p_t$, where the p_t is the momentum longitudinal component along the reference trajectory. Since p_x and p_y are small compared to p_t, x' and y' can be approximated by the horizontal θ and vertical ϕ angles with respect to the reference trajectory.

Three more parameters are needed to complete the phase space coordinate set: x and y, the two transverse distances of particles from the central trajectory, and l, the difference in path length between a given trajectory and the reference one. The path length is defined as the distance, along the particle trajectory, between the starting point of the beam line (the target position for magnetic spectrometry) and the intersection between the trajectory and a plane normal to the central trajectory, at the fixed t. When using thin targets l_i is essentially zero for all the trajectories and can be omitted. In summary, each particle is characterized by a vector of observables $P \equiv (x, \theta, y, \phi, l, \delta)$.

In particular, as the charged particle beam moves through the spectrometer, the final position vector $P_f \equiv (x_f, \theta_f, y_f, \phi_f, l_f, \delta_f)$ is connected to the initial one $P_i \equiv (x_i, \theta_i, y_i, \phi_i, \delta_i)$ through the relation:

$$\mathcal{M}: P_i \rightarrow P_f \tag{5.1}$$

which describes a non linear transport relation, characteristic of the particular optical system. More explicitly

$$\begin{aligned} x_f &= \mathcal{M}_1(x_i, \theta_i, y_i, \phi_i, \delta_i) \\ \theta_f &= \mathcal{M}_2(x_i, \theta_i, y_i, \phi_i, \delta_i) \\ y_f &= \mathcal{M}_3(x_i, \theta_i, y_i, \phi_i, \delta_i) \\ \phi_f &= \mathcal{M}_4(x_i, \theta_i, y_i, \phi_i, \delta_i) \\ l_f &= \mathcal{M}_5(x_i, \theta_i, y_i, \phi_i, \delta_i) \\ \delta_f &= \delta_i \end{aligned} \tag{5.2}$$

where the last equality expresses the conservation of the ion momentum modulus in magnetic fields, in absence of degrading materials. It is possible to write the Taylor expansion of Eq. (5.2) in tensor notation, as

$$x_j(f) = \sum_k R_{jk} x_k(i) + \sum_{k,l} T_{jkl} x_k(i) x_l(i) + \cdots \tag{5.3}$$

where x_j is the generic phase space coordinate and R_{jk} and T_{jkl} are the first and the second order transfer matrix elements, respectively. The coefficients of the second and higher order terms in Eq. (5.3) are typically referred to as *aberrations*, since they determine deviations from the ideal first order optical properties. The first order truncation of Eq. (5.3) gives a good description of the particle dynamics in case of magnetic spectrometers with very small angular acceptance. On the contrary, higher order terms of the Taylor expansion are needed in case of large acceptance devices [114].

Some of the high order aberrations in the MAGNEX spectrometer were compensated via hardware, i.e. a careful shaping of the magnets. The chosen strategy was to restrict the hardware corrections to only few parameters, principally connected with the design of the bending magnet [114]. For example, in order to compensate the 2nd order aberration T_{126}, the Focal Plane Detector (FPD) [115] was installed with the entrance surface rotated of θ_{tilt} = 59.2° with respect to the central trajectory.

However, hardware techniques did not provide a satisfactory minimization of all the important aberrations terms, so a careful software correction was implemented. This was possible thanks to a fully algebraic approach to determine the ion trajectory inside the spectrometer [116]. The technique requires an accurate knowledge of the geometric and magnetic structure of the spectrometer [117][118][119][120], the use of powerful algorithms for solving the high-order transport equations [121] and the precise

measurements of the ions positions and directions at the focus by a suitable FPD. It is important noticing that the measured parameters at the focal plane must be determined in the spectrometer reference frame where the transport equations are defined. This in turn puts subtle constraints on the absolute alignment of the FPD and the magnets compared to the object point. The FPD detector was conceived in order to provide an accurate measurement of the phase space vector $P_f \equiv (x_f, \theta_f, y_f, \phi_f)$, as described in Section 5.3. The ray-reconstruction technique has been applied to the data analyzed in this work, as described in details in Section 6.4.

5.3 The MAGNEX Focal Plane Detector

In a large acceptance magnetic spectrometer as MAGNEX, the traditional requirement on the measurement of the position in the dispersive direction (X_{foc}) is extended to a more complex tracking of the impact point $P_{foc} \equiv (X_{foc}, Y_{foc})$ and the direction (characterized by the horizontal and vertical angles θ_{foc} and ϕ_{foc}, respectively) of the ejectiles in a three-dimensional space. Moreover, rather strict requirements are set in order to measure and identify slow heavy ions with a low detection threshold. In order to fulfill all of these requirements the FPD needs to be a sophisticated device where several specialized sections coexist.

The MAGNEX FPD [115] is a gas filled hybrid detector with a wall of silicon detectors at the back. It measures the horizontal and vertical positions of each incident ion at four sequential positions along the ions trajectory. Also, it measures the energy loss in the gas and the residual energy released in the silicon detectors. The FPD design and operation principle are described in details in ref. [115]. In the following Sections some of the main features are reported.

5.3.1 Design and construction

The MAGNEX FPD basically consists of a proportional drift chamber divided in five sections, four of which are position-sensitive, and a wall of stopping silicon detectors at the back [115]. A schematic drawing of the detector is shown in Fig. 5.4.

The FPD is placed 1.91 m downstream the exit pole face of the MAGNEX dipole where, according to ion optics calculations [109][114], the focal plane of the spectrometer is defined. The FPD vessel is mounted on a movable carriage that can translates of ± 0.08 m along to the spectrometer optical axis, in order to adapt the detector position to different focus conditions. The FPD is installed with the entrance surface rotated of $\theta_{tilt} = 59.2°$ with respect to a plane normal to the reference trajectory in order to reduce the effect of chromatic aberrations [114].

The drift chamber active volume is 1360 mm wide, 200 mm high and 96 mm deep with a cathode plate below and a Frisch grid above (see Fig. 5.4-a). The gas typically used is N35 isobutane (99.95% pure) at pressures between 5 and 100 mbar depending on the experimental needs. A continuous gas flowing system is equipped in order to maintain stable pressure operations and to preserve the gas purity. A Mylar entrance window of area 920X220 mm^2 and typical thickness of 1.5 μm contains the gas. It is supported by twenty silicon coated stainless multistrands wires 0.5 mm in diameter, arranged horizontally and spaced 10 mm each other.

The Frisch grid is made of 10 gold-plated tungsten wires, 50 μm in diameter, spaced 5 mm between centers. The uniformity of the electric field in the 200 mm high drift region between the cathode (usually at applied voltage between -900 V and -1500 V) and the Frisch grid (connected to the ground) is guaranteed by a partition grid consisting of 41 rectangular rings parallel to the cathode and arranged at 5 mm one from the other.

The proportional counter section includes five sets of amplifying wires, sequentially defined as DC1, DC2, PC, DC3, DC4 (see Fig. 5.4-b). They are gold-plated tungsten wires located 20 mm above the Frisch grid and spaced 8 mm apart. The DC wires are 20 μm in diameter whereas the PC ones are 100 μm. Each of the DC counters is made of a unique amplifying wire, while for the PC one eight wires are connected in common. The high voltage to the proportional wires (usually from +600 V to +1300 V) is provided by a unique power supply.

A set of 224 induction pads orientated along the spectrometer optical axis is located 5 mm above each DC proportional wire, as shown in Fig. 5.5. The entire patterned electrode is engraved on a six-layered 8 mm thick printed circuit board. Each pad is 6 mm long and 5.9 mm wide and separated by 0.1 mm from its neighbor.

A *wall* of 60 silicon pad detectors, arranged in 20 columns and 3 rows, is located at the back of the gas detector. Each silicon detector has an active area of 70 mm (height) × 50 mm (width) and is 500 μm thick. The silicon columns are mounted orthogonally to the spectrometer optical axis. The columns are mechanically supported and electrically connected by a mother board built on a 6 mm thick double sided printed circuit. A picture of the silicon detector wall is shown in Fig. 5.6.

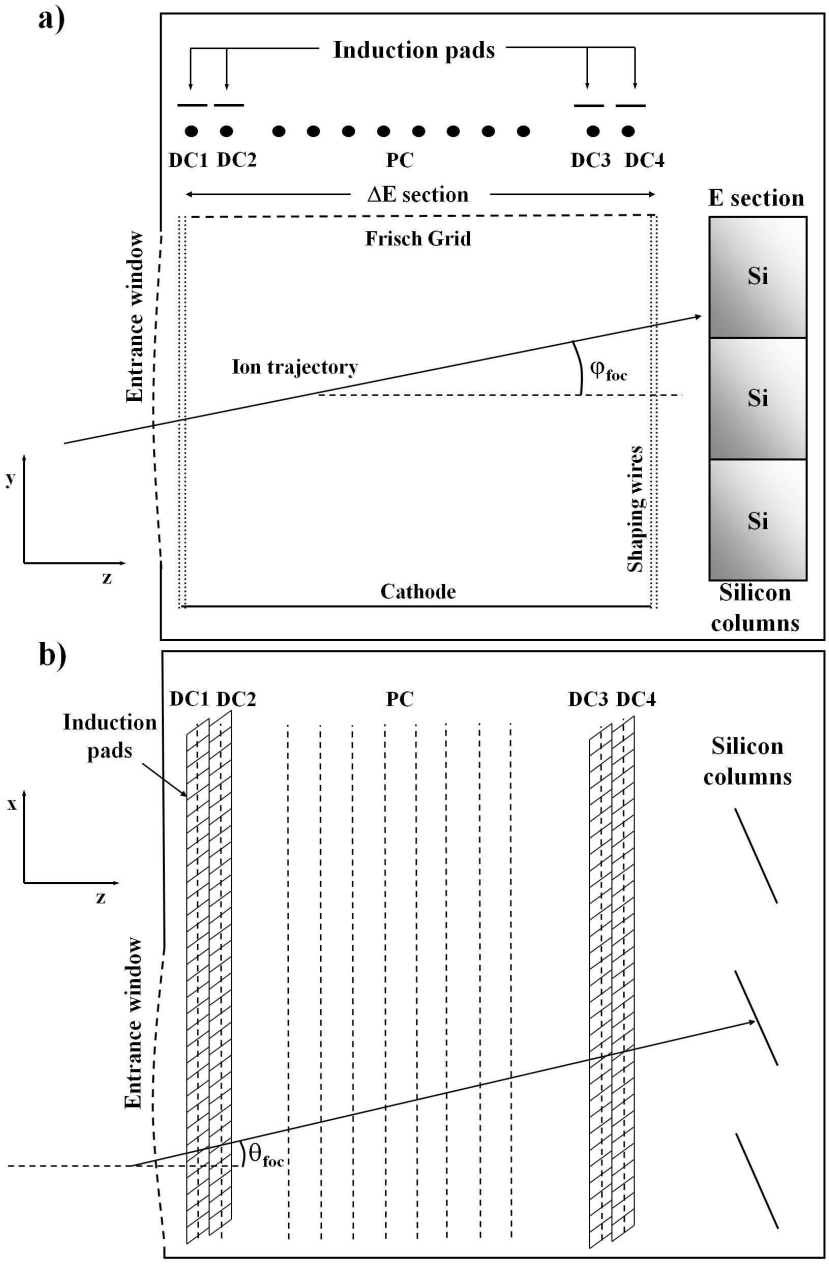

Fig. 5.4. Schematic view of the MAGNEX Focal Plane Detector: a) side view; b) top view.

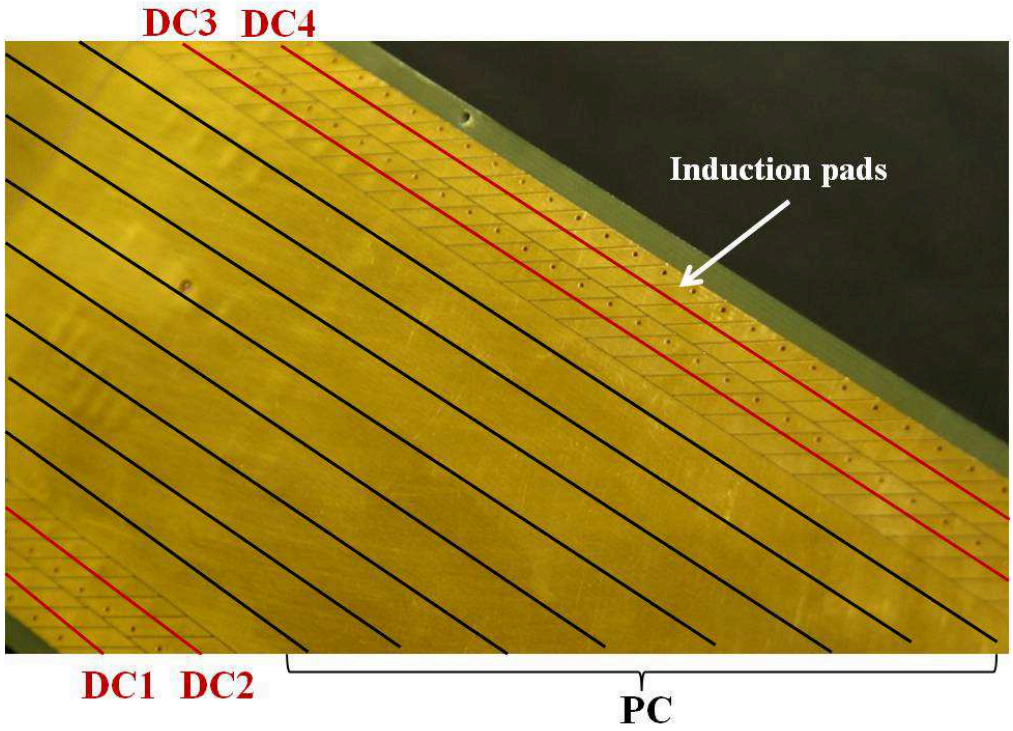

Fig. 5.5. Picture of a part of the induction pads.

Fig. 5.6. Picture of the FPD silicon detectors wall.

5.3.2 Principle of operation

The ions coming from the dipole cross the FPD Mylar window and leave a track of ionized atoms and primary electrons in the gas between the cathode and the Frisch-grid, as schematically represented in Fig. 5.4. Under a uniform electric field of about 50 V/cm, the electrons drift towards the Frisch-grid with typical velocities of 3-5 cm/μs, depending on the actual voltage and gas pressure [122]. After the grid, the electrons are accelerated in an electric field that becomes much stronger close to the DC and PC wires, where a multiplication by a factor around 100-200 occurs. The avalanche produces a signal proportional to the energy lost by the ions in each section, thus providing five sequential measurements of the energy loss (ΔE_1, ΔE_2, ΔE_{PC}, ΔE_3, ΔE_4) for each event. The signals, having rise times of about 150 nsec, are shaped and amplified by charge-sensitive preamplifiers [123] with a sensitivity of about 200mV/MeV (silicon equivalent). The amplified signals are then sent to a 16-channel NIM module where they are split and distributed to a shaping amplifier and a Constant Fraction Discriminator (CFD) with a delay line of 200 nsec. The shaped output (6 μs shaping time), proportional to the energy loss, is used for the particle identification, as described in Section 6.2. The logic outputs, extracted only for the DC wires, are used as a STOP for the measurement of the electrons drift time as described below. The schematic diagram of the electronics and read-out of the ΔE_i measurements is shown in Fig. 5.7.

The electron avalanche near the wires also induces charge on the closest induction pads. These signals are then pre-amplified and shaped by an analog multiplexed read-out system based on 16 channels GASSIPLEX chips [124] mounted on the upper side of the board in the gas environment [125]. The multiplexed signals from each of the four DC chains are read-out and digitally converted by modules of Read-out for Analog Multiplexed Signals (C-RAMS) [126]. The center of gravity of the charge distribution at each DC section is then extracted using the algorithm described in Section 6.1.2. Exploiting the regular pattern of the stripped electrode, it is possible to convert with high accuracy the measured centroid to the horizontal position X_1, X_2, X_3, X_4 in meter units. In this way, four positions are independently determined, allowing the extraction of the horizontal position and angle of the ion track at the spectrometer focal plane. Note that these measured quantities are referred to the spectrometer optical axis (X_{foc} and θ_{foc}) to be used for the ray-reconstruction.

Therefore, the projection of the optical axis over the stripped anode has been determined for each DC section within 0.1 mm accuracy by means of direct optical alignments.

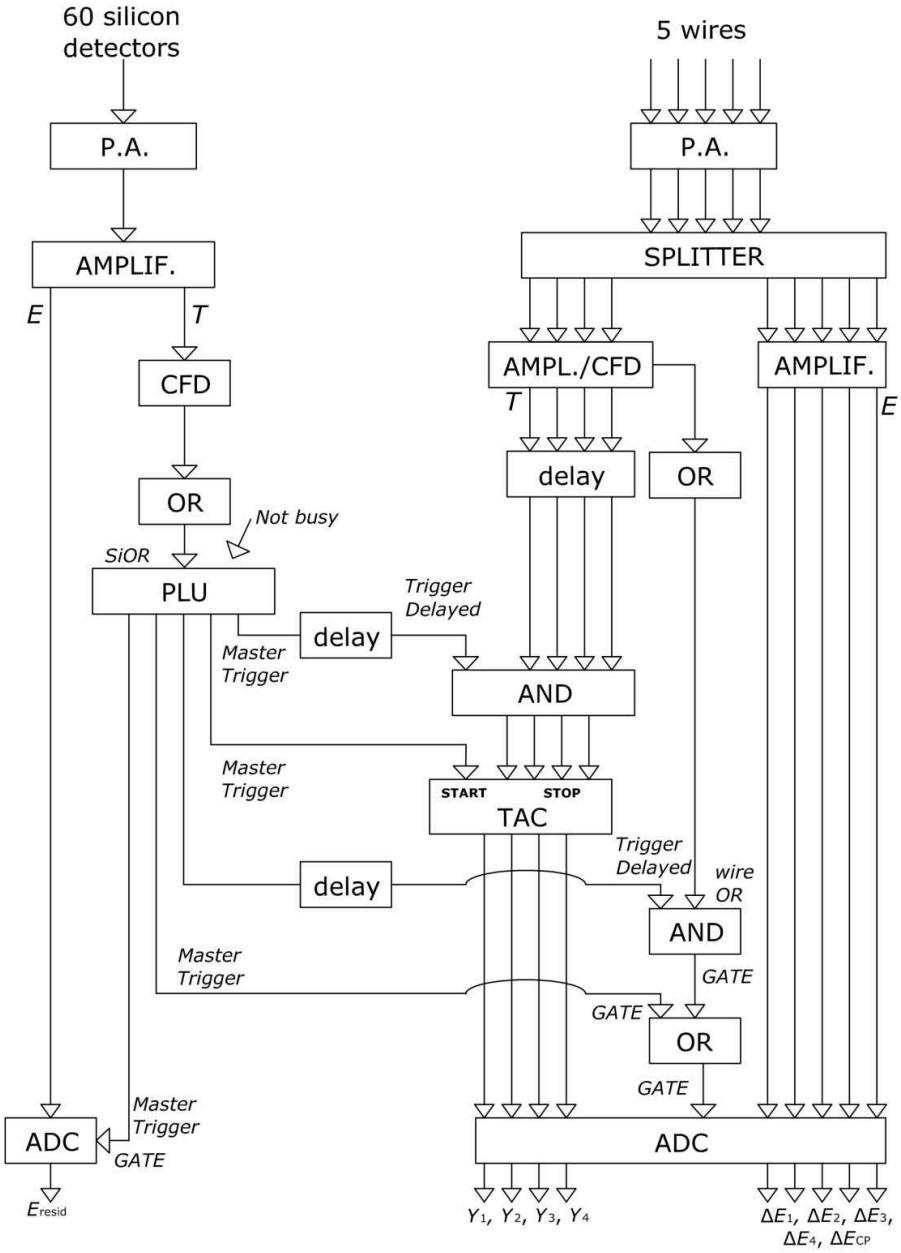

Fig. 5.7. Schematic diagram of the electronics and read-out of the E_{resid}, ΔE_i and Y_i measurements.

The charged particles crossing the gas section reach the silicon detector wall. Charge pre-amplifiers similar to the ones used for the wires signals [123], typically with sensitivities from 5 to 90mV/MeV depending on the experimental needs and working in

the gas environment, are used. The outputs are sent to 16-channel shaping amplifiers providing shaped (0.25 μm shaping time) and timing outputs. The former are used to measure the residual energy (E_{resid}) of the ions after crossing the gas. The latter are sent to CFDs and give multipurpose timing signals of MAGNEX. The logic OR is used as START signal for the electrons drift times measurements and also to trigger the data acquisition and to generate the gate for the ΔE and drift time measurements.

Four subsequent electron drift times in the gas are measured by the delay between the signal generated by the silicon detectors (START) and the DC wires (STOP), using four standard TAC + ADC read-out chains. Thanks to the almost constant velocity of the electrons in the gas, these times are used to determine the vertical positions Y_1, Y_2, Y_3, Y_4 of the ion tracks at the z position corresponding to the DC wires and consequently the vertical angle. The vertical coordinates need an external absolute calibration to be correctly transformed in the optical reference frame, as described in Section 6.1.3. In this way, the vertical position Y_{foc} and angle ϕ_{foc} of the ion track at the focal plane are determined. The schematic diagram of the electronics and read-out of E_{resid} and Y_i measurements is shown in Fig. 5.7.

5.4 Spectrometer setting

5.4.1 Magnetic fields

The magnetic fields of the MAGNEX quadrupole and dipole were set in order to focus the ^{16}O ejectiles corresponding to the $^{14}C_{g.s.}$ (or $^{15}C_{g.s.}$) in the focal plane position corresponding to a relative momentum δ = 0.08. The spectrometer parameters set for each run are listed in Table 5.2. In order to obtain the desired focusing conditions, the magnetic fields values were calculated using the COSYsetup program [127]. Putting as input the kinematic parameters of the reaction and the desired δ, the program searches the correct setting of the magnetic fields among a set of tabulated values, calculated for several configurations. The dipole field was measured by a NMR probe inserted in a socket of the magnet vacuum chamber. It is possible to extract the magnetic field in each point of the beam envelope from a detailed map of the magnet provided by the manufacturer. The estimated error in the determination of the dipole field is ~ 0.1% [118]. The quadrupole

field is determined from the high precision ($3 \cdot 10^5$) measurement of the supplied current. Long term drifts and possible hysteresis effects are monitored making the average of the measured values of four Hall probes permanently located at 0.1815 m from the quadrupole symmetry axis. The FPD shift was fixed at d = -0.08 m for all the runs.

Table 5.2. Magnetic settings for each run.

Target	θ_{lab}^{opt} (deg)	$B\rho$ (Tm)	B_Q (T)
^{12}C	6	0.6319	0.3502
	12	0.6119	0.3346
	18	0.5904	0.3258
^{13}C	6	0.5939	0.3315
	12	0.5799	0.3122
	18	0.5591	0.3087

5.4.2 Focal Plane Detector setting

The FPD was filled with 99.95% pure isobutan gas (C_4H_{10}) at 7 mbar pressure. The cathode was supplied at -950 V while the Frisch-grid was grounded. The high voltage in the proportional wires DC1, DC2, DC3, DC4 and PC was +750 V, and the lateral shaping partition grid between the Frisch-grid and the proportional wires was supplied by a separate generator at -400 V. The silicon detectors were powered with 60 V voltage in a full depletion mode. The setting allows to detect the ^{16}O ejectiles by the silicon detectors with a clear separation of the other reaction products, achievable by an off-line procedure that will be described in Section 6.2.

Chapter 6
The $^{12}C(^{18}O,^{16}O)^{14}C$ and $^{13}C(^{18}O,^{16}O)^{15}C$ reactions: data reduction

The present Chapter is devoted to the detailed description of the data reduction procedure, made up of several steps. First, an accurate calibration of the horizontal and vertical positions is necessary, since such parameters are used as input for the 10th order ray-reconstruction procedure. They must be determined in the spectrometer reference frame, where the transport equations are defined. The next step consists in the identification of the ^{16}O ejectiles, which is performed combining two techniques: the usual ΔE-E one for the atomic number identification (Z parameter) and an innovative mass identification (A parameter) technique which exploits the property of the Lorentz force applied to a charged particle in a magnetic field normal to its momentum. Then, looking at the final phase space parameters, the transport map along the spectrometer is constructed up to the 10th order. The whole procedure is described for the data referring to the $^{13}C(^{18}O,^{16}O)^{15}C$ reaction at θ_{lab}^{opt} = 12°. The same procedure was applied to the other data sets.

After the application of the ray-reconstruction technique to the identified data at the focal plane, the excitation energy spectra and the cross section angular distributions can be extracted, since the procedure gives the reconstructed kinetic energy of the ejectiles and the scattering angle in the laboratory frame.

6.1 Calibration of the *X* and *Y* parameters

6.1.1 Relative calibration of the response of the induction pads

In order to obtain the horizontal position parameters X_1, X_2, X_3, X_4 at the focus, it is necessary to perform a relative calibration of the response of the induction pads for each DC detector. To accomplish this, four pulses of different amplitudes (2, 5, 8 and 10 V), generated by a precision pulser, were sent directly onto the wire of a given DC. In this way, the same charge was instantly generated in front of each pad of the DC for each value of the pulse amplitude, and the relative GASSIPLEX histograms were built. A linear fit correlating the amplitudes of the signal for each channel with those of a reference one was done. An typical fit is shown in Fig. 6.1. In this way, a relative calibration of the different electronic channels of the pads induction electrode was obtained.

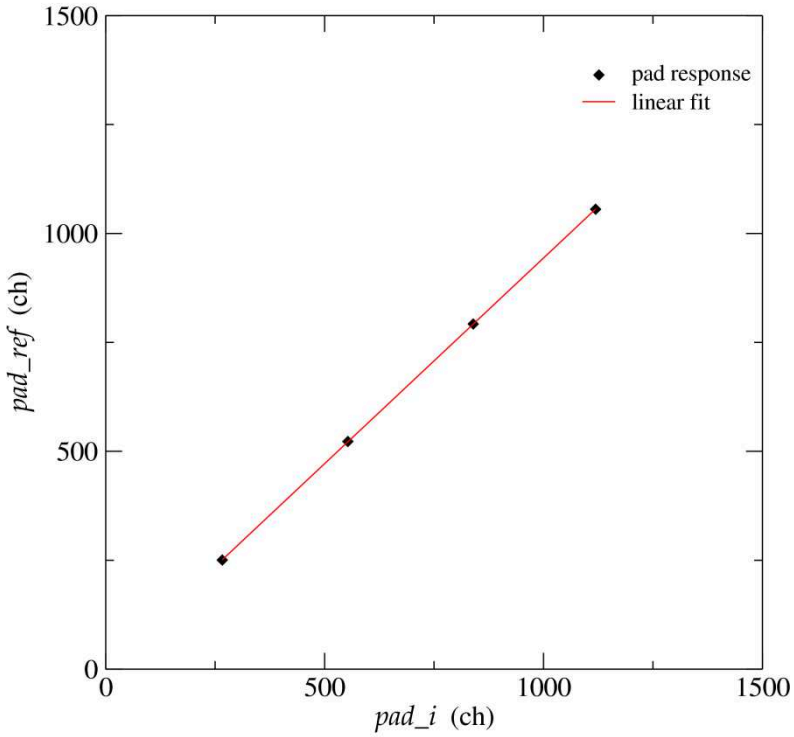

Fig. 6.1. Linear fit correlating the response of a pad (*pad_i*) with the response of a reference one (*pad_ref*).

6.1.2 Algorithm for the horizontal position calculation

Once the relative calibration has been performed, the position of the avalanche of a typical event can be determined extracting the center of gravity of the discrete distribution. A proper centroid finding algorithm must be adopted to this aim, which accounts for the particular geometrical configuration of the pads with respect to the multiplication wires, as described in Section 5.3.1. In fact, the main consequence of the rotation of the induction pads with respect to the wires is a variable number of excited pads and very different shapes of the charge distribution for different events. These two effects are dependent on the horizontal trajectory angle, as it is shown in Fig. 6.2, where examples of the induced charge distribution over the DC2 patterned electrode are shown. It has been demonstrated in ref. [128] that, in such conditions, any standard centroid-finding algorithm [129][130] fails in the determination of the centroid.

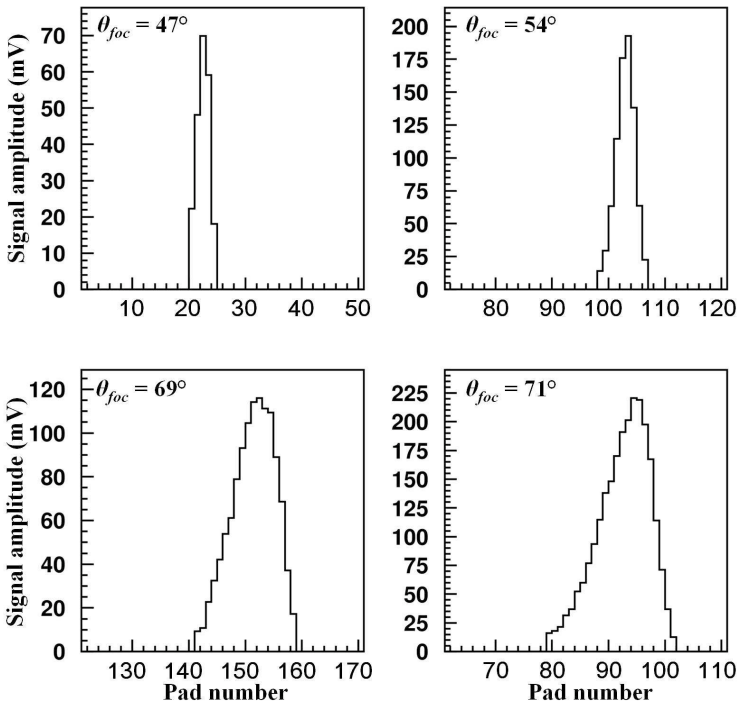

Fig. 6.2. Examples of the induced charge distribution over the DC2 patterned electrode. The corresponding values of θ_{foc} are indicated.

A new technique for the determination of the horizontal position from the induced charge distribution is presented and applied to the measurement of ejectiles through the MAGNEX FPD in ref. [128] and used in the present work. Such a technique basically consists of the use of the center of gravity algorithm (COG) described in ref. [130]

upgraded by the implementation of an iterative procedure to set the proper threshold event by event, even for those with low signal to noise ratio.

In detail, the centroid pad number $\bar{n}$ is calculated by weighting each pad number n_j with the charge q_j induced on that pad:

$$\bar{n} = \frac{\sum(q_j - b)n_j}{\tilde{Q}} \qquad \tilde{Q} = \sum(q_j - b) \quad for \quad q_j - b > 0 \tag{6.1}$$

where a pad is included in the sum if the charge induced on it is above a threshold (bias) *b*. As observed in ref. [130], a careful choice of the threshold improves the quality and the stability of the measurement. The optimal bias level *b* should be set proportional to the total charge measured $b = kQ = k\sum q_j$, where *k* can vary between 5×10^{-3} and 2.5×10^{-2}.

In order to analyze the charge distribution and test the quality of the chosen threshold and the calculated centroid, the behavior of the standard deviation (σ) of the distribution is also studied

$$\sigma = \sqrt{\frac{\sum(n_j - \bar{n})^2(q_j - b)}{\tilde{Q}}} \qquad for \quad (q_j - b) > 0 \tag{6.2}$$

If the threshold is properly set σ should range from ~ 1 (in the case of three bins exceeding the bias level in the distribution) to ~ 5 (for 20 bins). The improving of the standard COG algorithm consists in taking σ as the control parameter of an iterative procedure. In particular, when the σ parameter exceeds the accepted values ($1 < \sigma < 5$), the bias level is increased of a small quantity in successive iterations, controlled by the *i* index:

$$b_i = (k + 0.002i)Q \tag{6.3}$$

The iterations are repeated until the σ value becomes smaller than 5. Typically a number of iterations smaller than 40 is enough to obtain the correct bias level. Using this algorithm a precise determination of the centroid of the charge distribution with a very good efficiency (~ 97%) is obtained [128].

After the determination of the avalanche position, it is possible to obtain the horizontal position X_i for each DC, since the horizontal size of each pad is known (d = 6 mm within 0.01 mm). Such X_i parameters are used for the reconstruction of the linear ion track through the detector, since the longitudinal positions Z_1, Z_2, Z_3, Z_4 of the wires are very accurately defined by mechanical construction (tolerance 0.1 mm). An example of the correlation between the obtained X_i positions and the Z_i distances between the 4 DCs is shown in Fig. 6.3. Thanks to precise reference points embedded in the dipole magnet provided by the manufacturer, it is possible to precisely determine by optical sights the intersection point of the spectrometer optical axis with the focal plane detector. This gives the optical zero for the horizontal position X_i and consequently allows to built the X_{foc} optical variable. The latter is one of the parameters needed for the ray-reconstruction procedure described in Section 6.4. Analogously, the angular coefficient of the track (corresponding to the linear fit in Fig. 6.3) gives directly the horizontal angle of incidence in the focal plane θ_{foc}, which represent another input parameter for the ray-reconstruction.

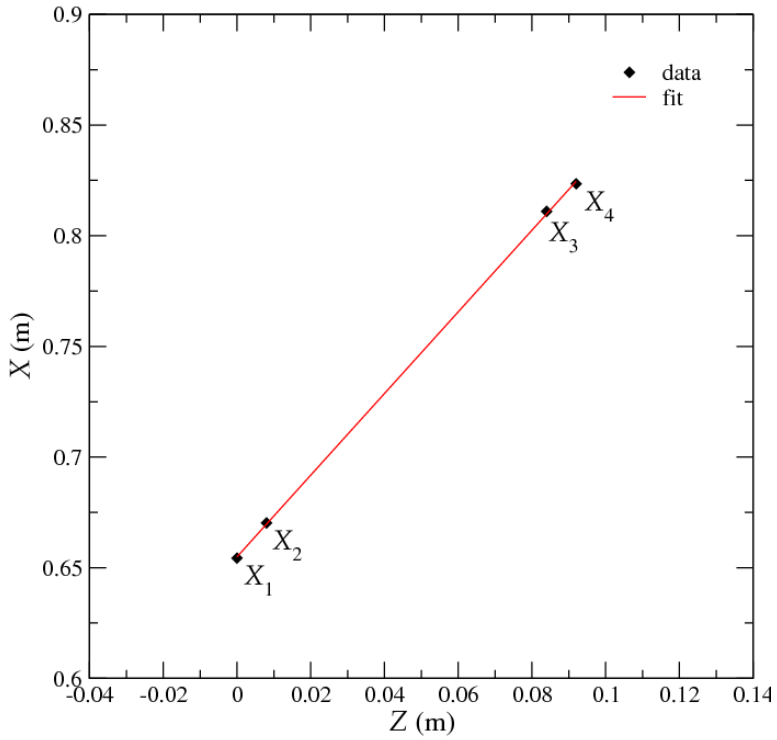

Fig. 6.3. Correlation between the X_i positions for one event and the Z_i distances between the 4 DCs. Z = 0 is assumed for DC1.

6.1.3 Calibration of the vertical position parameter

As discussed in Section 5.3, the vertical position of the ions in the FPD is determined at four different *Z* positions by the measurements of the drift times of electrons moving towards the four DC wires. Unlike the horizontal coordinate case, no internal mechanical structure can be used for the absolute calibration of the vertical one, thus an external alignment is required. In particular, a system composed by a collimated α source and a diaphragm with horizontal slits was mounted in an arm in front of the FPD detector. The system can be moved parallel to the DC wires sliding on a rail, as shown in Fig. 6.4. The diaphragm has 14 slits (2 for each height) and each of them is 1 mm wide and 26 mm long. Two neighbor slits are vertically separated by 20 mm. The entire system was mounted parallel to the optical axis of the spectrometer. In this configuration a series of beams defined in the spectrometer reference frame illuminates the detector. An example of the measured *Y* coordinates is shown in Fig. 6.5.

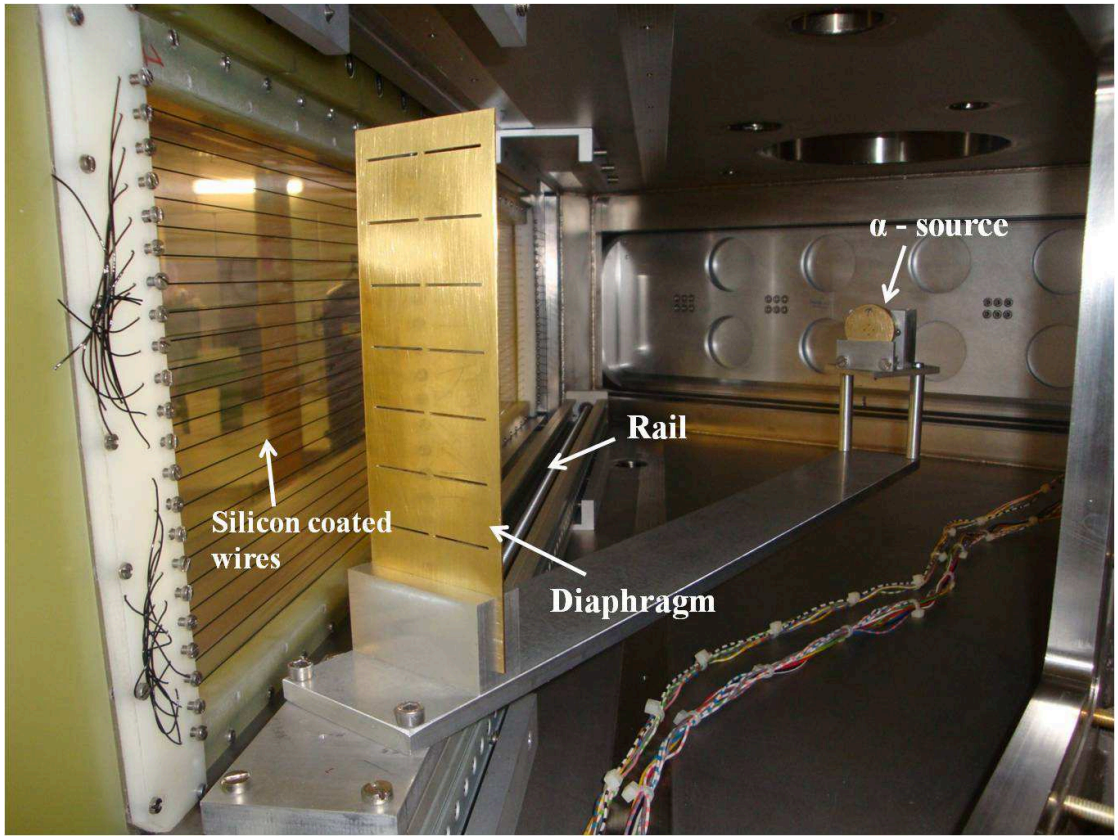

Fig. 6.4. System used for the calibration of the vertical position parameter.

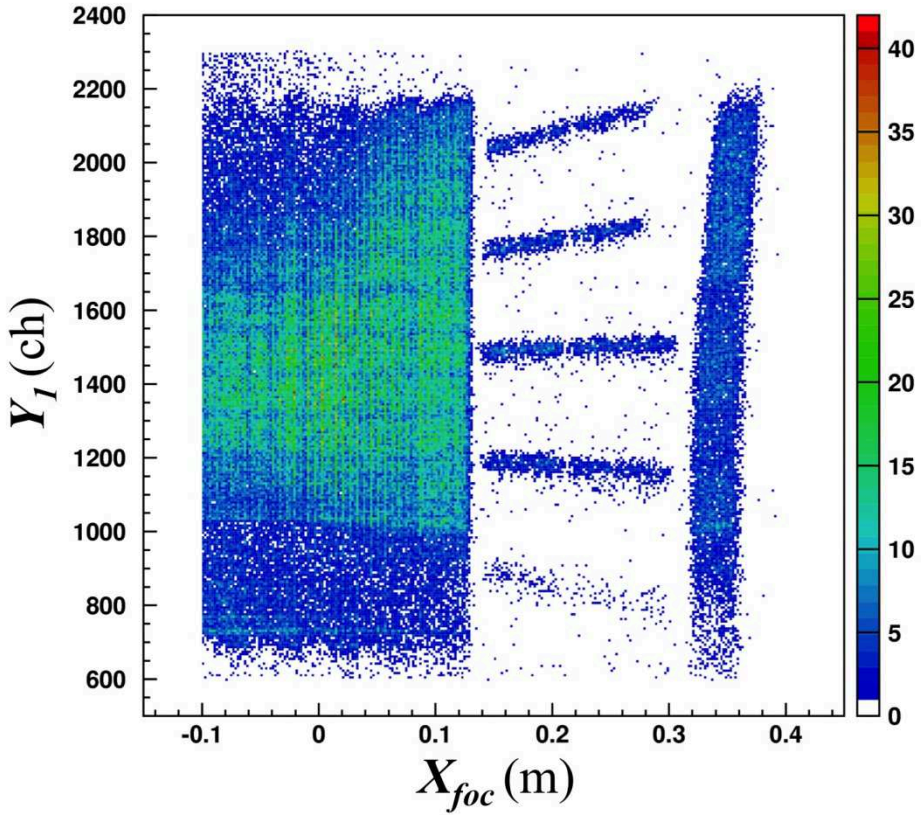

Fig. 6.5. Plot of the vertical coordinates versus the horizontal ones measured in the DC1 detector using the configuration shown in Fig. 6.4. The vertical inclination of the slits images is due to a geometrical perspective effect.

The absolute position of both the α source (X_α, Y_α, Z_α) emitting hole (1 mm diameter) and of the diaphragm apertures were determined by precise optical alignment with respect to the spectrometer symmetry plane. The schematic view of the coordinates used for determining the trajectory of an α particle passing through a slit is depicted in Fig. 6.6. Considering the FPD reference frame, it is possible to write simple equations describing the trajectory of an α particle:

$$\begin{cases} X = X_\alpha + t(X_O + \Delta X - X_\alpha) \\ Y = Y_\alpha + t(Y_O - Y_\alpha) \\ Z = Z_\alpha + t(Z_O + \Delta Z - Z_\alpha) \end{cases} \tag{6.4}$$

where the α index refers to the α-source, the O index labels the central axis of the diaphragm and ΔX and ΔZ represent the x and y projection of the slit, respectively. The latter two are connected by the relation $\Delta Z = -\Delta X \tan\theta_{tilt}$ (see Fig. 6.6).

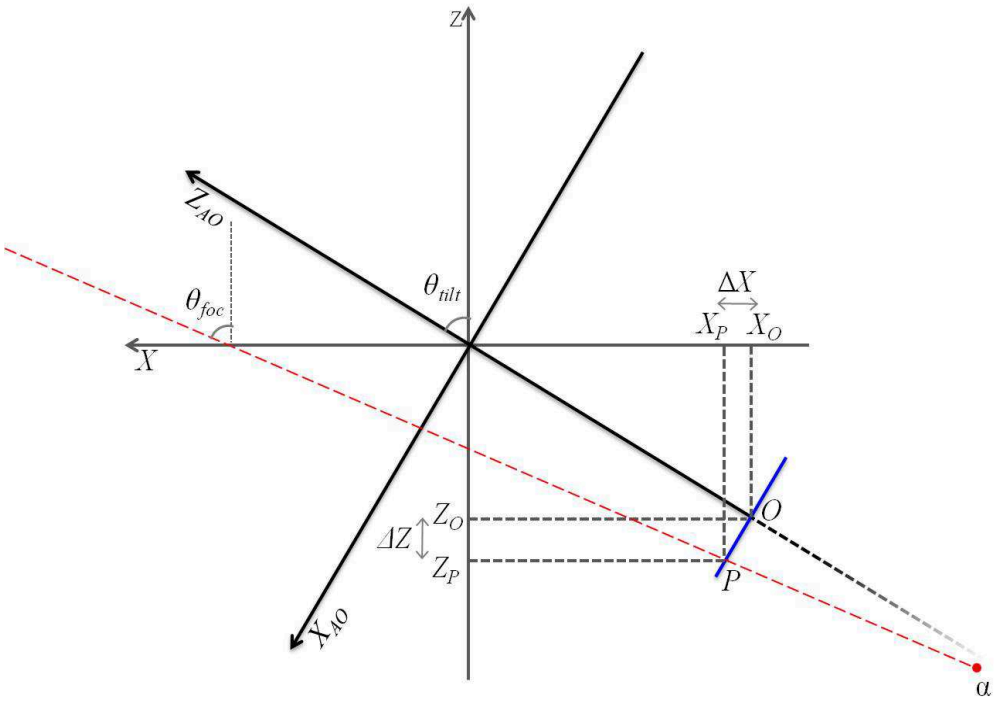

Fig. 6.6. Schematic plane view of the coordinate system adopted to obtain the equation for the trajectory of an α particle in the FPD reference frame. The central point and a general point of a slit are indicated with $O(x_O, z_O)$ and $P(x_P, z_p)$, respectively. The track of an α passing through the point P is indicate as the red dashed line.

Since the Z coordinates of the four DCs are known and once the X positions are measured, it is possible to solve the system (6.4) and obtain the Y coordinates for each trajectory. The absolute calibration of the vertical position was then achieved by a linear fit of the expected positions versus the measured ones for each DC. A remarkable linearity was observed despite the long drift path of the electrons, as shown in Fig. 6.7, where the resulting fit for the DC1 detector is plotted. The possible dependence of the Y_i measurement on the X_i parameter was not fully verified with this procedure, because it was not possible to move the arm along all the regions of the detector. Therefore, a supplemental calibration check was done. Considering a typical Y_i spectrum, shown in Fig. 6.8, some regularly spaced minima are evident. These are due to the shadows of the horizontal silicon coated wires used to support the Mylar window (as shown in Fig. 6.4). The position of such wires was also determined by optical measurements in the spectrometer frame. Therefore, the final absolute calibration of the Y parameter was obtained by comparing the position of the holes in each Y_i spectrum with the known projection of the wires positions at each DC. Similarly to what done for the horizontal

positions, the Y_i parameters are used to reconstruct the linear ion track through the detector, using the known longitudinal positions Z_i of the wires. An example of the correlation between the obtained Y_i positions and the Z_i distances between the 4 DCs is shown in Fig. 6.9. The angular coefficient of the track (corresponding to the linear fit in Fig. 6.9) gives directly the vertical angle of incidence at the focal plane ϕ_{foc}, which is another input parameter for the ray-reconstruction.

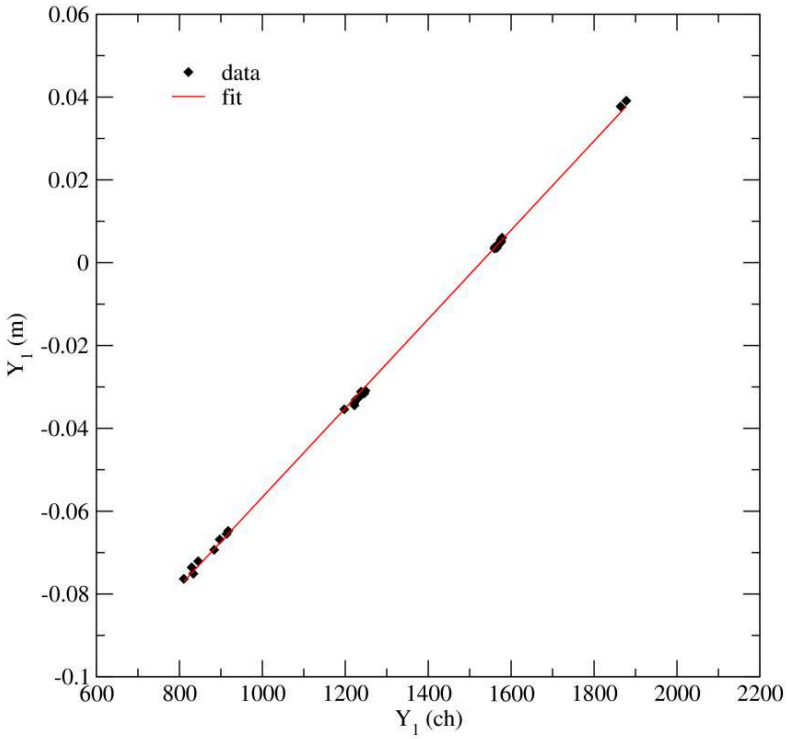

Fig. 6.7. Linear fit correlating the measured vertical positions (ch) to the expected positions (m) for the DC1 detector. The measured positions refers to the loci representing the slits images shown in Fig. 6.5.

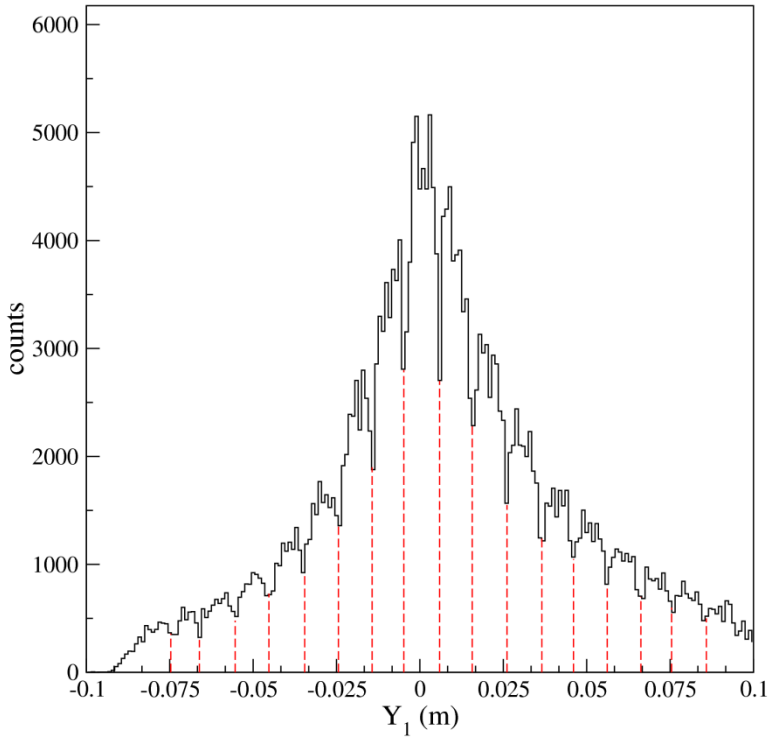

Fig. 6.8. Typical Y_i spectrum with no events selection. The minima due to the shadows of the silicon coated wires are indicated with the red dashed lines.

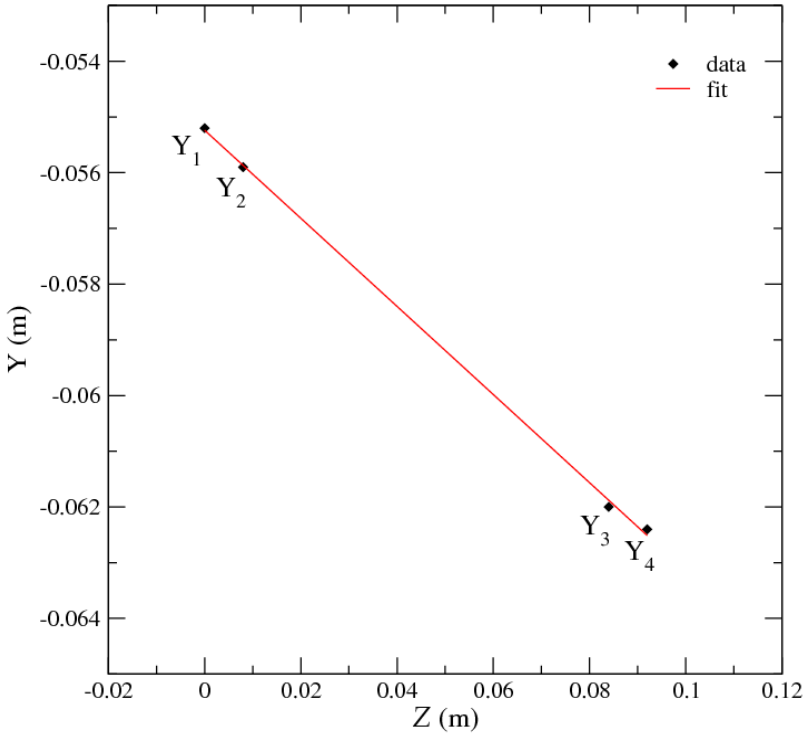

Fig. 6.9. Correlation between the Y_i positions for one event and the Z_i distances between the 4 DCs. $Z = 0$ is assumed for DC1.

6.2 The identification of ^{16}O

After the calibration procedure the ^{16}O ejectile identification was performed. The first step consists in the identification of the atomic number (Z) of the ejectiles performed using the standard *ΔE-E* technique, based on the Bethe-Bloch formula [131]. A typical *ΔE-E* bidimensional plot is shown in Fig. 6.10 for a single silicon detector together with a coarse graphical contour that includes the Oxygen ejectiles. In particular, the plotted parameters are the residual energy measured by the silicon detectors (E_{resid}) in abscissa, and the energy-loss in the gas measured by the PC counter, corrected for the angle of the detected ions measured in the focal plane (ΔE_{PC}^{corr}), in ordinate. Such angle correction is necessary in order to account for the different path lengths in the gas, as consequence of the different incident angle θ_{foc} in the focal plane. Since the FPD is rotated by θ_{tilt} = 59.2°, the correction is:

$$\Delta E_{PC}^{corr} = \Delta E_{PC} \frac{cos\theta_{tilt}}{cos\theta_{foc}} \tag{6.5}$$

The absolute calibration of the E_{resid} and ΔE_{PC}^{corr} is not necessary, because they are used only for particle identification purposes. The oxygen isotopes loci in the Δ*E-E* plot were identified through supplementary elastic scattering runs.

The selection done in the *ΔE-E* plot is not enough to clearly separate the ^{16}O ejectile among all the Oxygen isotopes produced in the reaction. A standard way to identify the ejectiles in a magnetic spectrometer is to couple the *ΔE-E* technique to the measurement of the Time of Flight (TOF) along the instrument. This requires the generation of a start signal for the TOF using an appropriate start detector close to the target. Nevertheless, the use of such a technique limits the performances of the spectrometer itself, indeed the straggling effect introduced by the start detector deteriorate the final energy and angular resolutions.

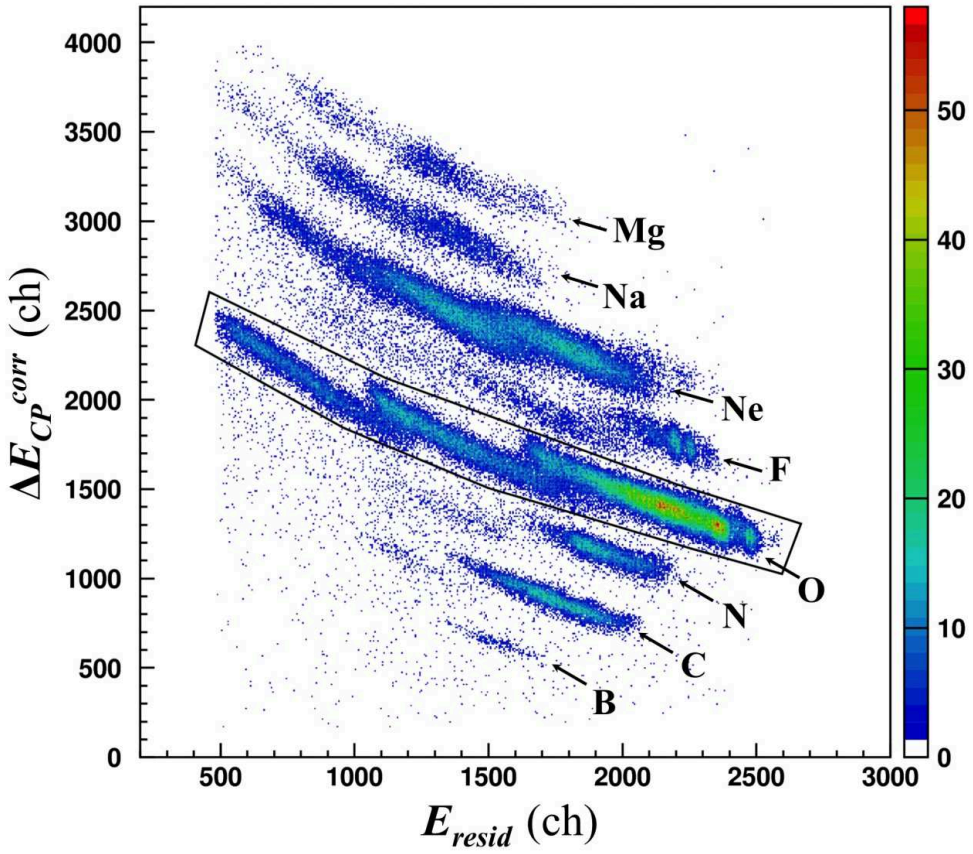

Fig. 6.10. Typical ΔE_{PC}^{corr} vs E_{resid} matrix for the unselected ejectiles detected in the reaction ^{13}C + ^{18}O at 84 MeV incident energy for a single silicon detector. The different ion species and a coarse graphical contour on the ^{16}O region are also indicated.

An innovative particle identification technique for large acceptance spectrometers was introduced in ref. [132]. Such a technique exploits the property of the Lorentz force, which determines the trajectory of a charged particle in a magnetic field normal to its momentum

$$B\rho = \frac{p}{q} \tag{6.6}$$

where p and q are the momentum and electric charge of the ion, respectively, while ρ is the radius of curvature of the ion trajectory inside a dispersive element (bending magnet) with field induction B. In a non-relativistic approximation, the momentum p is related to the kinetic energy E and, approximately, to the residual energy measured by the silicons E_{resid}, by a quadratic relation $p = \sqrt{2mE}$, where m is the ion mass. Since the curvature ρ is related to the position at the focal plane X_{foc}, the relationship between the two measured

quantities (X_{foc} and E_{resid}) is approximately quadratic with a factor depending on the ratio m/q^2

$$X_{foc}^2 \propto \frac{m}{q^2} E_{resid} \tag{6.7}$$

Therefore, in a X_{foc} versus E_{resid} plot the ions are distributed on different curves according to the ratio m/q^2. The clear separation between the different Oxygen isotopes is evident in Fig. 6.11, where the X_{foc}-E_{resid} matrix is shown for the data selected with the graphical condition on the ΔE_{PC}^{corr}- E_{resid} one (Fig. 6.10). Three main groups are visible corresponding to three different charge states (8^+, 7^+ and 6^+). Inside each group, the different oxygen isotopes are clearly separated (^{18}O, ^{17}O and ^{16}O). For the present data analysis, it was chosen to select the $^{16}O^{8+}$ ejectiles, as done with the graphical contour shown in Fig. 6.11.

When dealing with a large acceptance device as the MAGNEX spectrometer, a better mass resolution in the identification technique can be achieved performing a precise reconstruction of the ions kinetic energy, as demonstrated in ref. [132]. However, when a high mass resolution is not necessary, as in the present experimental conditions, the identification procedure is successfully performed using the X_{foc}-E_{resid} correlation.

For the complete particle identification, the AND condition between the two different graphical conditions, in the ΔE_{PC}^{corr}-E_{resid} and X_{foc}-E_{resid}, respectively, was used for each silicon detector. A final OR operation between the selection conditions for each silicon detector guaranteed a clean selection of all the detected $^{16}O^{8+}$ ejectiles.

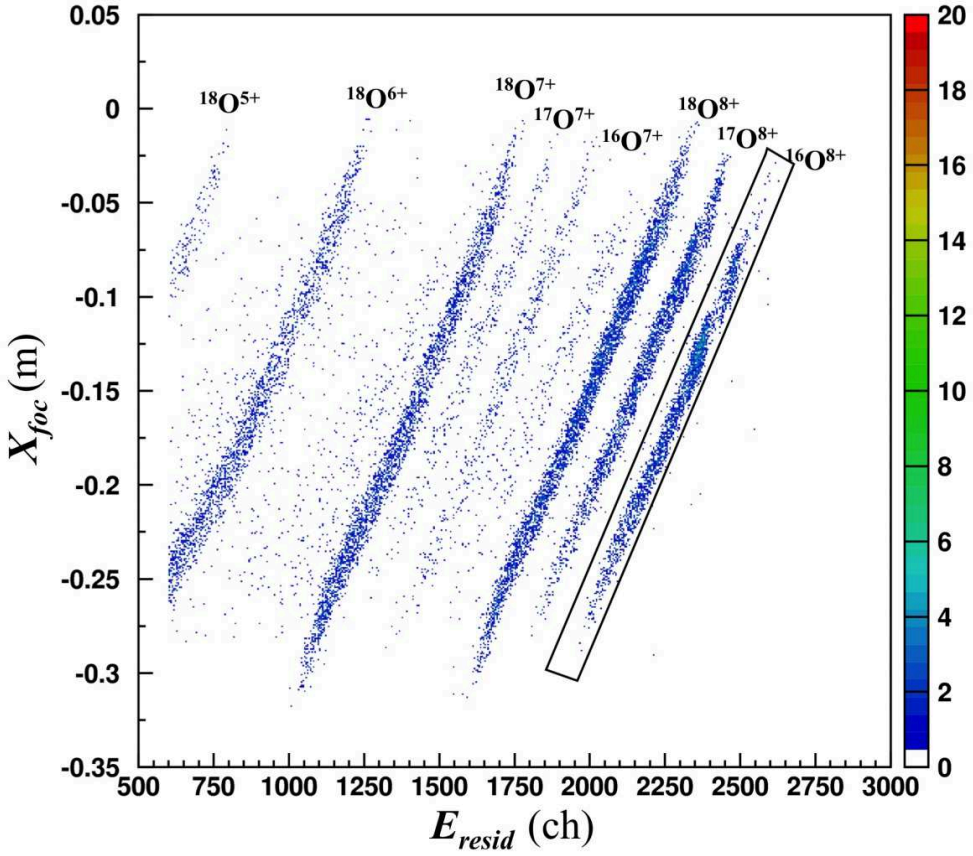

Fig. 6.11. Typical X_{foc}-E_{resid} matrix plotted with the graphical condition of Fig. 6.10 on the ΔE_{PC}^{corr}-E_{resid} for the same silicon detector. The different Oxygen isotopes and a graphical contour selecting the ^{16}O ejectiles are also indicated.

6.3 The final phase space parameters

Once the identification procedure was completed, the final phase space parameters (X_{foc}, θ_{foc}, Y_{foc} and ϕ_{foc}) were analyzed in detail. They provide information about the achieved horizontal and vertical focusing and about aberrations.

For example, a plot of Y_{foc} versus X_{foc} for the selected $^{16}O^{8+}$ events shows the typical *butterfly* shape, as shown in Fig. 6.12. This shape is characteristic of the final vertical phase space and it indicates that the vertical trajectories are focused only for a certain value of the ion momentum δ^*. Indeed, this is expected in a QD spectrometer as MAGNEX, since the chromatic aberrations [109] avoid the focusing of ions with momentum deviation $\delta \neq \delta^*$. In abscissa, $X_{foc} = 0$ corresponds to the trajectories in the optical axis. However, in the present data, the focusing appears at X_{foc} ~ -0.15 m, indicating that the chosen

quadrupole field focused only particle with $B\rho$ less than the reference one ($\delta = 0$). In the right side of the plot in Fig. 6.12, some well correlated loci are present, resulting in almost vertical lines. These correspond to the population of ^{15}C states in the $^{13}C(^{18}O,^{16}O)^{15}C$ reaction. For example, for X_{foc} ~ +0.3 m, events corresponding to the ground and the first excited state are evident. These appears in the focal plane region corresponding to a relative momentum $\delta = 0.08$, as expected from the chosen magnetic fields setting (reported in Section 5.4.1). The not exact verticality of the lines in an indication of non negligible presence of 3rd and higher order aberrations in the vertical phase space, especially in focal plane regions far from the optical axis.

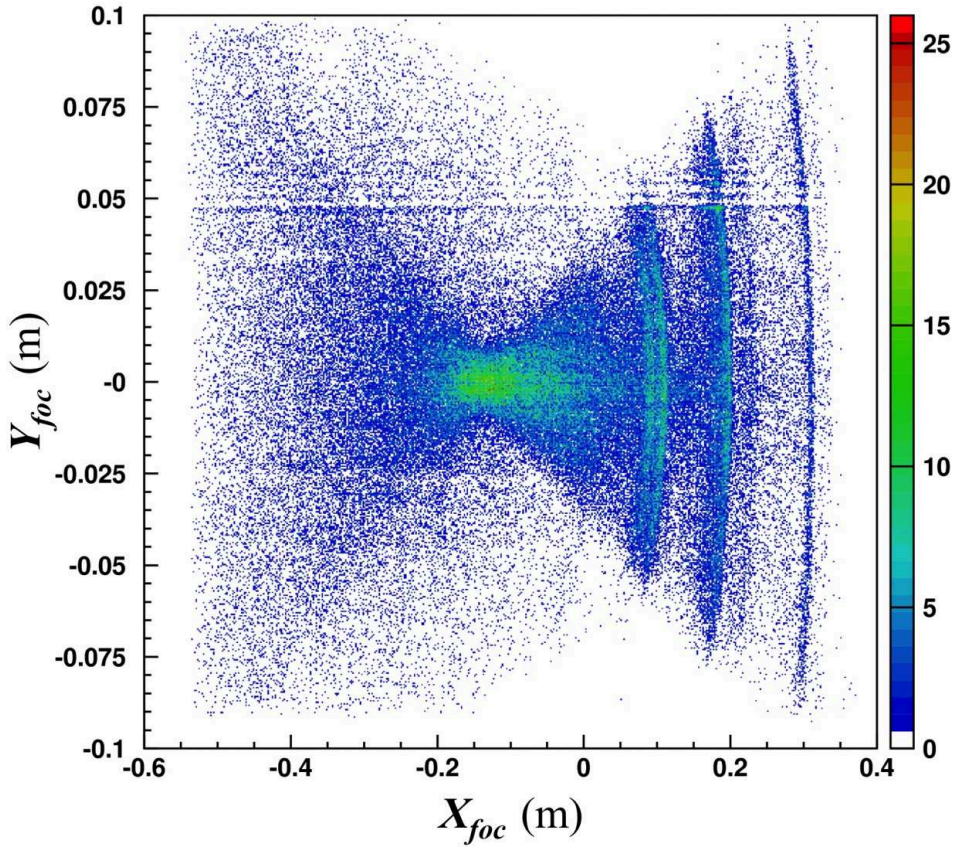

Fig. 6.12. Typical Y_{foc}-X_{foc} matrix for the selected $^{16}O^{8+}$ events belonging to the $^{13}C(^{18}O,^{16}O)^{15}C$ reaction at 84 MeV and $\theta_{lab}^{opt} = 12°$.

A plot of the horizontal angle θ_{foc} versus the horizontal position X_{foc} is shown in Fig. 6.13, for the same events of Fig. 6.12. Since the FPD is inclined by 59.2° (1.033 rad) with respect to the plane perpendicular to the optical axis, the measured θ_{foc} are distributed around that angle in the plot. The correlated events corresponding to the states populated in

the $^{13}C(^{18}O,^{16}O)^{15}C$ reaction are clearly evident also in this representation. The deviation of the loci from vertical lines is due both to the kinematical effect [114] and to second order aberrations. The curvature of the loci, especially visible near the borders, is due to the strong effect of the high order aberrations in the horizontal phase space.

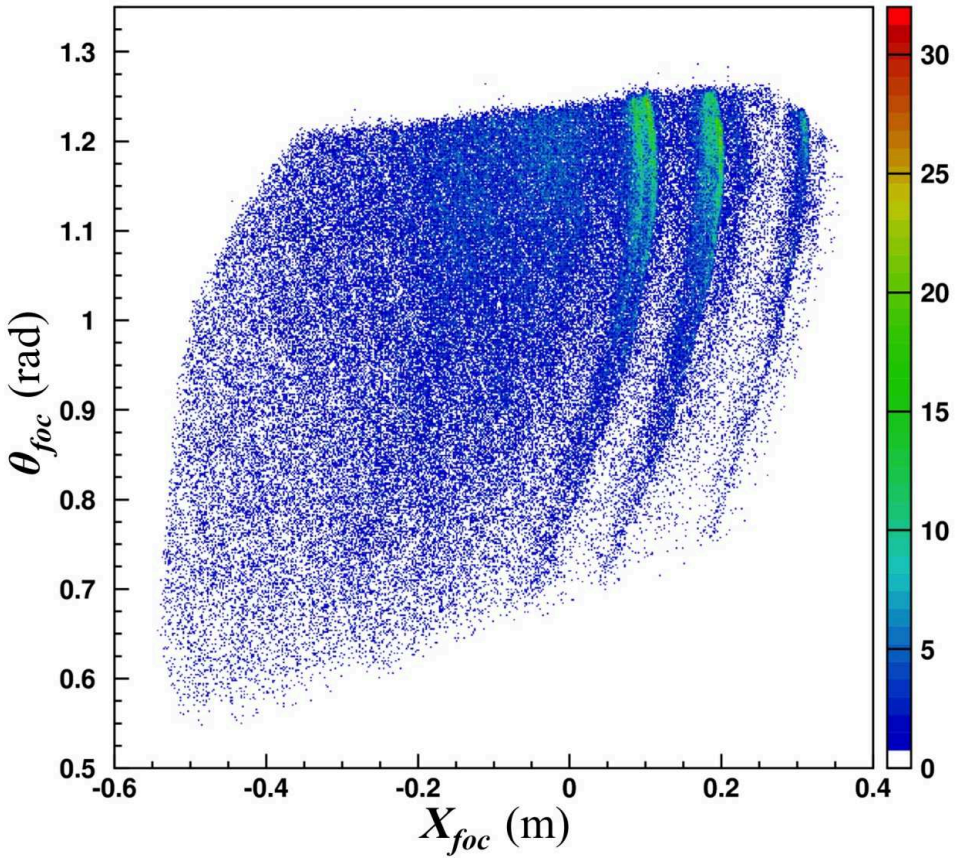

Fig. 6.13. Typical θ_{foc}-X_{foc} matrix for the selected $^{16}O^{8+}$ events belonging to the $^{13}C(^{18}O,^{16}O)^{15}C$ reaction at 84 MeV and θ_{lab}^{opt} = 12°.

6.4 Application of the ray-reconstruction technique

The ray-reconstruction procedure was applied to each set of data analyzed, in order to obtain the excitation energy spectra of the residual nuclei and the cross section angular distributions for the main transitions. Four main steps are necessary to carry out the reconstruction, as described in the following Sections.

The practical way to tune the trajectory reconstruction to a physics case is to compare the measured phase space parameters at the focal plane, shown in Section 6.3, with the simulated ones, which represent a model of the spectrometer response to the selected

reaction. The closer the simulated description is to the measured one the better is the model of the transport operator.

6.4.1 Creation of the direct transport map

The first step of the reconstruction procedure is to built a transport map which describes the evolution of the phase-space parameters from the target point to the focal plane. Using the matrix formalism introduced in Section 5.2.1, the initial coordinates $\boldsymbol{P}_i = (\theta_i, y_i, \phi_i, \delta)$ are connected to the final ones $\boldsymbol{P}_f = (x_f, \theta_f, y_f, \phi_f)$ through the relation (5.1). In the MAGNEX case, eq. (5.1) is solved by an algebraic technique based on the formalism of differential algebra [121][133] implemented in the COSY INFINITY program [134]. Such a technique allows to calculate the map up to high order without long ray-tracing procedures. For the present data analysis, the direct transport map ($\mathcal{M}$) was created to the 10^{th} order.

In the COSY INFINITY input, the geometry of the spectrometer (distances between the magnetic elements, length of the drift spaces, and slits defining the solid angle) and the size and location of the FPD were set as the experimental ones. These quantities were accurately measured by optical devices, within a sub-millimeter precision. This guarantees the mathematical compatibility between the transport matrix and the phase space vector measured at the focal plane. The measured dipole and quadrupole magnetic strengths were used (see Section 5.4.1). The three-dimensional field shapes are described as Enge functions [135] obtained from interpolations of measured data [117] [118][119][120].

Tricky input parameters for the creation of the transport matrices are the Effective Field Boundaries (EFB) of the dipole magnet, which are mathematically represented as 5^{th} order polynomials in the COSY INFINITY language. In fact, there is a weak dependence of the shape of the entrance and exit EFB on the magnetic field strength and therefore they were carefully optimized for each magnetic setting looking at the resulting transport simulations, as described in the following Section.

6.4.2 Simulations of the direct transport

In order to test the goodness of the created transport map, a set of events corresponding to the $^{13}C(^{18}O,^{16}O)^{15}C$ reaction at 84 MeV were generated by Monte Carlo routines [127]. The ^{16}O ejectiles connected to the excitation of seven ^{15}C known states from ref. [102](the g.s. and states at 0.74, 3.10, 4.22, 4.66, 6.84 and 7.35 MeV) were tracked through the spectrometer by the application of the direct transport map.

The ^{18}O beam energy value is another important parameter required to perform the simulation. This is not exactly equal to the nominal beam energy (E_{beam} = 84 MeV), because of the energy loss in the target suffered by both the ^{18}O projectiles and the ^{16}O ejectiles before entering the spectrometer. Since the simulation program does not take into account the energy loss in the crossed layers, the *effective* energy beam was estimated by means of kinematic and energy loss calculations, using the programs CATKIN [136] and SRIM-2008 [137], respectively, following the scheme shown in Fig. 6.14. It was assumed that on average the reaction takes place in the middle of the target. The ^{18}O energy loss ($\Delta E'$) after crossing half ^{13}C target was estimated, thus obtaining a value E'_{beam} = E_{beam} - $\Delta E'$. The E'_{beam} was used to perform the kinematical calculation for the reaction ^{18}O + ^{13}C → ^{16}O + ^{15}C, obtaining the ^{16}O ejectiles energy ($E_{ejectile}$) emitted at the central angle θ_{lab}^{opt} = 12°. Following the assumed scheme, the ^{16}O ejectiles cross the remaining half-target with an inclination θ_{lab}^{opt}, losing the energy amount $\Delta E''$. The ejectiles energy before entering the spectrometer is thus $E'_{ejectile}$ = $E_{ejectile}$ - $\Delta E''$. Finally, the effective energy beam (E_{beam}^{eff}) was determined as that necessary to obtain an ^{16}O ejectile at $E'_{ejectile}$ and angle θ_{lab}^{opt} without any energy loss ($\Delta E'$ = 0, $\Delta E''$ = 0). The effective energies obtained for each data set are reported in Table 6.1.

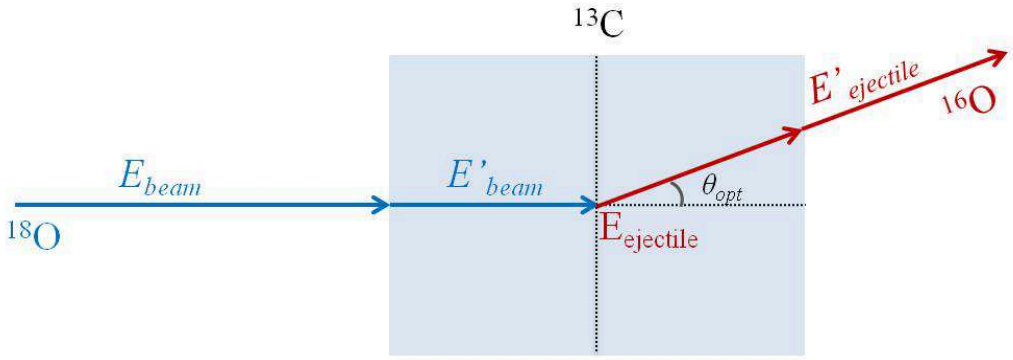

Fig. 6.14. Effective beam energy calculation scheme.

The result of the performed simulation is shown in Fig. 6.15 for the data set already shown in Section 6.3. Despite the highly non-linear aberrations, the simulated data (red points) give a rather faithful representation of the experimental ones (black points) both in the horizontal (θ_{foc}-X_{foc} plot) and vertical (Y_{foc}-X_{foc} plot) phase spaces. The accuracy of the description of the final phase space by the direct transport matrix is estimated about -0.5 ± 0.9 mm and 3 ± 5 mr in X_{foc} and θ_{foc}, respectively, similarly to what found in ref. [116].

Table 6.1. Effective energy beams for the analyzed data.

Target	θ_{lab}^{opt}(deg)	E_{beam} (MeV)	E_{beam}^{eff} (MeV)
^{12}C	6	84.02	83.81
	12	84.10	83.88
	18	84.10	83.82
^{13}C	6	84.02	83.82
	12	84.10	83.88
	18	84.10	83.80

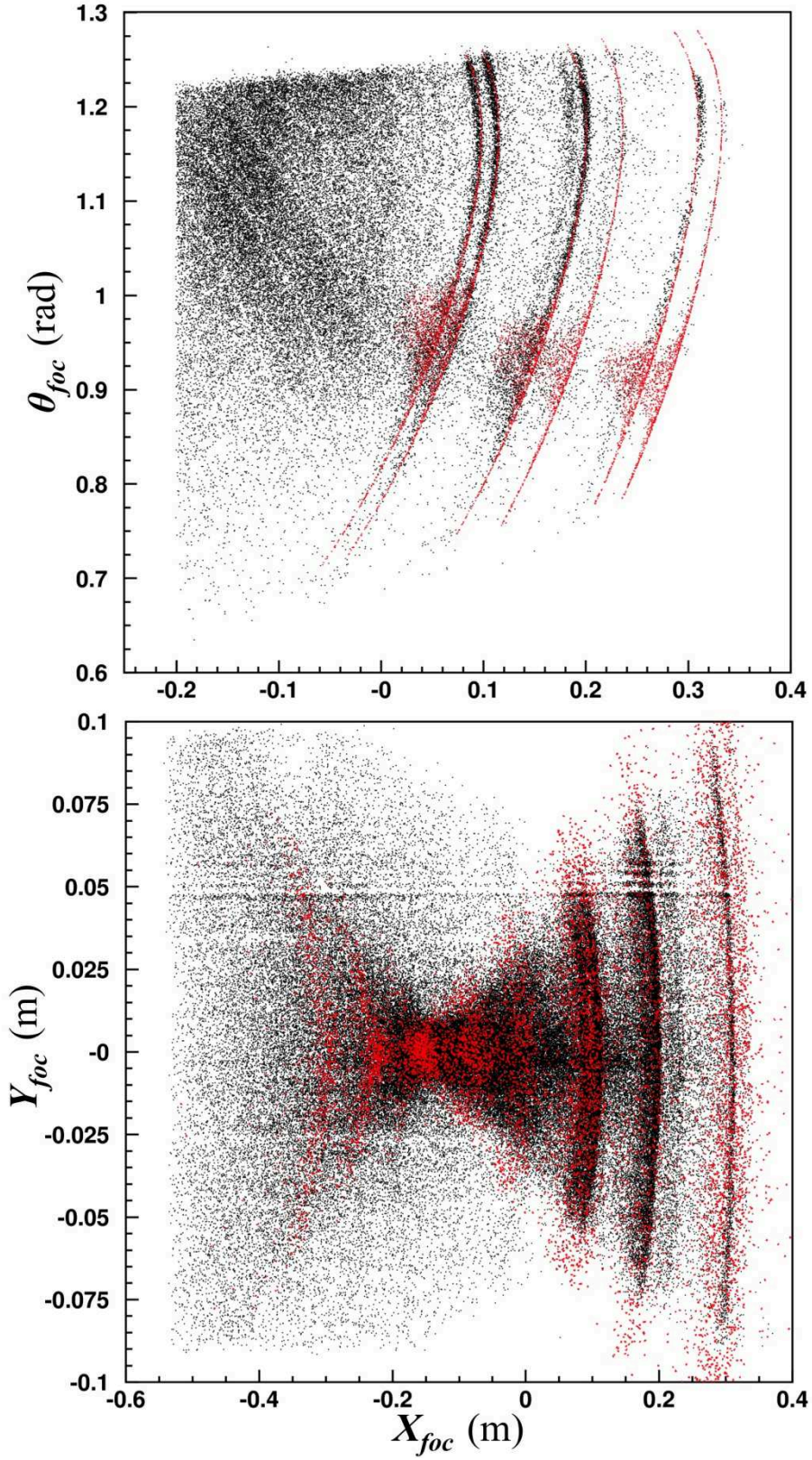

Fig. 6.15. Comparison between the experimental (black points) and the simulated (red points) data in the θ_{foc}-X_{foc} (top panel) and Y_{foc}-X_{foc} (bottom panel) representations.

6.4.3 Creation of the inverse transport map

The COSY INFINITY program makes it possible to invert the transport equations in order to get the initial coordinates $\boldsymbol{P}_i$ from the measured final ones $\boldsymbol{P}_f$. To the first order the inverse matrix ($\mathcal{M}^{-1}$) has the simple structure:

$$\mathcal{M}^{-1} = \begin{pmatrix} (\theta|x) & (\theta|\theta) & (\theta|y) & (\theta|\phi) \\ (y|x) & (y|\theta) & (y|y) & (y|\phi) \\ (\phi|x) & (\phi|\theta) & (\phi|y) & (\phi|\phi) \\ (\delta|x) & (\delta|\theta) & (\delta|y) & (\delta|\phi) \end{pmatrix} \tag{6.8}$$

The notation used is $(a|b) = \left(\partial a_i / \partial\, b_f\right)_{opt}$ where the derivatives are calculated along the central trajectory and the central momentum.

The complete map contains the derivative terms up to the 10th order, such that a initial phase space parameter, for example θ_i, is given by

$$\theta_i = \sum_{n=1}^{10} \left(\frac{\partial^n \theta_i}{\partial x_f^m \partial \theta_f^p \partial y_f^q \partial \phi_f^r} \right)_{opt} \cdot x_f^m \theta_f^p y_f^q \phi_f^r \quad con\ (m+p+q+r) = n \tag{6.9}$$

The application of the inverse map to the final measured parameters allows to compensate the effect of the high order aberrations that affect the spectrometer, because they are contained in the constructed operator.

6.4.4 Application of the inverse transport map to the experimental data

Thanks to the trajectory reconstruction technique, it is possible to obtain the initial phase space parameters at the target point. These are directly related to the physical quantities of interest, such as the modulus of the ejectile momentum and the scattering angle.

A plot of the initial vertical angle versus the initial horizontal one (ϕ_i-θ_i) is shown in Fig. 6.16. The reconstructed angular acceptance corresponds to the real one (-7.16° < ϕ_i < 7.16° and -5.16° < θ_i < 6.3°). However, the plot does not have the ideal rectangular shape. This results in a reduction of the differential solid angle especially at the borders of the

phase space. Such efficiency losses were studied in ref. [138] and found to be due to a cut-off of the beam envelope from the vacuum vessels. This effect must be taken into account when extracting the cross section angular distributions. The procedure will be described in details in Section 6.7.

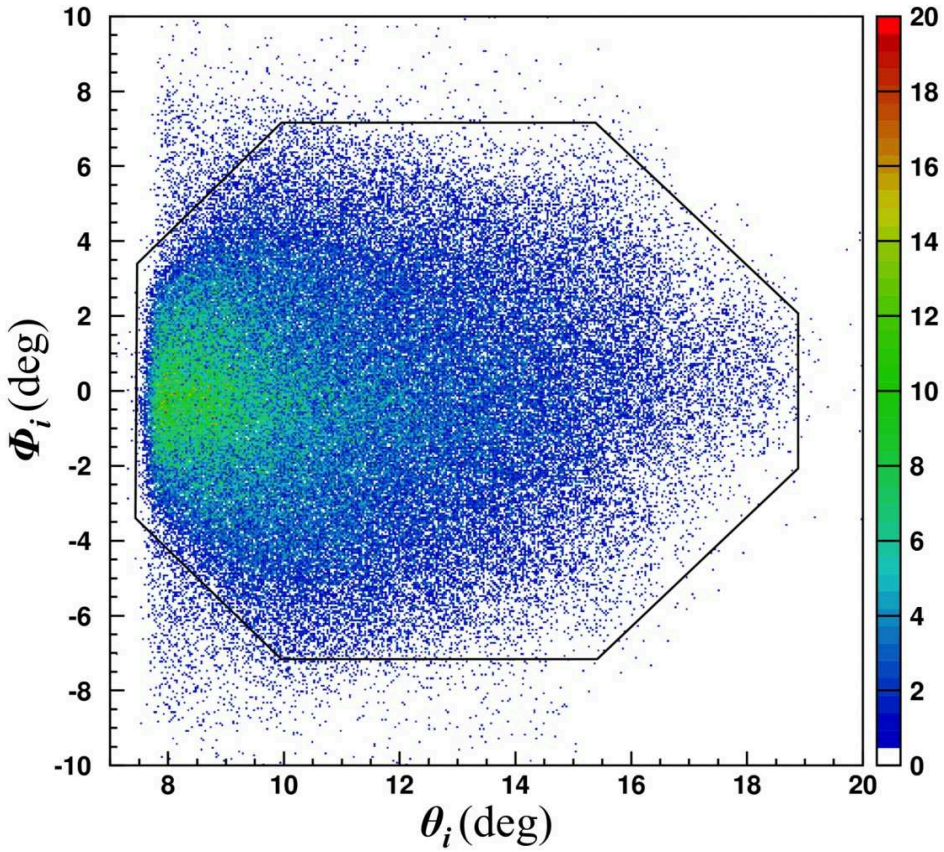

Fig. 6.16. Reconstructed ϕ_i- θ_i plot for the same experimental conditions of Fig. 6.12. The contour of the locus is shown with the black line, representing the spectrometer solid angle acceptance.

Once the initial angles are known, it is possible to extract from geometrical relations, the laboratory scattering angle, as

$$\theta_{lab} = arccos \frac{\cos(\theta_{opt}) - sin(\theta_{opt})tan(\theta_i)}{\sqrt{1 + tan^2(\theta_i) + tan^2(\phi_i)}} \tag{6.10}$$

Then, from the reconstructed relative momentum δ, it is deduced the initial kinetic energy of the ejectiles. The corresponding Q-values, or equivalently the excitation energy

E_x, are finally obtained by a missing mass calculation based on relativistic energy and momentum conservation laws, supposing a binary reaction

$$E_x = Q_0 - Q = Q_0 - K\left(1 + \frac{M_e}{M_r}\right) + E_{beam}\left(1 - \frac{M_b}{M_r}\right) + 2\frac{\sqrt{M_b M_e}}{M_r}\sqrt{E_{beam}K}cos\theta_{lab} \qquad (6.11)$$

where M_e, M_r, M_b are the ejectile, residual and beam masses, respectively, K is the kinetic energy of the ejectile (related to the δ parameter) and Q_0 is the ground state to ground state Q-value (for the present case Q_0 = -2.793 MeV). A plot of θ_{lab} versus E_x is shown in Fig. 6.17. The ^{15}C ground and several excited states are well visible as vertical and straight loci, as expected since the E_x parameter does not depend on the scattering angle for transitions to the ^{15}C states. The efficiency cut around 20 MeV excitation energy is due to the acceptance of the spectrometer [138].

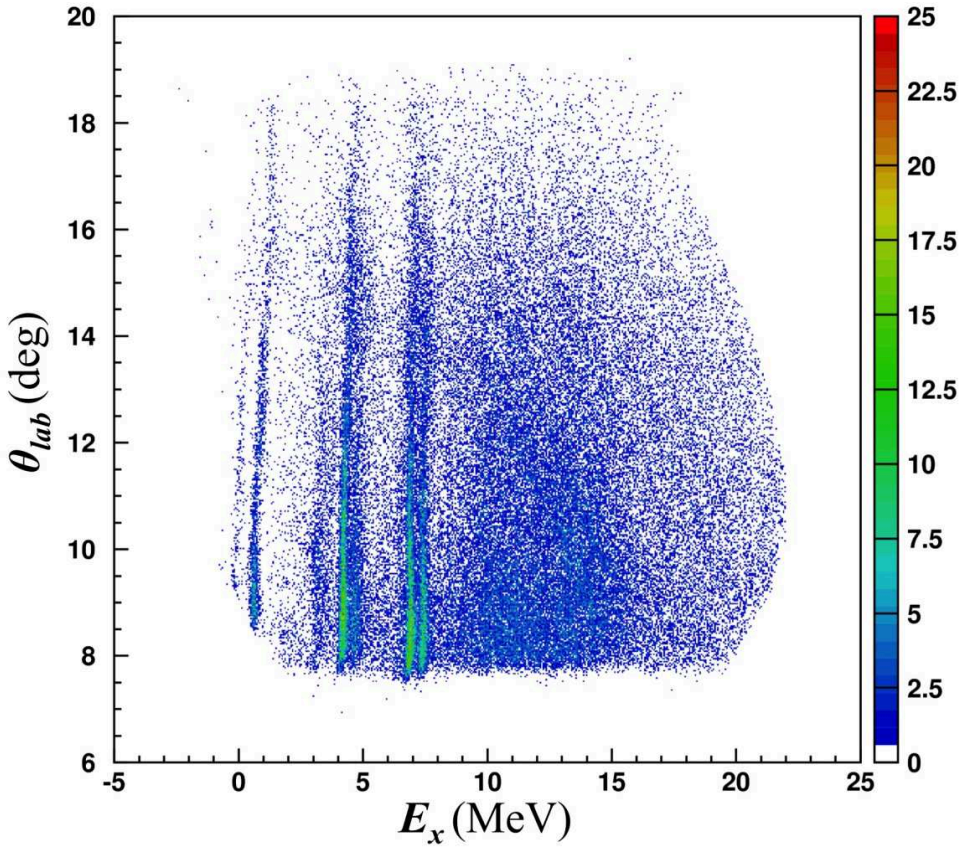

Fig. 6.17. Plot of the reconstructed θ_{lab} against the ^{15}C excitation energy (E_x) for the $^{13}C(^{18}O,^{16}O)^{15}C$ in the same experimental conditions of Fig. 6.12.

6.5 Background subtraction

A projection of the reconstructed data shown in Fig. 6.17 on the excitation energy axis provides a more quantitative comparison of the different transition yields. It is also useful to correctly evaluate and subtract the background contribution which comes mainly from impurities of ^{12}C in the ^{13}C target. The data runs on ^{12}C target at θ_{lab}^{opt} = 12° were performed at the same experimental conditions and magnetic fields of the ^{13}C one. These runs were reconstructed using the same transport map and considering the same kinematics of the ^{13}C(^{18}O,^{16}O)^{15}C reaction, thus obtaining the reconstructed background spectra in the $E_x^{(15C)}$ representation. A projection of the $E_x^{(15C)}$ spectrum obtained using the ^{13}C target is shown in Fig. 6.18-a for scattering angles 9.5° < θ_{lab} < 10.5°. The observed peaks represent transitions to different ^{15}C and ^{14}C states. The same spectrum when using the ^{12}C target is shown in Fig. 6.18-b. From a comparison between the two spectra it appears that the region at 3.5 MeV excitation energy in ^{15}C spectrum is contaminated by a doublet of ^{14}C peaks. In order to subtract properly this background, a careful normalization of the data runs on ^{12}C was performed. In particular, the ^{14}C peak indicated in Fig. 6.18 with the red dashed line was integrated in the two spectra, obtaining the numbers of counts $\bar{N}_{^{13}C}$ and $\bar{N}_{^{12}C}$. The normalization coefficient was defined as follows:

$$S_{^{12}C} = \frac{\bar{N}_{^{13}C}}{\bar{N}_{^{12}C}} = 0.43 \tag{6.12}$$

The total background was then subtracted as

$$N_{tot} = N_{^{13}C} - S_{^{12}C} \cdot N_{^{12}C} \tag{6.13}$$

The normalized background spectrum from ^{12}C target superimposed on the ^{15}C spectrum is shown in Fig. 6.19. It appears that the background contribution is typically small.

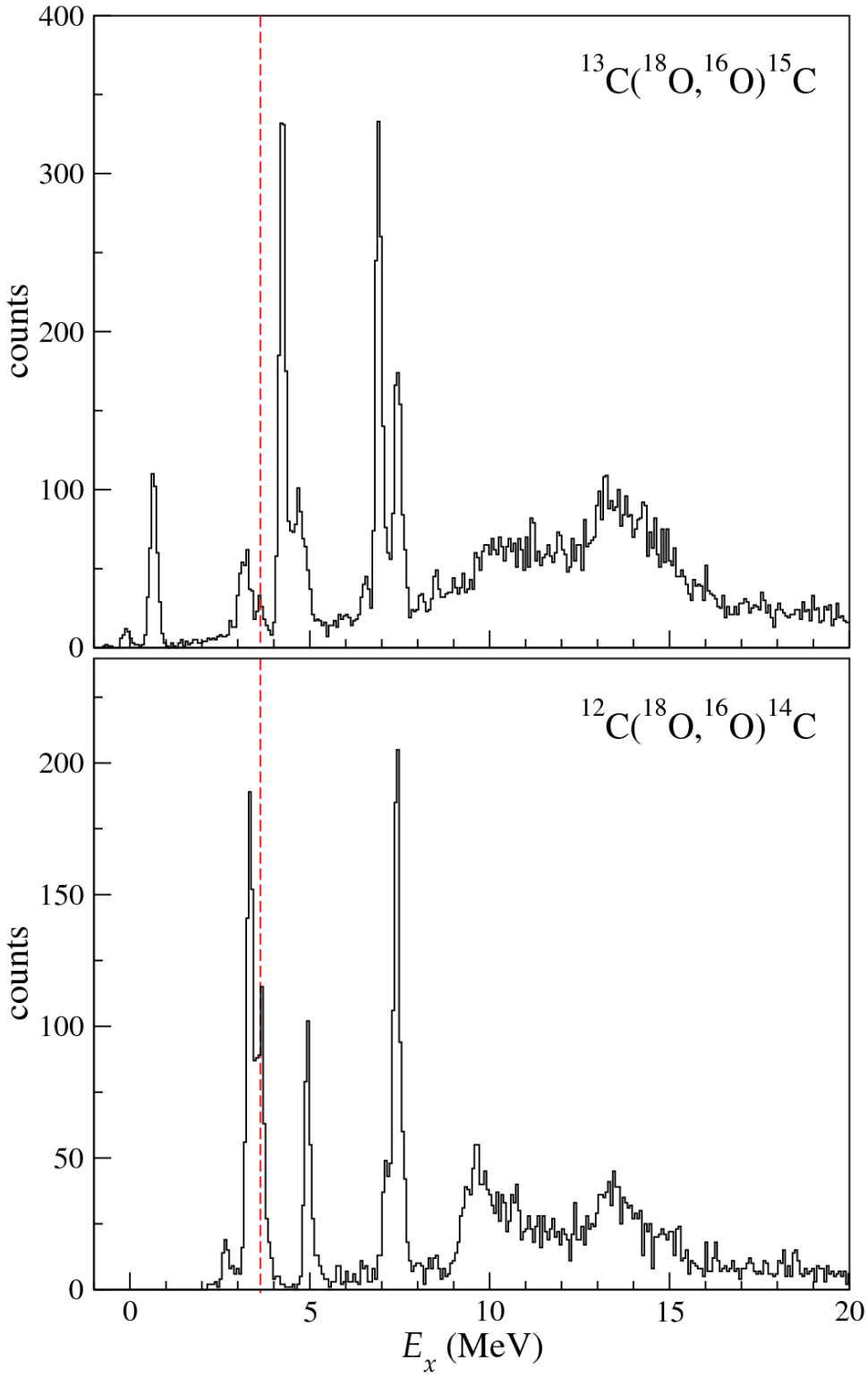

Fig. 6.18. Excitation energy spectra for ^{15}C (upper panel) and ^{14}C (bottom panel) at $9.5° < \theta_{lab} < 10.5°$. Both spectra are reconstructed using the kinematics of $^{13}C(^{18}O,^{16}O)^{15}C$ reaction. The ^{14}C peak used for the background normalization is indicated with the red dashed line.

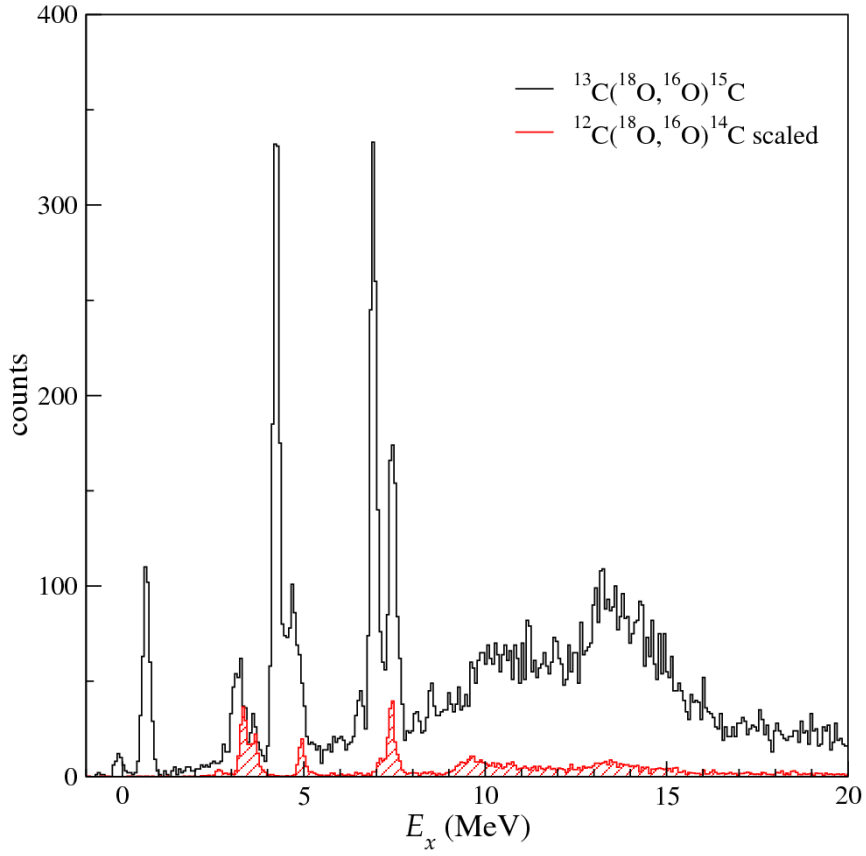

Fig. 6.19. Excitation energy spectrum of the $^{13}C(^{18}O,^{16}O)^{15}C$ reaction at 9.5° < θ_{lab} < 10.5°. The red hatched histogram represents the normalized background of the $^{12}C(^{18}O,^{16}O)^{14}C$ reaction coming from ^{12}C impurities in the ^{13}C target.

6.6 Excitation energy spectra

The described data reduction procedure was applied to the data set corresponding to the other angular settings of the $^{13}C(^{18}O,^{16}O)^{15}C$ reaction (θ_{lab}^{opt} = 6°, 18°) and to the $^{12}C(^{18}O,^{16}O)^{14}C$ reaction (θ_{lab}^{opt} = 6°, 12°, 18°). Examples of the obtained ^{15}C and ^{14}C spectra at 9° < θ_{foc} < 10° are shown in Fig. 6.20 and Fig. 6.21, respectively. For the ^{15}C case, the spectrum is obtained after the background subtraction. A complete list of the observed states is reported in Table 6.2. The estimated energy resolution is ~ 200 keV, mainly determined by multiple scattering phenomena in the target. This was obtained from the best fit of the peaks by Gaussian functions. In particular, a least square algorithm with fixed centers and variable widths was used [139]. By comparison with known resonances [22] [89], an accuracy of ± 0.02 keV was found, consistent with the results of ref. [116].

Two narrow peaks of ^{15}C are present in Fig. 6.20 below the one-neutron separation energy (S_n = 1.218 MeV), corresponding to the population of the ground and the only bound excited state at 0.73 MeV. Above the one-neutron separation threshold narrow resonances at E_x = 3.12, 4.21, 4.65, 6.85, 7.36 MeV are clearly identified. These are the same strongly populated in the (t,p) reaction [22], as reported in Section 4.4.2. In addition, above the two-neutron emission threshold (S_{2n} = 9.394 MeV) two large structures are strongly excited at energies E_x = 10.5 ± 0.1 and 13.7 ± 0.1 MeV with FWHM 2.5 ± 0.3 MeV for both. These structures have never been observed in ^{15}C spectra in any kind of reaction (cf. Chapter 4). The FWHM were determined by best fit assuming Gaussian shapes and accounting for a three-body continuous background normalized to the region beyond 16 MeV. Other function shapes and background models were also used whose results are included in the error bars.

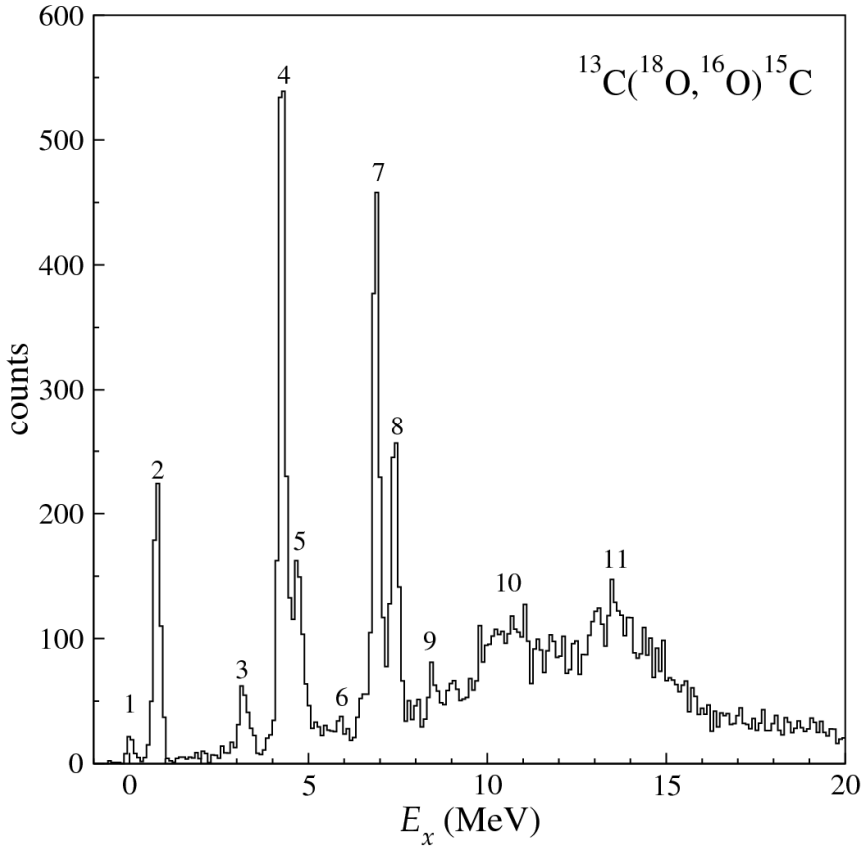

Fig. 6.20. Excitation energy spectrum of the $^{13}C(^{18}O,^{16}O)^{15}C$ reaction at $9° < \theta_{lab} < 10°$. The background contribution due to the presence of ^{12}C in the target is subtracted. The labeled peaks are listed in Table 6.2.

As regards the ^{14}C, the ground and bound states at E_x = 6.10, 6.71, 7.00 MeV are populated below the one-neutron separation energy (S_n = 8.176 MeV) (see Fig. 6.21). Narrow resonances are observed at E_x = 8.33, 9.81, 10.43, 10.73, 12.88 MeV. These states were also strongly populated in (t,p) reactions (see Section 4.4.2). Similarly to the case of ^{15}C, two broad structures at about 13.5 and 16.9 MeV are observed above the two neutron emission threshold (S_{2n} = 13.122 MeV). The first bump is likely connected to the unresolved transitions to the known resonances at 12.58, 12.87, 12.96, 13.4, 13.9 MeV in ^{14}C. The second one is mainly determined by a wide unknown structure at E_x = 16.9 MeV ± 0.1 with a FWHM 1.2 ± 0.3 MeV. However, a small contribution from the known narrow resonances at E_x = 16.43 and 16.74 (1^+) MeV cannot be excluded.

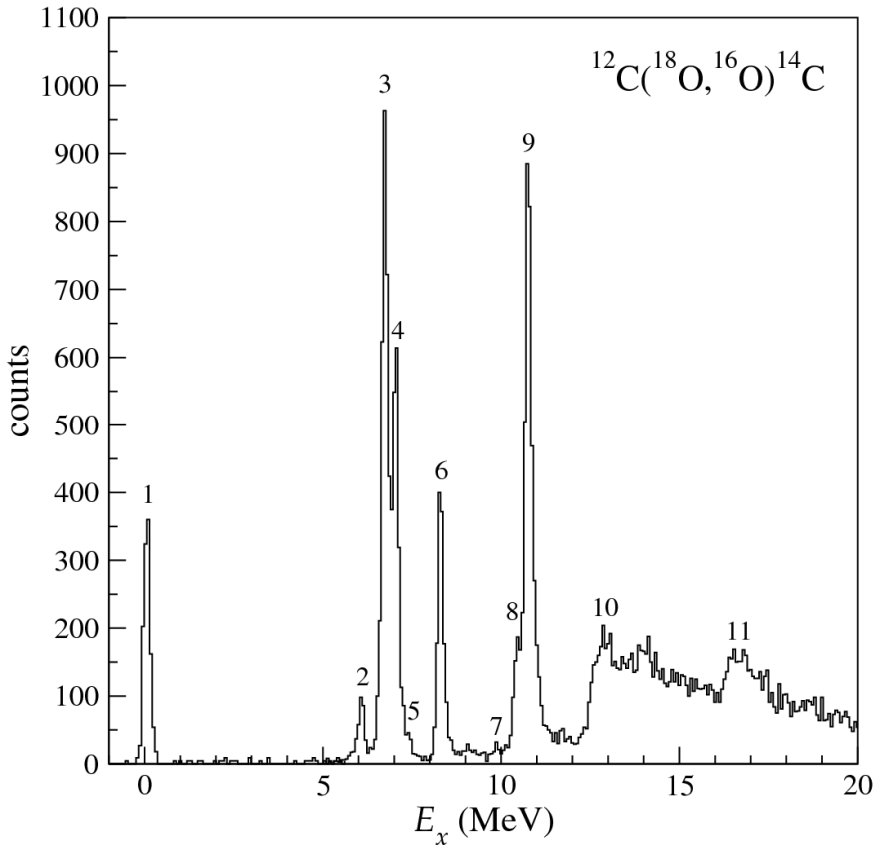

Fig. 6.21. Excitation energy spectrum of the $^{12}C(^{18}O,^{16}O)^{14}C$ reaction at 9° < θ_{lab} < 10°. The labeled peaks are listed in Table 6.2.

Table 6.2. Main spectroscopic features of the ^{15}C and ^{14}C populated states.

^{15}C states	**Excitation energy** (MeV)	**Excitation energy** (literature)[2]	J^{π} (literature)[2]
1	0.00 ± 0.02	0	$1/2^+$
2	0.73 ± 0.02	0.74	$5/2^+$
3	3.12 ± 0.02	3.10	$1/2^-$
4	4.21 ± 0.02	4.22	$5/2^-$
5	4.65 ± 0.02	4.66	$3/2^-$
6	5.87 ± 0.02	5.87	$1/2^-$
7	6.85 ± 0.02	6.84	$7/2^-$
8	7.36 ± 0.02	7.35	$9/2^-$
9	8.47 ± 0.02	8.47	$9/2 \rightarrow 13/2$
10	10.5 ± 0.1		
11	13.7 ± 0.1		$1/2^-$ ([3])
^{14}C states	**Excitation energy** (MeV)	**Excitation energy** (literature)[2]	J^{π} (literature)[2]
1	0.00 ± 0.02	0	0^+
2	6.10 ± 0.02	6.09	1^-
3	6.71 ± 0.02	6.73	3^-
4	7.00 ± 0.02	7.01	2^+
5	7.36 ± 0.02	7.34	2^-
6	8.33 ± 0.02	8.32	2^+
7	9.81 ± 0.02	9.80	0^+
8	10.43 ± 0.02	10.44, 10.5	
9	10.73 ± 0.02	10.75	4^+
10	12.88 ± 0.02	12.96	3^-
11	16.9 ± 0.1		0^+ ([3])

[2] From ref. [102].
[3] As demonstrated in Chapter 8.

6.7 Cross section angular distributions

In this Section, the extraction of the absolute cross section angular distributions for the strongest transitions observed for ^{15}C and ^{14}C is described. The advantage of working with a large acceptance spectrometer is that, for a given set of measurements under identical experimental conditions, a wide range of scattering angles is covered. As a consequence, a consistent part of a cross section angular distribution can be measured in a single run in the same experimental conditions, resulting in a reduction of the uncertainty due to the normalization of runs at different angles. In particular, in a single angular setting the spectrometer accepts events between about ± 6° in the laboratory reference frame. Considering the three angular settings of the experiment (θ_{opt}^{lab} = 6°, 12° and 18°), the total covered angular range is about $3° < \theta_{lab} < 24°$ (it does not start from 0° because in the run at θ_{opt}^{lab} = 6° the entrance slit at small angles was closed at 3° in order to avoid beam haloes) with an overlap of about 6° between two contiguous settings.

In general, for a given nuclear transition, the differential cross section is defined as:

$$\frac{d\sigma}{d\Omega}(\theta) = \frac{N(\theta)}{N_{beam} N_{target} \Delta\Omega \, t_{\text{live}} \, \epsilon} \tag{6.14}$$

where $N(\theta)$ is the number of counts measured at the angle θ, N_{beam} is the number of incident ions, N_{target} is the number of target nuclei for unit surface, $\Delta\Omega$ is the solid angle spanned by the detector, t_{live} is the live time coefficient and ϵ is a factor which takes into account the overall efficiency.

The number of incident particles N_{beam} in Eq. (6.14) is related to the charge collected by the Faraday cup (Q_F) during each experimental run. At the beam energy of the experiment (84 MeV), the ^{18}O ions emerging from the target are fully stripped [140], thus making particularly simple the relation between Q_F and N_{beam} ($N_{beam} = Q_F/8e$, where e is the electron charge). The total charge integrated in each run is reported in Table 6.3. The number of target nuclei for unit surface (N_{target}) is calculated from the known target density and thickness. The obtained values are $N_{target}^{^{13}C}$ = 2.4 ± 0.1 · 10^{18} ions/cm^2 and $N_{target}^{^{12}C}$ = 2.5 ± 0.1 · 10^{18} ions/cm^2. The live time coefficient (t_{live}) corresponds to the ratio between the recorded data (FPD.*live*) and the total acquisition triggers (FPD.*raw*); both of them are

stored in the VME scaler modules during the data acquisition. The electronic set-up ensures very accurate estimation of this dead time coefficient. The obtained values are listed in Table 6.3.

Table 6.3. Obtained values for the total charge collected by the Faraday cup, the number of incident ions (N_{beam}) and the live time coefficient (t_{live}).

Target	θ_{lab}^{opt} (deg)	**Integrated charge** (μC)	N_{beam} (10^{13} ions)	t_{live} (%)
^{12}C	8	34.4 ± 0.7	2.68 ± 0.05	44.0
	12	41.0 ± 0.8	3.20 ± 0.06	69.4
	18	73 ± 1	5.7 ± 0.1	52.0
^{13}C	6	25.9 ± 0.5	2.02 ± 0.04	92.9
	12	111 ± 2	8.7 ± 0.2	73.2
	18	489 ± 10	38.1 ± 0.8	66.2

As regards the solid angle $\Delta\Omega$, the geometry relevant for its determination is shown in Fig. 6.22. In principle, the spectrometer solid angle acceptance is defined by 4 slits located at 260 mm from the target and before the quadrupole entrance (green line in Fig. 6.22-b). However, the overall efficiency losses in the spectrometer correspond to an effective reduction of the solid angle, as demonstrated in ref. [138]. The actual solid angle acceptance is deduced taking the contour of the reconstructed (θ_i, ϕ_i) locus in the laboratory reference frame, as shown in Fig. 6.16. The technique used to calculate the differential solid angle $\Delta\Omega$ is shown in Fig. 6.22-b, where the (θ_i, ϕ_i) contour for θ_{lab}^{opt} = 12° is drawn and the circular rings corresponding to laboratory angle bins of $\Delta\theta_{lab}$ = 0.5° are superimposed. The area defined by the interception between the circular ring enclosed in the (θ_{lab}, $\theta_{lab} + \Delta\theta_{lab}$) interval and the ($\theta_i$, ϕ_i) contour was calculated (hatched region in Fig. 6.22-b) , thus obtaining the actual differential solid angle for each θ_{lab} bin. The chosen angular bin corresponds to an angular interval of about 0.5° in the laboratory frame. Following this procedure, a quite precise measure (~ 2%) of the solid angle is achieved. The measured scattering angles in the laboratory frame were then transformed in the centre of mass one, multiplying by the Jacobian determinant of the transformation, which depends on the angle and excitation energy.

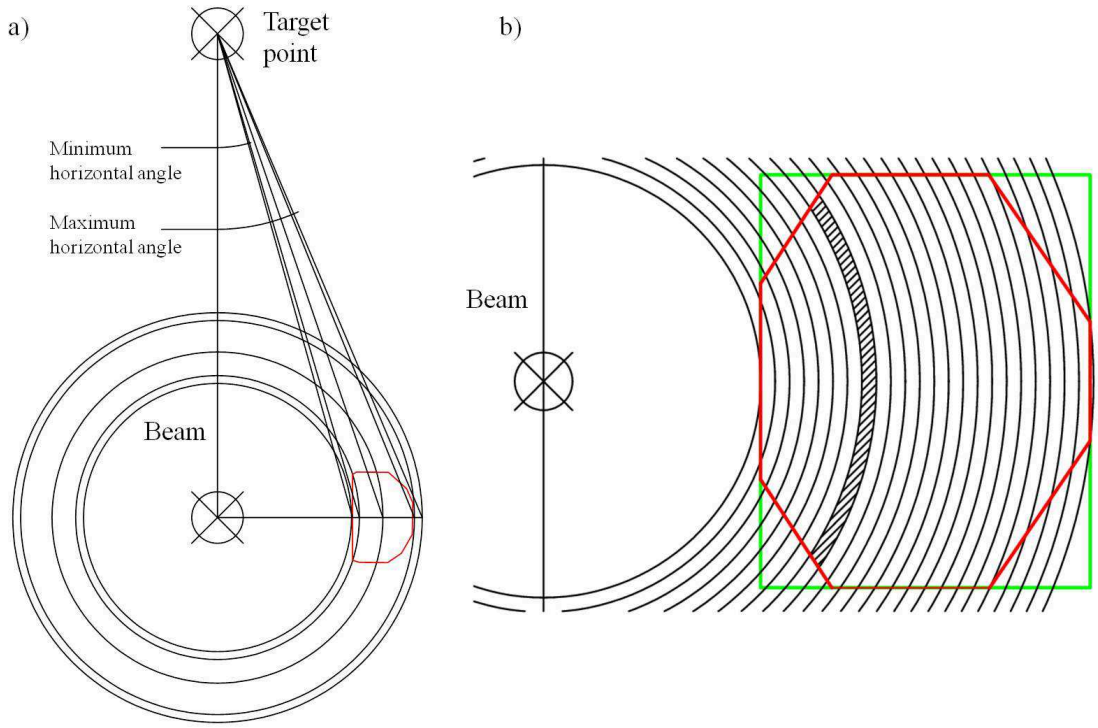

Fig. 6.22. a) Geometry for the determination of the solid angle. b) Differential solid angle determination. The effective spectrometer aperture, (determined by the same (θ_i, ϕ_i) contour of Fig. 6.16) and the spectrometer diaphragms aperture are indicated as the red and green line, respectively. The differential solid angle for a single angular bin is defined by the interception between the circular ring enclosed in the (θ_{lab}, θ_{lab} + $\Delta\theta_{lab}$) interval and the (θ_i, ϕ_i) contour (black hatched region).

The coefficient ϵ was estimated taking into account the FPD detection efficiency (~ 95%) and the loss of events due to bad ray-reconstruction (~ 8%). The latter was calculated making the ratio between the well reconstructed events and the total identified events at the focal plane for each considered transition.

The technique used to determine the number of counts $N(\theta)$ is described in the following Sections considering three cases: (i) bound states; (ii) narrow resonant states; (iii) unknown wide bumps in the continuum.

6.7.1 Bound states

The only bound states in ^{15}C are the ground and the 0.73 MeV one. The corresponding region in the energy spectra is not contaminated by the background due to impurities of ^{12}C in the target, as shown in Fig. 6.19. Moreover, the relative loci are quite well separated in the reconstructed (E_x, θ_{lab}) plot (shown in Fig. 6.17). Therefore, the number of counts $N(\theta)$ for these transitions was determined making a graphical selection in the (E_x, θ_{lab}) plot (as shown in Fig. 6.23-a) and projecting on the θ_{lab} axis choosing an angular bin of $\Delta\theta_{lab}$ = 0.5°. Once the $N(\theta)$ are extracted at each θ the angular distributions of the absolute cross sections are built following eq. (6.14). The resulting angular distributions are shown in Fig. 6.24.

The same procedure was applied for the ^{14}C g.s. (the used graphical selection is shown in Fig. 6.23-b). On the other hand, the loci corresponding to the 6.71 and 7.00 MeV bound states of ^{14}C are very close each other and it was not possible to do a selection in the (E_x, θ_{lab}) matrix. In order to unfold them, a two-Gaussian fitting model was applied in the one-dimensional energy spectra. The routines of MINUIT [139] were used for this purpose. As a general rule the centroids and widths of two transitions were forced to vary in narrow ranges around the values accepted in literature and, at the end of the procedure, they were fixed, allowing only the heights to be varied. The results are shown in Fig. 6.25. The area of the obtained Gaussian functions gives the number of counts for each angular bin. The angular distributions for the ^{14}C are shown in Fig. 6.26.

In the angular distributions plots, the error bars on only the vertical axis are drawn (see Section 6.7.4 for their evaluation), since the uncertainty on the angle determination is quite small (~ 0.2°).

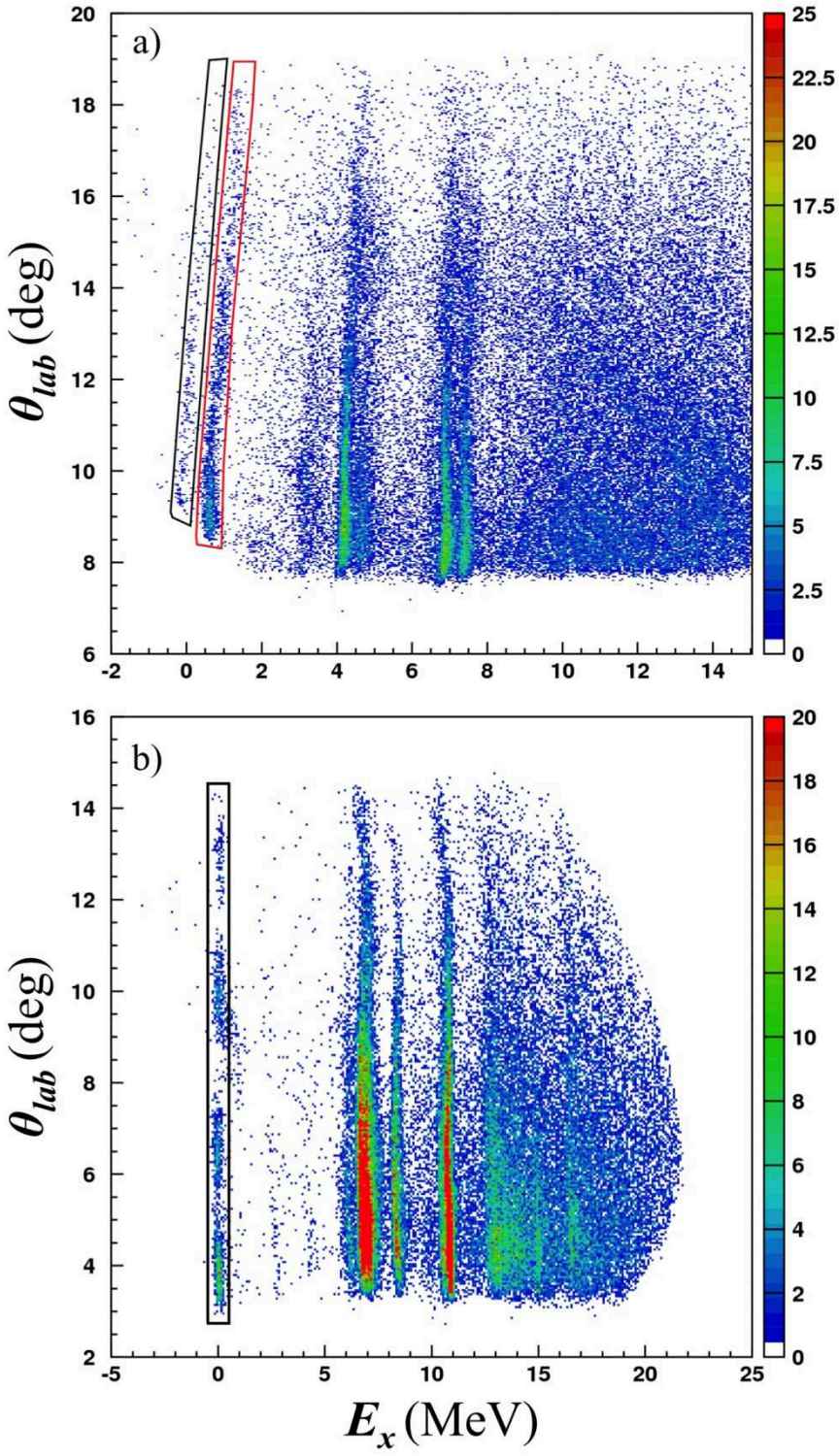

Fig. 6.23. (E_x, θ_{lab}) plots. Graphical contours used to determine the angular distribution of (a) the ^{15}C g.s. (black line) and 0.73 MeV (red line) excited state and (b) the ^{14}C g.s. (black line).

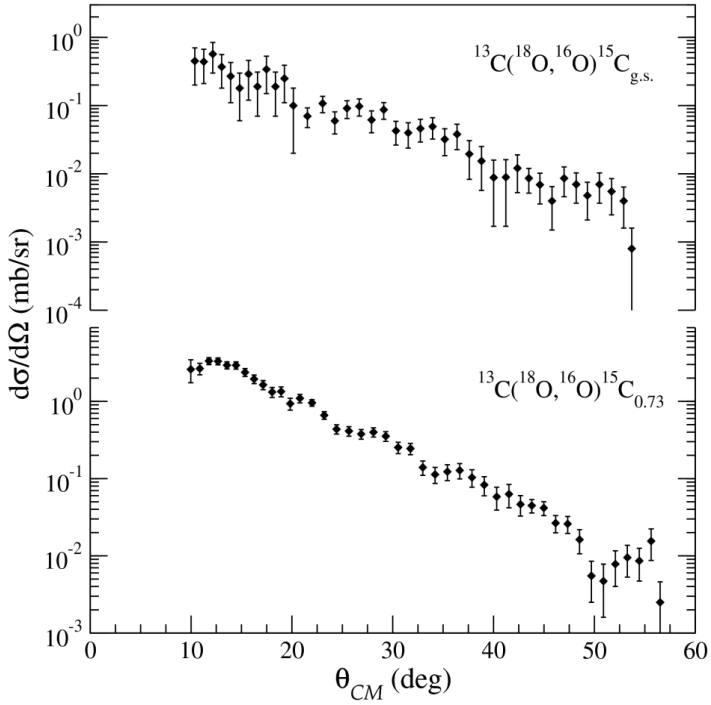

Fig. 6.24. Angular distributions for ^{15}C g.s. and 0.73 MeV state.

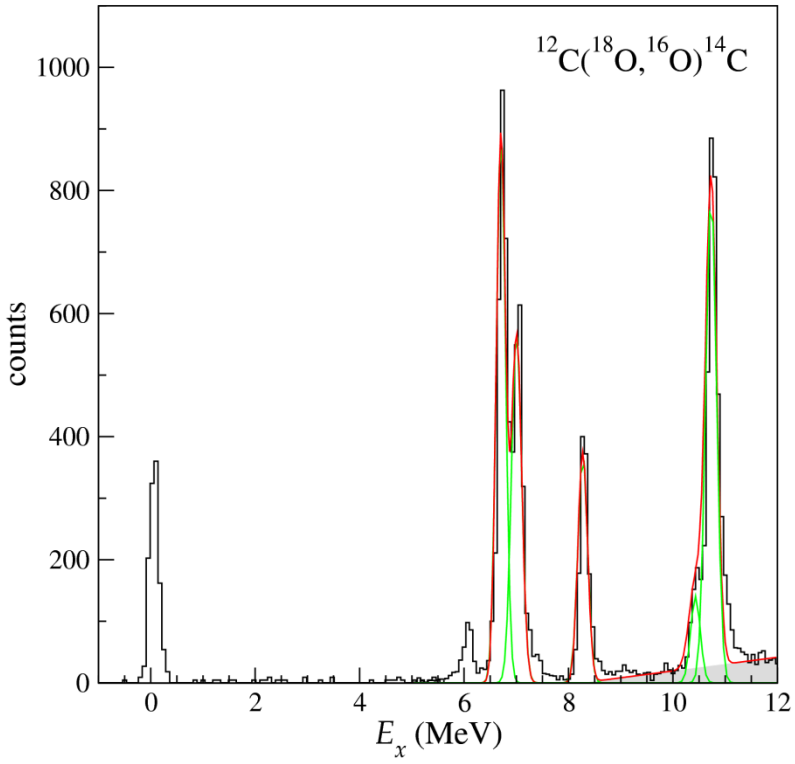

Fig. 6.25. Excitation energy spectra for the $^{12}C(^{18}O,^{16}O)^{14}C$ reaction at 84 MeV incident energy for 9° < θ_{lab} < 10°. The modeled 3-body continuum, the fitted peaks and the sum of them are shown with the grey area, the green Gaussians and the red continuous line, respectively.

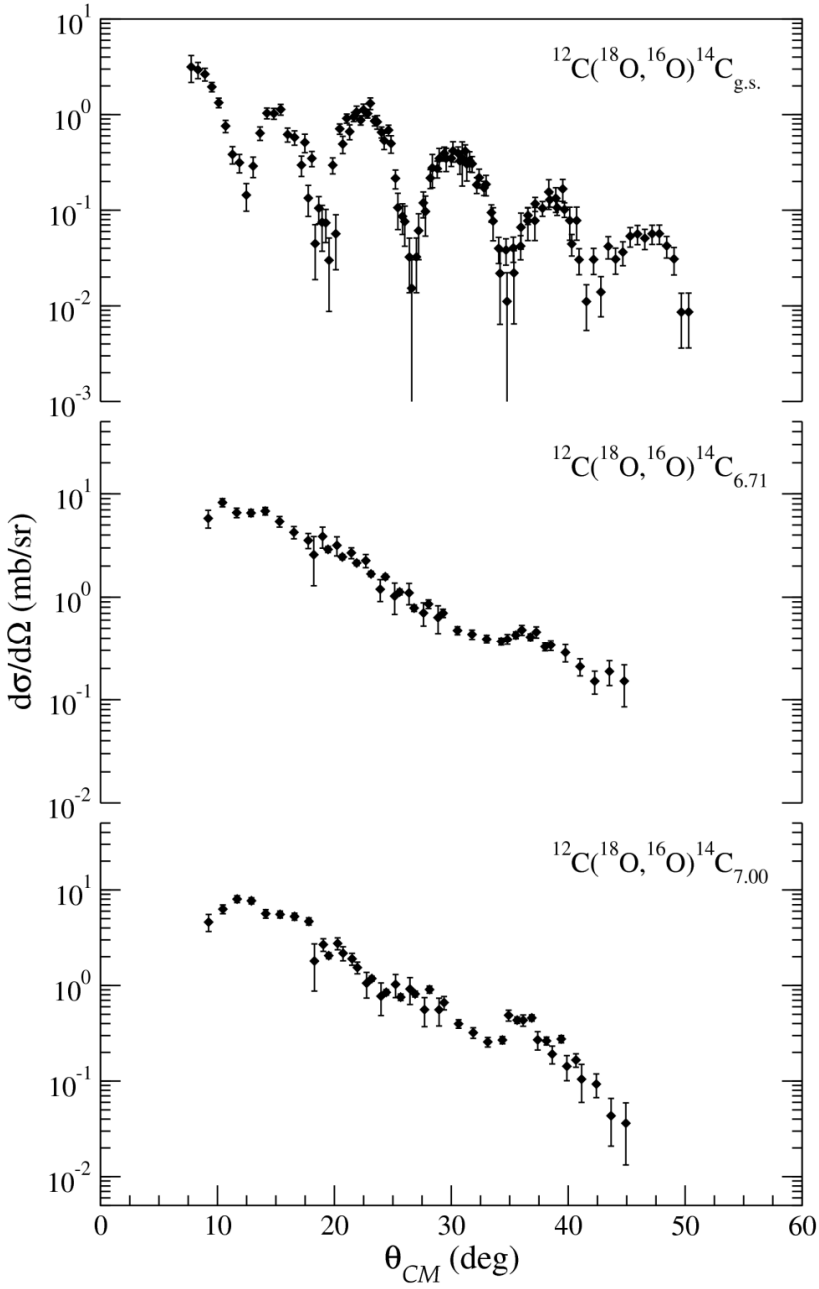

Fig. 6.26. Angular distributions for ^{14}C transitions to the g.s. and to 6.71 and 7.00 MeV states.

6.7.2 Narrow resonant states

In the energy region above the one-neutron emission threshold, a continuous background is present in the spectra coming from three-body reactions. The background associated to the $^{13}C(^{18}O,^{16}O)^{14}C + n$ channel in the ^{15}C spectrum and to $^{12}C(^{18}O,^{16}O)^{13}C + n$ channel in the ^{14}C one were modeled assuming a non-resonant 3-body phase space in the

exit channel [141], as shown by the grey area in Fig. 6.27 and Fig. 6.25, respectively. After the subtraction of such a background, the extraction of the $N(\theta)$ parameter is the same discussed in the previous Section.

For the ^{15}C case, all the fits were performed in the background subtracted spectra (see Section 6.5). The results are shown in Fig. 6.27. The angular distributions for transitions at E_x = 3.12, 4.21, 4.65, 6.85, 7.36 MeV are shown in Fig. 6.28. The obtained angular distributions for the ^{14}C case are shown in Fig. 6.29 for the transitions at E_x = 8.33, 10.43, 10.73 MeV.

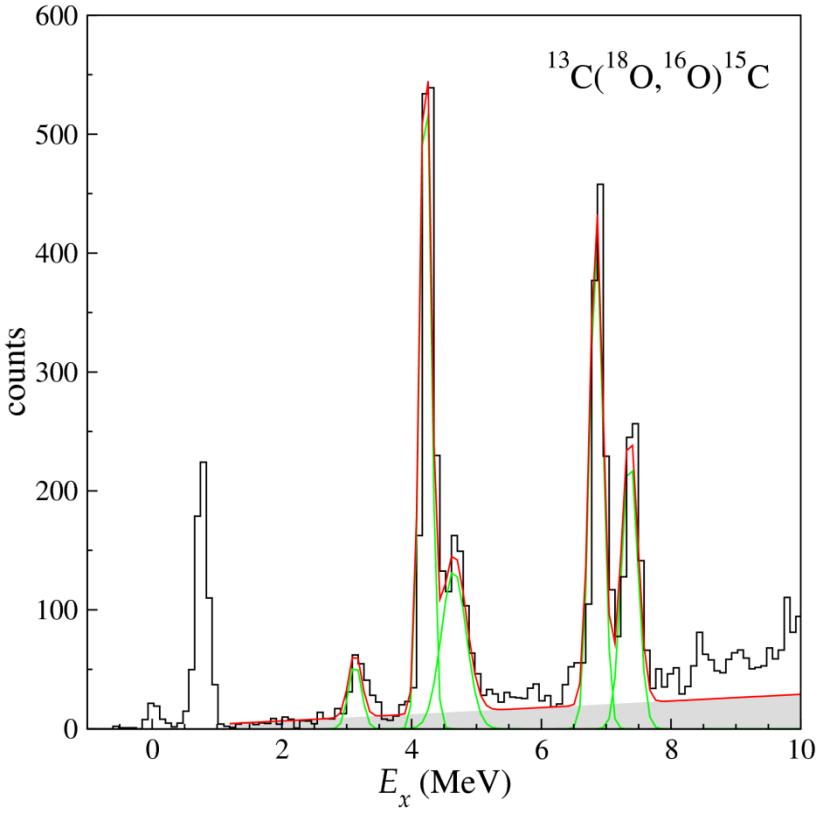

Fig. 6.27. Excitation energy spectra for the $^{13}C(^{18}O,^{16}O)^{15}C$ reaction at 84 MeV incident energy for 9° < θ_{lab} < 10°. The modeled 3-body continuum, the fitted peaks and the sum of them are shown with the grey area, the green Gaussians and the red continuous line, respectively.

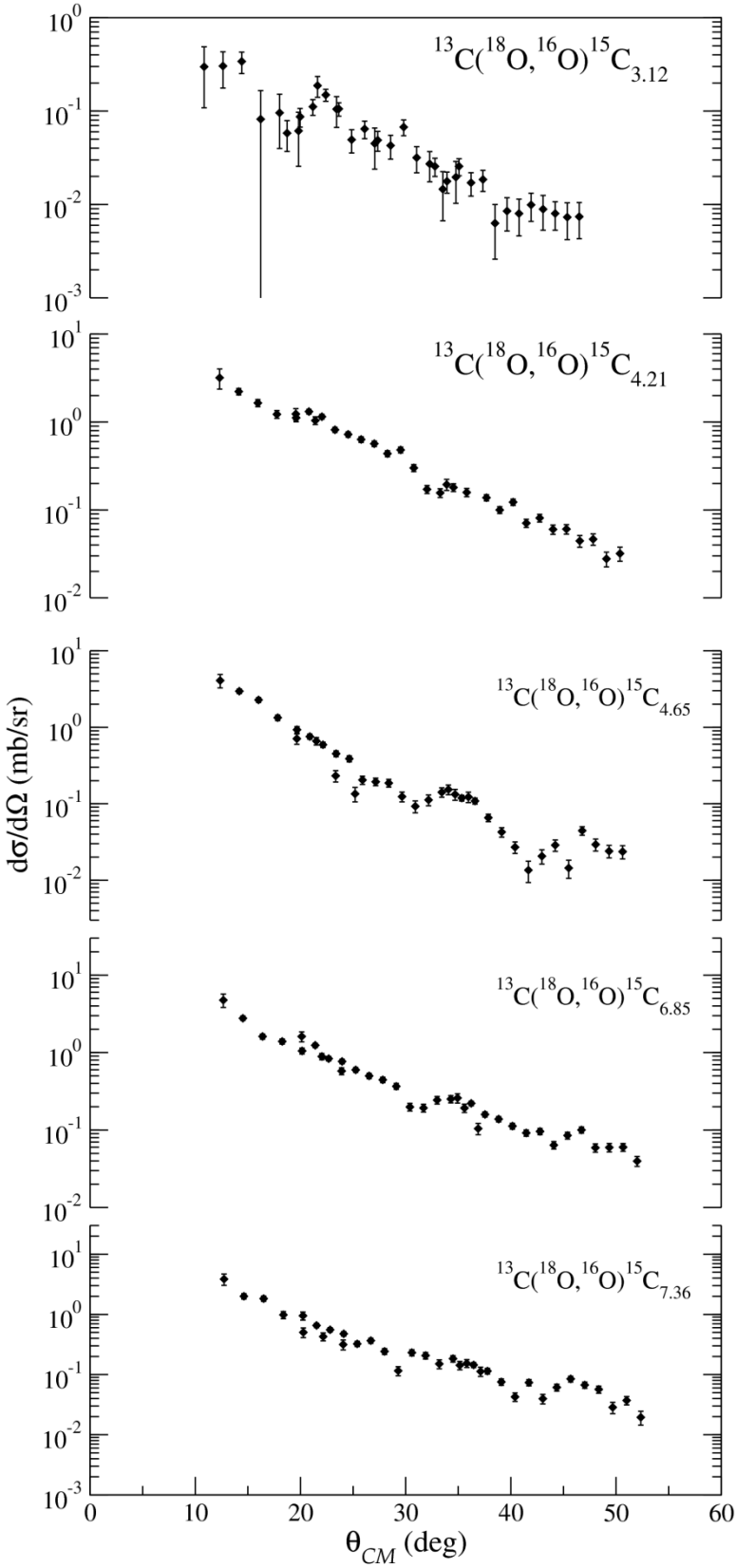

Fig. 6.28. Angular distributions for ^{15}C transitions to 3.12, 4.21, 4.65, 6.85 and 7.36 MeV states.

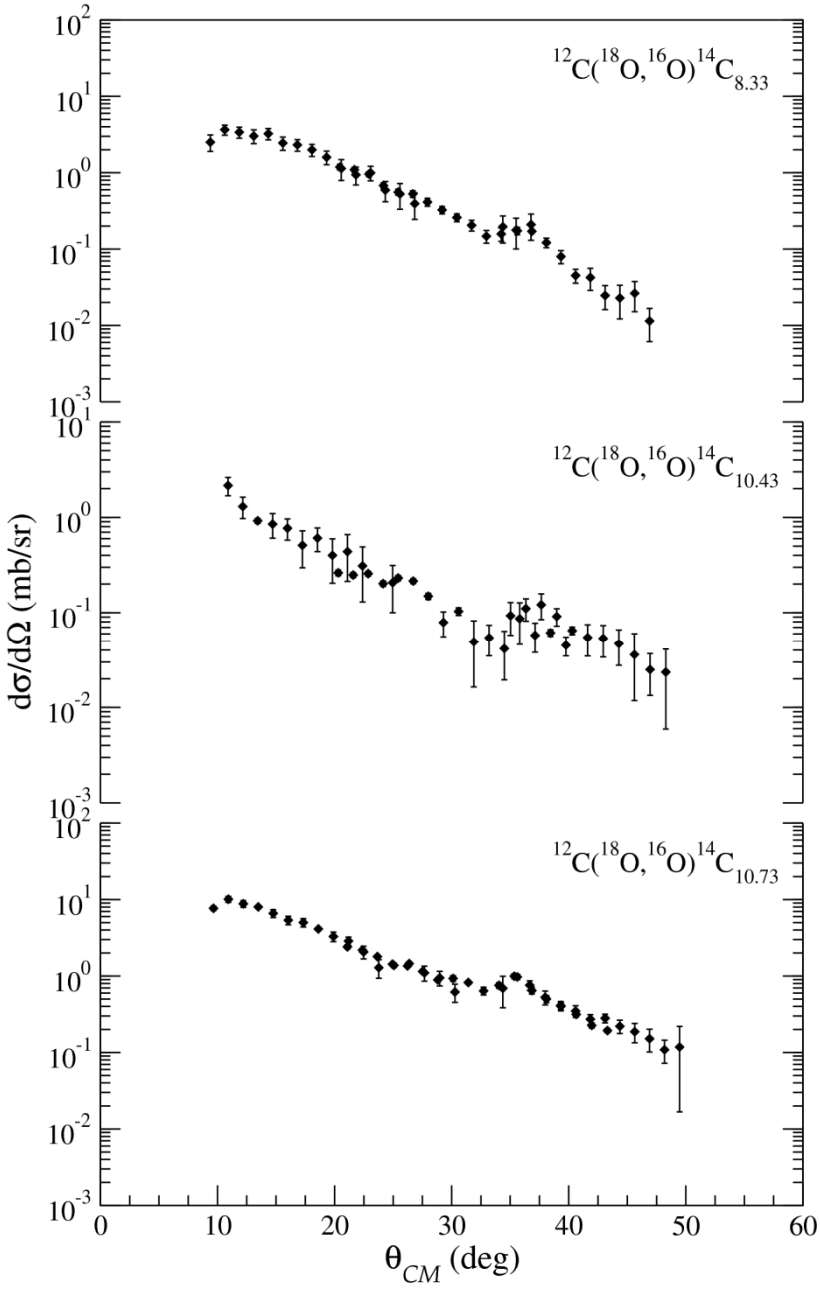

Fig. 6.29. Angular distributions for ^{14}C transitions to 8.33, 10.43 and 10.73 MeV states.

6.7.3 Bumps in the continuum

The cross section angular distributions for the wide structures observed above the two-neutron emission threshold were also extracted. In such cases the chosen angular bin was $\Delta\theta_{lab}$ = 1°, since the statistics was lower with respect to the narrow peaks cases. For the bumps at E_x = 10.5 and 13.7 MeV in the ^{15}C spectrum, the contribution to the angular

distributions due to the continuous background in the spectra was estimated at each angle by a least-squared approach with a Gaussian model shape superimposed on a linear background as shown in Fig. 6.30. This background model is confirmed by two-neutron break-up calculations, as described in Section 8.2. The resulting angular distributions are shown in Fig. 6.31.

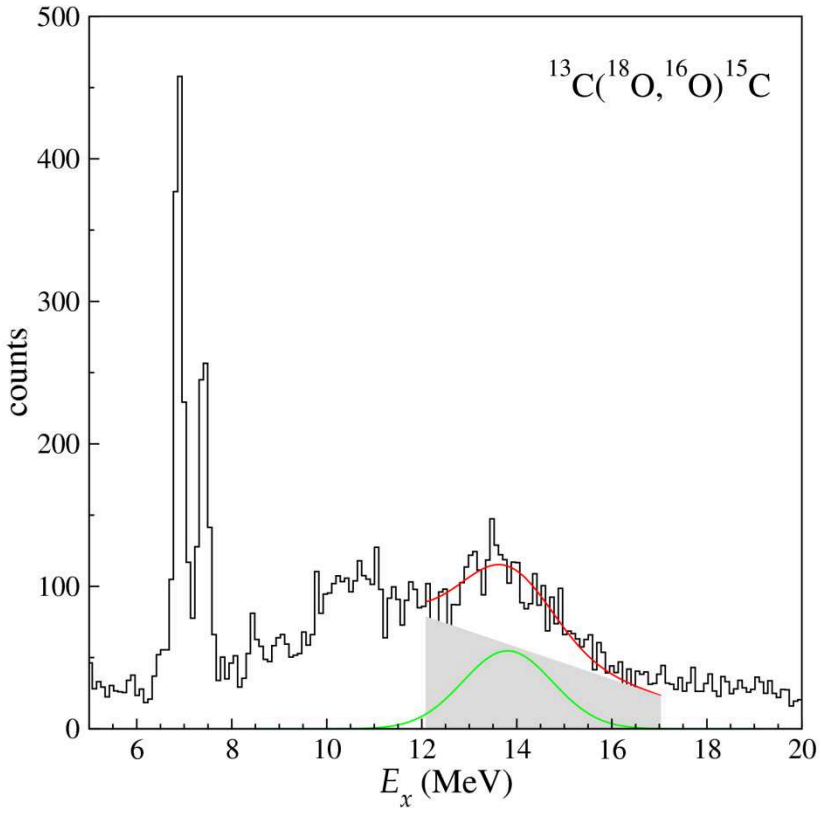

Fig. 6.30. Excitation energy spectra for the $^{13}C(^{18}O,^{16}O)^{15}C$ reaction at $9° < \theta_{lab} < 10°$. The modeled 3-body continuum, the fitted peak and the sum of them are shown with the grey area, the green Gaussian and the red continuous line, respectively.

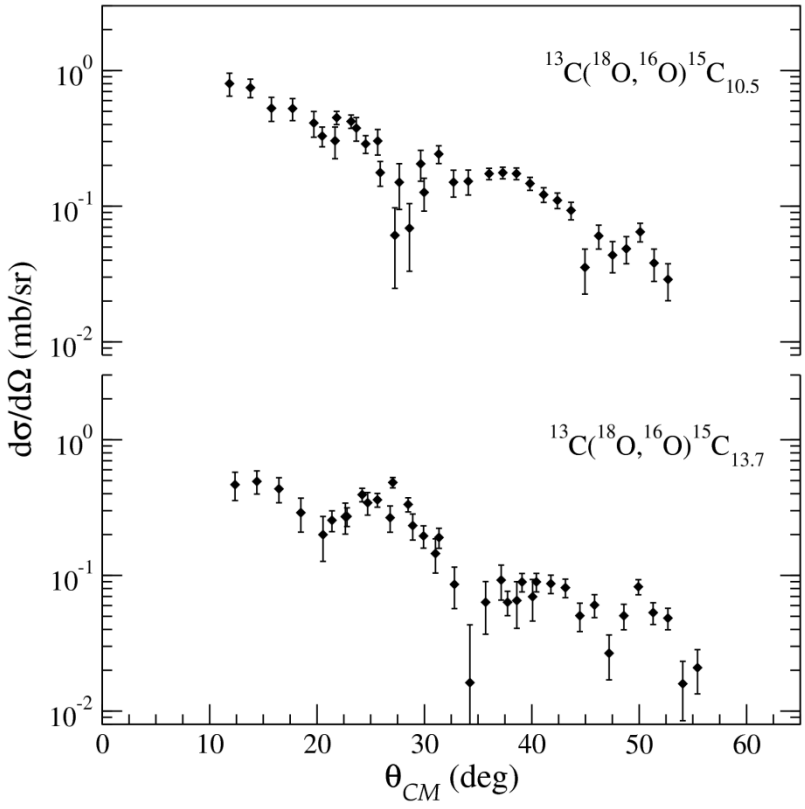

Fig. 6.31. Angular distributions for ^{15}C transitions to the bumps at 10.5 and 13.7 MeV.

For the bump at E_x = 16.9 MeV in ^{14}C a one-Gaussian plus a linear background was used to extract $N(\theta)$. In order to account for possible contamination from the known narrow resonances at E_x = 16.43 and 16.72 MeV, a three-Gaussian model was also used, assuming the same background underneath (see Fig. 6.32). The results were the same within the quoted error bars, thus demonstrating that the contribution from these resonances is negligible. The resulting angular distribution is shown in Fig. 6.33.

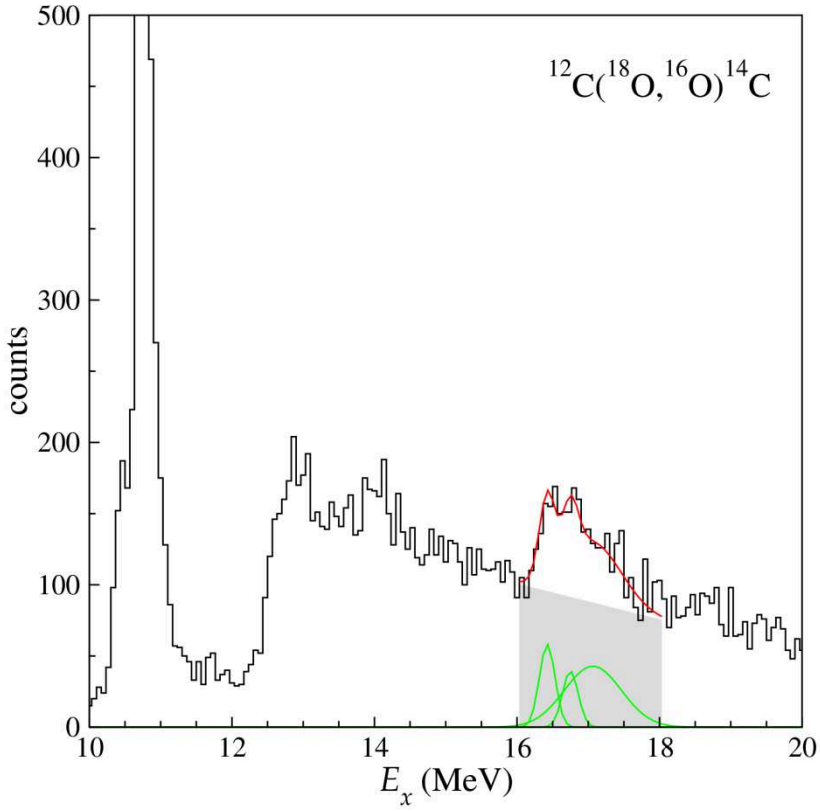

Fig. 6.32. Excitation energy spectra for the $^{12}C(^{18}O,^{16}O)^{14}C$ reaction at $9° < \theta_{lab} < 10°$. The modeled 3-body continuum, the fitted peaks and the sum of them are shown with the grey area, the green Gaussians and the red continuous line, respectively.

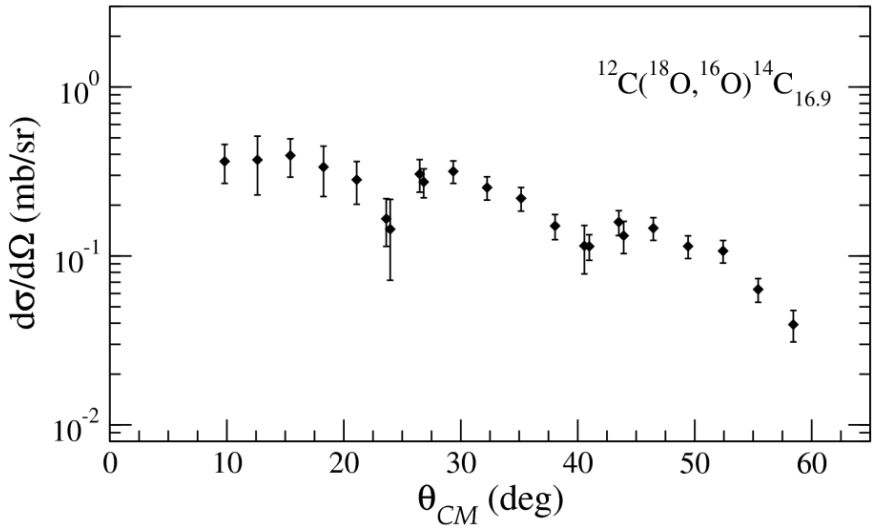

Fig. 6.33. Angular distributions for ^{14}C transition to the bump at 16.9 MeV.

6.7.4 Estimation of the cross section uncertainties

The cross section uncertainties were determined by applying the error propagation on eq. (6.14). The uncertainties on the parameters N_{beam}, N_{target}, $\Delta\Omega$ and ϵ are common to all the points of the angular distribution. They can be regarded as an overall uncertainty of about 10% in the vertical scale shown in the above Figures, which was not included in the error bars. Other sources of uncertainty come from the solid angle determination (~ 2%), the statistical error and the background subtraction, which is the leading term when dealing with the broad bumps in the continuum.

The error on the estimation of the solid angle comes from the determination of θ_i and ϕ_i (see Section 6.7). The error in the determination of ϕ_i, which is of about ± 0.4° [116], corresponds to a common factor for all the angular distribution bins. The θ_i parameter has an uncertainty of ± 0.2°, as demonstrated in ref. [116], and this influences more the bins corresponding to the border of the acceptance. The effect was evaluated considering the variation of the area (shown in Fig. 6.22-b) caused by variation of the θ_i within ± 0.2°.

The error on $N(\theta)$ was extracted from the application of the error propagation on the following formulas

$$\begin{aligned} N_{tot}^{^{15}C} &= N_{^{13}C} - S_{^{12}C}\overline{N}_{^{12}C} - N_{bu} \\ N_{tot}^{^{14}C} &= N_{^{12}C} - N_{bu} \end{aligned} \tag{6.15}$$

which express the most general form used to calculate the number of counts for a transition to states of the ^{15}C and ^{14}C nuclei. For the ^{15}C case, $N_{^{13}C}$ represent the total counts, $S_{^{12}C}\overline{N}_{^{12}C}$ is the background due to ^{12}C impurities in the ^{13}C target and N_{bu} is the break-up background. The terms relative to the ^{14}C case have analogous meaning.

The number of counts $N_{^{13}C}$ and $N_{^{12}C}$ were evaluated calculating the area (A) of the corresponding Gaussian function fit, given by

$$A = \sqrt{2\pi}h\sigma \tag{6.16}$$

where h and σ are the height and standard deviation, respectively.

The propagation of error law applied to eq.s (6.15) gives

$$\Delta N_{tot}^{^{15}C} = \sqrt{\left(\frac{\partial N_{tot}}{\partial N_{^{13}C}}\right)^2 \left(\Delta N_{^{13}C}\right)^2 + \left(\frac{\partial N_{tot}}{\partial S_{^{12}C}}\right)^2 \left(\Delta S_{^{12}C}\right)^2 + \left(\frac{\partial N_{tot}}{\partial \bar{N}_{^{12}C}}\right)^2 \left(\Delta \bar{N}_{^{12}C}\right)^2 + \left(\frac{\partial N_{tot}}{\partial N_{bu}}\right)^2 (\Delta N_{bu})^2}$$
$$\Delta N_{tot}^{^{14}C} = \sqrt{\left(\frac{\partial N_{tot}}{\partial N_{^{12}C}}\right)^2 \left(\Delta N_{^{12}C}\right)^2 + \left(\frac{\partial N_{tot}}{\partial N_{bu}}\right)^2 (\Delta N_{bu})^2} \quad (6.17)$$

Considering that the error on the estimation of $N_{^{13}C}$ and $N_{^{12}C}$ is dominated by the error on the Gaussian height, since the σ parameter was fixed in each fit, and the statistical error is dominant for the estimation of $\Delta\bar{N}_{^{12}C}$ ($\Delta N = \sqrt{N}$), eq.s (6.17) becomes

$$\Delta N_{tot}^{^{15}C} \approx \sqrt{\sqrt{2\pi}\sigma\Delta h + \bar{N}_{^{12}C}^2 \left(\Delta S_{^{12}C}\right)^2 + S_{^{12}C}^2 \bar{N}_{^{12}C} + (\Delta N_{bu})^2}$$
$$\Delta N_{tot}^{^{14}C} \approx \sqrt{\sqrt{2\pi}\sigma\Delta h + (\Delta N_{bu})^2} \quad (6.18)$$

where $\Delta S_{^{12}C}$ and ΔN_{bu} are the errors on the evaluation of the normalization coefficient $S_{^{12}C}$ and of the break-up background, respectively. The former can be calculated by applying the propagation of error law to Eq. (6.12):

$$\Delta S_{^{12}C} \approx \frac{\sqrt{\bar{N}_{^{13}C}}}{\bar{N}_{^{12}C}} \sqrt{1 + \frac{\bar{N}_{^{13}C}}{\bar{N}_{^{12}C}}} \quad (6.19)$$

As regards the error on the determination of the break-up background ΔN_{bu}, it was found to be dominated by the statistical error on the total integral.

For certain transitions the determination of N_{tot} contains less term than eq.s (6.15) and consequently the propagation of errors is simpler. For example, when considering the bound states of ^{15}C and ^{14}C the only source of error in $N(\theta)$ is the statistical one. Similarly for the other bound states, where the break-up background is missing.

In summary, the cross section were extracted with typical uncertainties of about 10-20%, which is enough to learn about details of the reaction mechanism, as discussed in the following Chapters.

Chapter 7

Data analysis: the reaction mechanism

The present Chapter is devoted to the analysis of the reaction mechanism of the $^{12}C(^{18}O,^{16}O)^{14}C$ and $^{13}C(^{18}O,^{16}O)^{15}C$ transfer reactions at 84 MeV incident energy. An important issue when dealing with two-neutron transfer reactions is that the direct one-step transfer of a correlated pair and the transfer of uncorrelated neutrons by two-step mechanisms contribute coherently to the observed cross section [5]. From a spectroscopic point of view, the former only allows the excitation of pair modes in the residual nucleus, where the two neutrons cluster together with an intrinsic angular momentum *S* orbiting around the core with an angular momentum *L* (*L-S* coupling). On the other hand, the uncorrelated transfer is more effective in exciting configurations where each neutron independently couples with the core with an angular momentum *j* (*j-j* coupling). As a consequence, selecting experimental conditions of dominance of the correlated transfer is helpful in understanding the nature of the pairing correlations in nuclei.

In this context, the relative importance of the one-step pair transfer and the sequential uncorrelated transfer of the two neutrons in the ($^{18}O,^{16}O$) reaction were evaluated. This was done studying some particular observables described in the present Chapter. First, the transfer yields of different reaction channels (inelastic, one- and two-neutron transfer) were extracted, as reported in Section 7.1. Then, a comparison between the ^{14}C energy spectra populated via the $^{13}C(^{18}O,^{17}O)^{14}C$ and the $^{12}C(^{18}O,^{16}O)^{14}C$ reactions was done, as described in Section 0. Finally, DWBA and CRC calculations of the cross section angular distributions were performed, as discussed in Section 7.3. The results emerging from such analysis indicate the dominance of a correlated transfer of the two neutrons.

7.1 Transfer yields

In order to highlight the relative importance of the different reaction channels it is useful to compare the yields of the corresponding ejectiles. In this context, the comparison between the ^{16}O (two-neutron transfer), ^{17}O (one-neutron transfer) and ^{18}O (inelastic scattering) production yields from the $^{18}O + ^{13}C$ and $^{18}O + ^{12}C$ collisions was done. This was possible thanks to the clear identification of the different Oxygen isotopes by the particle identification procedure described in Section 6.2 (see Fig. 6.11).

In order to retrieve the transfer yields, events relative to the continuum background (coming from break-up) were discarded. This was done looking at the excitation energy spectra obtained applying the ray-reconstruction technique to each reaction channel. The continuum background was modeled and subtracted, as described in Section 6.7. the yields of the different oxygen ions were then calculated from the integration of the resulting spectra. The obtained values relative to the $^{18}O + ^{12}C$ and $^{18}O + ^{13}C$ collisions are found to be very similar each other, as listed in Table 7.1. If the sequential transfer of the two neutrons is dominant a transition amplitude given by the product of two independent terms is expected. Consequently, the experimental two-neutron transfer yield should be much lower than the measured one. This is normally found in literature for multi-nucleon transfer reactions induced by heavy ions [5]. In fact, suppression factors of at least 3 are found in the two-neutron transfer yields with respect to the one-neutron ones in agreement with semi-classical calculations based on uncorrelated transfer of neutrons.

Table 7.1. Yields of ^{16}O, ^{17}O and ^{18}O isotopes for $^{18}O + ^{12}C$ and $^{18}O + ^{13}C$ collisions.

Reaction	**Inelastic** (^{18}O) (counts × 10^5)	**1*n*-transfer** (^{17}O) (counts × 10^5)	**2*n*-transfer** (^{16}O) (counts × 10^5)
$^{18}O + ^{12}C$	1.694 ± 0.006	0.950 ± 0.005	0.924 ± 0.005
$^{18}O + ^{13}C$	1.869 ± 0.007	1.284 ± 0.007	0.814 ± 0.006

The yield values reported in Table 7.1 indicate a striking result: in the $^{18}O + ^{12}C$ the two-neutron removal process appears as probable as the one-neutron removal one and in the $^{18}O + ^{13}C$ a small suppression factor of ~1.6 is found. The inelastic channel is a little higher than the other two. This finding suggests that in the (^{18}O,^{16}O) reaction there is a

relevant contribution from the correlated transfer of the neutron pair at least at the energies investigated in this work.

7.2 The ^{14}C spectrum via one- and two-neutron transfer

In order to study the selectivity of the (^{18}O, ^{16}O) reaction, it is interesting to compare the ^{14}C spectra populated via the two- and one-neutron transfer. The latter was obtained selecting the ^{17}O ejectiles in the ^{18}O + ^{13}C collisions. The reconstructed ^{14}C energy spectra from the ^{13}C(^{18}O,^{17}O) and ^{12}C(^{18}O,^{16}O) reactions are shown in Fig. 7.1. The two spectra shown have very different features. In the spectrum corresponding to the (^{18}O,^{17}O) reaction (top panel of Fig. 7.1), peaks connected to the ^{17}O ejectile excitation are identified. These (marked with ^{1}, ^{2} and ^{3} in Fig. 7.1) present a sensibly larger width than those corresponding to the $^{17}O_{g.s.}$ due to the Doppler broadening associated to the in-flight γ-decay [142].

The ^{14}C spectrum populated via the (^{18}O,^{17}O) reaction (top panel of Fig. 7.1) is very similar to those obtained in the ^{13}C(d,p)^{14}C reactions, reported in Section 4.3, and a pure single particle picture of the populated ^{14}C states can explain its structure. For example, the coupling of the $p_{1/2}$ hole in the $^{13}C_{g.s.}$ with the *sd* neutron orbitals generates well defined 1*p*-3*h* doublets with respect the ^{16}O vacuum (see note 1 p. 60). The most excited one is the 3^-, 2^- at 6.71 and 7.36 MeV, respectively, with $|\left[\left(^{13}C_{g.s.}\right)^{1/2^-} \otimes \left(1d_{5/2}\right)_\nu^{5/2^+}\right]^{2^-,3^-}\rangle$ single particle configuration. On the contrary, states with well known dominant configuration of two neutrons in the *sd*-shell coupled with a ^{12}C core, such as the 2^+ 8.33 MeV and the 4^+ 10.73 MeV states [88] [89] [97] are very weakly populated. Considering the (^{18}O,^{17}O) reaction, these states can be excited only by a two-step mechanism in which a transfer of the neutron to the *sd*-shell plus a promotion of the $p_{1/2}$ neutron of the $^{13}C_{g.s.}$ to the same shell happen. The low population of these states indicates that the two-step mechanism is suppressed in the (^{18}O,^{17}O) reaction.

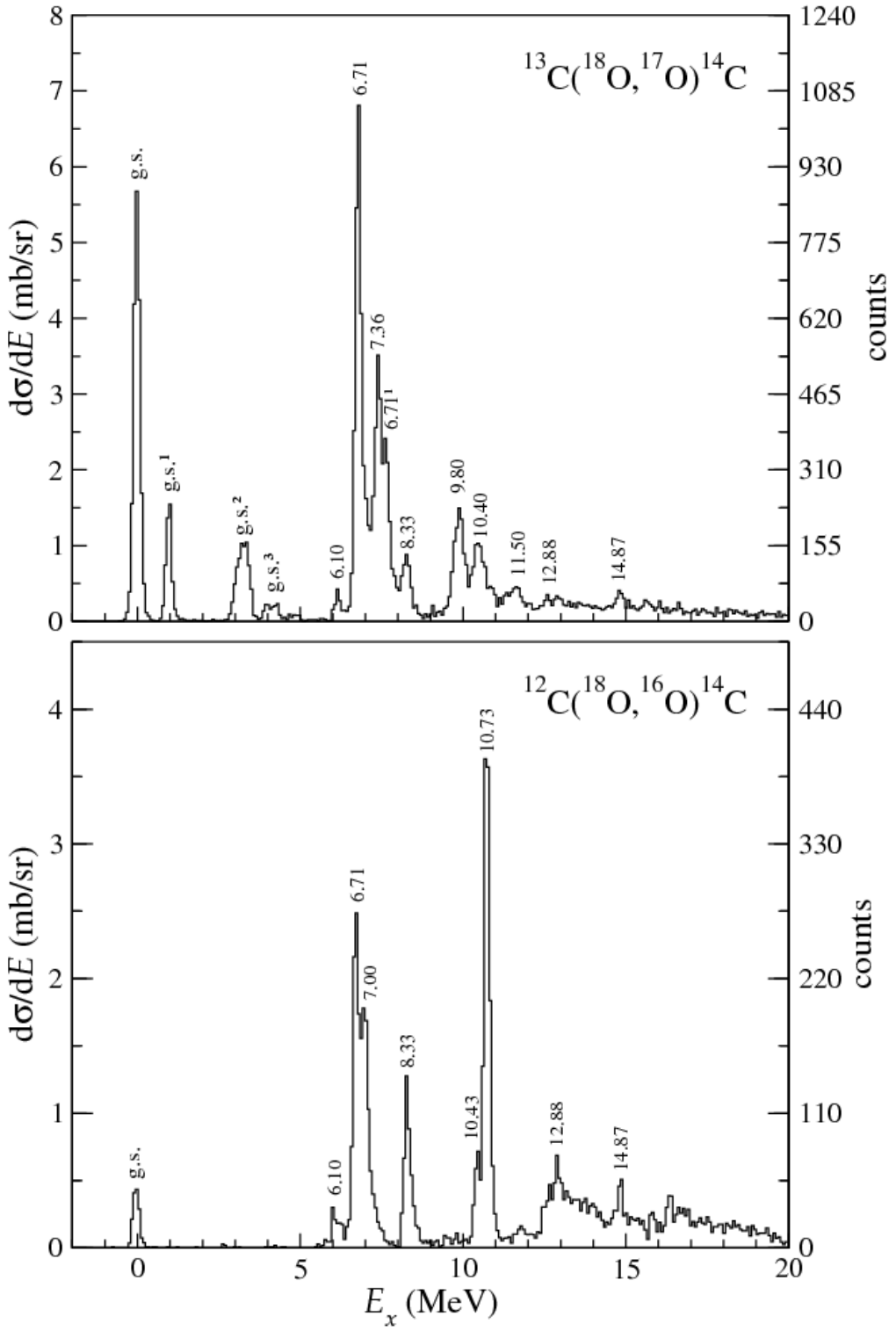

Fig. 7.1. ^{14}C energy spectra for the one- (top panel) and two- (bottom panel) neutron transfer reactions induced by the ^{18}O at 84 MeV for $3° < \theta_{lab} < 5°$. In the top panel the peaks marked with [1], [2] and [3] represent the transition to the excited states of ^{17}O ejectiles at 0.87, 3.06, 3.84 MeV, respectively. For the definition of the differential cross section scale ($d\sigma/dE$) see eq. (8.8).

On the other hand, the ^{14}C spectrum obtained via the (^{18}O,^{16}O) reaction (bottom panel of Fig. 7.1) shows the population of the same states strongly excited in the ^{12}C(t,p)^{14}C reactions, as reported in Section 4.4.2. Indeed, both of them can be described as a two-neutron cluster coupled to the ^{12}C core. For example, the 4^+ 10.73 MeV state in the strong coupling scheme (*L-S* coupling) is described as a main configuration of a cluster of neutrons with $L = 4$ [88] [89]. The possible description of this state in the weak coupling model (*j-j* coupling) as stretched configurations in the $n + n + {}^{12}$C system [17] is not very appropriate at least at the studied low incident energies near the Coulomb barrier. The three 2^+ states at 7.00, 8.33 and 10.43 MeV are rather strong populated in the present two-neutron transfer as well as in the (t,p) reactions [89] and very weakly or not observed in the (^{18}O,^{17}O) nor in the (d,p) reaction [97]. Indeed, these states are known to be strongly mixed with major configuration of two neutrons in the *sd*-shell [88]. As regarding the 12.88 and 14.87 MeV states, already observed in (t,p) and other two-neutron transfer reactions and well populated in the present case, a core excited configuration with the ^{12}C(2^+) state is proposed in ref. [88].

The strongest evidence of the dominance of the direct one-step transfer in the (^{18}O,^{16}O) reaction can be found in the behavior of the previous mentioned 3^-, 2^- doublet at 6.71 and 7.36 MeV. In the weak coupling model, the doublet is predicted to be populated with comparable strength in a two-neutron transfer reaction as a result of a two-step mechanism [17]. Differently, the assumption made in the *L-S* model of a relative *S* state for the two neutrons implies a parity transfer of $(-1)^L$ and hence forbids a 2^- state. Thus, in a one-step transfer of a pair of neutrons with intrinsic spin $S_{2n} = 0$, isospin $T_{2n} = 1$ and orbital angular momentum $L = 3$ respect to the ^{12}C(0^+) core, only the population of the natural parity 3^- state is allowed. In the spectrum relative to the (^{18}O,^{16}O) reaction, shown in Fig. 7.1 the natural parity state at 6.71 MeV is well excited whereas the 2^- state at 7.36 MeV is very weakly populated, thus confirming the existence of a strong coupling and the direct one-step nature of the transfer to such states.

7.3 DWBA and CRC calculations

As mentioned in Section 2.6, the optical model plays a central role in the description of heavy-ion collisions, since it is extensively used in studies concerning the elastic scattering process as well as in more complicated reactions through the DWBA or coupled-channel formalisms (CRC) [3]. The latter are widely used in the description of transfer reactions between heavy nuclei. The first order DWBA gives satisfactory results wherever the reaction mechanism is predominantly one-step. Nevertheless, since the transfer process usually involves multi-step routes, more refined approaches must be developed. In principle a complete treatment of the transfer process should contain a description of: (i) the one-step channel (transition between the partitions $\alpha \rightarrow \beta$) with the inclusion of all the possible inelastic excitations of the target, projectile, ejectile or residual nucleus (see Fig. 7.2-a); (ii) the sequential channel, with the inclusion of intermediate partitions γ (see Fig. 7.2-b) and (iii) the non-orthogonal term deriving from the limited model space used in actual calculations in both the (i) and (ii) approaches (see Section 7.3.3). However, such kind of model is still not available in the state of the art theory.

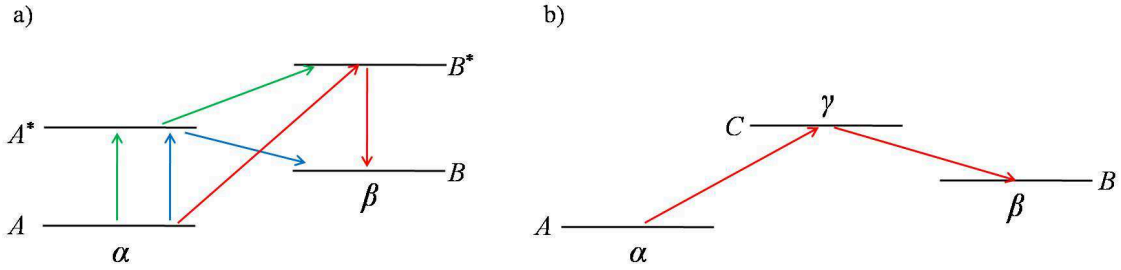

Fig. 7.2. Schematic representation of some multi-step transfer processes. The one-step channel with the inclusion of inelastic excitations (a) and the sequential channel (b) are drawn.

As mentioned in Section 2.8, a possible way to describe the two-neutron transfer reactions is the second order DWBA approach, recently applied in ref. [80][82] to calculate the absolute differential cross sections for the reactions $^{A}Sn(p,t)^{A-2}Sn_{g.s.}$. This kind of calculations does not take into account the inelastic excitations of the involved nuclei, which are relevant routes when considering heavy-ion induced reactions. For instance, in ref. [87] the $^{74}Ge(^{18}O,^{16}O)^{76}Ge$ and $^{76}Ge(^{16}O,^{18}O)^{74}Ge$ reactions were studied in terms of exact finite-range (EFR) coupled-channel Born approximation (CCBA). It was found that

the excitation of the $^{18}O^{*}$ 2^{+} state at 1.98 MeV has to be included in the CCBA analysis in order to reproduce the experimental angular distributions for the transitions to $^{76}Ge_{g.s.}$ and $^{74}Ge_{g.s.}$. In such cases, where inelastic excitations are strong, it is necessary to include them, and this can be done by replacing the DWBA optical model calculations with coupled-channels calculations.

In the past, several theoretical difficulties limited the correct description of heavy-ion induced transfer reactions. For example, the standard technique to extract the optical potential from fits of elastic scattering angular distributions fails in reproducing the transfer differential cross section [143][144]. Moreover, the finite size of nuclei and the recoil effects are relevant in heavy-ion reactions and must be taken into account [145][146]. Computational problems have historically limited the successful calculation of finite range form factors in multi-nucleon transfers. Due to the mentioned uncertainties, even the most successful calculations based on the CCBA required the use of scaling factors or *unhappiness factors*, always larger than 1 and even as high as hundreds, to reproduce the absolute cross section, whose origin has not been really clarified so far [87][147].

In this thesis work, the transitions to low lying states of the residual nucleus for the $^{12}C(^{18}O,^{16}O)^{14}C$ reaction are described for the first time within a CRC scheme, with the use of the São Paulo parameter-free double-folding optical potential (SPP) [148][149][150] [151][152]. The contribution of the two-step sequential transfer was also calculated. The obtained results demonstrate again the dominance of the direct transfer of a pair for the investigated reaction and the capability of such a theoretical framework to quantitatively describe the experimental angular distributions. The São Paulo optical potential, a brief description of the CRC formalism and the resulting calculations are described in the following Sections.

7.3.1 The São Paulo parameter-free double-folding optical potential

In general, the complex and energy-dependent optical potential is composed of a bare and a polarization part, the latter containing the contribution arising from non-elastic couplings. In principle, the bare (or nuclear) potential between two heavy ions can be associated with the Coulomb plus strong nucleon-nucleon interaction folded into a product of the nucleon densities of the nuclei [153].

The double-folding potential has the form [151]

$$V_F(\quad) = \int \rho_1(r_1)\rho_2(r_2)v_{NN}(\boldsymbol{R} - \boldsymbol{r}_1 + \boldsymbol{r}_2)d\boldsymbol{r}_1 d\boldsymbol{r}_2 \tag{7.1}$$

where R is the distance between the centers of the nuclei, ρ_i are the respective nucleon distributions and $v_{NN}(\boldsymbol{r})$ is the effective nucleon-nucleon interaction. One of the most widely used realistic interaction is known as M3Y [153][154], which is expressed as sums of three Yukawa terms and can usually assume two versions: Reid and Paris.

In its standard formulation, the SPP assumes a wide and systematic dataset of nuclear densities, deduced from Hartree-Fock-Bogoliubov (HFB) calculations and experimental scattering data [151] and accounts for the Pauli non-locality (PNL) due to the exchange of identical nucleons among the colliding systems. The latter term is found to be equivalent to a velocity-dependent nuclear interaction. In fact, the potential is usually expressed in the local equivalent (LE) version as

$$V_{LE}(R, E) = V_F(R)e^{-\frac{4v^2(R)}{c^2}} \tag{7.2}$$

where $V_F(R)$ is the double-folding potential (7.1) and the exponential term is the local velocity ($v(R)$) dependent correction for PNL, which determines an effective velocity dependent scaling.

As discussed in ref. [152] for stable nuclei, the imaginary potential is able to account for the average effect of the dissipative processes as well as for the coupling to continuum states. It is proportional to the bare SPP with a constant proportionality factor, independently of energy and system

$$W(R) = 0.6 \cdot V_{LE}(R) \tag{7.3}$$

As regards the nuclear densities, in the case of ^{18}O a slightly larger matter diffuseness (0.61 fm) compared to the average one extracted from the systematic (0.56 fm) was found to be a better choice [155][156] and was used for the present calculations.

The SPP used for the cross section calculations of the $^{12}C(^{18}O,^{16}O)^{14}C$ reaction is shown in Fig. 7.3, where the three component are visible: Coulomb potential (V_C), local equivalent potential (V_{LE}) and imaginary part (W).

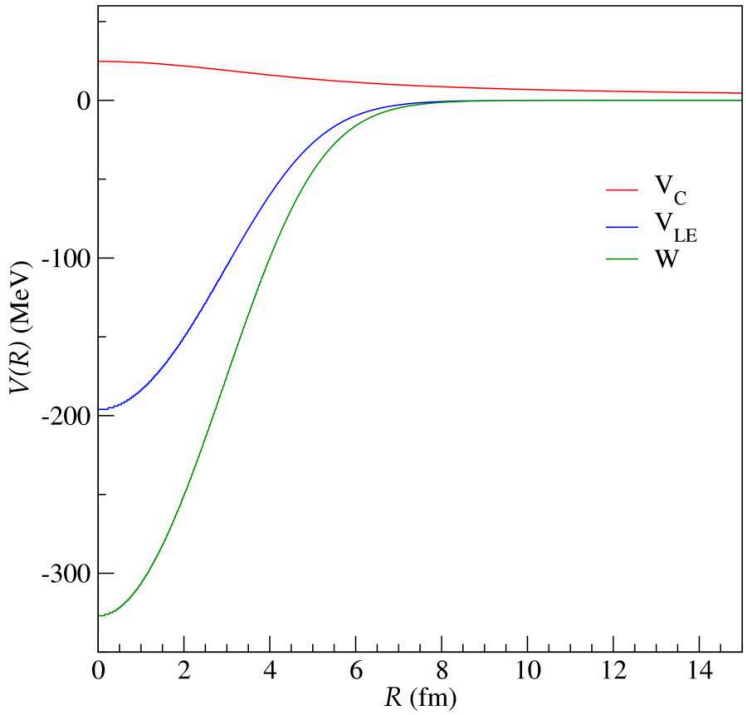

Fig. 7.3. The São Paulo potential. The Coulomb potential (V_C), the local equivalent potential (V_{LE}) and the imaginary part (W) are indicated as a red, blue and green line, respectively.

7.3.2 Coupled Reaction Channels method

The coupled-channels methods consist in solving a relatively small set of coupled equations that results from considering a model wavefunction with a small number of terms. In particular, the CRC method allows to take into account the inelastic transitions involved within the partitions α and β in a transfer reaction. The situation is schematically drawn in Fig. 7.2-a. A complete treatment of the formalism of the CRC method can be found in ref. [3]. In this Section a simple model involving only two terms in the model function is briefly described.

As already mentioned in Section 2.7, the total wavefunction of a system may be expanded in a complete and infinite set of internal states ψ_α for one particular partition α

$$\Psi = \sum_{\alpha} \xi_{\alpha}(\boldsymbol{r}_{\alpha})\psi_{\alpha}(x_{\alpha}) \tag{2.22}$$

where $\boldsymbol{r}_{\alpha}$ is the channel coordinate for the α partition (see ref. [3] for definition) and x_{α} represents the corresponding internal coordinates. The Hamiltonian of the α partition can be written as $H = H_{\alpha} + K_{\alpha} + V_{\alpha}$, where H_{α} is the sum of the internal Hamiltonians for the two nuclei, K_{α} is the kinetic energy of their relative motion and V_{α} is their mutual interaction. Considering the Schrödinger equation $(E - H)\,\Psi = 0$, multiplying the left by one state among the possible ψ_{α}^{*} and integrating over the internal coordinates x_{α}, the infinite set of coupled equations for the channel functions $\xi_{\alpha}(\boldsymbol{r}_{\alpha})$ is obtained, which have the form

$$[E - \varepsilon_{\alpha} - K_{\alpha} - (\alpha|V_{\alpha}|\alpha)]\xi_{\alpha}(\boldsymbol{r}_{\alpha}) = \sum_{\alpha' \neq \alpha} (\alpha|V_{\alpha}|\alpha')\,\xi_{\alpha'}(\boldsymbol{r}_{\alpha}) \tag{2.23}$$

where the interaction matrix elements are integrals over the internal coordinates x_{α} [3]. In the practical case, the exact wavefunction Ψ is replaced by a model one Ψ_{model}, where the sum over α in (2.22) is truncated to a limited number of terms.

When considering transfer reactions between two partitions α and β, the minimal model wavefunction required consists in just two terms

$$\Psi_{model} = u_{\alpha}(\boldsymbol{r}_{\alpha})\psi_{\alpha}(x_{\alpha}) + u_{\beta}(\boldsymbol{r}_{\beta})\psi_{\beta}(x_{\beta}) \tag{7.4}$$

where the symbol u_{α} instead of ξ_{α} is used, since the model and exact channel functions differ. The corresponding effective Hamiltonian H is such that $(E - H)\,\Psi_{model} = 0$. Considering the two equivalent form of $H = H_{\alpha} + K_{\alpha} + V_{\alpha} = H_{\beta} + K_{\beta} + V_{\beta}$, a pair of coupled equations for u_{α} and u_{β} is obtained

$$\begin{aligned} [(E - \varepsilon_{\alpha}) - K_{\alpha} - (\alpha|V_{\alpha}|\alpha)]u_{\alpha}(\boldsymbol{r}_{\alpha}) &= \left(\psi_{\alpha}|H - E|u_{\beta}\psi_{\beta}\right) \\ \left[(E - \varepsilon_{\beta}) - K_{\beta} - \left(\beta|V_{\beta}|\beta\right)\right]u_{\beta}\left(\boldsymbol{r}_{\beta}\right) &= \left(\psi_{\beta}|H - E|u_{\alpha}\psi_{\alpha}\right) \end{aligned} \tag{7.5}$$

which are integro-differential equations and represent the most simple form of CRC equations. As soon as supplemental states are included in the model function (7.4), the number of coupled equations increases as well. For the present calculations several intermediate states were included in the model, as indicated in Section 7.3.3.

7.3.3 Cross-section calculations

Exact Finite Range (EFR) DWBA and CRC cross-section calculations were performed using the São Paulo potential for the $^{12}C(^{18}O,^{16}O)$ transitions to the ^{14}C ground and 8.33 and 10.73 excited states. The calculations were implemented within the FRESCO code [157]. The wave functions, used in the form factor calculations, are generated by a Woods-Saxon shaped potential, whose parameters are given in Table 7.2. The depth of the potential was varied to fit the experimental binding energies for one and two neutrons. The deformation parameters for the collective excitation in the entrance partition were taken from ref. [158]. The EFR, prior, full real remnant approximation was used. The calculations were performed assuming a cluster model in which the two neutrons are paired anti-parallel and coupled to a zero intrinsic angular momentum ($S = 0$) (L-S coupling). The assumed coupling scheme for the one-step two-neutron transfer calculation is shown in Fig. 7.4-a.

Table 7.2. Wood-Saxon potential parameters used for the EFR-CRC calculations. The Coulomb radius (r_c), the depth (V_0), the radius (r_0) and the diffuseness (a_0) are listed.

	^{16}O	^{12}C
r_c (fm)	1.2	1.25
V_0 (MeV)	60.0	60.0
r_0 (fm)	1.20	1.25
a_0 (fm)	0.6	0.65

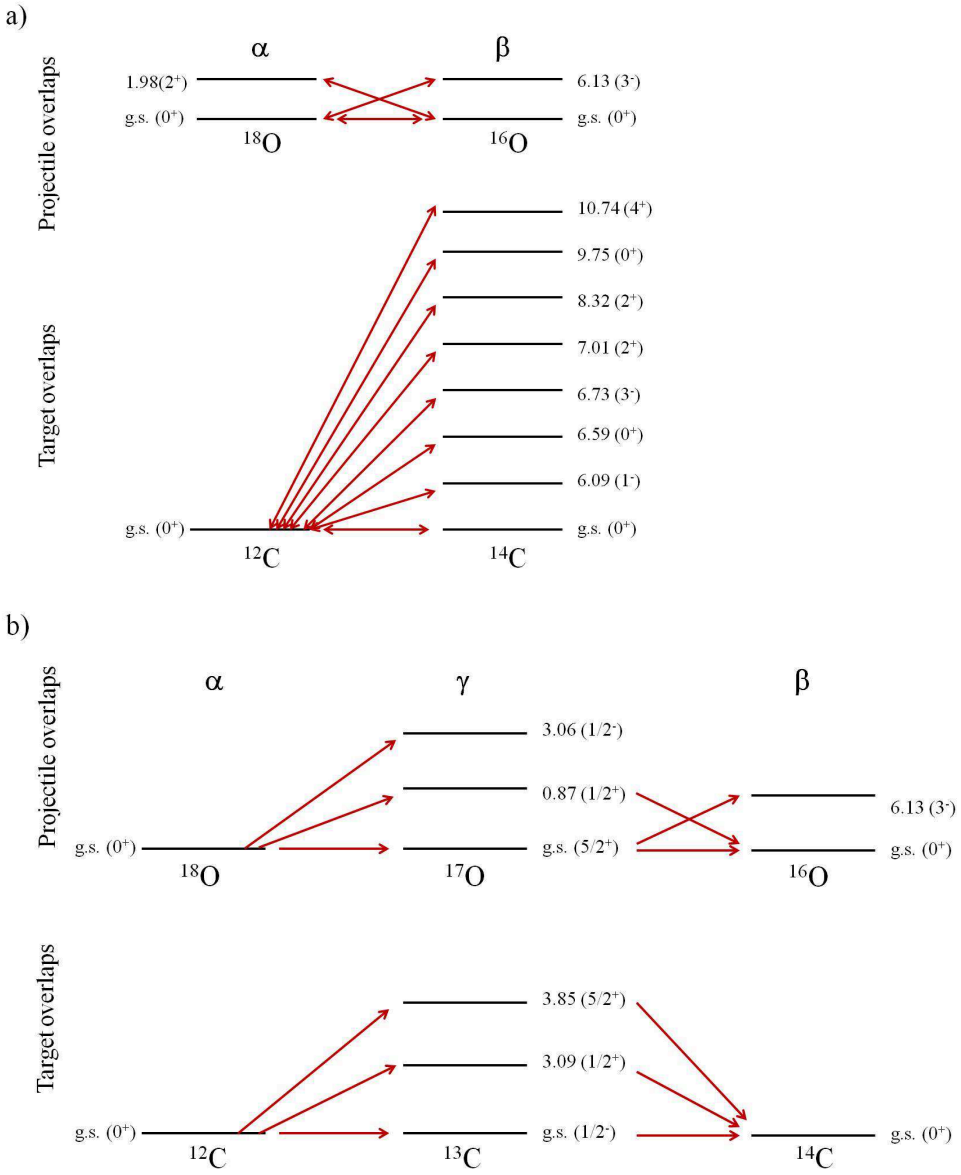

Fig. 7.4. Coupling schemes adopted for the calculations of the one-step (a) and sequential (b) two-neutron transfer.

The experimental and calculated cross-section angular distributions are shown in Fig. 7.5. The transition to the $^{14}C_{g.s.}$ exhibits an oscillating pattern characteristic of the expected $L = 0$ angular momentum transfer. The other transitions, characterized by $L \neq 0$, do not show such pronounced oscillations. Such a phenomenon is typical of heavy-ion transfer reactions near the Coulomb barrier, as mentioned in Section 2.5, and is likely connected to an equal population of the different transferred angular momenta projections M, which are out of phase each other. The $L = 0$ transition contains only one of these components and thus no mixing is possible. The present data confirm this finding. This key feature can be

exploited to clearly disentangle the $L = 0$ mode from the others, by the appearance of the oscillations in the experimental angular distributions. This point is crucial for the GPV identification.

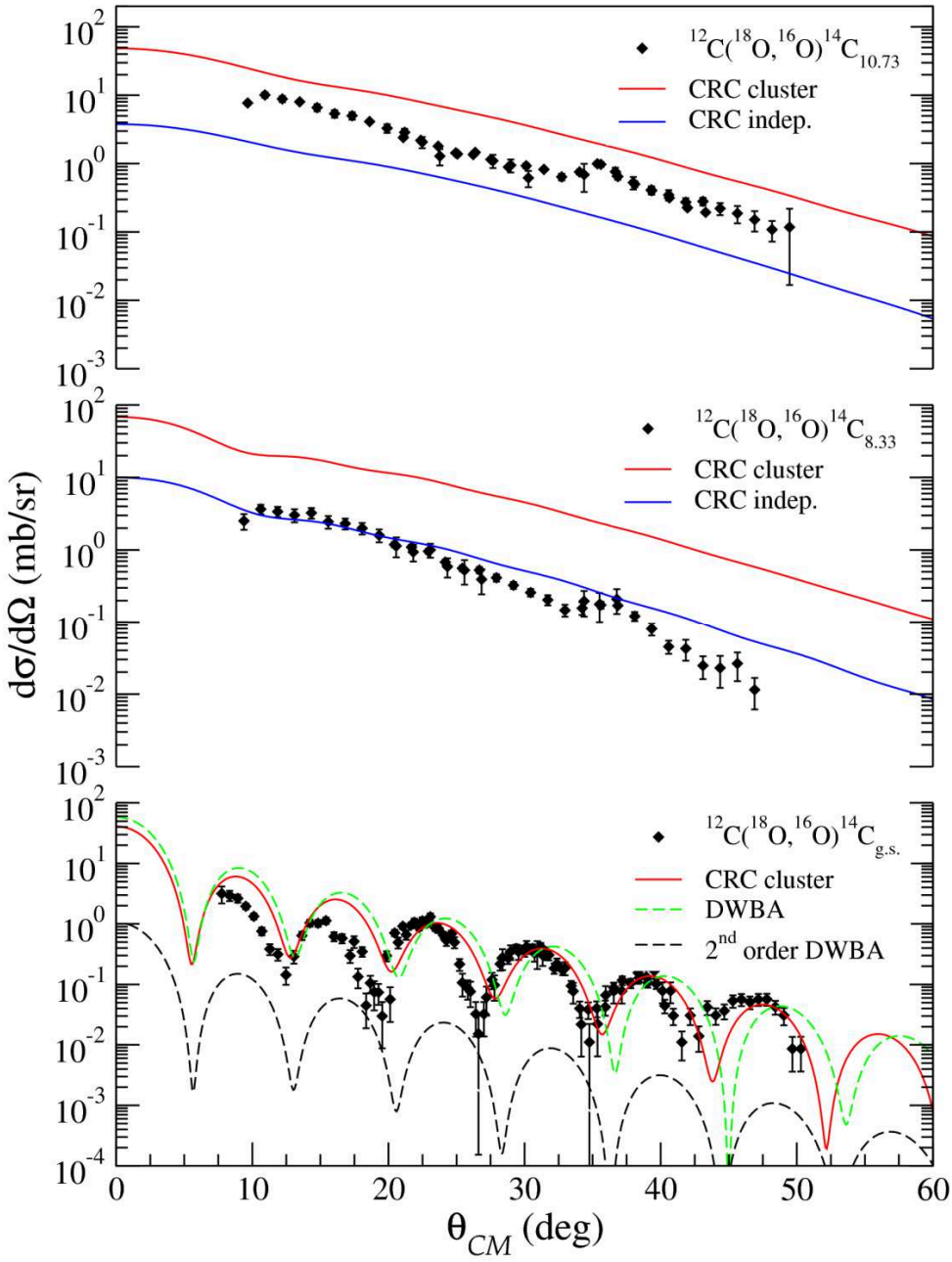

Fig. 7.5. Cross-section angular distributions for the $^{12}C(^{18}O,^{16}O)$ transitions to the ^{14}C ground and 8.33 and 10.73 excited states. The EFR-CRC calculations assuming the cluster model are shown with the red solid line. The one-step DWBA and the sequential DWBA calculations for the $^{14}C_{g.s.}$ are shown with the green and black dashed lines, respectively. The EFR-CRC calculations assuming the independent transfer model are shown with the blue solid line for $^{14}C_{8.33}$ and $^{14}C_{10.73}$ transitions.

Considering the transition to the ground state, the experimental behavior is well reproduced by the performed CRC calculations (red solid line in Fig. 7.5). In particular, both the shape and the absolute value of angular distribution are reproduced without the use of unhappiness factors. One-step DWBA calculations have been also performed, as shown in Fig. 7.5 (green dashed line), and the agreement with the experimental value is good as well. Therefore, it can be inferred that the coupling with the intermediate states of the $^{13}C + ^{17}O$ partition has only a weak influence in such transition. This finding is another signature of the dominance of the one-step channel in the present (^{18}O,^{16}O) reaction.

This is confirmed also when looking at the supplementary two-neutron sequential transfer calculations, which were performed within the two-step DWBA formalism, introducing the intermediate partition $^{13}C + ^{17}O$. The used Wood-Saxon parameters are listed in Table 7.3. The coupling scheme is drawn in Fig. 7.4-b. The results of the two-step sequential transfer calculations (black dashed line in Fig. 7.5) show an identical oscillating pattern as the direct transfer but account only for a negligible contribution (~ 5%) to the absolute cross section.

Table 7.3. Wood-Saxon parameters used for the two-step DWBA calculation. The Coulomb radius (r_c), the depth (V_0), the radius (r_0) and the diffuseness (a_0) are listed. The same parameters relative to the spin-orbit part (V_{SO}, r_{SO}, a_{SO}) are also listed.

	^{17}O	^{16}O	^{12}C	^{13}C
r_c (fm)	1.25	1.25	1.25	1.25
V_0 (MeV)	60.0	60.0	90.0	90.0
r_0 (fm)	1.20	1.20	1.25	1.25
a_0 (fm)	0.6	0.6	0.65	0.65
V_{SO} (MeV)	6.0	6.0	7.0	7.0
r_{SO} (fm)	1.20	1.20	1.25	1.25
a_{SO} (fm)	0.6	0.6	0.65	0.65

Concerning the transitions to the 8.33 and 10.73 MeV resonances, the CRC calculations performed assuming the cluster model (red solid lines in Fig. 7.5) overestimate the cross section. This is due to the probable dominance of one *j-j* component in the adopted cluster wavefunction. Supplemental calculations assuming an independent transfer of the two neutrons were performed (*j-j* coupling), as shown in Fig. 7.5 (blue solid line). Further details are beyond the scope of the present work and will be published elsewhere [159]. It

is worth noticing that both cluster and independent CRC calculations do not show oscillations in the $L \neq 0$ transitions, thus confirming the experimental behavior.

In the described approach, the non-orthogonal term between the α and β partitions is included in the CRC one-step calculations while the sequential cross-section is obtained in DWBA by separate calculations. The sensibly small contribution of this latter gives a justification of such approximated approach.

Chapter 8

Data analysis: GPV evidence

In the present Chapter, an analysis of the measured excitation energy spectra is described. The main purpose is to explain the broad structures observed in ^{14}C and ^{15}C spectra above the two-neutron separation energy, since they do not correspond to anything previously reported. In particular, such strength is found to be concentrated in two wide bumps at 13.7 MeV in the ^{15}C spectrum and at 16.9 MeV in the ^{14}C one.

First, the projectile break-up contribution in the inclusive energy spectra was evaluated. Such calculations are reported in detail in Section 8.2. The break-up channel seems to explain a major part of the high energy excitation region, but the above mentioned bumps are not described.

In order to shed light on such structures, QRPA calculations were performed for analyzing the 0^+ excitations in the ^{14}C energy spectra. The resulting response function shows a collective structure at about 16 MeV excitation energy, which is consistent with the experimentally observed bump in ^{14}C. The adopted theoretical approach and the results of such QRPA calculations are described in details in Section 8.3. This finding is one the signatures which supports the interpretation of such bumps as the population of the GPV resonance. Other signatures are described in Section 8.4.

8.1 Features of the energy spectra

Looking for a clearer interpretation, the ^{15}C and ^{14}C excitation energy spectra, shown in Fig. 6.20 and Fig. 6.21, can be divided into three regions bounded by S_n and S_{2n} (for ^{15}C S_n = 1.218 MeV and S_{2n} = 9.349 MeV, for ^{14}C S_n =8.176 MeV and S_{2n} = 13.122 MeV).

Considering the ^{15}C case, the three regions are: (i) between 0 and 1.218 MeV, where the ^{15}C bound states lie, (ii) between 1.218 and 9.394 MeV, where the continuum of the system ^{14}C+*n* mixes together with the negative parity quasi-bound states of the system ^{13}C + 2*n*, typically labeled as 2*p*-3*h* configurations and (iii) above 9.394 MeV, where the ^{13}C + 2*n* system is also unbound and a supplementary continuous distribution is expected from this channel.

As regards the first region, there are only two states, i.e. the ground and the first excited state at E_x = 0.73 MeV. A dominant $|^{15}C_{g.s.}(1/2^+)\rangle = |^{14}C_{g.s.}(0^+) \otimes (2s_{1/2})_v\rangle$ single particle configuration characterizes the ground state and a $|^{15}C_{0.73}(5/2^+)\rangle = |^{14}C_{g.s.}(0^+) \otimes (1d_{5/2})_v\rangle$ configuration is relative to the excited state, both with a spectroscopic factor close to one [96]. In the past, these states have been customarily referred to as 1*p*-2*h* configurations on a ^{16}O 0^+ ground state core (see note 1 p. 60).

In the second region the 2*p*-3*h* states at 3.12, 4.21, 4.65, 6.85 and 7.36 MeV are strongly excited as well as in the (t,p) reaction (see Section 4.4.2), where their complex nature of a *p*-shell neutron hole coupled with a two-neutron pair in the *sd*-shell was ascertained [22]. In the ^{15}C excitation energy spectra (see Fig. 6.20) peaks corresponding to the population of these states are present on the top of a continuous background whose shape arises from unbound non-resonant ^{14}C + *n* system phase space. The known narrow resonances with 1*p*-2*h* structure at 4.78, 5.81, 6.37, 6.43, 6.54, 7.10 MeV [99][100] and the Fano resonance at 8.50 MeV [106] are not observed or rather weakly populated, similarly to the measurements with (t,p) reactions.

Above 9.394 MeV, an enhancement of the yield is observed corresponding to the population of two large unknown structures at about 10.5 and 13.7 MeV. On the contrary, the narrow resonances with 3*p*-4*h* structure observed at 9.79, 10.25, 11.02, 11.83, 13.1, 13.8, 14.57, 16.0, 17.8 and 19.0 MeV in the ^{12}C(^{12}C,^{9}C)^{15}C reaction [21] (see Section 4.5) and partly in the ^{9}Be(^{7}Li,p)^{15}C reaction [104] (see Section 4.6) are not observed or rather weakly populated.

A remarkably similar behavior is observed in the ^{14}C spectrum shown in Fig. 6.21. Narrow peaks are present up to the corresponding S_{2n} energy threshold and a sudden enhancement of the yield, distributed in larger structures, is observed just above. The narrow peaks correspond to transitions to well-known excited states of ^{14}C, efficiently populated also by (t,p) reactions [89] (see Section 4.4.2). The ^{14}C states at 7.00 and 10.73

MeV, whose main configuration requires the coupling of two neutrons in the *sd*-shell with the $^{12}C_{g.s.}(0^+)$ ground state core [88] are strongly populated. Near the S_{2n} threshold, the narrow states at 12.58, 12.89 and 12.96 MeV are superimposed to a large structure, steeply emerging at the threshold and slowing down up to about 16 MeV energy. A second unreported structure is also observed at about 16.9 MeV.

8.2 Break-up calculations

In order to isolate the spectral characteristics of the resonant-like excitations in the ^{15}C and ^{14}C nuclei, it is important to identify the various components of the projectile break-up present in the inclusive excitation energy spectra.

An accurate and complete model of the correlated two-neutron removal mechanism populating final continuum states is still not available, mainly because of the difficulties of introducing a simple, but coherent, treatment of neutron-neutron correlations in the reaction dynamics. A recent attempt to develop such a model is found in ref. [160].

The state of the art of the formalism about two-neutron transfer to bound states of the residual nucleus has been summarized in Chapter 2, following the review done in ref. [5], where the theoretical aim was to obtain the inclusive angular distributions of the ejectiles. On the other hand, for transfer to the continuum, several angular momenta mix and the angular distributions are thus less useful. The energy distribution of the ejectile is the best observable to analyze in such cases, from which the excitation energy spectrum of the residual nucleus can be obtained, as seen in Section 6.4.4.

A complete description of the measured energy spectra would require a coherent treatment of both one- and two-particle configurations for the bound and unbound systems. Moreover, the cross section should be built as a coherent sum of the sequential transfer contribution plus the direct pair transfer one. The construction of such a model is a very ambitious task, but still beyond the present status of the theory.

Therefore, as a first step, exploratory calculations on ^{15}C [161] and ^{14}C using a generalization of the one-nucleon transfer to unbound states model reported in ref. [162] were performed. The method extends the formalism of the transfer to bound states [163][164] to the case of unbound ones [165][166], assuming an uncorrelated removal of the two neutrons. The specific treatment of nucleon-nucleon correlations beyond the

residual nucleus mean field, as, for example, those due to the neutron-neutron pairing in the *sd*-shells are not included in the model. In the following Sections, a brief description of the adopted theory and the obtained results are described.

8.2.1 Theoretical description

First, the ^{15}C case was considered. The reaction ^{13}C(^{18}O,^{16}O)^{15}C was interpreted as a two-step mechanism:

$$\begin{aligned} &E_x > S_n && {}^{18}\mathrm{O} + {}^{13}\mathrm{C} \rightarrow {}^{17}\mathrm{O} + {}^{14}\mathrm{C}_{\mathrm{g.s.}} \rightarrow {}^{16}\mathrm{O} + {}^{14}\mathrm{C}_{\mathrm{g.s.}} + n \\ &E_x > S_{2n} && {}^{18}\mathrm{O} + {}^{13}\mathrm{C} \rightarrow {}^{17}\mathrm{O} + {}^{13}\mathrm{C}_{\mathrm{g.s.}} + n \rightarrow {}^{16}\mathrm{O} + {}^{13}\mathrm{C}_{\mathrm{g.s.}} + n + n \end{aligned} \qquad (8.1)$$

This should account for a sizable component of the observed spectra. The justification relies on the fact that there is an almost perfect matching condition (consistent with ref. [19]) between the single neutron separation energy of ^{18}O, S_n (^{18}O) = 8.044 MeV, and the energy needed by the ^{13}C nucleus to get one neutron, i.e., the single neutron separation energy of ^{14}C: S_n(^{14}C) = 8.176 MeV. Thus, in the first step of the reaction, the ground state to ground state *Q*-value is very small, Q_0 = 0.132 MeV, which implies an almost perfect match and thus a sudden process for the first neutron transfer, while the other neutron is transferred to the continuum of the ^{14}C system. At very low energies carried by the neutron, the ground and first bound excited state (at 0.74 MeV) of ^{15}C are populated. At higher neutron energies, the resonances of ^{15}C are excited up to the 2*n* threshold energy. Crossing this threshold, the transfer to the continuum of ^{14}C + *n* and the transfer to the continuum of ^{13}C + *n* + *n*, originated in the first step, merge together.

The inclusive stripping spectra contain contributions from (i) elastic break-up, in which the neutron is emitted from the projectile leaving the target in the ground state, (ii) inelastic break-up, in which the neutron scatters inelastically on the target, and (iii) transfer of the neutron to resonant states of the target. The relative contribution of each process to the inclusive spectra depends on the incident energy [167].

According to the model described in ref. [167], the transfer probability from an initial bound state of definite energy ε_i, angular momentum l_i, and spin j_i to a final continuum states of positive energy ε_f is given by

$$\frac{dP}{d\varepsilon_f}(j_f, j_i) = \sum_{j_f} \left(|1 - \bar{S}_{j_f}|^2 + T_{j_f} \right) B(j_f, j_i) \tag{8.2}$$

where

$$T_{ij} = 1 - |\bar{S}_{j_f}|^2 \tag{8.3}$$

where $\bar{S}_{j_f}$ is the energy-averaged (due to the continuum conditions) and angular-momentum dependent optical model *S*-matrix, which describes the neutron-target interaction, T_{ij} is the transmission coefficient and $B(j_f, j_i)$ is the elementary transfer probability. The latter depends on the details of the initial and final states, on the energy of relative motion and on the distance of closest approach between the two nuclei, as given in ref. [166]. In eq. (8.2), the sum is over all possible final angular momenta j_f corresponding to the given final energy. The calculation of the *S*-matrix, strongly related to the choice of the neutron target optical potential, is a key point of this formalism. The first term in eq. (8.2), proportional to $|1 - \bar{S}_{j_f}|^2$, gives the neutron elastic break-up or diffraction, while the second term proportional to the transmission coefficient, gives the neutron absorption (or stripping) by the target.

The relative motion of projectile and target is treated semi-classically [162]. Thus, an approximate formula for the total transfer cross section can be obtained from eq. (8.2) by integrating over the core-target distances of closest approach (b):

$$\frac{d\sigma_{1n}}{d\varepsilon_f} = C^2 S \int_0^\infty b db \frac{dP(b)}{d\varepsilon_f} P_{el}(b) \tag{8.4}$$

and the total break-up cross section is obtained by integrating over the neutron final continuum energy ε_f, calculated with respect to the target. In eq. (8.4), C^2S is the spectroscopic factor of the neutron single particle initial state, $dP(b)/d\varepsilon_f$ is given by (8.2) and P_{el} is the core survival probability in the elastic channel [168]. The latter can be written in terms of the parameterized *S*-matrix for the core-target scattering as

$$P_{el}(b) = |S_{cT}|^2 = \exp\left(-\ln 2 \exp[(R_s - d)/\Delta]\right) \tag{8.5}$$

where Δ = 0.6 fm is a diffuseness-like parameter and it was adopted the definition of the strong absorption radius, according to ref. [169], as $R_s = 1.4(A_P^{1/3} + A_T^{1/3})$ in fm, which corresponds to the distance of closest approach for a trajectory that is 50% absorbed from the elastic channel. It is possible to use eq.(8.5) since the conditions for the semi-classical approximation to the relative ion-ion scattering apply to the reaction discussed in this work. Eq. (8.4) gives the final neutron energy distribution which is related by energy conservation to the measured ejectile energy distribution [166].

The break-up reactions are sensitive only to the outermost tails of the single particle initial state wave functions, which are taken as Hankel functions. This is taken into account in the adopted model. The knowledge of both initial and final single-particle states of the transferred nucleon is thus required to perform the calculations. For this reason, it is important to distinguish between bound and unbound states, since the potential used to describe them can be rather different, in particular for neutron-rich nuclei.

In principle, the optical potential necessary to calculate the *S*-matrix, that determines the final states in the continuum, is energy dependent. In the present case the final energy range sampled by the neutron in the continuum is less than 20 MeV. In this energy range, the optical potentials for neutron scattering on light nuclei are poorly known, because of the strong variation of the cross section characterized by very sharp resonances. Thus, a constant potential from the parameterization given in ref. [170] for n + ^{13}C and E = 10 MeV was adopted. In fact, it was found that an energy-dependent potential would only change the overall normalization within 30%. The used potential has a Woods-Saxon real volume plus a spin-orbit and surface imaginary terms.

The radial wave functions of the initial (projectile) bound states were obtained as numerical solution of the Schrodinger equation with depths (V_0) of the Woods-Saxon potentials adjusted to reproduce the experimental separation energies ε. In particular, a radius of 2.91 fm and diffuseness of 0.56 fm were used for the central potential and depth of 5.5 MeV, radius of 2.96 fm and diffuseness of 0.5 fm for the spin-orbit term. The results are given in Table 8.1. From the bound states wave functions, the asymptotic normalization constants C_i of the single particle states are obtained. It is interesting to note that the asymptotic normalization constants in Table 8.1 are consistent with those used for a recent calculation of reactions rates of astrophysical interest involving the same oxygen and carbon nuclei studied here [171].

Table 8.1. Parameters for ^{17}O and ^{18}O bound state calculation.

	^{17}O ($1d_{5/2}$)	^{18}O($1d_{5/2}$)
ε (MeV)	-4.143	-8.044
V_0 (MeV)	-62.7	-68.1
C_i (fm$^{-1/2}$)	0.69	1.34

Considering the ^{14}C case the two step mechanism is similar to (8.1):

$$\begin{aligned} &E_x > S_n && {}^{18}\mathrm{O} + {}^{12}\mathrm{C} \rightarrow {}^{17}\mathrm{O} + {}^{13}\mathrm{C}_{\mathrm{g.s.}} \rightarrow {}^{16}\mathrm{O} + {}^{13}\mathrm{C}_{\mathrm{g.s.}} + n \\ &E_x > S_{2n} && {}^{18}\mathrm{O} + {}^{12}\mathrm{C} \rightarrow {}^{17}\mathrm{O} + {}^{12}\mathrm{C}_{\mathrm{g.s.}} + n \rightarrow {}^{16}\mathrm{O} + {}^{12}\mathrm{C}_{\mathrm{g.s.}} + n + n \end{aligned} \tag{8.6}$$

In general, the sudden hypothesis can be applied if the adiabatic parameter ω is << 1 [172]. The latter is defined as

$$\omega = \frac{|Q_0|}{\hbar v} b \tag{8.7}$$

where Q_0 is the ground to ground state Q-value, v is the neutron velocity and b is the distance of closest approach. In the present case, considering the ^{18}O energy beam of 84 MeV and $Q_0 = S_n(^{13}\mathrm{C}) - S_n(^{18}\mathrm{O}) = 4.946 - 8.044 = -3.098$ MeV, $\omega \sim 0.46$ is obtained. The break-up model was thus applied also to the ^{18}O + ^{12}C reaction using for n + ^{12}C the parametrizations of ref.[170]. The parameters for the radial wave functions of the projectile bound states are the same listed in Table 8.1.

8.2.2 The ^{18}O + ^{13}C case

In order to compare the calculations obtained using the approach described above to the experimental data, the continuum spectra of ^{15}C and ^{14}C were converted in differential cross section by integrating in the solid angle

$$\frac{d\sigma}{dE} = \int f(\theta, \varphi, E) d\Omega = \int_0^{2\pi} d\varphi \int_{\theta_{min}}^{\theta_{max}} f(\theta, \varphi, E) d\theta \tag{8.8}$$

The resulting spectrum for the ^{15}C nucleus, corresponding to an angular range 7.5° < θ_{lab} < 17.5°, is shown in Fig. 8.1 together with the break-up calculations.

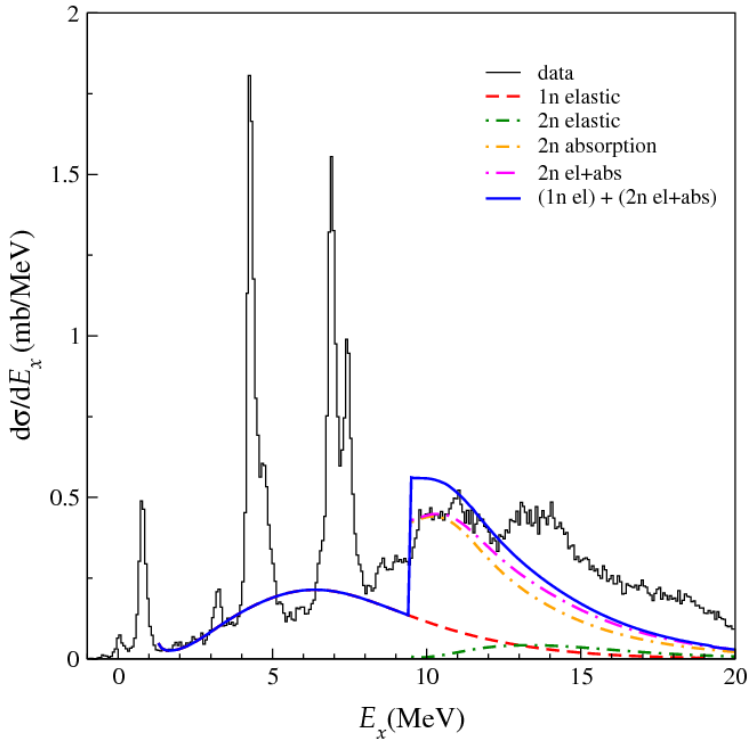

Fig. 8.1. Inclusive energy spectrum of the reaction ^{13}C(^{18}O,^{16}O)^{15}C at 7.5° < θ_{lab} < 17.5° and theoretical calculations of various break-up components (see text). The red dashed (1n elastic) and green dashed-dotted (2n elastic) curves represent the one- and two-neutron elastic break-up, respectively. The orange dashed-dotted curve (2n absorption) represents the two-neutron absorption term. The magenta dashed-dotted curve (2n el+abs) is the sum of two-neutron elastic break-up and absorption. Finally, the blue solid curve ((1n el) + (2n el+abs)) is the sum of all contributions folded with the experimental resolution. In the experimental spectrum, plotted with a bin size of 70 keV, the background from the ^{12}C impurity has been subtracted.

Between S_n and S_{2n}, the shown calculation contains the three-body physical background relative only to the elastic break-up (red dashed curve), as given by the first term of eq. (8.2). In fact, in this region the absorption observed in the experimental data is dominated by the narrow 2*p*-3*h* resonances stabilized by *n*-*n* pairing, which is not taken into account in the adopted approach. The knowledge of a correct energy and angular momentum dependence of the *n*-*n* pair+core optical potential would be necessary to give a precise description of such resonances. This could be achieved only with a microscopically calculated optical potential, which is still an unresolved problem. Therefore, a description of the absorption based on the optical model is not feasible in this region.

On the other hand, above the S_{2n} threshold the resonances are quite smooth and both elastic (green dashed-dotted curve) and absorption (orange dashed-dotted curve) terms were calculated. All calculations include a spectroscopic factor of 0.8 for the initial state, according to ref. [173].

The structure at 10.5 MeV in the experimental spectrum is reproduced in the calculation as a convolution of the peak calculated in the $^{13}C + n + n$ channel and the tail of the $^{14}C + n$ elastic break-up (see the blue solid curve in Fig. 8.1). The main contribution comes from the absorption of the two neutrons. This means that a $^{13}C + n + n$ resonant configuration can account for the observed structure, without the need of introducing specific *n-n* correlations.

In order to understand the origin of the strength distribution in the spectrum, an estimate of the contribution of each single l value to the total sum was done. This is possible since eq. (8.2) contains an incoherent sum over final angular momenta. The partial wave decomposition of the n-^{14}C elastic break-up cross sections between S_n and S_{2n} is shown in Fig. 8.2. The main contribution in this region comes from the $d_{5/2}$ and the $d_{3/2}$ states, a result that is consistent with the literature [174]. It also appears from Fig. 8.2 that above S_{2n} the main source of cross section comes from configurations where both neutrons are transferred to the $d_{5/2}$ and the $d_{3/2}$ continuum orbitals.

To summarize, the presented calculations give a good account for the continuum background in the ^{15}C excitation energy spectrum. In particular, the bump at 10.5 MeV is described in terms of an enhanced probability, near the S_{2n} threshold, of exciting $^{13}C + n + n$ configurations where the two neutrons are mainly transferred to $d_{5/2}$ or $d_{3/2}$ resonances of the resulting ^{15}C nucleus. Also, the average behavior of the spectrum at higher energies is reasonably well described within the assumption of the independent transfer of neutrons.

The model cannot account for the strong population of narrow resonances with known $2p$-$3h$ configuration observed between S_n and S_{2n}, because of the lack of *n-n* correlations. Also, the bump at 13.7 MeV is missing and this indicates that a more complete description of the $^{13}C + n + n$ system, including the *n-n* correlations, is required to describe this structure. Similarly to what observed between S_n and S_{2n}, the existence of $^{13}C + (n\text{-}n)$ pair resonances could act in redistributing and/or adding further strength beyond the S_{2n} threshold.

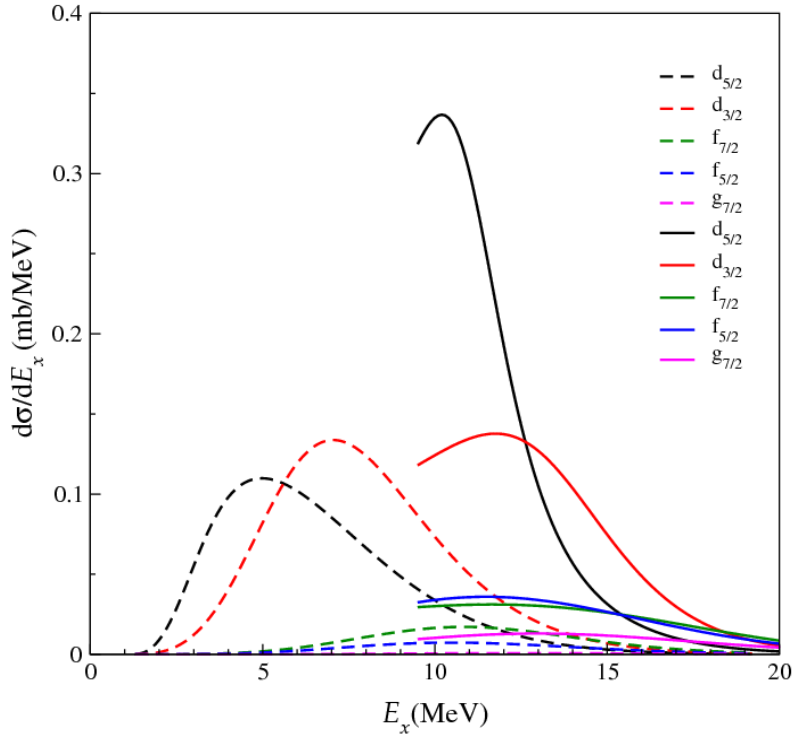

Fig. 8.2. Dominant contributions to the partial wave decomposition of the theoretical energy spectrum shown in Fig. 8.1. The legend indicates the single particle angular momentum of each individual strength distribution. The lines starting at E_x = 1.218 MeV refer to the ^{14}C + n system while those starting at 9.394 MeV to the ^{13}C + n + n (see text).

8.2.3 The ^{18}O + ^{12}C case

The differential cross section spectrum with the resulting calculations for the ^{14}C nucleus are shown in Fig. 8.3. Between S_n and S_{2n} only the elastic break-up is shown (red dashed curve), while above S_{2n} both the elastic (green dashed-dotted curve) and absorption (orange dashed-dotted curve) terms are shown.

The results are very similar to the case of ^{15}C. In the region above S_{2n} the enhancement of the yield is explained with the absorption of the two neutrons. The partial wave decomposition of the n-^{13}C break-up cross section is shown in Fig. 8.4. The main contribution comes from the $d_{5/2}$ and $d_{3/2}$ states, as well as in the ^{15}C case. The calculations give a good description of the continuum background in the ^{14}C excitation energy spectrum. On the other hand, the unknown bump at 16.9 MeV cannot be explained within this approach. This indicates that a description of the ^{12}C + n + n which includes the n-n correlations would be required to describe this structure. The study of the angular

distributions and of the decaying products for these systems, allows to shed more light on the role of such *n*-*n* correlations.

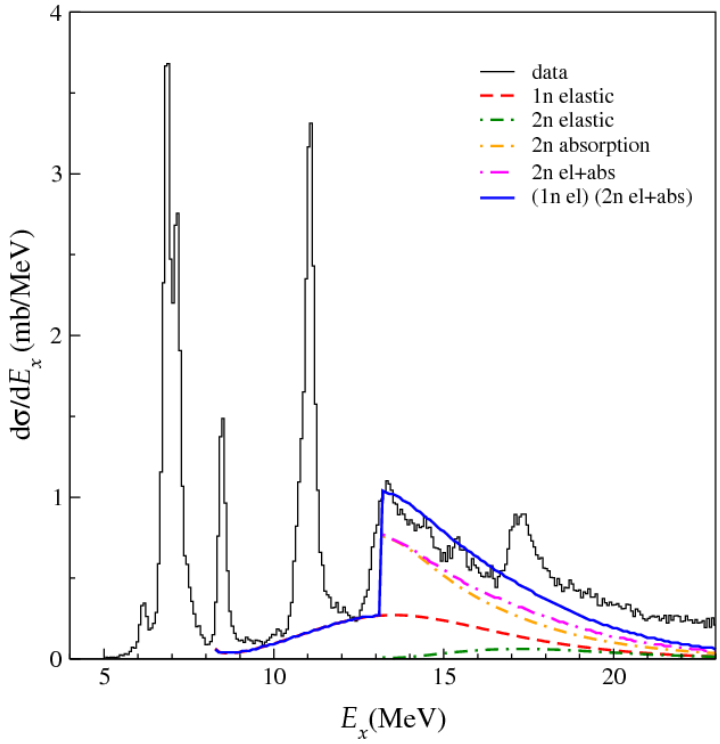

Fig. 8.3. Inclusive energy spectrum of the reaction ^{12}C(^{18}O,^{16}O)^{14}C at 7.5° < θ_{lab} < 17.5° and theoretical calculations of various break-up components (see text). The one- and two-neutron elastic break-up are shown as the red dashed (1n elastic) and the green dashed-dotted (2n elastic) curves, respectively. The two-neutron absorption term is shown as the orange dashed-dotted curve (2n absorption). The sum of the two-neutron elastic and absorption terms and the sum of all the contributions are shown as the magenta dashed-dotted curve (2n el+abs) and the blue solid curve ((1n el) + (2n el+abs)), respectively.

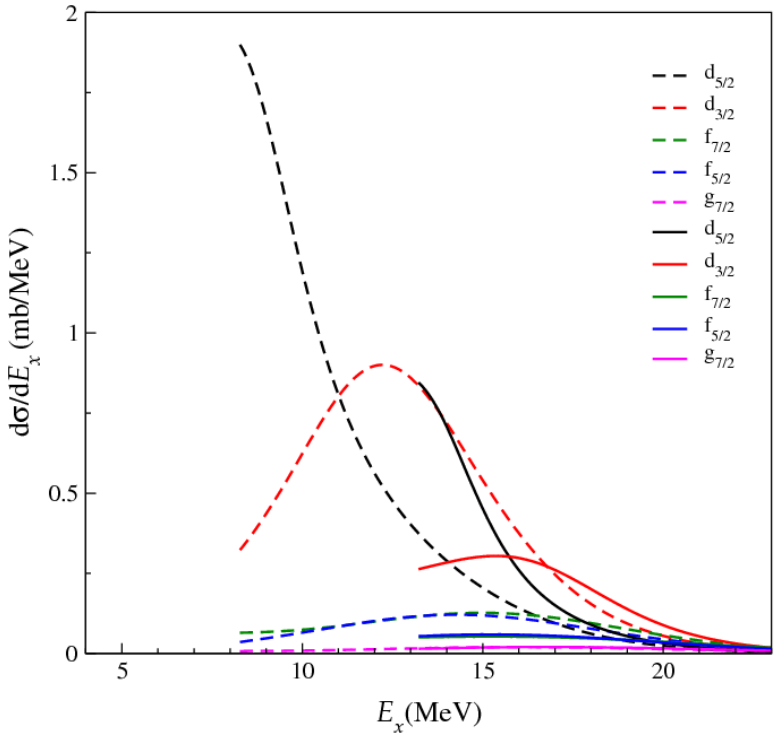

Fig. 8.4. Dominant contributions to the partial wave decomposition of the theoretical energy spectrum shown in Fig. 8.3. The legend indicates the single particle angular momentum of each individual strength distribution. The lines starting at E_x = 8.17 MeV refer to the $^{13}C + n$ system while those starting at 13.12 MeV to the $^{12}C + n + n$ (see text).

8.3 QRPA calculations

The presence of a GPV in the energy region where the bumps were observed is supported by QRPA calculations of the 0^+ excitations in the energy spectra. The two-particle transfer modes are usually described using the pp-RPA [45] [46] in the case of closed shell nuclei and the QRPA [4] [10] in open shell nuclei.

In the present case, the calculations of the response function corresponding to the transfer of a neutron pair to the ^{12}C nucleus was done following the same approach of ref [11][12]. The results of the same kind of calculations for the oxygen isotopes are reported in Section 1.3.3. In the following Sections a brief description of the adopted QRPA approach and the resulting response function are described and compared with the experimental results.

8.3.1 Treatment of the pairing interaction: from HF to HFB theory

Many properties of nuclei can be described in terms of a model consisting in independent particles moving in an average potential whose space dependence closely follows the matter distribution. This is the assumption made in the mean field Hartree-Foch (HF) theory [2].

The HF method takes into account the particle-hole part of the interaction, that is the long-range part of the force which binds nucleons in the nucleus. The particle-particle correlations are caused by the short-range attractive part of the force, i.e. the pairing force. The treatment of these correlations can be done formally in the same framework of the particle-hole part by introducing generalized product wave functions consisting of *quasi-particles* (*qp*). The particle-particle correlations are taken into account in the Bardeen-Cooper-Schrieffer (BCS) or Hartree-Foch-Bogoliubov (HFB) theories [2]. Within these models the basic properties of the ground states of nuclei were explained.

In order to include the pairing interaction in the mean field description of nuclei, the same BCS theory of solid state physics was applied [6]. The ground state of an even-even nucleus is defined as

$$|\mathrm{BCS}\rangle = \prod_{k>0}(u_k + v_k a_k^+ a_{\bar{k}}^+)|-\rangle \tag{8.9}$$

where $|-\rangle$ is the vacuum state and a^+ is the particle creation operator. The product runs only over half configuration space, as indicated by $k > 0$. A conjugate state $\bar{k} < 0$ exists for each $k > 0$ one and the states $\{k, \bar{k}\}$ generate the whole single-particle space. The $|v_k|^2$ and $|u_k|^2$ represent the *occupation probabilities* of a certain pair state $(k, \bar{k})$ and are linked by the condition $|v_k|^2 + |u_k|^2 = 1$. Since the $|\mathrm{BCS}\rangle$ is written as a superposition of different numbers of pairs, the number of particle is not conserved. In solid state physics, where N ~ 10^{23}, the violation of particle number has no influence on any physical quantity. On the contrary, this is actually a great disadvantage in nuclear physics, where in many cases gives rise to serious drawbacks.

In order to solve this problem a condition is imposed on the expectation value of the particle number

$$\langle \mathrm{BCS}|\hat{N}|\mathrm{BCS}\rangle = N \text{ or } Z \tag{8.10}$$

This can be achieved by adding the term $-\lambda\widehat{N}$ to the variational Hamiltonian $H' = H - \lambda\widehat{N}$, where the Lagrange multiplier λ is fixed by the condition (8.10). λ is called *chemical potential* or Fermi energy because it represents the increase of the energy $E = \langle \mathrm{BCS}|H|\mathrm{BCS}\rangle$ for a change of the particle number $\lambda = dE/dN$.

However, condition (8.10) constrains only the mean value of the particle number, thus an uncertainty is still present. These fluctuations in the particle number affect most light ions and this is one of the reasons which make the BCS and HFB theories more precise in case of heavy ions.

The pairing interaction gives an additional energy to each pair of nucleons with respect to the value they have in the HF calculation. This energy is usually indicated as the pairing gap Δ, which is accessible experimentally measuring the odd-even mass differences [1] (as reported in Section 1.1). The pairing gap equation in the BCS theory is found to be [2]

$$\Delta_k = -\frac{1}{2}\sum_{k>0} \bar{v}_{kk'\bar{k}\bar{k}'} \frac{\Delta_{k'}}{\sqrt{\tilde{\varepsilon}_{k'}^2 + \Delta_{k'}^2}} \tag{8.11}$$

where $\bar{v}_{kk'\bar{k}\bar{k}'}$ represents the overlap of the wave functions between the k and k' states and $\Delta_{k'}$ and $\varepsilon_{k'}$ are the pairing gap and the single-particle energy of the k' state, respectively.

It can be demonstrated [2] that in the limit of $\Delta \to 0$, $|v_k|^2 = 1$ for occupied levels and $|v_k|^2 = 0$ for unoccupied ones. In this case $|v_k|^2$ is a step function, as in the HF case (see left panel of Fig. 8.5), whereas in the interacting case $\Delta \neq 0$ the step function is somewhat smeared out. In fact, due to the pairing interaction, the nucleons gain energy ($\Delta \sim 1$ - 2 MeV) when they are paired and this corresponds to the possibility to be promoted to a level above the Fermi energy. This yields a partial depletion of the states below and a partial filling of the states above the Fermi level (see right panel of Fig. 8.5).

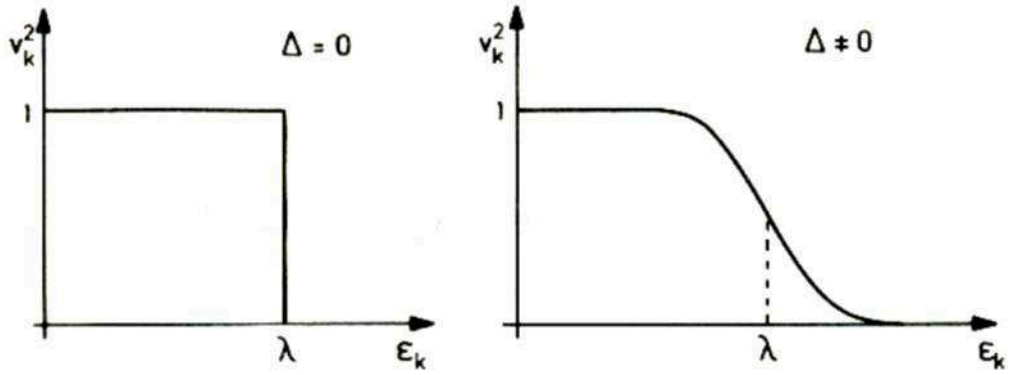

Fig. 8.5. The occupation probabilities $|v_k|^2$ in the non-interacting case ($\Delta = 0$) and in the interacting one ($\Delta \neq 0$). λ represents the Fermi energy.

The $|\mathrm{BCS}\rangle$ ground state can be also written as a product state of a new type of fermions: the *Bogoliubov quasi-particles*. This is possible by introducing new creation and annihilation operators through a linear Bogoliubov transformation [2]:

$$\begin{aligned} \alpha_k^+ &= u_k a_k^+ - v_k a_{\bar{k}} \\ \alpha_k &= u_k a_{\bar{k}}^+ + v_k a_k \end{aligned} \tag{8.12}$$

Using (8.12), the $|\mathrm{BCS}\rangle$ ground state become

$$|\mathrm{BCS}\rangle \propto \prod_{k \lesseqgtr 0} \alpha_k \, |-\rangle \tag{8.13}$$

In this way, a representation of the ground state of pairwise interacting particles in terms of a gas of non-interacting quasi-particles is achieved. A quasi-particle has some properties of a bare particle and some of a bare hole: above the Fermi surface, where $|v_k|^2$ is small it is nearly a particle, while below the Fermi surface, where $|u_k|^2$ is small, it is nearly a hole. The use of this transformation allow to treat the ground state of open-shell nuclei with the inclusion of the pairing force (HFB theory) with the same formalism of the HF theory.

In the practical cases, the BCS or HFB equations have to be solved on a computer with an iterative procedure, and it is important the choice of the levels which contribute most to the sum appearing in the gap equation (8.11) for including them in the calculations. The

effect of the pairing force results to be restricted to the neighborhood of the Fermi surface, where Δ_k is different from zero. Indeed, if the state k is near the Fermi surface, the main contributions in the sum (8.11) come from states k' in the vicinity of the Fermi level, where the overlap term $\bar{v}_{kk'\bar{k}\bar{k}'}$ is larger. On the contrary, when k is far from the Fermi surface the contribution from $k' \simeq k$ is small because $\tilde{\varepsilon}_{k'}^2 \gg \Delta_{k'}^2$, and the contribution for k' at the Fermi surface is small as well because of the small overlap. Thus, only states near to the Fermi level are included in the HFB calculations.

The restriction of the pairing to the vicinity of the Fermi level permits also to treat neutrons and protons separately. This is more valid when considering heavy nuclei, with A ~ 150, where $(N - Z) \geq 20$. In these cases the neutron and proton levels close to the Fermi energy have very small overlap compared to that of protons and neutrons themselves. Therefore, the proton-neutron pairing is usually neglected. The same is done for light nuclei, although this approximation is less appropriate.

The HFB theory is a more complete extension of the BCS quasi-particles (defined by the operators reported in (8.12)), where the most general linear transformation from the particle operator a_l^+, a_l to the quasi-particle operators β_k^+, β_k is used:

$$\beta_k^+ = \sum_l U_{lk} a_l^+ + V_{lk} a_l \tag{8.14}$$

where both k and l indices run over the whole configuration space. The Hermitian conjugation of eq. (8.14) gives the operator β_k. The coefficients U and V are not completely arbitrary. The new operators β_k^+, β_k are required to obey to the same fermion commutation relations as the old ones [2]. With this transformation, the ground state of the many body system $|\Phi\rangle$ is represented as the vacuum with respect to the quasi-particles, i.e. $\beta_k|\Phi\rangle = 0$ for all k.

8.3.2 QRPA and two-particle response

The analysis of the whole spectrum of nuclear excitations within the independent particle models (HF or HFB) is able to explain a series of excited states as *p-h* or two-quasiparticle excitations, but there also many other excitations which cannot be reproduced

with these approaches. This is because in the HF or HFB approaches the residual interaction is neglected, but it becomes important for the excited states. For example the giant resonances (e.g. GDR, GQR, etc.) can only be explained microscopically assuming a coherent participation of many nucleons in the nucleus [2]. A general method which takes into account the residual interaction and allows to explain the high-lying as well as low-lying collective vibrations is the RPA or QRPA approach. The formalism of the two methods is the same, but the RPA considers only the *p-h* excitations whereas the QRPA approach is more general because it includes at the same time the *p-h*, *p-p* and *h-h* excitations. The following discussion is focused on sketching the QRPA approach, for which detailed description can be found in ref. [2].

The principal ingredients of such a method are the ground state system $|0\rangle$ (called vacuum state) and the residual interaction which perturbs it by a small amount. In the HFB calculations, the exact Hamiltonian of the system is decomposed as

$$H = T + V = T + U_{HFB} + (V - U_{HFB}) = T + U_{HFB} + V_{res} \tag{8.15}$$

where U_{HFB} is the mean field potential used for the calculation of the $|HFB\rangle$ ground state. The residual interaction V_{res} is defined as

$$V_{res} = V - U_{HFB} = \sum_{i<j} v(i,j) - \sum_{i} V(i) \tag{8.16}$$

where $v(i,j)$ is the nucleon-nucleon potential. The residual interaction contains contributions also from the pairing interaction, which is included in the HFB approach.

A way in which the QRPA equations can be derived is the formalism of the *linear response theory*, which is useful when density dependent interactions are involved, as in the present case (see Section 8.3.3). It investigates the influence on the system of an external time-dependent field

$$F(t) = Fe^{-i\omega t} + F^{+}e^{i\omega t} \tag{8.17}$$

where F includes both particle-hole and two-particle operators

$$F = \sum_{ij} F_{ij}^{11} a_i^+ a_j + \sum_{ij} (F_{ij}^{12} a_i^+ a_j^+ + F_{ij}^{21} a_i a_j) \tag{8.18}$$

It is assumed that this field is weak and introduces only small changes in the nuclear density, which can be treated in a linear order. The nuclear density is found to oscillate with this external field and resonances are obtained whenever the frequency ω is close to an excitation energy of the system. The wave function $|\Phi(t)\rangle$ of the nuclear system in an external, time dependent field is no longer stationary. The corresponding density *R* obey to the Time Dependent Hartree Foch (TDHF) equation of motion [2]

$$\hbar\omega \frac{\partial R}{\partial t} = [h(R) + F(t), R(t)] \tag{8.19}$$

where $h(R)$ is the HFB field. In the hypothesis of a weak external field, the variation of the density *R* is expressed in terms of three quantities [12], namely ρ', k' and $\bar{k}'$, which are written as a column vector

$$\boldsymbol{\rho}' = \begin{pmatrix} \rho' \\ k' \\ \bar{k}' \end{pmatrix} \tag{8.20}$$

where

$$\begin{aligned} \rho' &= \langle 0 | a_j^+ a_j | ' \rangle \\ k' &= \langle 0 | a_j a_i | ' \rangle \\ \bar{k}' &= \langle 0 | a_j^+ a_i^+ | ' \rangle \end{aligned} \tag{8.21}$$

The first component ρ' corresponds to the variation of the particle density, while k' and $\bar{k}'$ correspond to variations of the *abnormal density* (or pairing density), namely they represent the fluctuations of the pairing tensor associated with the pairing vibrations. The state $|'\rangle$ denotes the change on the ground state wave function $|0\rangle$ due to the external field. In the three dimensional space introduced by the vector (8.20), the first dimension represents the *p-h* subspace, the second the *p-p* one and the third the *h-h* one.

It is convenient to solve eq. (8.19) in the *qp* representation using the *qp* creation and annihilation operators β_k^+ and β_k, defined with transformation (8.14), to express the *R* density [12]. Following the same procedure of ref. [12], the variation of the HFB Hamiltonian is given by

$$\boldsymbol{h} = \boldsymbol{V}\boldsymbol{\rho}' \tag{8.22}$$

where *V* is the matrix of the residual interaction, which in the linear response theory is expressed in terms of the second derivatives of the HFB energy functional

$$\boldsymbol{V}^{\alpha\beta}(\boldsymbol{r}\sigma, \boldsymbol{r}'\sigma') = \frac{\partial^2 E}{\partial\rho_\beta(\boldsymbol{r}'\sigma')\partial\rho_{\bar{\alpha}}(\boldsymbol{r}\sigma)} \qquad \alpha,\beta = 1, 2, 3 \tag{8.23}$$

where α and β are the row indexes and the notation $\bar{\alpha}$ means that whenever α is 2 or 3 then $\bar{\alpha}$ is 3 or 2.

Introducing as external field the three dimensional column vector

$$\boldsymbol{F} = \begin{pmatrix} F^{11} \\ F^{12} \\ F^{21} \end{pmatrix} \tag{8.24}$$

the density changes can be written in the standard form

$$\boldsymbol{\rho}' = \boldsymbol{G}\boldsymbol{F} \tag{8.25}$$

where $\boldsymbol{G}$ is a 3×3 matrix and represents the QRPA Green's function (also called *response function*) obeying to the Bethe-Salpeter equation

$$\boldsymbol{G} = \boldsymbol{G}_0 + \boldsymbol{G}_0\boldsymbol{V}\boldsymbol{G} = \frac{\boldsymbol{G}_0}{1 - \boldsymbol{G}_0\boldsymbol{V}} \tag{8.26}$$

$\boldsymbol{G}_0$ is the unperturbed Green's function completely determined once the HFB wave functions are calculated [12]. In this way, from the knowledge of the unperturbed response function $\boldsymbol{G}_0$ and the external field *F* it is possible to calculate the strength function

associated with that perturbation. In particular, the strength function describing the two-particle transfer from the ground state of a nucleus with A nucleons to the excited states of a nucleus with $A + 2$ nucleons is given by

$$S(\omega) = -\frac{1}{\pi} Im \int F^{12*}(\boldsymbol{r}) \boldsymbol{G}^{22}(\boldsymbol{r}, \boldsymbol{r}'; \omega) F^{12}(\boldsymbol{r}') d\boldsymbol{r} d\boldsymbol{r}' \tag{8.27}$$

where $\mathbf{G}^{22}$ denotes the (*pp*,*pp*) component of the response function.

8.3.3 Strength function

The QRPA model presented in Section 8.3.2 was applied to calculate the strength function of a neutron pair transferred to the ^{12}C nucleus. The first step is to calculate the ^{12}C ground state within the HFB approach [175]. The HFB equation were solved in coordinate space assuming spherical symmetry. The mean field quantities were evaluated using the Skyrme interaction SLy4 [176] while for the pairing interaction a zero-range density-dependent interaction was taken given by

$$V_{pair} = V_0 \left[1 - \left(\frac{\rho(r)}{\rho_0} \right)^{\alpha} \right] \delta(\boldsymbol{r}_1 - \boldsymbol{r}_2) \tag{8.28}$$

where V_0, ρ_0 and α are the parameters of the force. Due to its zero range, this force should be used in the HFB calculations with a cutoff in *qp* energies. Using the same prescriptions of ref. [12] it was chosen a *qp* cutoff of 60 MeV and the obtained value is V_0 = -570 MeV fm^3. The parameter ρ_0 is set to the usual saturation density, 0.16 fm^{-3}. The value of the parameter α was chosen so as to reproduce the trend of the experimental pairing gap and it was found α = 1. The obtained HFB *qp* energies corresponding to the $1p_{1/2}$, $1d_{5/2}$, $2s_{1/2}$, $2p_{3/2}$, $2p_{1/2}$, $1d_{3/2}$ and $1f_{7/2}$ states are listed in Table 8.2.

In the QRPA calculations the full discrete and continuum *qp* spectrum was included up to 60 MeV. The HFB states, which generate a two-quasiparticle spectrum with a maximum energy of 120 MeV, are used to construct the unperturbed response function G_0. The residual interaction is derived from the two-body force used in the HFB according to eq. (8.23). The strength function for the two-neutron transfer was calculated using eq. (8.27).

For the radial function $F^{12}(r)$ the form r^L was taken, which is equal to unity for the $L = 0$ pair transfer mode considered here.

Table 8.2. ^{12}C single-quasiparticle neutron energies calculated in the HFB model.

	Single-*qp* energy (MeV)
$1p_{1/2}$	4.51
$1d_{5/2}$	10.89
$2s_{1/2}$	10.96
$2p_{3/2}$	13.19
$2p_{1/2}$	13.25
$1d_{3/2}$	13.80
$1f_{7/2}$	14.79

The results for the $L = 0$ strength function corresponding to a neutron pair transferred to the ^{12}C nucleus are shown in Fig. 8.6. When looking at the unperturbed response function G_0 (dashed line of Fig. 8.6) it is possible to recognize the $^{14}C_{g.s.}$ at 9.02 MeV and the other states at higher energies corresponding to the addition of two *qp* in the ^{12}C nucleus. In particular the $1d_{5/2}$ and $2s_{1/2}$ states are at ~ 22 MeV, the $2p_{3/2}$ and $2p_{1/2}$ at ~ 26 MeV and the $1d_{3/2}$ and $1f_{7/2}$ ones at ~ 28 MeV. As expected, the effect of the residual interaction (solid line of Fig. 8.6) is to shift down the position of the two-quasiparticle resonant states and increase their strength. In particular, the doublet at 21 MeV in the G_0 (corresponding to $1d_{5/2}$ and $2s_{1/2}$ orbitals) is split in two states at about 9.8 and 13.5 MeV in the G response function, whereas the $2p_{3/2}$, $2p_{1/2}$, $1d_{3/2}$, $1f_{7/2}$ and orbitals above contributes together to form the structure at 25.5 MeV, which can be identified as the GPV.

In order to make a comparison between the resulting strength function and the experimental energy spectra, it is necessary to shift the energy scale of the calculations, since it is referred to the $^{12}C_{g.s.}$. Thus, the proper energy shift corresponds to the HFB mass difference between the ^{12}C and the ^{14}C nuclei, i.e. 9.05 MeV (as it can be deduced from the G_0 response function of Fig. 8.6). Considering this energy shift the predicted GPV is located at $E_x = 25.5 - 9.05 = 16.45$ MeV with respect to the $^{14}C_{g.s.}$, a value consistent with the experimental centroid of the bump ($E_x^{exp} = 16.9$ MeV).

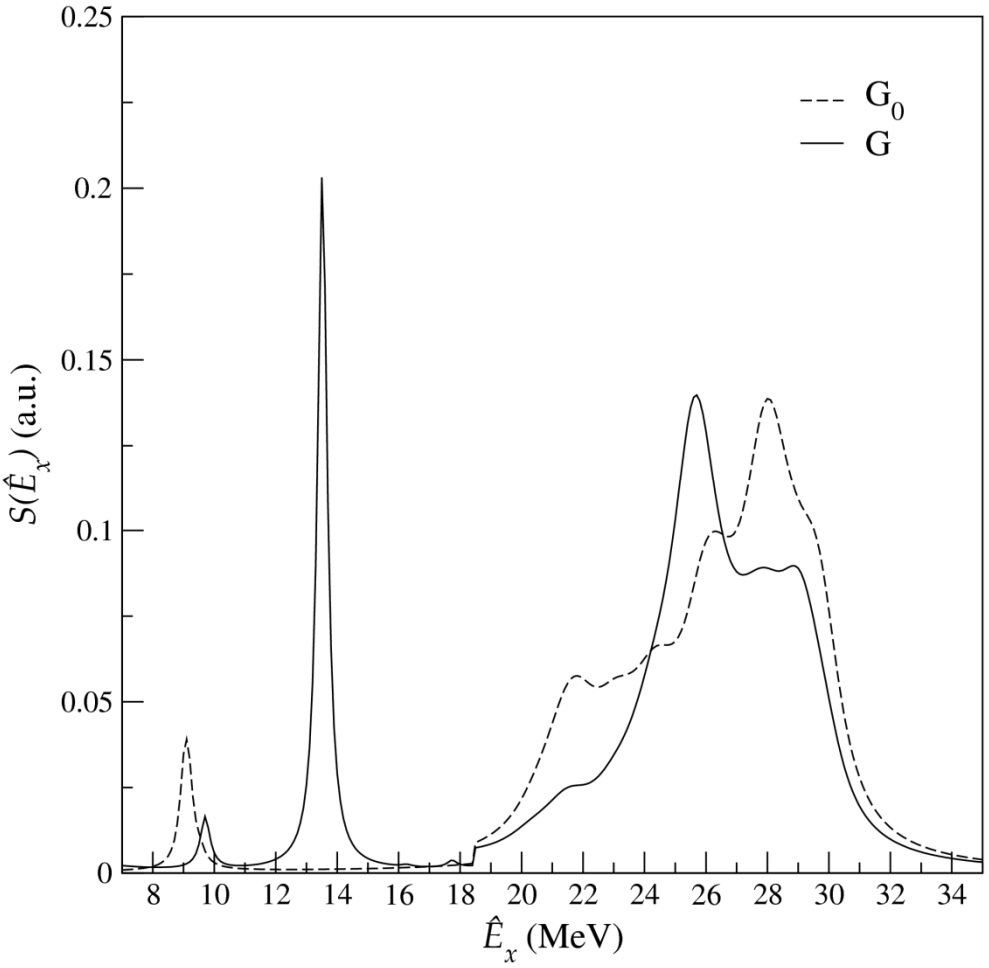

Fig. 8.6. The L = 0 QRPA response function for the two-neutron transfer on ^{12}C. The unperturbed response (G_0) and the QRPA response (G) are indicated with the dashed and the solid line, respectively. The results are displayed as function of E, the excitation energy with respect to the ^{12}C ground state.

8.4 GPV signatures

The continuum background analysis, described in Section 8.2, have shown that for the ^{15}C residual nucleus the dominant contribution just above S_{2n} comes from the absorption of the neutrons in the d shell of the ^{13}C + n + n system. Similar results are found for the calculations done in the ^{14}C case. The obtained break-up background cannot explain neither the large structure at 13.7 MeV in the ^{15}C spectrum nor that at 16.9 MeV in the ^{14}C one. The possible presence of a GPV cannot be neither ruled out nor fully verified within those calculations, because such a model does not include neutron-neutron correlations.

A first indication of the possible presence of a GPV in the ^{14}C spectrum were found from the QRPA calculations described in Section 8.3. The GPV excitation energy resulting from such calculations is consistent with the experimental value.

In the following Sections many other signatures which support the interpretation of the observed bumps as the population of the GPV are listed and fully investigated.

8.4.1 The pairing energy scale

In order to investigate a probable common origin of the two observed structures in ^{15}C and ^{14}C, the excitation energy compared to the target ground state was computed as

$$E^t_x = E_x + M_r - M_t \tag{8.29}$$

where M_t and M_r represent the mass of the target and of the residue, respectively. The E^t_x is a more suitable parameter when comparing the data with theoretically derived *p-p* excitations built on the target mean field. When applying such a scaling of the excitation energies, it is obtained

$$\begin{aligned} &^{15}\mathrm{C} \qquad E^t_x = 13.7 + 6.7 = 20.4 \text{ MeV} \\ &^{14}\mathrm{C} \qquad E^t_x = 16.9 + 3.0 = 19.9 \text{ MeV} \end{aligned} \tag{8.30}$$

The energy of the two bumps is thus found at about the same value in both nuclei. This is consistent with the results of ref. [11], where the predicted energy of the GPV was found to be at about 20 MeV for all the studied Oxygen isotopes (see Section 1.3.3). Furthermore, the same QRPA calculations done for the ^{14}C case (described in Section 8.3) are consistent with a collective structure at about 16.5 MeV residual nucleus excitation energy.

8.4.2 The $1d_{3/2}$ *missing state*

Another important similarity between the spectra of ^{14}C and ^{15}C is related to the $1d_{3/2}$ *missing state*. In fact, it is known that in Carbon isotopes the $2s_{1/2}$ and $1d_{5/2}$ orbitals are at similar single particle energies (normally at about 1 MeV), while the $1d_{3/2}$ is at about 5 MeV from the former [177]. A simple estimation of the two-neutron 0^+ states built on these single particle orbitals would predict a doublet with $[1d_{5/2}\otimes 1d_{5/2}]_{0+}$ and $[2s_{1/2}\otimes 2s_{1/2}]_{0+}$ configurations at low excitation energy and an isolated state with $[1d_{3/2}\otimes 1d_{3/2}]_{0+}$ configuration about 10 MeV above that. The introduction of the residual neutron-neutron interaction generates a relevant mixing between the $[1d_{5/2}\otimes 1d_{5/2}]_{0+}$ and $[2s_{1/2}\otimes 2s_{1/2}]_{0+}$ configurations [177] with a minor influence on the high-lying $[1d_{3/2}\otimes 1d_{3/2}]_{0+}$ state. This has been partially demonstrated in the case of ^{14}C in ref. [89] where the two low-lying 0^+ states are found at 6.59 and 9.75 MeV, while no observation of the high-lying state at the expected energy of about 16 MeV is reported. In the present spectrum of ^{14}C (shown in Fig. 6.21) the population of the states at 6.59 and 9.75 MeV is strongly suppressed and a relevant yield is observed at 16.9 MeV.

An analogous situation is expected for ^{15}C, where the two-neutron 0^+ states built within the *sd* $n = 2$ harmonic oscillator shell couple with the $1/2^-$ single hole configuration in the $n = 1$. This coupling is weak also because of the different angular momentum and parities of the involved single particle orbitals. This is confirmed by the observed splitting of each ^{14}C two-neutron state, built on the $n = 2$, with $J^\pi(^{14}\mathrm{C})$ spin-parity, in a doublet of states at close energies characterized by $J^\pi(^{15}\mathrm{C}) = (J(^{14}\mathrm{C}) - 1/2)^{-\pi}$, $(J(^{14}\mathrm{C}) + 1/2)^{-\pi}$ spin-parity when $J > 0$. These doublets have been clearly recognized in ^{13}C(t,p)^{15}C reaction studied by Truong and Fortune [22] (see Section 4.4.2). When $J = 0$ three $1/2^-$ state should be obtained. Two of them are the states at 3.03 and 5.89 MeV, mainly characterized by $[(1p_{1/2}^{-1})^{1/2-}\otimes(1d_{5/2}\otimes 1d_{5/2})^{0+}]^{1/2-}$ and $[(1p_{1/2}^{-1})^{1/2-}\otimes(2s_{1/2}\otimes 2s_{1/2})^{0+}]^{1/2-}$ configuration, respectively. The third expected $1/2^-$ state, corresponding to the $[(1p_{1/2}^{-1})^{1/2-}\otimes(1d_{3/2}\otimes 1d_{3/2})^{0+}]^{1/2-}$ configuration, was missing in their spectra. All of the mentioned states are populated with the present reaction in the ^{15}C spectrum, as seen in Fig. 6.20, with a much reduced cross section for the 3.03 and 5.89 MeV $1/2^-$ ones. As in the case of ^{14}C, a strong concentration of the experimental cross section is observed at 13.7 MeV, i.e. about 10 MeV above the first $1/2^-$ state.

8.4.3 The angular distributions

A very important ingredient of the data analysis is the study of the absolute cross section angular distributions. In fact, the indication of the presence of the GPV can be confirmed if the shape of the cross section angular distribution for the observed bumps suggests an $L = 0$ transfer. The cross section angular distributions for the ^{15}C bump at 13.7 MeV and the ^{14}C one at 16.9 MeV are compared to those of the transition to the $^{14}C_{g.s.}$ ($L = 0$), the 0.73 MeV state of ^{15}C ($L = 3$) and the 10.73 MeV state of ^{14}C ($L = 4$) in Fig. 8.7. A clear indication of an oscillating pattern is present only in the ^{14}C 0^+ ground state and in the two bumps, while the other transitions exhibit an almost featureless shape.

As it was shown in Chapter 7, the (^{18}O,^{16}O) reaction proceeds mainly by a direct pair transfer at the beam energies considered in the present work. It has also been shown that the $L = 0$ modes can be easily recognized by their typical oscillating pattern. Indeed, the oscillations are largely smeared for transitions characterized by higher multipolarities, because of an equal population of the possible M states, which are out of phase [18], as mentioned in Section 2.5. Such finding strongly supports the dominant $L = 0$ nature of the broad bumps, which behave as the ^{14}C ground state. Such finding allow to assign a spin $1/2^-$ to the 13.7 MeV resonance in ^{15}C and 0^+ to that at 16.9 MeV in ^{14}C as written in Table 6.2. For the other expected $L = 0$ transitions the scarce integrated yield did not allow the extraction of the angular distribution.

Moreover, the angular distributions of the two bumps (at 10.5 and 13.7 MeV) observed in the ^{15}C spectrum, shown in Fig. 6.31, appears to be very different each other. In fact, as demonstrated in Section 8.2, the first bump contains strong contributions from the sequential break-up and this is confirmed by its smooth angular distribution, whereas the oscillating pattern of the second bump angular distributions suggests that it correspond to a resonant state of the ^{15}C nucleus.

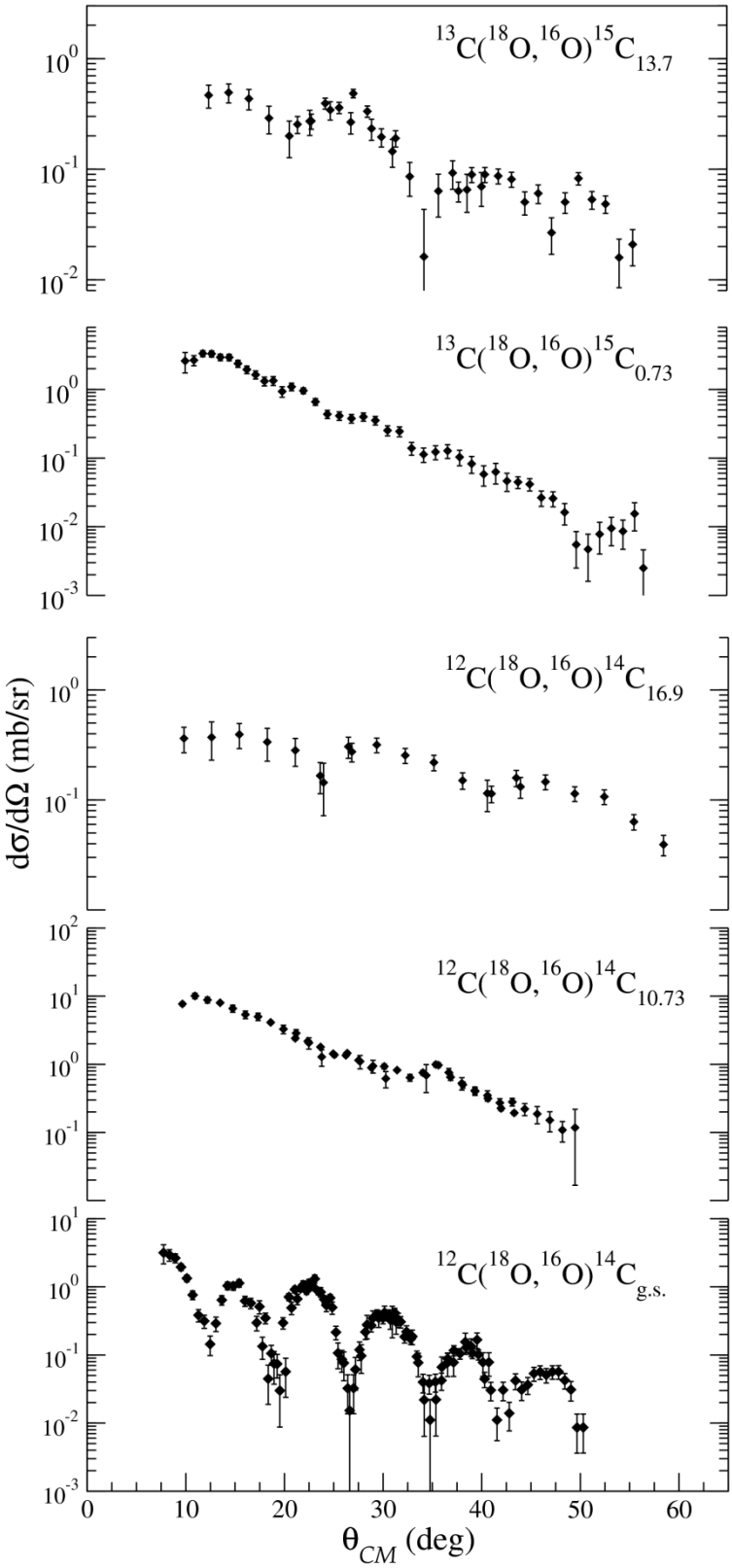

Fig. 8.7. Angular distributions for the $^{12}C(^{18}O,^{16}O)^{14}C$ and $^{13}C(^{18}O,^{16}O)^{15}C$ reactions at 84 MeV incident energies.

8.4.4 Quasi-elastic transfer and semi-classical approaches

In order to extract nuclear structure information from the measured cross section a factorization into the scattering cross section $\left(\frac{d\sigma(\theta)}{d\Omega}\right)_{sc}$, the transfer probability $P_{tr}(\theta)$ and quantal corrections $F(Q,L)$ was assumed

$$\left(\frac{d\sigma(\theta)}{d\Omega}\right)_{tr} = \left(\frac{d\sigma(\theta)}{d\Omega}\right)_{sc} P_{tr}(\theta)F(Q,L) \tag{8.31}$$

according to ref. [5]. Such approximation is known to be rather appropriate when a semi-classical description of the relative motion holds. As already mentioned in Section 2.3.2, such a description is appropriate when the Sommerfeld parameter (defined in eq. (2.8)) is sensibly larger than unity, as in the present cases ($\eta = 3.5$).

The third factor of eq. (8.31) corresponds to two different matching aspects: one related to the scattering orbits and the other to the internal matching of the bound states wavefunctions. It is possible to remove the effect of these matching conditions on the cross section by evaluating the $F(Q,L)$ factor. Describing the two neutron transfer reaction as $a(= b + x) + A \rightarrow b + B\ (= A + x)$ and considering the $\Delta L = 0$ transitions only, the quantal correction is:

$$F(Q) = \exp[-C_1 \Delta Q^2] \tag{8.32}$$

C_1 was evaluated according to ref. [5]

$$C_1 = \frac{R_0 m_{12}(1/\alpha)}{4(2E - E_B)\hbar^2} \tag{8.33}$$

where R_0 is the strong interaction radius, m_{12} is the target-projectile reduced mass ($m_{12} = m_a m_A/(m_a + m_A)$), E is the beam energy, E_B is the projectile binding energy ($E_B = S_{2n}$) and α is the decay constant, determined as

$$\alpha = \sqrt{2\mu E_B/\hbar^2} \tag{8.34}$$

where μ is the reduced mass of the valence particle ($\mu = m_x m_b/(m_x + m_b)$, with m_x mass of the 2*n* cluster).

In eq. (8.32), ΔQ was evaluated according to ref. [51], as

$$\Delta Q = -\frac{1}{2}\frac{m_x(m_b - m_A)}{m_a + m_A}v^2 + m_{12}\ddot{r}\frac{m_x}{2}\left(\frac{R_A - R_a + R_0}{m_A} - \frac{R_b - R_B + R_0}{m_b}\right) \quad (8.35)$$

where $\ddot{r}$ corresponds to the acceleration of the ejectile.

The quantal correction faction $F(Q, L)$ was evaluated using eq.s (8.33) (8.34) and (8.35). In particular the $\ddot{r}$ parameter was calculated solving the semi-classical equation of motion using *Mathematica*7 program [178]. Then, the scattering cross section $\left(\frac{d\sigma(\theta)}{d\Omega}\right)_{sc}$ was calculated by CC calculations using the Sao Paulo potential, in the same way described in Section 7.3.

Finally, the $P_{tr}(\theta)$ for the transition to the ground state and the bump at 16.9 MeV for the ^{14}C case, and the transition to the bump at 13.7 MeV for the ^{15}C one were extracted from the factorization (8.32) in the angular region $20° < \theta_{CM} < 25°$, where the bumps cross section is near its maximum value, considering the measured $\left(\frac{d\sigma(\theta)}{d\Omega}\right)_{tr}$. The obtained results are listed in Table 8.3. The observed strength for the two bumps is of the same order of magnitude of the $^{14}C_{g.s.}$. This result is consistent with the prediction of ref. [7], where the GPV strength is expected to be comparable with that of the ground state pairing vibration ($^{14}C_{g.s.}$ in the present case). This result support again the hypothesis of the population of a collective L = 0 resonance in the high part of the excitation energy spectrum.

Table 8.3. Transfer probabilities ($P_{tr}(\theta)$) for L = 0 transitions in the ^{12}C(^{18}O,^{16}O)^{14}C and ^{13}C(^{18}O,^{16}O)^{15}C reactions at 84 MeV for $20° < \theta_{CM} < 25°$.

Reaction channel	**Transfer probability** ($\times 10^{-4}$)	$\boldsymbol{P_{tr}(i)/P_{tr}(^{14}C_{gs})}$
$^{14}C_{g.s.}$	9.4	1
$^{14}C_{16.9}$	14.5	1.5
$^{15}C_{13.6}$	19.3	2.0

8.4.5 Measured widths

The measured widths of the two systems (FWHM = 2.5 MeV for the 13.7 MeV bump in ^{15}C and FWHM = 1.5 MeV for the 16.9 MeV bump in ^{14}C, see Section 6.6) are compatible with the GPV resonance, for which the FWHM was predicted to be in the range of 2-5 MeV for heavy nuclei [7]. The different values of the bump widths for ^{15}C and ^{14}C indicate a different half life, which is shorter in the case of ^{15}C. This can be due to various contributions.

First the ^{15}C bump is ~ 0.6 MeV higher above S_{2n} in the continuum than the ^{14}C one, so it has a larger *escape width* [8]. Moreover, the GPV mode can couple with the single particle excitations only in the ^{15}C case, where the $1p_{1/2}$ and $np_{1/2}$ transitions of the unpaired neutron can give a supplemental width (*spreading width*). In the ^{14}C case single particle excitations does not preserve the 0^+ angular momentum and the spreading mechanism is thus estimated to be smaller. On the other hand, in ^{14}C a coupling with the *h-h* 0^+ excitations is expected, leading to a *Landau width*. These mechanisms resemble what is found for GR [8]. In particular, the escape width was found to be the dominant contribution for light nuclei while the spreading and Landau mechanisms could generate structures on the main bump.

Conclusions

In the present work the $^{12}C(^{18}O,^{16}O)^{14}C$ and $^{13}C(^{18}O,^{16}O)^{15}C$ two-neutron transfer reactions at 84 MeV incident energy were investigated. These studies are inserted in a research line that aims at a systematic exploration of the reaction mechanism and the possible population of the GPV resonance via the ($^{18}O,^{16}O$) reaction on medium-light nuclei (in the mass region $10 \leq A \leq 20$). The ^{18}O beam was delivered by the Tandem van der Graaf installed at the Laboratori Nazionali del Sud (LNS-INFN) in Catania. The ejectiles were momentum analyzed and detected by the MAGNEX large acceptance magnetic spectrometer. This is an ideal instrument in order to perform such kinds of reactions, since it conjugates good energy and angular resolutions with a large acceptance both in solid angle and momentum. Applying the ray-reconstruction procedure to the experimental data, spectra up to ~22 MeV excitation energy were extracted for the residual nucleus. The population of the ground plus several known bound and resonant states of the residual nuclei are observed. For the ^{14}C case they lie at E_x = 6.10, 6.71, 7.00, 7.36, 8.33, 9.81, 10.43, 10.73, 12.88, 16.43, 16.74 MeV, whereas for the ^{15}C case states at E_x = 0.73, 3.12, 4.21, 4.65, 5.87, 6.85, 7.36 are populated. Such states are the same strongly populated in (t,p) reactions. In addition, two unknown broad structures are observed in the higher part of the excitation energy spectra, namely at 16.9 ± 0.1 MeV (FWHM = 1.2 ± 0.3 MeV) in the ^{14}C spectrum and at 13.7 ± 0.1 MeV (FWHM = 2.5 ± 0.3 MeV) in the ^{15}C one. The cross section angular distributions are extracted for the most excited transitions and for the unknown bumps in a wide angular range ($6° < \theta_{CM} < 55°$).

The data analysis of the experimental results is focused on both reaction mechanism aspects and nuclear structure investigations. From the reaction mechanism point of view, the direct one-step transfer of a correlated pair of neutrons is found to be dominant in ($^{18}O,^{16}O$) reactions, at least for the energies considered in this work. This finding is deduced evaluating some specific observables. First, the extracted transfer yields of the different reaction channels (inelastic, one- and two-neutron transfer) in the $^{18}O + ^{12}C$ and $^{18}O + ^{13}C$ collisions suggests the dominance of the correlated transfer (Section 7.1). Indeed,

the two-neutron removal process is found to be as probable as the one-neutron removal one for the $^{18}O + ^{12}C$ case, and reduced of a factor 1.6 in the $^{18}O + ^{13}C$ one. Such finding is very different from what usually found in literature, where reduction factor of at least 3 were found in the two-neutron transfer yields with respect to one-neutron ones.

Another signature of the correlated transfer dominance is found comparing the ^{14}C spectra populated via one- and two-neutron transfers (Section 0). The resulting spectra present very different features. In the (^{18}O,^{16}O) channel, states with configurations mainly described as a two-neutron cluster plus a ^{12}C core are strongly populated. Moreover, among the 3^-, 2^- doublet at 6.71 and 7.36 MeV, strongly excited in (^{18}O,^{17}O) reaction, only one state is populated in (^{18}O,^{16}O), the one with natural parity. In fact, a correlated one-step transfer of the two neutrons cannot populate states with un-natural parity.

The transitions to low lying states of the residual nucleus for the $^{12}C(^{18}O,^{16}O)^{14}C$ reaction are described for the first time within the a CRC scheme, using the São Paulo parameter-free double folding optical potential (Section 7.3). The obtained results demonstrate again the dominance of the direct transfer of a pair for the present reaction and the capability of such a theoretical framework to quantitatively describe the experimental angular distributions. Indeed, as regards the transition to the ^{14}C ground state, which shows oscillations typical of an $L = 0$ transition, DWBA as well as CRC calculation are consistent with the experimental results, both in shape and magnitude. The contribution of the two-step sequential transfer is also calculated and it is found to account for less than 5% of the total cross section. An interesting feature emerging from the angular distribution shape is that only the $L = 0$ transitions exhibits a clear oscillating pattern, whereas for $L \neq 0$ an almost flat trend is observed. Such a phenomenon is typical of heavy-ion transfer reactions near the Coulomb barrier and has been likely connected to the different phases of the transfer amplitude components associated to the different transferred angular momenta projections M. This finding can be exploited as a clear way to distinguish the $L = 0$ mode from the others by the appearance of the oscillations in the experimental angular distributions. This can be an important tool to recognize the GPV mode, which requires an $L = 0$ transfer.

In the second part of the data analysis the origin of the two unknown structures at 16.9 MeV in ^{14}C and 13.7 MeV in ^{15}C is investigated. The obtained results demonstrate that they correspond to the excitation of the GPV resonance. Several aspects of the analysis

converge to such conclusion. First of all, the break-up component in the spectra are evaluated assuming an uncorrelated removal of the two neutrons (Section 8.2). The results give a good account for the continuum background in the ^{15}C and ^{14}C spectra. Above the two-neutron emission threshold the enhancement of the cross section is explained as an increased probability to absorb two neutrons in the $d_{5/2}$ and $d_{3/2}$ states. However, the model is not able to reproduce the narrow resonances observed between S_n and S_{2n}, because of the lack of *n-n* correlations. Also, the bumps at 13.7 MeV in ^{15}C and 16.9 MeV in ^{14}C are missing and this indicates that the inclusion of *n-n* correlations is required to describe such structures.

The presence of a GPV in the energy region where the bumps are observed is supported also by QRPA calculations of the 0^+ excitations in the ^{14}C energy spectra. In particular, calculations of the response function corresponding to the transfer of a neutron pair to the ^{12}C nucleus are performed following the linear response approach and considering a zero-range density dependent pairing force (Section 8.3). A collective structure at about 16.5 MeV excitation energy with respect to the $^{14}C_{g.s.}$ is found in the calculated strength function, consistent with the experimental centroid of the ^{14}C bump at 16.9 MeV. This is one of the signatures which support the hypothesis of the GPV nature of such bump. Supplemental analysis of the features of the two structures in ^{14}C and ^{15}C demonstrate their common origin. In fact, if the excitation energy scale is referred to the target nucleus, scaling for the mass difference between the target and the residual nuclei, the excitation energy of the two bumps is found at the same value of ~ 20 MeV (Section 8.4.1). Moreover, the observed excitation energy corresponds in both nuclei to about 10 MeV above the first 0^+ state, where the $[1d_{3/2}\otimes 1d_{3/2}]_{0+}$ is expected to be. Moreover, the cross section angular distributions of the bumps show a clear oscillating pattern similar to that of the $^{14}C_{g.s.}$, thus indicating an $L = 0$ character of such transitions (Section 8.4.3). Finally, the bumps are found to have about the same strength as the transition to the $^{14}C_{g.s.}$, deduced from the extraction of the semi-classical transfer probabilities (Section 8.4.4), consistently with the theoretical predictions of the GPV strength with respect to the ground state one.

To summarize, the obtained results about the origin of the 16.9 MeV structure in ^{14}C and the 13.7 MeV one in ^{15}C populated via the (^{18}O,^{16}O) reaction at 84 MeV incident energy demonstrate that they correspond to the excitation of the long searched GPV, since they are found at the right predicted excitation energy and width (Section 8.4.5) and they

are populated with an $L = 0$ transfer and a large strength. This is the first experimental observation of the GPV and confirms the symmetry between *p-h* and *p-p* or *h-h* excitations.

The same (^{18}O,^{16}O) reaction on ^{12}C and ^{13}C target has been very recently performed at LNS-INFN at higher energy using a cyclotron ^{18}O beam at 270 MeV. The analysis of such experiment will hopefully help to understand the evolution of the GPV with increasing energy. Moreover, it is also interesting to study how the angular distributions are modified increasing the beam energy. In fact, it is predicted that above a threshold energy the oscillations in the angular distributions should appear also for $L \neq 0$. If such a condition (*good l-matching*) is reached in the (^{18}O,^{16}O) reaction at 270 MeV, this kind of reactions can be used as a complete spectroscopic tool for nuclear structure studies.

Acknowledgements

Concluding my Ph.D. course, there are many people that I would like to thank for giving me, in different ways, the support and the guidance necessary to go on in these years and to complete this work.

My first thanks goes to my tutor, Prof. Francesco Cappuzzello, that has guided and spurred me in these years. Working together day by day, he taught me how to scientifically face any problem. Special thank to Dr. Manuela Cavallaro, for the stimulating discussions and the useful suggestions. Billions of thanks to Mariangela Bondì and Dario Nicolosi for their continuous help and support and for having been close to me every day during this work. I would like to thank also the other members of my research group, Prof. Angelo Cunsolo, Prof. Nino Foti, Dr. Roberto Linares, Dr. Marzio De Napoli, Dr. Titti Agodi and Stefania Tropea, for the pleasant time spent working together.

Special thanks to Prof. Elias Khan, for kindly welcoming me during my visit in Orsay. Working with him has been a very fruitful experience. Thanks a lot to Prof. Jesus Lubian, Prof. Angela Bonaccorso and Cristina Rea, who helped me in finding the results of this thesis. They have always shown me their willingness to clarify all my doubts. Thanks also to Prof. Andrea Vitturi and Dr. Lorenzo Fortunato, for the fruitful discussions and suggestions.

Special thanks also to Dr. Roberta Spartà, who shared with me this journey, Cristina Schillaci, Valentina Scuderi, Lorenzo Neri for the pleasant time we spent together in our incubator office.

There are many other people who were close to me throughout these years. The biggest thanks goes to my parents for all the love they give me every day and to my brother Giorgio, who, though distant, could make me feel his support.

I sincerely thank my beloved husband Sebba, for always believing in me.

I also thank my friends, who have always been close to me: Laura, Simone, Antonella, Ciro, Alessio, Vanessa, Spita, Giorgia.

References

[1] A. Bohr and B. Mottelson, *Nuclear Structure* 1 - 2, Benjamin, New York (1969).

[2] P. Ring and P. Shuck, *The nuclear many body problem*, Springer-Verlag Berlin Heidelberg (1980).

[3] G.R. Satchler, *Direct Nuclear Reactions* Oxford University press, Oxford (1983).

[4] R.A. Broglia, O. Hansen, and C. Riedel, *Adv. Nucl. Phys.* 6 (1973) 287.

[5] W. von Oertzen and A. Vitturi, *Rep. Prog. Phys.* 64 (2001) 1247.

[6] J. Bardeen, L.N. Cooper, and J.R. Schrieffer, *Phys. Rev.* 106 (1957) 162.

[7] R.A. Broglia and D.R. Bes, *Phys. Lett.* B 69 (1977) 129.

[8] K.A. Snover, *Ann. Rev. Nucl. Part. Sci.* 36 (1986) 545.

[9] M.W. Herzog, R.J. Liotta, and L.J. Sibanda, *Phys. Rev.* C 31 (1985) 259.

[10] L. Fortunato, W. von Oertzen, H.M. Sofia, and A. Vitturi, *Eur. Phys. J.* A 14 (2002) 37.

[11] E. Khan, N. Sandulescu, N.V. Giai, and M. Grasso, *Phys. Rev.* C 69 (2004) 014314.

[12] E. Khan, N. Sandulescu, M. Grasso, and N.V. Giai, *Phys. Rev.* C 66 (2002) 024309.

[13] G.M Crawley et al., *Phys. Rev.* C 22 (1980) 316.

[14] G.M. Crawley, W. Benenson, D. Weber, and B. Zwieglinski, *Phys. Rev. Lett.* 39 (1977) 1451.

[15] B. Mouginot et al., *Phys. Rev.* C 83 (2011) 037302.

[16] B. Mouginot, *Ph.D. Thesis* Université Paris Sud 11 (2010).

[17] N. Anyas-Weiss et al., *Phys. Reports* C 12 (1974) 201.

[18] S. Kahana and A.J. Baltz, *Adv. Nucl. Phys.* 9 (1977) 1.

[19] D.M. Brink, *Phys. Lett.* B 40 (1972) 37.

[20] P.D. Bond et al., *Phys. Lett.* B 47 (1973) 231.

[21] H.G. Bohlen et al., *Phys. Rev.* C 68 (2003) 054606.

[22] S. Truong and H.T. Fortune, *Phys. Rev.* C 28 (1983) 977.

[23] N. Bohr and J.A. Wheeler, *Phys. Rev.* 56 (1939) 426.

[24] A. Bohr, B.R. Mottelson, and D. Pines, *Phys. Rev.* 110 (1958) 936.

[25] G. Potel, F. Barranco, E. Vigezzi, and R.A. Broglia, *Phys. Rev. Lett.* 105 (2010) 172502.

[26] B. Avez, C. Simenel, and Ph. Chomaz, *Phys. Rev.* C 78 (2008) 044318.

[27] D.R. Bes and R.A. Sorensen, *Adv. Nucl. Phys.* 2 (1969) 129.

[28] E. Khan, M. Grasso, and J. Margueron, *Phys. Rev.* C 80 (2009) 044328.

[29] E. Pllumbi et al., *Phys. Rev.* C 83 (2011) 034613.

[30] N. Zeldes, A. Grill, and A. Simievic, *Mat. Fys. Skr. Dan. Vid. Selsk.* 3 (1967) no.5.

[31] B. Cederwall et al., *Nature* 469 (2011) 68.

[32] J. Speth and A. van der Woude, *Rep. Prog. Phys.* 44 (1981) 719.

[33] Yu.V. Gaponov and Yu.S. Lutostansky, *Phys. of Atomic Nuclei* 73 (2010) 1360.

[34] G.F. Bertsch, R.A. Broglia, and C. Riedel, *Nucl. Phys.* A 91 (1967) 123.

[35] F. Catara, A. Insolia, E. Maglione, and A. Vitturi, *Phys. Rev.* C 29 (1984) 1091.

[36] P. Lotti, F. Cazzola, P.F. Bortignon, R.A. Broglia, and A. Vitturi, *Phys. Rev.* C 40 (1989) 1791.

[37] J.H.E. Mattauch, W. Thiele, and A.H. Wapstra, *Nucl. Phys.* 67 (1965) 1.

[38] G.E. Holland, N. Stein, C.A. Whitten, and D.A. Bromley, *Proc. Intern. Conf. on Nuclear Structure*, ed. J. Sanada, Phys. SOC. of Japan (1968) 703.

[39] P. Mukherjee and B.L. Cohen, *Phys. Rev.* 127 (1962) 1284.

[40] G. Igo, E.R. Flynn, B.J. Dropesky, and P.D. Barnes, *Phys. Rev.* C 3 (1971) 349.

[41] E.R. Flynn et al., *Phys. Rev.* C 3 (1971) 2371.

[42] C.H. Dasso and G. Pollarolo, *Phys. Lett.* B 155 (1985) 223.

[43] D.M. Brink, *Nucl. Phys.* 4 (1957) 215.

[44] L. Fortunato, *Phys. At. Nucl.* 66 (2003) 1445.

[45] A. Bouyssy and N. Vinh Mau, *Nucl. Phys.* A 224 (1974) 331.

[46] G. Ripka and R. Padjen, *Nucl. Phys.* A 132 (1969) 489.

[47] G.M. Crawley et al., *Phys. Rev.* C 23 (1981) 589.

[48] A.M. Moro, J.P. Fernandez-Garcia, M.A.G. Alvarez, and M. Rodriguez-Gallardo, *EPJ Web of Conf.* 17 (2011) 08001.

[49] M. Assié et al., *Eur. Phys. J.* A 42 (2009) 441.

[50] R. Neveling, F. Smit, H. Fujita, and R. Newman, *K600 User Manual* March 2008.

[51] R.A. Broglia and A. Winther, *Heavy-Ion reactions*, Addison-Wesley, Reading, Mass (1981).

[52] K.S. Krane, *Introductory Nuclear Physics*, Oregon State University, Jhon Wiley & Sons (1987).

[53] T. Honda, Y. Kudo, and H. Horie, *Prog. Theoret. Phys.* 63 (1980) 872.

[54] B.H. Wildenthal, B.M. Preedom, E. Newman, and M.R. Cates, *Phys. Rev. Lett.* 19 (1967) 960.

[55] G.R. Satchler, W.C. Parkinson, and D.L. Hendrie, *Phys. Rev.* 187 (1969) 1491.

[56] L.D. Landau and E.M. Lifshitz, *Quantum Mechanics*, Pergamon Press, London, Addison-Wesley, Reading, Mass (1958).

[57] K.W. Ford and J.A. Wheeler, *Ann. Phys. (N. Y.)* 7 (1959) 259.

[58] G. Breit and M.E. Ebel, *Phys. Rev.* 103 (1956) 679.

[59] R.A. Broglia and A. Winther, *Phys. Reports* 4 (1972) 153.

[60] H. Goldstein, *Classical Mechanics*, Addison-Wesley, Cambridge, Mass (1951).

[61] H.J. Korner, G.C. Morrison, L.R. Greenwood, and R.H. Siemssen, *Phys. Rev.* C 7 (1973) 107.

[62] M.J. Schneider, C. Chasman, E.H. Auerbach, A.J. Baltz, and S. Kahana, *Phys. Rev. Lett.* 31 (1973) 320.

[63] C. Chasman, S. Kahana, and M.J. Schneider, *Phys. Rev. Lett.* 31 (1973) 1074.

[64] W.T. Pinkston, D.H. Feng, M. Vallieres, and P.J. Iano, *Nucl. Phys.* A 351 (1981) 127.

[65] D.M. Brink and G.R. Satchler, *Angular momentum*, 2nd ed., reprint. Oxford University Press, Oxford (1971).

[66] T.A. Brody and M. Moshinsky, *Table of transformation brackets*, Gordon and Breach, New York (1967).

[67] D.H. Feng and T. Tamura, *Computer Phys. Commun.* 10 (1975) 87.

[68] D.H. Feng, T. Udagawa, and T. Tamura, *Nucl. Phys.* A 274 (1976) 262.

[69] N.K. Glendenning, *Annu. Rev. Nucl. Sci.* 13 (1963) 191.

[70] R.M. Drisko and F. Rybicki, *Phys. Rev. Lett.* 16 (1966) 275.

[71] B.F. Bayman and N.M. Hintz, *Phys. Rev.* 172 (1968) 1113.

[72] B.F. Bayman, *Phys. Rev. Lett.* 25 (1970) 1768.

[73] B.F. Bayman and D.H. Feng, *Nucl. Phys.* A 205 (1973) 513.

[74] B.F. Bayman, *Phys. Rev. Lett.* 32 (1974) 71.

[75] T. Tamura, T. Udagawa, and K.S. Low, *Phys. Lett.* B 48 (1974) 285.

[76] T. Takemasa, *Phys. Rev.* C 13 (1976) 2343.

[77] R.J. Ascuitto and E. Seglie, *Treatise on Heavy Ion Science*, vol. 1, ed. D.A. Bromley, New York: Plenum (1984).

[78] M. Iragashi and K. Kubo, *Phys. Rep.* 199 (1991) 1.

[79] L.J.B. Goldfarb and W. von Oertzen, *Heavy Ion Collisions*, vol. 1, ed. R. Bock, Amsterdam: North-Holland (1980).

[80] G. Potel, A. Idini, F. Barranco, E. Vigezzi, and R.A. Broglia, *Eur. Phys. J Web of Conferences* 17 (2011) 01004.

[81] B.F. Bayman and J. Chen, *Phys. Rev.* C 26 (1982) 1509.

[82] G. Potel et al., *Phys. Rev. Lett.* 107 (2011) 092501.

[83] P. Guazzoni et al., *Phys. Rev.* C 69 (2004) 024619.

[84] P. Guazzoni et al., *Phys. Rev.* C 74 (2006) 054605.

[85] P. Guazzoni et al., *Phys. Rev.* C 78 (2008) 064608.

[86] P. Guazzoni et al., *Phys. Rev.* C 83 (2011) 044614.

[87] M.-C. Lemaire and K.S. Low, *Phys. Rev.* C 16 (1977) 183.

[88] W. von Oertzen et al., *Eur. Phys. J.* A 21 (2004) 193.

[89] S. Mordechai et al., *Nucl. Phys.* A 301 (1978) 463.

[90] D.J. Millener and D. Kurath, *Nucl. Phys.* A 255 (1975) 315.

[91] W von Oertzen et al., *Eur. Phys. J.* A 21 (2004) 193.

[92] M. Yasue et al., *Nucl. Phys.* A 509 (1990) 141.

[93] H.T. Fortune and G.S. Stephans, *Phys. Rev.* C 25 (1982) 1.

[94] J.D. Goss et al., *Phys. Rev.* C 12 (1975) 1730.

[95] D. Bazin et al., *Phys. Rev.* C 57 (1998) 2156.

[96] G. Murillo, S. Sen, and S.E. Darden, *Nucl. Phys.* A 579 (1994) 125.

[97] R.J. Peterson, H.C. Bhang, J.J. Hamill, and T.G. Masterson, *Nucl. Phys.* A 425 (1984) 469.

[98] W.E. Moore and J.N. McGruer, *Bull. Am. Phys. Soc.* 4 (1959) 17.

[99] J.D. Goss, A.A. Rollefson, C.P. Browne, R.A. Blue, and H.R. Weller, *Phys. Rev.* C 8 (1973) 514.

[100] S.E. Dardeen, G. Murillo, and S. Sen, *Phys. Rev.* C 32 (1985) 1764.

[101] R. Jahn, D.P. Stahel, G.J. Wozniak, R.J. deMeijer, and J. Cerny, *Phys. Rev.* C 18 (1978) 9.

[102] F. Ajzenberg-Selove, *Nucl. Phys.* A 268 (1976) 1.

[103] F. Ajzenberg-Selove, H.G. Bingham, and J.D. Garret, *Nucl. Phys.* A 202 (1973) 152.

[104] J.D. Garret, F. Ajzenberg-Selove, and H.G. Bingham, *Phys. Rev.* C 10 (1974) 1730.

[105] A. Celler et al., *Phys. Rev.* C 43 (1991) 639.

[106] F. Cappuzzello et al., *Europhys. Lett.* 65 (2004) 766.

[107] Mod.439, Digital Current Integrator, Ortec, USA.

[108] Mod. V820, 32 Channel Latching Scaler, CAEN S.p.A., Viareggio, Italy.

[109] A. Cunsolo et al., *Nucl. Instr. Methods* A 481 (2002) 48.

[110] F. Cappuzzello, D. Carbone, M. Cavallaro, and A. Cunsolo, *MAGNEX: an innovative large acceptance spectrometer for nuclear for nuclear reaction studies* in Magnets: Types, Uses and Safety (Nova Publisher Inc., New York, 2011) pp.1-63.

[111] D. Rifuggiato et al., *J. Phys.: Conf. Ser.* 267 (2011) 012007.

[112] H.A. Enge, *Nucl. Instr. Methods* 162 (1979) 161.

[113] D.C. Carey, *The Optics of Charged Particle Beams*, Harwood Academic Publishers, 1987.

[114] A. Cunsolo et al., *Nucl. Instr. Methods* A 484 (2002) 56.

[115] M. Cavallaro et al., *Eur. Phys. J.* A 48 (2012) 59.

[116] F. Cappuzzello, D. Carbone, and M. Cavallaro, *Nucl. Instr. Methods* A 638 (2011) 74.

[117] A. Lazzaro et al., *Nucl. Instr. Methods* A 570 (2007) 192.

[118] A. Lazzaro et al., *Nucl. Instr. Methods* A 585 (2008) 136.

[119] A. Lazzaro et al., *Nucl. Instr. Methods* A 591 (2008) 394.

[120] A. Lazzaro et al., *Nucl. Instr. Methods* A 602 (2009) 494.

[121] K. Makino and M. Berz, *Nucl. Instr. Methods* A 427 (1999) 338.

[122] B. Schmidt, *Nucl. Instr. Methods* A 252 (1986) 579.

[123] C. Boiano, R. Bassini, A. Pullia, and A. Pagano, *IEEE Trans. Nucl. Sci.* 51 (2004) 1931.

[124] M. Bordessoule, F. Bartol, M. Lemonnier, and J.C. Santiard, *Nucl. Instr. Methods* A 390 (1997) 79.

[125] C. Boiano et al., *IEEE Trans. Nucl. Sci.* 55 (2008) 3563.

[126] MOD. V550, CAEN Readout for Analogue Multiplexed Signal - Technical Information Manual. Viareggio, Italy, Aug. 2002.

[127] A. Lazzaro, *Ph.D. Thesis*, University of Catania (2003).

[128] D. Carbone, F. Cappuzzello, and M. Cavallaro, *Eur. Phys. J* A 48 (2012) 60.

[129] K. Lau and J. Pyrlik, *Nucl. Instr. Methods* A 354 (1995) 376.

[130] G. Charpak, G. Melchart, G. Petersen, and F. Sauli, *Nucl. Instr. Methods* 167 (1979) 455.

[131] G.F. Knoll, *Radiation Detection and Measurement*, John Wiley & Sons, Inc. (2000).

[132] F. Cappuzzello et al., *Nucl. Instr. Methods* A 621 (2010) 419.

[133] M. Berz, *AIP Conf. Proc.* 249 (1991) 456.

[134] M. Berz and K. Makino, *COSY INFINITY* Version 8.1, Department of Physics and Astronomy and NSCL, Michigan State University, East Lansing, USA, 2001.

[135] H.A. Enge, *Rev. Sci. Instr.* 35 (1964) 278.

[136] W.N. Catford, , CATKIN 2005.

[137] J.F. Ziegler, M.D. Ziegler, and J.P. Biersack, , SRIM-2008 3.

[138] M. Cavallaro et al., *Nucl. Instr. Methods* A 637 (2011) 77.

[139] MINUIT, Function Minimization and Error Analysis, CERN Program Library Long Writeup D506, version 92.1 (1992).

[140] J.A. Winger, B.M. Sherril, and D.J. Morrissey, *Nucl. Instr. Methods* B 70 (1992) 380.

[141] G.G. Ohlsen, *Nucl. Instr. Methods* 37 (1965) 240.

[142] H.G. Bohlen and W. von Oertzen, *Z. Phys.* A 285 (1978) 371.

[143] K.S. Low and T. Tamura, *Phys. Rev.* C 11 (1975) 789.

[144] C. Olmer et al., *Phys. Rev.* C 18 (1978) 205.

[145] R.M. DeVries and K.I. Kubo, *Phys. Rev. Lett.* 30 (1973) 325.

[146] D.G. Kovar et al., *Phys. Rev. Lett.* 30 (1973) 1075.

[147] M.C. Mermaz et al., *Phys. Rev.* C 20 (1979) 2130.

[148] M.A. Candido Ribeiro, L.C. Chamon, D. Pereira, M.S. Hussein, and D. Galetti, *Phys. Rev. Lett.* 78 (1997) 3270.

[149] L.C. Chamon, D. Pereira, M.S. Hussein, M.A. Cândido Ribeiro, and D. Galetti, *Phys. Rev. Lett.* 79 (1997) 5218.

[150] L.C. Chamon, D. Pereira, and M.S. Hussein, *Phys. Rev.* C 58 (1998) 576.

[151] L.C. Chamon et al., *Phys. Rev.* C 66 (2002) 014610.

[152] D. Pereira, J. Lubian, J.R.B. Oliveira, D.P. de Sousa, and L.C. Chamon, *Phys. Lett.* B 679 (2009) 330.

[153] G.R. Satchler and W.G. Love, *Phys. Rep.* 55 (1979) 183.

[154] M.E. Brandan and G.R. Satchler, *Phys. Rep.* 285 (1997) 143.

[155] J.F.P. Huiza et al., *Phys. Rev.* C 82 (2010) 054603.

[156] E. Crema et al., *Phys. Rev.* C 84 (2011) 024601.

[157] I.J. Thompson, *Comp. Phys. Rep.* 7 (1988) 167.

[158] S. Raman, C.W. Nester Jr., and P. Tikkanen, *At. Data Tables* 78 (2001) 1.

[159] M. Cavallaro et al., *Phys. Lett.* B (to be submitted).

[160] M. Assié and D. Lacroix, *Phys. Rev. Lett.* 102 (2009) 202501.

[161] F. Cappuzzello et al., *Phys. Lett.* B 711 (2012) 347.

[162] A. Bonaccorso, I. Lhenry, and T. Soumijarvi, *Phys. Rev.* C 49 (1994) 329.

[163] L. Lo Monaco and D.M. Brink, *J. Phys.* G 11 (1985) 935.

[164] A. Bonaccorso, D.M. Brink, and L. Lo Monaco, *J. Phys.* G 13 (1987) 1407.

[165] A. Bonaccorso and D.M. Brink, *Phys. Rev.* C 38 (1988) 1776.

[166] A. Bonaccorso and D.M. Brink, *Phys. Rev.* C 43 (1991) 299.

[167] A. Bonaccorso and D.M. Brink, *Phys. Rev.* C 44 (1991) 1559.

[168] A. Bonaccorso, *Phys. Rev.* C 60 (1999) 054604.

[169] D.M. Brink, *Semi-Classical Methods for Nucleus-Nucleus Scattering* , Cambridge University Press, 1986.

[170] J.H: Dave and C.R. Gould, *Phys. Rev.* C 28 (1983) 2212.

[171] J.T. Huang, C.A. Bertulani, and V. Guimaraes, *Atomic Data and Nuclear Data Tables* 96 (2010) 824.

[172] A. Winther and K. Alder, *Nucl. Phys.* A 319 (1979) 518.

[173] S. Burzynski et al., *Nucl. Phys.* A 399 (1983) 230.

[174] S. Kox et al., *Phys. Rev.* C 35 (1987) 1678.

[175] M. Grasso, N. Sandulescu, N. Van Giai, and R.J. Liotta, *Phys. Rev.* C 64 (2001) 064321.

[176] E. Chabanat, P. Bonche, P. Haensel, J. Meyer, and R. Schaeffer, *Nucl. Phys.* A635 (1998) 231.

[177] S. Lie, *Nucl. Phys.* A 181 (1972) 517.

[178] Wolfram Research, Inc., *Mathematica* Version 7.0, Champaign, IL (2008).